Doctoral Dissertation
Doctoral Program in Aerospace Engineering ($38^{th}$cycle)

# Optical Fiber Data Sensor Fusion for Aerospace Systems Lifecycle Management

By

**Alessandro Aimasso**
******

**Supervisor(s):**
Prof. Matteo Davide Lorenzo Dalla Vedova, Supervisor
Prof. Paolo Maggiore, Co-Supervisor

**Doctoral Examination Committee:**
Prof. Francesco Tornabene, Referee, Università del Salento
Prof. Daniel Milanese, Referee, Università di Parma
Dott. Pietro Ferraro, CNR ISASI Applied Sciences and Intelligent Systems
Dott.sa Sara Coppola, CNR ISASI Applied Sciences and Intelligent Systems

Politecnico di Torino
2026

# Declaration

I hereby declare that, the contents and organization of this dissertation constitute my own original work and does not compromise in any way the rights of third parties, including those relating to the security of personal data.

Alessandro Aimasso
2026

*To those who believed in it.*
*To those who would have liked to be there.*

# Acknowledgements

I would like to express my sincere gratitude to my supervisors, Professor Dalla Vedova and Professor Maggiore, for their invaluable, constant, and genuinely human support throughout my PhD journey. I am deeply grateful for their technical guidance, the trust they placed in me, the opportunities they provided, and their unwavering encouragement and presence throughout this entire path. My sincere thanks also go to Eng. Ferro for his valuable advice and for the opportunity to test integrated optical fibers in lunar regolith within the framework of an international collaboration with ESA. Finally, I would like to thank the entire ICARUS PoliTo Team for their incredible support during the flight tests, as well as all the students who, in different ways, contributed to the development of the project and the underlying technology.

# Abstract

This thesis presents the development and validation of an integrated optical sensing and data fusion framework for aerospace systems lifecycle management, based on Fiber Bragg Grating (FBG) technology. The work adopts a system-level perspective, addressing the entire data chain from sensing to information extraction. Starting from the design, characterization, and integration of FBG sensors within different materials, dedicated calibration methodologies were developed to ensure reliable strain and temperature measurements under operational conditions. To support scalable and real-time data handling, specific telemetry architectures were designed and implemented. In parallel, data visualization tools were introduced to enhance human–machine interaction, including desktop-based applications and augmented reality interfaces. The proposed framework was validated through a progressive experimental campaign, ranging from laboratory tests to full-scale flight experiments on instrumented UAV platforms. Distributed FBG sensor networks embedded within the aircraft structure were used to acquire high-resolution strain data under real operating conditions. The core contribution of this work lies in demonstrating that FBG data, when properly processed and fused, can be used not only for structural health monitoring but also for the estimation of complex parameters, such as flight dynamics ones. By exploiting physically-based models and appropriate combinations of strain measurements, key quantities such as load factor, roll rate, and pitch rate were reconstructed directly from the optical data. The comparison with inertial measurement unit (IMU) measurements shows strong agreement, validating the proposed data fusion approach in real flight conditions. These results highlight the potential of optical sensing technologies as enabling tools for multifunctional monitoring, supporting both structural assessment and dynamic state estimation. Overall, this research demonstrates how distributed optical sensing and data fusion can contribute to the development of intelligent aerospace systems, capable of self-monitoring and enhanced decision support across their operational lifecycle.

# Contents

# List of Figures

# List of Tables

# Chapter 1

# Introduction

The development of complex systems across all engineering fields requires the capability to measure a large amount of data. Such information must necessarily be acquired through the use of sensor networks, appropriately distributed and capable of providing the physical parameters required to support control logic. It is therefore evident that there is a strong demand for reliable and accurate sensors that maximize the trade-off between cost, quality, and quantity of the information provided, as well as the physical footprint of the overall measurement chain.

In the aerospace sector, these requirements are further intensified by the need for extremely accurate data — necessary to comply with stringent safety standards — while operating in highly hostile environments. Fiber-optic sensing, and in particular Fiber Bragg Grating (FBG) sensors, represents one of the most effective compromises to satisfy all these requirements. The intrinsic physical properties of optical fibers enable high performance even under extreme operating conditions, allow the measurement of a large number of parameters, and significantly reduce physical encumbrance.

Unlike traditional sensors, however, fiber-optic sensing does not yet provide a fully "plug-and-play" experience for the end user, as is the case, for example, with thermocouples or strain gauges. The use of optical sensing, and specifically FBG-based sensing, requires a system-level approach that can be broadly structured into three main phases:

- the definition of the physical parameters of interest, the number of measurement points required to characterize the phenomenon under investigation, and the geometric path imposed on the optical communication line;
- the definition of the fiber integration methodology, including the development of suitable packaging solutions for individual sensors, depending on the physical parameter to be measured;
- the calibration process (for individual sensors), as well as the design of control logic and data sensor fusion algorithms for integrated, system-level monitoring.

As will be extensively discussed in the following chapters, the response of FBG sensors is strongly correlated with the application conditions of the optical fiber itself. Consequently, the design, implementation, and development of data processing and control logic are essential in order to obtain reliable, repeatable, and engineering-relevant information.

The overall research activity described in this doctoral thesis therefore focuses on the analysis of all these aspects. In particular, the experimental activities were primarily aimed at testing, verifying, and validating usage procedures that are as standardized as possible for the measurement of individual physical parameters (such as temperature or strain). Building upon these foundations, the complexity of the monitored systems was progressively increased, with the objective of achieving a more integrated and modular use of optical fibers. Ultimately, this approach aims at the development of "intelligent systems" and innovative human–machine and machine–digital twin interface methodologies.

The ability to develop reliable and repeatable individual measurement systems thus becomes a fundamental prerequisite for the design of more complex sensor networks, in which individual FBG sensors are adapted to the geometry under investigation and the measured data are integrated into appropriate control logic or data sensor fusion algorithms, combining basic FBG measurement techniques with the specific complexity of the application. In Figure 1.1 a schematic representation of the overall workflow is shown.

The structure of this thesis reflects the approach described above, in order to improve clarity and logical flow. It is nevertheless important to emphasize that the subject matter inherently requires an iterative working methodology, dictated by the strong interdependence between system-level monitoring through optical fibers,

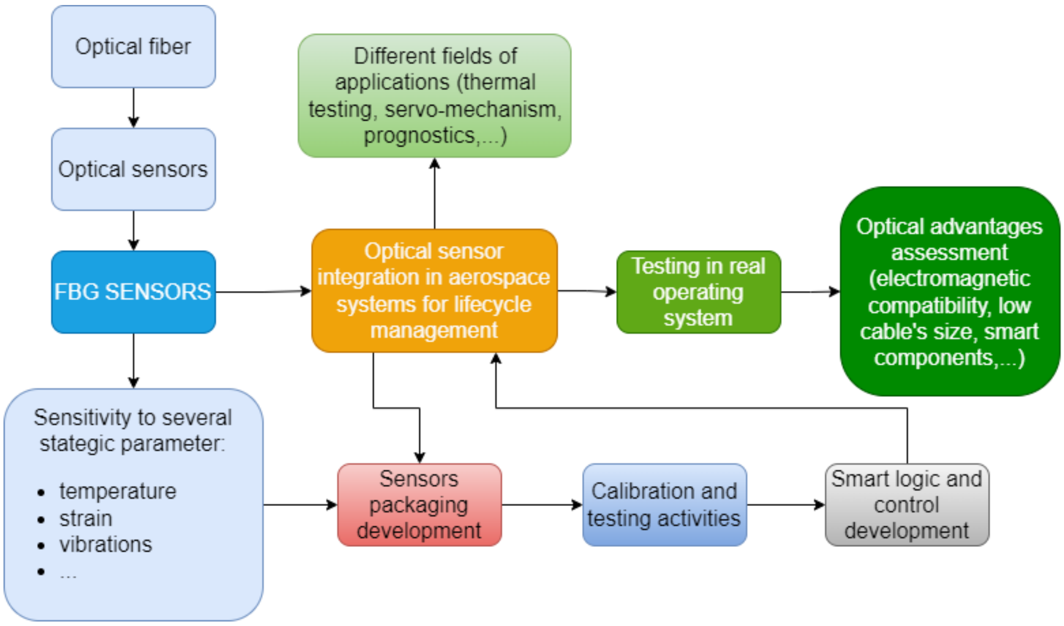


Fig. 1.1 The overall approach and workloagic adopted for FBG sensors network integration.

the development of "smart" components, and the integration strategies adopted for individual sensors.

Chapters 2 and 3 address, respectively, the operating physics of FBG sensors — including the associated instrumentation and procedures required to assemble a measurement line — and a state-of-the-art review of the use of this technology for aerospace system monitoring.

Chapter 4 analyzes the thermal response of FBG sensors. It describes the procedures adopted to develop different engineering solutions for thermal sensing, both point-based and distributed through the multiplexing of multiple gratings, and includes an industrial test campaign in the space sector.

Chapter 5 focuses on the mechanical characterization of FBG sensors, analyzing their capability to measure strain under both static and dynamic conditions, as well as in the presence of simultaneous thermal loading.

Chapter 6 discusses the development of proof-of-concept laboratory prototypes employing FBG sensors as pressure sensors, level sensors, and load cells, highlighting the influence of the adopted materials on the recorded optical response.

Chapter 7 presents the operational procedures developed for the integration of optical sensor networks into systems with complex geometries, addressing all aspects from design to installation of the measurement line.

Chapter 8 analyzes the development and testing of carbon-fiber-reinforced laminated specimens with optical fibers directly embedded within the composite material. This approach forms the basis for the development of “smart structures” capable of autonomously providing thermal and mechanical information about their physical state and, when combined with appropriate digital models, enabling data sensor fusion and virtual sensing strategies.

Chapter 9 presents a case study on the integration of an optical sensor network for multifunctional monitoring of a complex system, along with related in-depth analyses.

Chapter 10 examines different human–machine interface methodologies for data processing and visualization, comparing post-processing approaches, real-time desktop applications, and real-time visualization through augmented reality headsets.

Chapter 11 focuses on the use of augmented reality for the visualization of data provided by FBG sensors.

Chapter 12 analyzes the development and testing of the first UAV with embedded optical sensors. In this chapter, the main aspects previously discussed and tested are verified in flight, including near real-time data transmission and analysis.

Chapter 13 describes the ideation, implementation and testing of a "smart UAV" through an FBG sensor network directly integrated into the structure, defining a flight attitude monitoring algorithm entirely based on optical sensor data.

This schematic overview of the thesis chapters highlights the modular and progressive approach adopted throughout the work. After the state-of-the-art analysis, the initial chapters focus on the development of sensors for the measurement of specific physical parameters of increasing complexity. This phase was primarily aimed at identifying practical methodologies for the use of the technology, as well as defining and standardizing application procedures to enable the deployment of FBG sensors in meaningful engineering contexts.

The expertise developed in the creation, calibration, and management of individual sensors represented the first step toward the definition and realization of complex sensor networks integrated into systems of varying nature, geometry, and thermo-mechanical characteristics. The realization of embedded samples and specimens therefore constituted a natural progression toward the application of optical sensing to complex geometries, while simultaneously enabling the analysis - on relatively simple specimens - of the possibility to reconstruct system-level behavior through the appropriate interpretation of combined sensor responses.

All the information, procedures, and competencies developed and described in the first eleven chapters of the thesis find their ultimate application in Chapters 12 and 13. The integration of optical sensing onboard flying UAVs represents the application of the knowledge gained from simplified case studies to a real system characterized by significant complexity. The results obtained from the individual experimental campaigns enabled the realization of an optical sensing system integrated into a composite structure, capable of characterizing the vehicle attitude and instantaneous load factor by combining, in real time, the data provided by individual sensors. This result is not currently available in the literature and was achieved precisely thanks to the methodological and experimental groundwork described throughout this thesis.

# Chapter 2

# Optical Fiber and Sensors

Optical fiber is a dielectric waveguide that enables the transmission of information in the form of light signals through a mechanism of multiple reflections. It can be made from different materials; however, the most commonly used type for industrial applications and telecommunications is silica fiber [1]. The optical fiber consists of a cylindrical structure characterized by several concentric layers: the innermost part is called the core; moving outward, there are the cladding, the coating, and any additional protective layers.

The *core* is the innermost part and allows the transmission of the desired information in the form of a light signal. Its diameter varies from $9\,\mu m$ to $50\,\mu m$, depending on the type of fiber considered (single-mode or multi-mode).

The *cladding* is the intermediate layer and is essential to ensure the correct functioning of the optical fiber, as it enables total internal reflection of the light beam due to having a slightly lower refractive index than the core. It typically has a diameter of $125\,\mu m$.

The *coating* is the outermost layer and its function is to provide mechanical and chemical protection to the two inner layers. It is generally made of acrylate or polyimide and has a diameter of $250\,\mu m$. Beyond the coating, additional protective layers may be added, usually made of polymeric material.

Optical information is transmitted through the fiber by exploiting a mechanism of multiple reflections. Light is introduced into the core with an appropriate orientation, and each time it reaches the core–cladding interface it undergoes total internal reflection, allowing it to propagate along the core.

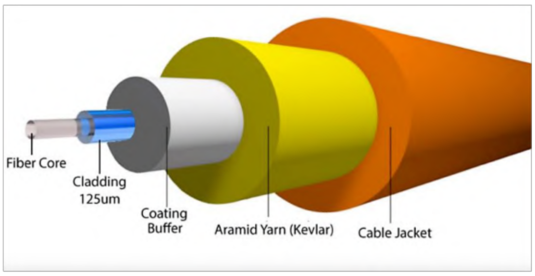


Fig. 2.1 Optical fiber layers.

This phenomenon is a specific application of the well-known Snell's law:

$$n_1 \sin \vartheta_1 = n_2 \sin \vartheta_2 \tag{2.1}$$

where $n_1$ and $n_2$ are the refractive indices of the core and the cladding, respectively; $\vartheta_1$ is the angle of incidence and $\vartheta_2$ is the angle of refraction, both defined with respect to the normal to the interface between the two media.

By setting $\vartheta_2 = \pi/2$, the critical case is obtained, which separates reflection from refraction into the cladding (and thus signal loss). Substituting this value into equation 2.1, the corresponding value of $\vartheta_1$ is obtained:

$$\vartheta_1 = \arcsin\left(\frac{n_2}{n_1}\right) \tag{2.2}$$

However, the light beam entering the core originates from the external environment (generally the instrumentation that generates the light itself), which has its own refractive index. Consequently, Snell's law must also be considered at the interface between the external medium and the fiber core.

The value of $\vartheta_1$ calculated for the critical case determines the maximum angle $\alpha_{max}$ allowed for light entering the fiber. The set of allowable directions defines the *acceptance cone*.

To calculate the acceptance angle $\alpha_{max}$, Snell's law is applied at the source/core interface:

$$n_0 \sin(\alpha) = n_1 \sin\left(\frac{\pi}{2} - \vartheta_1\right) \tag{2.3}$$

where $n_0$ is the refractive index of the external environment and $\alpha$ is the angle of incidence.

From this relation it is possible to derive:

$$\sin(\alpha) = \frac{n_1}{n_0}\cos(\vartheta_1) \tag{2.4}$$

Considering the critical condition for total internal reflection inside the fiber:

$$\cos(\vartheta_1) = \frac{n_0}{n_1}\sin(\alpha) \tag{2.5}$$

and squaring both sides:

$$\cos^2(\vartheta_1) = \frac{n_0^2}{n_1^2}\sin^2(\alpha) = 1 - \sin^2(\vartheta_1) \tag{2.6}$$

Substituting the critical value of $\vartheta_1$:

$$n_0^2 \sin^2(\alpha_{max}) = n_1^2 - n_2^2 \tag{2.7}$$

Therefore:

$$\alpha_{max} = \arcsin\left(\frac{\sqrt{n_1^2 - n_2^2}}{n_0}\right) \tag{2.8}$$

The coefficient $\sqrt{n_1^2 - n_2^2}$ is defined as the *Numerical Aperture* (NA). Thus:

$$\alpha_{max} = \arcsin\left(\frac{NA}{n_0}\right) \tag{2.9}$$

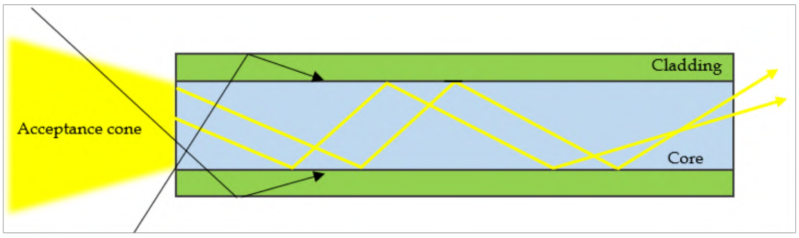


Fig. 2.2 Scheme of light propagation inside optical fiber.

A first macro-classification of optical fibers is represented by the distinction between single-mode and multi-mode fibers [2].
*Single-mode* fibers allow the propagation of only one optical mode. The core diameter is extremely small (typically not exceeding $10\,\mu m$), allowing the beam to propagate almost parallel to the axis of the fiber.
*Multi-mode* fibers, on the other hand, allow light to propagate in multiple modes. Consequently, the core diameter is much larger (approximately $50\,\mu m$). This larger diameter allows light rays with the same wavelength but different angles of incidence (always smaller than the acceptance angle) to enter the fiber. These rays propagate at the same speed but along different optical paths, reaching the detector at different times and producing temporal broadening of the transmitted pulse. This phenomenon is known as *modal dispersion*. It limits the rate at which adjacent pulses can be transmitted without overlapping, and therefore limits the maximum transmission speed of the optical communication system.
Single-mode fibers are widely used in telecommunications and industrial applications due to several advantages such as long service life (approximately 20 years), absence of modal dispersion, and low signal attenuation (less than $0.45\,\mathrm{dB/km}$). For this reason, throughout the present work reference will be made exclusively to single-mode optical fibers.

## 2.1 Optical Fiber Sensors

Optical fiber sensing technology includes several different classes of sensors. At the highest level, it is possible to distinguish between distributed sensors and point sensors [3].
*Distributed sensors* use the entire length of the optical fiber as the sensing element for data generation, and they can extend over several kilometers. These sensors rely

Table 2.1 Summary of fiber optic sensor types.

| **Category** | **Type** | **Principle** | **Measured Quantities** |
|---|---|---|---|
| Point Sensors | Intensity-based | Optical power variation | Displacement, pressure, vibration |
| | Interferometric | Phase variation (interference) | Strain, pressure, acoustic waves |
| | FBG | Wavelength shift (Bragg condition) | Strain, temperature |
| | Chemical / Biological | Absorption / fluorescence | pH, gas concentration, biomarkers |
| Distributed Sensors | Rayleigh scattering | Elastic scattering (OTDR) | Strain, vibration |
| | Raman scattering | Inelastic scattering | Temperature |
| | Brillouin scattering | Frequency shift (phonon interaction) | Strain, temperature |

on the analysis of scattering phenomena within the fiber, typically through Rayleigh, Raman, or Brillouin scattering mechanisms. By evaluating the time delay and spectral characteristics of the backscattered signal, it is possible to determine the spatial distribution of physical parameters along the fiber. Distributed sensing is particularly suitable for applications such as structural health monitoring, pipeline surveillance, power cable monitoring, and perimeter security, where continuous measurements over long distances are required.

*Point sensors*, on the other hand, perform measurements at specific and localized positions along the fiber. In this case, the sensitive element is located at a specific point of the fiber or, alternatively, an array of sensing points may be embedded along the fiber. Each of these points generates a variation in a specific characteristic of the optical spectrum propagating through the fiber. Typical examples include intensity-based sensors, which rely on variations in optical power; interferometric sensors, which detect phase changes in the optical signal; and Fiber Bragg Grating (FBG) sensors, where the measured quantity induces a shift in the reflected wavelength of a periodic grating inscribed in the fiber. These sensors are widely used for measuring parameters such as strain, temperature, pressure, and displacement. Table 2.1 report a schematic overview of the main types of optical sensors currently used in engineering applications.

## 2.2 Fiber Bragg Grating Sensors

Fiber Bragg Grating (FBG) sensors represent one of the best trade-offs currently available in terms of manufacturing cost, sensitivity, and measurement accuracy. An FBG is a fiber-embedded sensor consisting of a periodic and uniform modulation of the refractive index of the fiber core over a short section of optical fiber, typically a few millimeters in length. The portions of this section that exhibit a refractive index variation are periodically spaced by a distance known as the grating pitch, denoted as $\Lambda$ [4]. The grating can be considered an optical filter: when a broadband optical signal propagates along the fiber, the FBG allows all wavelengths that are not in resonance with the grating to pass through, while reflecting a very narrow spectral band centered at a specific wavelength. This wavelength, known as the Bragg wavelength, is defined as follows:

$$\Delta\lambda_B = 2n_{eff}\Lambda \tag{2.10}$$

where $\lambda_B$ is the Bragg wavelength (the reflected wavelength), $n_{eff}$ is the effective refractive index of the fiber core, and $\Lambda$ is the periodic spacing of the Bragg grating. This relationship highlights that the Bragg wavelength, which represents the output signal of the FBG sensor, is directly proportional to the grating pitch and to the effective refractive index of the fiber core.

Consequently, it is possible to establish a relationship between the variation of the Bragg wavelength and the variations of temperature and strain applied to the sensor. Using equation 2.10:

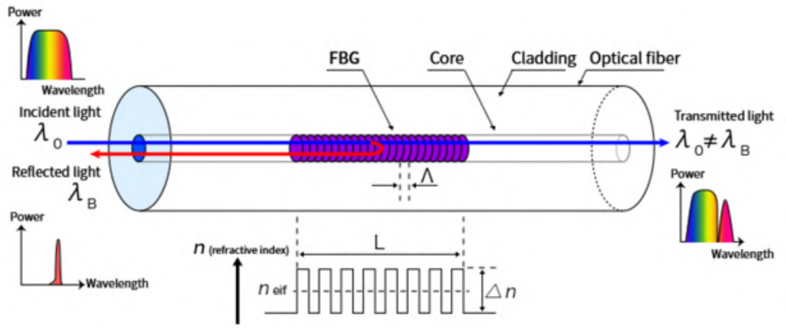


Fig. 2.3 Fiber Bragg Grating operating principle.

$$\frac{\Delta\lambda_B}{\lambda_B} = \frac{\Delta(n_{eff}\Lambda)}{n_{eff}\Lambda} \tag{2.11}$$

Equation 2.11 can be rewritten in order to explicitly show the contribution of strain and temperature:

$$\frac{\Delta\lambda_B}{\lambda_B} = \frac{\Delta(n_{eff}\Lambda)}{n_{eff}\Lambda} = \left(1+\frac{1}{n_{eff}}\frac{\delta n_{eff}}{\delta\varepsilon}\right)\Delta\varepsilon = (1+p_E)\Delta\varepsilon \tag{2.12}$$

$$\frac{\Delta\lambda_B}{\lambda_B} = \frac{\Delta(n_{eff}\Lambda)}{n_{eff}\Lambda} = \left(\frac{1}{\Lambda}\frac{\delta\Lambda}{\delta T}+\frac{1}{n_{eff}}\frac{\delta n_{eff}}{\delta T}\right)\Delta T = (\alpha_\Lambda+\alpha_n)\Delta T \tag{2.13}$$

By combining equations 2.12 and 2.13, the general expression describing the response of FBG sensors can be obtained:

$$\Delta\lambda_B = \lambda_B(1+p_E)\Delta\varepsilon + \lambda_B(\alpha_\Lambda+\alpha_n)\Delta T \tag{2.14}$$

where:

- $\lambda_B$ is the nominal reflected wavelength;
- $p_E$ is the strain-optic coefficient of the fiber;
- $\Delta\varepsilon$ is the variation of the fiber strain;
- $\alpha_\Lambda$ is the thermal expansion coefficient of the fiber;

- $\alpha_n$ is the thermo-optic coefficient of the fiber;
- $\Delta T$ is the temperature variation.

Equation 2.14 can be written in a simplified form as:

$$\Delta\lambda_B = K_T \Delta T + K_\varepsilon \Delta\varepsilon \tag{2.15}$$

Equation 2.15 represents the fundamental relationship governing the behavior of FBG sensors and constitutes the basis for interpreting all data generated by this sensing technology.

## 2.3 Materials and Instrumentation for Fiber Bragg Grating Sensor Network Development

This section presents the main equipment used to implement an optical measurement chain. Figure 2.4 illustrates the generic hardware architecture of the acquisition system. The system includes:

- an interrogator powered by an electrical supply;
- optical fibers physically connected to the interrogator;
- FBG sensors embedded within the fibers;
- a connection system (via cable or wireless) to a host PC for data storage and processing.

In addition to these elements, several tools are typically required for assembling the optical sensing network:

- fusion splicer;
- cleaver;
- stripper;

- connectors;
- feedthrough connectors;
- optical fiber segments containing FBG sensors.

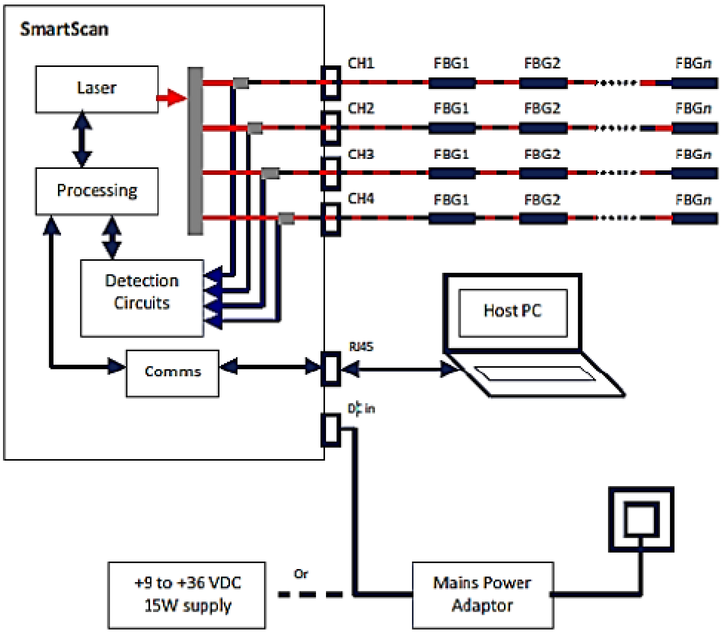


Fig. 2.4 General FBG sensors network acquisition system.

### 2.3.1 FBG Interrogator

The optical interrogator represents the core component of the data acquisition system, as the overall performance of the sensor network strongly depends on it. The interrogator performs a dual function: it sends a broadband optical spectrum into the fibers and, at the same time, detects the wavelengths reflected by the sensors, thereby identifying the different measurement points.

An interrogator is characterized by several parameters that determine the performance of the measurement system. The main parameters are:

- number of channels;
- number of sensors detectable per channel;

- emitted spectral bandwidth;
- sampling frequency.

The number of channels represents the number of physical fiber lines that can be simultaneously connected to the instrument. Together with the number of wavelengths detectable on each channel, it determines the maximum measurement capacity of the interrogator in terms of the number of simultaneous sensing points. Typically, widely used commercial models feature four channels, with up to sixteen sensors detectable per channel, resulting in a total of sixty-four measurement points.

The emitted spectral bandwidth represents the wavelength interval within which the interrogator both emits optical signals and identifies the reflected signals generated by the FBG sensors. This parameter is fundamental for two main reasons. First, a sensor operating outside this wavelength range cannot be detected by the interrogator. Second, the width of this interval can determine the effective number of measurement points that can be managed on a single fiber line, especially in the presence of significant thermal or mechanical variations affecting the sensors. Typical values for commercial interrogators correspond to a spectral bandwidth of approximately 40 nm, generally covering wavelengths between 1530 nm and 1570 nm.

Finally, the sampling frequency represents the number of measurements per second that the interrogator can perform on the wavelengths reflected by the connected sensors. This value may range from a few Hz up to several tens of kHz, allowing the acquisition of both static or quasi-static phenomena and highly dynamic events.

Several types of interrogators are available on the market. Variations in these parameters clearly affect the procurement cost and, in part, also the overall dimensions of the instrument.

Additional parameters that typically characterize an interrogator include:

- physical dimensions;
- industrial certifications;
- capability to upload data to cloud platforms;
- internal memory;

- supply voltage;
- integrated battery.

The interrogator model mainly employed in the research activities described in this thesis is the SmartScan. Table 2.2 reports its parameters listed above. Still

| **Measurement and Processing** | **SmartScan** |
|---|---|
| Wavelength Range | 40 nm (1528 – 1568 nm) |
| Number of Optical Channels | 4 |
| Maximum Number of Sensors/Channel | 16 |
| Scan Frequency (all sensors simultaneously) | 2.5 kHz |
| Maximum Scan Frequency (with reduced wavelength range) | 25 kHz |
| Repeatability | < 1 pm |
| Wavelength Stability | < 5 pm |

Table 2.2 SmartScan interrogator datasheet.

referring to the SmartScan device, some important features of the acquisition and data management software are also reported, as they play a fundamental role in any measurement acquisition phase:

- Wavelength–intensity plot (Figure 2.5). This plot provides a rapid, intuitive, and quantitative visualization of the connected sensors. The x-axis represents the spectral range within which the interrogator operates, while the y-axis represents the intensity of the wavelengths reflected by the sensors and detected by the instrument. Different colors are used to distinguish the channels of origin.
- Channel–sensor table. This table organizes the wavelengths reflected by the various sensors. The acquisition process consists of saving this table, instant by instant, into a file created on the host PC (Figure 2.6).

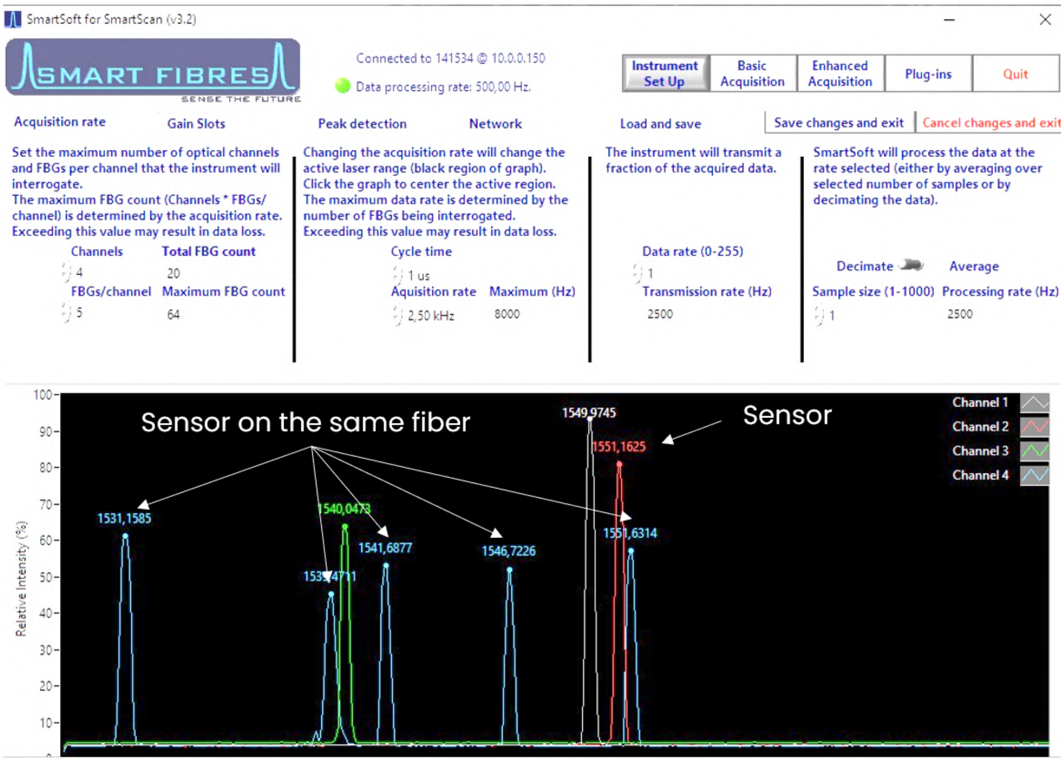


Fig. 2.5 Wavelength-Intensity plot.

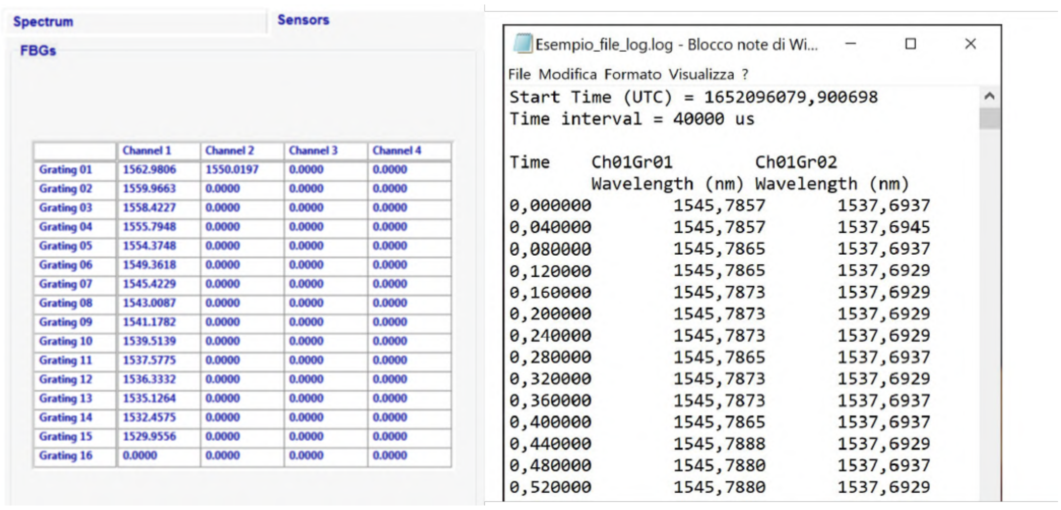


Fig. 2.6 Acquisition interface.

### 2.3.2 Commercial FBG Sensors

In the research activities carried out in this work, the sensors were always purchased directly from the commercial market. The typical commercial configuration consists of a segment of optical fiber of variable length (generally 1–2 m) in which the grating is located at the center. The sensor is commercially identified by its Bragg wavelength, namely the wavelength reflected by the grating under zero mechanical load and at ambient temperature.

The most widely used commercial sensors are manufactured using UV laser inscription, following specific fabrication techniques:

- *Phase mask*: a mask is placed between the UV laser beam (source) and the optical fiber. The shadow pattern generated by the phase mask determines the structure of the grating, based on the intensity distribution of the light reaching the fiber.
- *Femtosecond laser (point-by-point method)*: the laser emits optical pulses with durations of a few hundred femtoseconds and is used to inscribe the grating in the fiber point by point.
- *Interference lithography (or holographic lithography)*: this method uses two light beams. The original UV beam is split into two beams which, when directed toward the fiber, interfere with each other and generate a periodic intensity distribution along the fiber. The refractive index of the photosensitive fiber varies according to the light intensity to which it is exposed.

In general, for applications in harsh environments and/or aerospace-related contexts, gratings fabricated using femtosecond laser inscription are preferred, as they provide higher stability, improved measurement accuracy, and greater resistance to high temperatures.

### 2.3.3 Connectors and Feedthroughs

The interface between the sensors and the interrogator can only be managed through dedicated connectors, which ensure both the mechanical locking of the fiber and the correct alignment of the optical interfaces. In the applications discussed in this work,

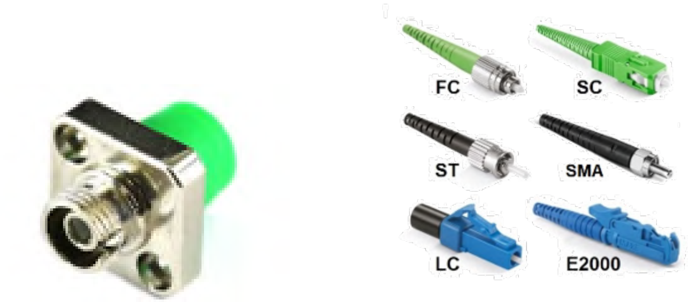


Fig. 2.7 FC-APC feedthrough and most common connectors.

FC-APC connectors were used almost exclusively. These connectors consist of a threaded metallic ferrule that guarantees excellent stability during operation, precise optical alignment, and is particularly suitable for repeated assembly and disassembly operations.

In a few cases, LC-APC connectors were also employed. These connectors feature an automatic snap-lock mechanism but do not include a threaded metallic ferrule. Although they allow easier and faster manual handling, they are less suitable for mechanically demanding environments (such as those characterized by strong oscillations or vibrations) and for applications requiring frequent insertion and removal operations.

Finally, when dealing with particularly complex routing geometries, the use of feedthrough connectors becomes advantageous. Feedthroughs are female–female connectors that allow the connection of two fiber segments terminated with connectors. In the applications described in this work, only FC-APC feedthrough connectors were used.

### 2.3.4 Fusion Splicer, Cleaver, Stripper, and Recoater

The fusion splicer is the instrument used to join two segments of optical fiber. Through micrometric actuators, on which the fiber ends are positioned and automatically aligned by infrared cameras, the machine precisely aligns the two fiber segments between a pair of electrodes. These electrodes generate an electric arc that locally melts the optical material, allowing the fibers to fuse together. The entire process is fully automated.

The cleaver and the stripper are two tools that support the splicing process. The stripper is used to remove the protective coating from the fiber, an operation that

is necessary to perform the splice. The stripper may be manual - similar to a wire stripper used for electrical cables - or automatic, equipped with a blade controlled by dedicated micro-actuators. The cleaver, on the other hand, is a high-precision mechanical cutting tool used to produce a clean and perpendicular cut on the fiber ends before splicing.
Finally, the recoater is the instrument used to restore the protective coating on the section of fiber that has been spliced by the fusion splicer. In this case as well, the process is controlled by high-precision micro-actuators and is fully automated.

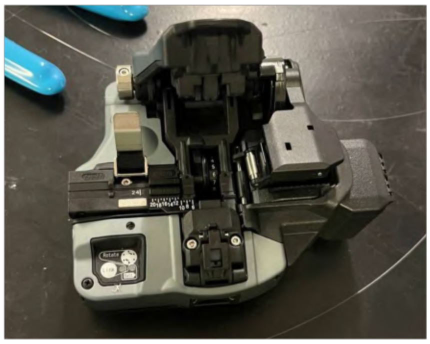

Fig. 2.8 Fusion splicer (left) and cleaver (right).

# Chapter 3

# FBG for Industrial and Aerospace Applications

Traditional sensing systems typically follow a relatively simple and standardized architecture. Regardless of the sensor type, the measured parameter, or the final application, two main components can generally be identified: a sensing element, which generates the information of interest by exploiting a specific physical principle, and a transmission cable that carries the generated electrical signal to the data acquisition and processing hardware. Fiber-optic sensing technologies introduce a fundamentally different paradigm. In these systems, the transmitted signal is optical rather than electrical, and the optical fiber itself is not merely a transmission medium. Instead, it simultaneously performs the role of sensing element and communication channel. This intrinsic dual functionality significantly modifies the traditional concept of a sensor and of the measurement process itself. The minimal invasiveness of optical fibers, combined with their capability to act both as sensing and transmission elements, enables the realization of so-called smart components. Such components are capable of continuously providing real-time information about their structural or operational condition throughout their entire service life.

Among optical fiber sensing technologies, Fiber Bragg Grating (FBG) sensors represent one of the most versatile and widely investigated solutions, with significant application potential across several engineering domains, including aerospace. The strong interest in this technology is mainly related to the unique combination of physical properties exhibited by optical fibers. First of all, optical fibers are inherently immune to electromagnetic interference, both in terms of emitted disturbances and susceptibility to external electromagnetic fields. Moreover, the complete absence of electrical conduction eliminates the need for shielding and prevents the generation of sparks, making optical fiber sensors particularly suitable for operation in potentially explosive environments. Another important advantage is related to the sensing architecture itself. The only active component required by the sensing system is the optical interrogator, which can be located at a considerable distance from the measurement point thanks to the extremely low attenuation of optical fibers. This allows the measurement unit to be positioned safely outside hazardous environments. These characteristics are complemented by high sensitivity, with typical resolutions reaching microstrain levels for deformation measurements and fractions of a degree for temperature sensing. Furthermore, optical fibers can operate over wide ranges of temperature and mechanical strain, making them suitable for demanding industrial and aerospace environments. From the intrinsic physical properties of optical fibers, additional advantages arise that cannot be easily replicated in traditional sensing systems. One of the most important features is the possibility of multiplexing multiple sensors along a single optical fiber. Each FBG reflects a specific Bragg wavelength, and multiple gratings can be placed in series along the same fiber without interfering with each other, provided that their Bragg wavelengths are properly separated. This capability allows the creation of distributed or quasi-distributed sensing networks using a single communication line.

For these reasons, FBG-based sensing represents a highly versatile and innovative solution with considerable potential for aerospace applications. The strategic interest in this technology primarily stems from the intrinsic physical characteristics of the optical fiber itself. From a sensing perspective, the Bragg grating exhibits high sensitivity to the physical parameters that modulate its response. In addition, because the measurement is purely optical, the sensing system does not require periodic recalibration, is not subject to mechanical wear, and does not suffer from signal degradation during transmission. As a result, FBG sensors can provide high reliability and measurement stability over long operational periods. Another fundamental aspect is the possibility of using the transmission medium itself as the sensing element. This unique feature enables the realization of integrated sensing systems in which the measurement infrastructure becomes part of the monitored structure. In addition, optical fibers exhibit several physical properties that are particularly compatible with the typical requirements of aerospace applications, including low weight, small dimensions, and high environmental robustness. The combination of these characteristics makes fiber optic sensing technologies - and FBG sensors in particular - extremely attractive for aerospace systems, where weight reduction, reliability, and distributed monitoring capabilities are essential requirements.

| **Advantages of Optical Fiber Sensors** |
|---|
| High sensitivity |
| Low weight and minimal invasiveness |
| Immunity to electromagnetic interference |
| Multiplexing capability |
| Absence of sparks and electrical conduction |
| Suitability for harsh and explosive environments |

Table 3.1 Main advantages of optical fiber sensing technology.

| Feature | Traditional Sensors | FBG Sensors |
|---|---|---|
| Signal type | Electrical | Optical |
| Immunity to electromagnetic interference | Low | Very high |
| Weight and size | Moderate / bulky wiring | Very low / compact fiber |
| Multiplexing capability | Limited | High (multiple sensors on one fiber) |
| Suitability for harsh environments | Limited | High |
| Spark generation risk | Possible | None |
| Installation distance from acquisition unit | Limited | Very long (km scale) |
| Maintenance and recalibration | Often required | Minimal |
| Signal degradation during transmission | Possible | Very low |
| Integration into materials | Difficult | Possible (embedded sensing) |

Table 3.2 Comparison between traditional sensing technologies and FBG-based sensing systems.

One of the most important application domains for FBG sensors is structural health monitoring (SHM). In civil engineering, FBG sensors are widely used for monitoring strain, temperature, displacement, and vibration in structures such as bridges, tunnels, dams, and large buildings. Their capability to be multiplexed along a single optical fiber allows the installation of dense sensing networks capable of providing real-time measurements over large infrastructures [5, 6]. In these applications, FBG sensors can be either surface-mounted or embedded directly within structural materials, enabling continuous monitoring of structural integrity and early detection of damage mechanisms such as fatigue or crack propagation.

Another important industrial sector where FBG sensing technology has been extensively deployed is the energy industry. In particular, FBG sensors are widely used for monitoring wind turbine structures, power transmission systems, and oil and gas infrastructure. In wind energy applications, FBG sensors are commonly embedded in wind turbine blades to measure strain and dynamic loading conditions during operation. These measurements provide valuable information for structural health monitoring and predictive maintenance strategies, helping to improve reliability and reduce operational costs [7, 8]. In electrical power systems, FBG sensors have been applied to monitor temperature and mechanical stress in power cables, transformers, and high-voltage equipment, where conventional electrical sensors may suffer from electromagnetic interference [9].

The oil and gas sector also represents a significant application area for FBG sensing technologies. Optical fiber sensors are particularly attractive in this domain because they can operate in high-pressure, high-temperature, and chemically aggressive environments. FBG sensors are used for monitoring parameters such as temperature, pressure, and mechanical strain in pipelines, offshore structures, and downhole oil wells. In these applications, they provide valuable information for leak detection, structural integrity monitoring, and reservoir management [10, 11].

Beyond these sectors, FBG sensors are increasingly employed in industrial process monitoring and smart manufacturing environments. Their passive nature, compact size, and multiplexing capability allow them to be integrated into complex machinery and industrial systems where continuous monitoring of temperature, strain, or vibration is required. This capability is particularly relevant in modern Industry 4.0 environments, where real-time sensing and data acquisition are essential for predictive maintenance and digital twin implementations [12, 13].

## 3.1 FBG for Harsh Environments

Fiber Bragg Grating sensors have attracted considerable interest for sensing applications in harsh environments due to their intrinsic physical properties. These characteristics make FBG sensors particularly suitable for applications where conventional electrical sensors may fail or require complex protection systems. Harsh environments are commonly encountered in several engineering fields, and this is particularly true for aerospace. In such conditions, sensing technologies must withstand extreme temperatures, radiation exposure, high pressures, corrosive chemical environments, and strong mechanical vibrations. Research on the use of FBG sensors in harsh environments has therefore focused on improving the robustness of optical fibers and gratings through specialized fabrication techniques, protective coatings, and advanced materials.

### 3.1.1 High-Temperature Sensing

One of the most extensively investigated topics in harsh-environment sensing is the use of FBG sensors for high-temperature measurements. Conventional Fiber Bragg Gratings written in germanium-doped silica fibers typically operate up to approximately 300–400 °C before the grating structure begins to degrade. To overcome this limitation, several research efforts have focused on developing high-temperature FBG sensors.

Erdogan [14] provided one of the most comprehensive theoretical analyses of fiber Bragg gratings, describing the optical properties of gratings and their sensitivity to strain and temperature.

Subsequent work by Cook et al. [15] introduced the concept of regenerated fiber Bragg gratings, which can operate at temperatures exceeding 1000 °C. Regenerated gratings are produced through thermal processing that stabilizes the grating structure, enabling sensing in extreme environments such as gas turbines.

Further developments were reported by Zhang and Grattan [16], who investigated high-temperature optical fiber sensing technologies and demonstrated the feasibility of using regenerated gratings in harsh industrial environments.

More recently, Wu et al. [17] demonstrated the use of fiber Bragg gratings written in sapphire optical fibers capable of operating at temperatures approaching 1600 °C. These sensors are particularly promising for applications in aerospace propulsion systems and high-temperature industrial processes.

### 3.1.2 Radiation-Resistant Optical Fiber Sensors

Radiation exposure represents another critical challenge for sensing technologies used in harsh environments. Radiation can induce changes in the refractive index of optical fibers and degrade sensor performance. Several studies have investigated the radiation response of FBG sensors.

Girard et al. [18] analyzed radiation effects in silica optical fibers used for sensing applications. Their study showed that radiation-induced attenuation and refractive index changes depend strongly on the fiber composition and manufacturing process.

Further work by Mihailov [19] reviewed the performance of fiber Bragg grating sensors in harsh environments and discussed techniques for improving radiation resistance. Rovera et al. [20] have demonstrated the performance of optical fiber sensors in high-radiation environments, which are particularly relevant for space applications. These works confirm that FBG sensors can operate under extreme conditions, although further research is required to improve their long-term reliability and environmental robustness.

### 3.1.3 High-Pressure and Deep-Sea Applications

Another important harsh environment is represented by high-pressure conditions, such as those encountered in oil and gas exploration or deep-sea monitoring. FBG sensors are particularly suitable for high-pressure sensing because the optical fiber itself can withstand significant mechanical stress while maintaining measurement accuracy.

Hartog [10] provided an extensive overview of distributed fiber optic sensing technologies used in oil and gas applications, including high-pressure sensing in pipelines and subsea systems.

Studies have demonstrated that FBG sensors can be integrated into pressure transducers or embedded within structural components to monitor mechanical loads and pressure variations in harsh industrial environments.

### 3.1.4 Chemically Aggressive Environments

In many industrial applications, sensing systems are exposed to chemically aggressive environments that can degrade conventional electrical sensors. Examples include petrochemical plants, chemical reactors, marine environments, and offshore infrastructures. Optical fibers are typically made of silica, which provides excellent chemical stability and resistance to corrosion. As a result, FBG sensors can operate reliably in environments involving corrosive gases, high humidity, and aggressive chemical compounds.

Yokogawa et al. [21] investigated the performance of fiber optic sensors in chemically aggressive industrial environments, demonstrating that properly packaged FBG sensors can maintain stable sensing performance even under corrosive conditions.

Similarly, Cusano et al. [22] explored the use of optical fiber sensors for chemical and environmental sensing applications, highlighting the advantages of silica-based optical fibers in chemically hostile environments.

Further studies by Leal-Junior et al. [23] demonstrated that optical fiber sensors can be used for monitoring environmental parameters in aggressive industrial environments due to their chemical inertness and immunity to electromagnetic interference.

These studies confirm that FBG sensors can operate reliably in chemically aggressive environments, especially when appropriate protective coatings and packaging techniques are used.

### 3.1.5 Extreme Mechanical Conditions

FBG sensors have also been investigated for sensing applications involving extreme mechanical conditions, including strong vibrations, high dynamic loads, and fatigue.

The high mechanical strength of silica optical fibers allows them to withstand significant strain levels while maintaining measurement accuracy. This property makes FBG sensors particularly attractive for applications involving rotating machinery, turbine blades, and structural components subjected to cyclic loading.

Kersey et al. [24] demonstrated that fiber Bragg gratings can measure strain with high resolution and can withstand significant mechanical deformation without degradation of sensing performance.

Further work by Lally et al. [25] investigated the use of FBG sensors for strain and vibration measurements in dynamic environments, showing that optical fiber sensors can operate reliably under high-frequency mechanical loads.

More recent studies by Guo et al. [26] examined the use of FBG sensors for monitoring vibration and structural dynamics in harsh mechanical environments, demonstrating their suitability for monitoring rotating machinery and structural fatigue.

These studies highlight the capability of FBG sensors to provide accurate measurements even under severe mechanical loading conditions.

## 3.2 FBG Integration in Materials

The integration of Fiber Bragg Grating sensors into structural materials represents a key aspect of their practical deployment in engineering applications. Unlike conventional sensors, which are typically attached externally to structures, optical fiber sensors can be integrated directly into the host material, enabling the development of so-called smart structures capable of monitoring their structural state throughout their operational life.

The small diameter of optical fibers (typically around 125 µm), combined with their mechanical flexibility and chemical stability, allows them to be integrated into a wide variety of materials, including composites, metals, and polymers. However, the integration process must be carefully designed to ensure efficient strain transfer between the host material and the optical fiber while avoiding damage to the fiber during manufacturing or operation.

Several integration approaches have been investigated in the literature, including surface bonding techniques, embedding within composite materials, integration in metallic structures, and the use of specialized coatings and packaging methods.

### 3.2.1 Surface Bonding Techniques

The most widely used method for installing FBG sensors on structural components is surface bonding. In this approach, the optical fiber is attached to the surface of the structure using an adhesive layer that ensures strain transfer between the host material and the fiber.

Surface bonding offers several advantages, including simplicity of installation and compatibility with existing structures. However, the quality of the strain transfer depends strongly on the properties of the adhesive layer.

Early work by Measures [5] investigated the use of surface-mounted optical fiber sensors for structural monitoring applications. The study demonstrated that properly bonded FBG sensors can accurately measure structural strain while maintaining good durability.

Further investigations by Li et al. [27] analyzed the strain transfer characteristics between the host structure and surface-bonded optical fibers, highlighting the importance of adhesive properties and bonding geometry.

More recently, Glisic and Inaudi [28] provided an extensive overview of installation techniques for fiber optic sensors in structural monitoring applications, including bonding procedures and long-term reliability considerations.

### 3.2.2 Embedded Sensors in Composite Materials

One of the most significant advantages of optical fiber sensors is the possibility of embedding them directly within composite materials during the manufacturing process.

Composite materials are widely used in aerospace structures due to their excellent strength-to-weight ratio. Embedding FBG sensors within composite laminates allows continuous monitoring of structural strain and damage evolution without affecting the aerodynamic profile of the structure.

One of the earliest demonstrations of embedded optical fiber sensing in composites was reported by Leng and Asundi [29], who investigated the integration of FBG sensors within composite laminates for structural health monitoring.

Further work by Takeda et al. [30] demonstrated the use of embedded FBG sensors for detecting impact damage in composite structures. Their experiments showed that strain measurements obtained from embedded sensors can provide valuable information about damage development within the structure.

More recent research by Kinet et al. [31] reviewed the use of embedded FBG sensors for structural health monitoring of composite materials, emphasizing the compatibility of optical fibers with advanced aerospace composites.

### 3.2.3 Integration in Metallic Structures

Although embedding optical fibers in composite materials is relatively straightforward, integration in metallic structures presents additional challenges due to the high temperatures involved in metal processing.

Several techniques have been investigated to enable the integration of optical fibers in metallic components.

One approach involves embedding the optical fiber during metal casting processes. Guo et al. [26] demonstrated the feasibility of embedding optical fibers within metallic structures using specialized protective coatings to prevent fiber damage during manufacturing.

Another approach involves the use of additive manufacturing techniques, which allow optical fibers to be integrated within metallic components during fabrication. This technique has recently attracted interest for applications in aerospace and advanced manufacturing.

### 3.2.4 Coatings and Packaging Techniques

To ensure reliable operation in harsh environments, FBG sensors are often protected using specialized coatings and packaging techniques.

Protective coatings can improve the mechanical strength of optical fibers and enhance their resistance to high temperatures, chemical corrosion, and mechanical stress.

For example, Mihailov [19] discussed the use of specialized coatings for FBG sensors designed to operate in harsh environments, including high-temperature and radiation environments.

Similarly, Zhang and Grattan [16] investigated packaging techniques for optical fiber sensors intended for high-temperature applications.

Proper packaging is particularly important when sensors are integrated into structural materials, as it ensures reliable strain transfer while protecting the fiber from mechanical damage.

## 3.3 FBG Applications in Aeronautical Systems

The aerospace sector imposes stringent requirements on sensing technologies, including minimal weight, high reliability, and the capability to operate under extreme environmental conditions. Optical fiber sensors are particularly well suited to meet these requirements because they combine low mass with the possibility of distributed sensing along a single optical fiber. As a result, FBG sensors have been widely investigated for monitoring aircraft structures, composite materials, aerodynamic loads, and propulsion systems. The literature on FBG sensing in aerospace applications can be broadly classified into four main research areas: structural health monitoring of aircraft structures, embedded sensing in composite materials, wing deformation and aerodynamic load monitoring, and sensing applications in propulsion systems.

### 3.3.1 Structural Health Monitoring of Aircraft Structures

Structural health monitoring (SHM) represents one of the most extensively studied applications of FBG sensors in aerospace engineering. Aircraft structures experience complex mechanical loads and fatigue cycles during operation, and continuous monitoring can significantly improve safety and maintenance strategies.

The use of FBG sensors for strain and temperature measurements was first systematically investigated by Kersey et al. [24], who demonstrated the high sensitivity and wavelength-encoded sensing capabilities of fiber Bragg gratings. Their work established the basis for the development of distributed sensing systems for structural monitoring.

Subsequent developments were presented by Measures [5], who explored the use of fiber optic sensors for monitoring structural behavior in aerospace components. The study demonstrated that distributed networks of FBG sensors could be deployed along aircraft structures to measure strain distributions in real time.

A large-scale demonstration of this concept was reported by Childers et al. [32], who implemented a sensing network consisting of several thousand FBG sensors installed on an aircraft structure and engine components. The system enabled simultaneous measurements of strain and temperature across multiple structural elements, illustrating the scalability of FBG sensing networks.

More recent studies have confirmed the suitability of FBG sensors for aircraft structural monitoring. Nicholas et. al [33] studied the deformation and associated loads of a full-scale CFRP (Carbon Fiber Reinforced Polymer) wing, inspired by the composite wings of gliders. The developed experimental system recreated the loading conditions typically experienced by wing panels; while the structure was sensorized with an array of more than 700 optical sensors. The results showed excellent consistency with the measurements performed using strain gauges, demonstrating the ability of the optical system to maximize the measurement points while minimizing the size of the sensors.

Many other similar applications are available in literature, for example, Di Sante [34] provided a comprehensive review of fiber optic sensors for monitoring composite aircraft structures, highlighting the advantages of FBG technology in detecting strain distributions and identifying structural damage. In the same fields, significative applications have been descripted by Hocha et al. [35] and Garcia et. al. [36]

More recently, Wada et al. [37] presented a flight demonstration of aircraft wing monitoring using optical fiber sensing technologies. This study represents a significant step forward, as it validates the use of fiber optic sensors under real flight conditions, demonstrating their capability to provide reliable strain measurements during operation.

These studies confirm that FBG sensors are a viable solution for structural health monitoring of aircraft structures, particularly when real-time and distributed sensing capabilities are required.

### 3.3.2 General Systems Monitoring

Beyond general structural monitoring, FBG sensors have also been applied to specific aircraft subsystems.

For example, Iele et al. [38] investigated the use of fiber optic sensors for load monitoring in aircraft landing gear systems. Their work demonstrated that FBG sensors can accurately measure strain and load conditions in critical components subjected to high mechanical stress.

This application is particularly relevant for aerospace systems, where accurate load monitoring is essential for both safety and maintenance optimization.

In addition, studies such as Gustafsson [39] have explored the use of FBG-based sensing systems for overheat detection in avionics systems, highlighting the potential of optical fiber sensors for monitoring thermal conditions in aircraft subsystems.

Finally, Behbahani et al. [40] discussed the integration of optical sensing and communication systems in avionics, highlighting the potential of fiber optic technologies for next-generation aircraft systems.

### 3.3.3 Embedded Sensing in Composite Materials

Modern aircraft increasingly rely on composite materials such as carbon fiber reinforced polymers (CFRP). Although these materials offer excellent mechanical properties, their complex failure mechanisms require advanced monitoring techniques capable of detecting structural damage before catastrophic failure occurs.

One of the first demonstrations of embedded sensing in composite materials was presented by Leng and Asundi [29], who investigated the integration of FBG sensors within composite laminates. Their work showed that optical fibers could be embedded during the manufacturing process without compromising the mechanical integrity of the structure.

Further research on damage monitoring in composite structures was conducted by Takeda et al. [30], who used embedded FBG sensors to monitor impact damage and fatigue behavior in composite wing structures. Their experimental results showed that strain measurements obtained from embedded sensors could be used to identify the onset of structural damage.

Recent studies have further explored the integration of optical sensors within advanced composite structures. Kinet et al. [31] reviewed the use of FBG sensors for structural health monitoring of composite materials, emphasizing their potential for embedded sensing in aerospace structures. Similarly, Gabardi et al. [41] demonstrated the feasibility of embedding FBG sensors within carbon composite structures to achieve high-accuracy strain measurements.

The integration of sensing elements within structural materials has led to the development of so-called smart materials and smart structures, which are capable of continuously monitoring their own mechanical state throughout their operational life.

### 3.3.4 Wing Shape and Aerodynamic Load Monitoring

Another important application area for FBG sensors in aerospace engineering concerns the monitoring of wing deformation and aerodynamic loads during flight. Aircraft wings undergo significant elastic deformation due to aerodynamic forces, and accurate knowledge of this deformation is essential for both structural monitoring and aerodynamic analysis.

Ma et al. [42] proposed a sensing system based on distributed FBG sensors for reconstructing the shape of an aircraft wing during operation. By measuring strain along the wing structure, the system was able to reconstruct the deformation of the wing with high accuracy.

Similarly, Nicolas et al. [43] investigated the use of large-scale FBG sensor networks to estimate aerodynamic load distributions along aircraft structures. Their work demonstrated that strain measurements obtained from distributed sensors could be used to infer structural loads acting on the wing.

In addition, Choi et al. [44] demonstrated the feasibility of performing in-flight structural monitoring using FBG sensors installed on aircraft wings. Their study confirmed that optical sensing systems can operate reliably under real flight conditions, providing valuable information on structural deformation and vibration.

These studies highlight the potential of FBG sensors not only for structural monitoring but also for aerodynamic analysis and flight testing.

### 3.3.5 Monitoring of Aerospace Propulsion Systems

In addition to structural applications, FBG sensors have also been investigated for monitoring propulsion systems and engine subsystems. Aircraft engines operate under extremely demanding conditions, including high temperatures, strong vibrations, and large mechanical loads.

Early investigations into harsh environment sensing were reported by Rao (1997) [45], who discussed the potential of FBG sensors for temperature and strain measurements in environments such as gas turbines.

More recent studies have explored the use of optical fiber sensing technologies for engine monitoring. Pakmehr et al. [46] investigated the application of optical fiber sensors for monitoring gas turbine engines, demonstrating the feasibility of measuring parameters such as exhaust gas temperature.

Advances in high-temperature sensing have also been reported. Cook et al. [15] developed regenerated FBG sensors capable of operating at temperatures exceeding 1000 °C, enabling sensing in extreme engine environments.

Further developments were presented by Kim et al. [47], who demonstrated the integration of FBG sensors within turbine blade structures manufactured using additive manufacturing techniques. Their work showed that embedded sensors could measure both temperature and strain within turbine blades during operation.

Similarly, Berexa et al. [48] investigated the integration of optical fiber temperature sensors within turbine blades, demonstrating the feasibility of monitoring temperature distributions within the hot sections of gas turbine engines.

Finally, Wu et al. [17] proposed sapphire-based FBG sensors capable of operating at temperatures approaching 1600 °C, offering promising solutions for sensing applications in the hottest regions of aerospace propulsion systems.

## 3.4 FBG applicationsin Space Systems

Spacecraft systems operate under extremely demanding environmental conditions, including large thermal gradients, vacuum, radiation exposure, and strong mechanical loads during launch. These conditions impose strict requirements on sensing technologies in terms of reliability, weight, and robustness. Research on FBG sensors for space applications can be broadly categorized into several main areas, including structural monitoring of spacecraft, thermal monitoring systems, sensing in cryogenic environments, monitoring of deployable space structures, and radiation-resistant optical sensing technologies.

### 3.4.1 Structural Health Monitoring of Spacecraft Structures

One of the earliest research directions in the use of FBG sensors in space applications concerns the monitoring of structural loads and deformations in spacecraft structures. During launch, spacecraft components are subjected to strong vibrations and mechanical stresses, making structural monitoring an important aspect of mission safety.

Early studies by Udd [13] highlighted the potential of optical fiber sensors for smart structures in aerospace systems, including spacecraft structures and satellite components. The work demonstrated that fiber optic sensors could be integrated within structural elements to monitor strain and deformation in real time.

Froggatt and Moore [49] explored the use of distributed fiber sensing techniques for monitoring structural strain in large aerospace structures, including spacecraft components.

Friebele et al. [50] and Kabashima et al. [51] demonstrated the feasibility of using FBG sensors for monitoring strain in spacecraft structures, particularly during ground testing and simulated space conditions.

Later, Measures [5] discussed the use of fiber optic sensors for structural monitoring in aerospace structures, including satellites and launch vehicles. The study demonstrated that networks of FBG sensors could provide distributed measurements of strain and structural loads.

Experimental investigations on structural monitoring of spacecraft structures were reported by Kersey et al. [24], who demonstrated that FBG sensors could provide accurate strain measurements suitable for aerospace applications.

More recent work by Shi et al. [52] investigated the use of distributed FBG sensor networks for spacecraft health monitoring, showing that multiple sensors can be deployed along structural elements to provide real-time strain measurements.

In addition, Juwet et al. [53] explored the use of FBG sensors for monitoring composite structures in reusable space applications, highlighting their potential for next-generation space vehicles.

### 3.4.2 Thermal Monitoring in Space Systems

Thermal monitoring represents another major application area for FBG sensors in spacecraft systems. Spacecraft are exposed to extreme temperature variations due to orbital conditions and solar radiation, making accurate temperature monitoring essential for the safe operation of onboard systems. FBG sensors are particularly well suited for temperature measurements because the Bragg wavelength shift depends on both strain and temperature variations. When properly calibrated, the sensors can provide highly accurate temperature measurements over wide ranges.

Rao [45] described the use of FBG sensors for temperature measurements in harsh environments, highlighting their potential for aerospace applications.

Kim et al. [54] investigated the use of FBG sensors for measuring thermal expansion in space structures, demonstrating their capability to provide accurate temperature-induced strain measurements.

Mihailov [19] reviewed the use of fiber Bragg grating sensors in harsh environments, including space applications, and discussed their ability to operate under large temperature variations.

Similarly, Abad et al. [55] developed a fiber optic sensing subsystem for temperature monitoring in spacecraft, validating the use of FBG sensors under in-flight conditions.

More recently, Leal-Junior et al. [23]investigated the use of optical fiber sensors for temperature monitoring in aerospace environments, demonstrating the feasibility of multiplexed sensing systems capable of monitoring temperature distributions across spacecraft structures.

Further studies such as Wang et al. [56] have focused on improving temperature measurement techniques using FBG sensors, particularly for applications involving high thermal gradients.

### 3.4.3 Cryogenic Sensing in Space Propulsion Systems

Many space missions involve the use of cryogenic propellants such as liquid hydrogen and liquid oxygen. Accurate temperature monitoring of cryogenic tanks is essential to ensure safe storage and efficient operation of propulsion systems.

FBG sensors have been investigated for cryogenic sensing because they can operate reliably at extremely low temperatures while providing high measurement resolution.

Early research by Kersey et al. [24] demonstrated that FBG sensors could operate over wide temperature ranges, including cryogenic environments.

Later studies explored the use of FBG sensors for cryogenic temperature measurements in space propulsion systems. For example, Rao [45] discussed the use of fiber optic sensors for cryogenic sensing applications.

More recent research has investigated the use of FBG sensors for monitoring cryogenic propellant tanks in space missions, highlighting their ability to provide distributed temperature measurements along fuel storage systems.

### 3.4.4 Monitoring of Deployable Space Structures

Many spacecraft systems include deployable structures such as solar panels, antennas, and booms. These structures must deploy reliably once the spacecraft reaches orbit, and monitoring their structural behavior is important for mission success.

FBG sensors have been proposed as a solution for monitoring deformation and structural loads in deployable structures.

For example, Measures [5] discussed the use of optical fiber sensors for monitoring deployable space structures such as satellite antennas and solar arrays.

Similarly, Kinet et al. [31] reviewed the use of FBG sensors for structural health monitoring of advanced structures, including aerospace and space applications.

These studies demonstrated that FBG sensors can provide valuable information about structural deformation during deployment and operation of space structures.

### 3.4.5 Radiation Effects on Fiber Optic Sensors

One of the major challenges for the use of optical fiber sensors in space is the presence of ionizing radiation. Radiation exposure can affect the optical properties of fibers and potentially degrade sensor performance.

Several studies have investigated the radiation resistance of FBG sensors. For example, Mihailov [57] analyzed the behavior of FBG sensors in radiation environments and discussed techniques for improving radiation resistance.

Further research by Kinet et al. [58] explored the effects of radiation on fiber optic sensors and evaluated the suitability of different fiber types for space applications.

These studies have shown that with appropriate fiber materials and sensor designs, FBG sensors can operate reliably in radiation environments typical of many space missions.

### 3.4.6 General Monitoring in Space Systems

Several studies in literature are available regarding general monitoring tasks for space systems. Starting from shape and general loads monitoring, Wei et al.[59] demonstrated the use of FBG sensors for monitoring the shape of satellite wing structures, enabling the reconstruction of structural deformation under operational conditions. More recently, Jiang et al. [60] proposed an array-based FBG sensing system for 3D reconstruction of spacecraft configurations, showing that distributed strain measurements can be used to reconstruct complex structural geometries.

A particularly important application of FBG sensors in space systems is the detection of impacts caused by micrometeoroids and orbital debris. Jin et al. [61] developed a method for detecting and locating micrometeoroid and orbital debris impacts using FBG sensors. Their work demonstrated that optical fiber sensors can detect high-frequency strain signals generated by impact events and determine their location.

FBG sensors have also been applied to monitoring fluid systems and spacecraft subsystems. Perikala et al. [62] developed an FBG-based flow sensor for space applications, demonstrating the feasibility of measuring fluid flow using optical fiber sensing technologies.

### 3.4.7 Experimental Demonstrations in Space Missions

A key step toward the adoption of FBG sensors in space systems is their validation in real operational conditions. Park et al. [63] investigated the use of FBG sensors in low Earth orbit environments, demonstrating their capability to operate under space conditions. Only in last year, Zhu et al. [64] proposed an on-orbit measurement method for spacecraft systems using optical sensing technologies, highlighting the increasing maturity of these systems.

In addition, Kruzelecky et al. [65] proposed demonstrator programs such as the Fiber Optic Sensor Demonstrator (FSD) described by have provided valuable experimental validation of optical fiber sensing technologies in space environments.

However, only limitate experience is available as on-orbit demonstration. The most notable example is the PROBA-2 satellite, developed by the European Space Agency (ESA). PROBA-2 is a technology demonstration mission designed to test innovative spacecraft technologies [66]. In the context of this mission, optical fiber sensors were investigated for monitoring spacecraft structures and temperature distributions. The objective was to evaluate the performance of optical fiber sensing technologies in real space conditions, including exposure to radiation and thermal cycling. Studies conducted within the PROBA-2 program demonstrated that optical fiber sensors could operate reliably in the space environment and provide accurate measurements of structural strain and temperature. These experimental programs represent an important step toward the integration of optical fiber sensing technologies into operational space missions.

### 3.4.8 Optical Fiber Sensors in ESA ARTES Programs

In addition to experimental demonstrations performed in space missions, optical fiber sensing technologies have also been investigated within several technology development programs promoted by the European Space Agency. Among these initiatives, the Advanced Research in Telecommunications Systems (ARTES) program has played an important role in supporting the development and qualification of innovative technologies for satellite telecommunications [67]. Within this framework, the ARTES-5 program focused on the development and validation of advanced payload technologies for space communication systems. Research activities conducted under this program explored the potential use of optical fiber sensing technologies for monitoring structural and thermal conditions in satellite payload systems. The interest in optical fiber sensors within the ARTES program is mainly related to their capability to provide distributed measurements with minimal mass and wiring complexity. These characteristics are particularly attractive for satellite platforms, where mass reduction and system reliability are critical design constraints. Studies performed in the context of ARTES technology development programs investigated the feasibility of integrating FBG sensors into satellite structures and communication payload components. In particular, the sensors were evaluated for monitoring temperature distributions, structural deformation, and thermal gradients in satellite subsystems. The results demonstrated that optical fiber sensing technologies could provide reliable measurements while significantly reducing cabling complexity compared with conventional electrical sensing systems. These technology development activities contributed to validating the suitability of FBG sensors for future satellite platforms and highlighted their potential role in next-generation spacecraft monitoring systems.

## 3.5 Gap in the Literature and Scope of this Thesis

The literature review has highlighted that several independent research efforts have already begun to evaluate the performance of FBG optical sensors in specific subsystems and well-defined experimental scenarios. These studies confirm the technical feasibility and reliability of FBG-based sensing for isolated measurements of temperature, strain, vibration, or pressure. However, a standardized and consolidated methodology for the system-level application of FBG sensors is still lacking. In particular, there is currently no widely adopted framework for the distributed integration of FBG sensing networks within a single product, aimed at maximizing the capability of measuring multiple physical parameters through a unified hardware architecture. The concept of employing FBG sensors in a fully integrated, multifunctional configuration - where a single optical infrastructure enables the simultaneous monitoring of several performance indicators - remains only partially explored. Similarly, the notions of virtual sensing and fully developed smart systems, enabled by deeply integrated optical sensing networks, have not yet reached a mature stage in aerospace applications. While isolated demonstrations are already available, a structured methodology that connects embedded sensing, real-time data fusion, and digital model updating is still under development.

For this reason, the present thesis first addresses well-established aspects of FBG technology - such as thermal sensitivity and mechanical strain response - with the objective of defining a repeatable and standardized methodology that enables autonomous and systematic use of optical sensors within the DIMEAS laboratory environment. Establishing this methodological foundation is a necessary step toward scaling the technology from laboratory validation to system-level integration. Subsequently, the proposed methodology is applied to both existing systems and specifically designed demonstrators in order to highlight the strengths, limitations, and future development perspectives of FBG-based sensing in aerospace applications. The knowledge and technical expertise developed throughout this research are ultimately consolidated in the realization of an innovative radio-controlled UAVs instrumented with a distributed and fully integrated FBG sensor network embedded directly within its composite structure.

This final demonstrator UAV serves as a proof of concept for the development of an intelligent structural system, in which the optical fiber acts not only as a sensing element but also as an intrinsic structural component, effectively transforming the structure itself into a distributed sensing platform. Through appropriate data processing and sensor fusion strategies, the embedded network enables the reconstruction of higher-level physical quantities. In the reference case of UAV, this means accelerations, angular rates, and load factor—typically obtained through conventional avionics instrumentation based on different physical principles.
The generation of such complex informational content serves a dual objective. On one hand, it demonstrates the feasibility of a novel sensing architecture that operates independently from traditional onboard avionics systems. On the other hand, it enables the measurement and estimation of physical parameters at locations that are difficult or impossible to instrument using conventional technologies. Ultimately, the distributed optical instrumentation developed in this work is conceived as a bridge between the physical system and its corresponding digital twin. Through embedded sensing, the physical structure becomes a direct and continuous source of high-density data, supporting the development, validation, and optimization of advanced digital models. In this perspective, FBG-based sensing is not merely a measurement tool, but a foundational technology for the realization of data-driven, intelligent aerospace systems.

# Chapter 4

# FBG for Thermal Monitoring

The simplest application of an FBG sensor for measuring a physical parameter is temperature measurement. This can be achieved by correlating the wavelength shift induced by the thermal expansion of the Bragg grating with the temperature variation. Recalling Eq. 2.10 and assuming that the entire strain acting on the grating is solely attributable to thermal expansion, it is possible to write:

$$\Delta\lambda = K_T \Delta T \tag{4.1}$$

Temperature measurement using FBG sensors is particularly important for several reasons:

- The Bragg grating ensures high sensitivity and the ability to operate effectively at both high and low temperatures.
- The Bragg grating can be employed either as a standalone temperature sensor, i.e., equipped with dedicated packaging, or as a temperature sensor directly integrated with the substrate on which the measurement is performed (surface-bonded or embedded within it).
- It enables thermal compensation for mechanical measurements.

In all these applications, the definition of the sensor calibration procedure becomes fundamental. Indeed, as already described in Section 2.2, for a simple optical fiber the coefficient $K_T$ can be expressed as:

$$K_T = \frac{(\alpha_\Lambda + \alpha)}{\lambda_B} \tag{4.2}$$

However, this equation accounts only for a bare silica optical fiber. This formulation, and the corresponding numerical value commonly reported in literature, may undergo slight variations depending on the manufacturing process of the individual sensor; more importantly, it remains valid only when no additional factors act on the grating. Consequently, for all applications in which the sensor is directly bonded to the measurement surface or embedded within the component manufacturing process, the resulting $K_T$ is determined by the combined effects of the optical fiber material, the material to which the fiber is applied, and the material used to bond the fiber to the substrate.

In order to quantitatively characterize the response of a generic optical sensor and to define an application methodology for engineering systems, different operating conditions were tested and the optical sensor response was analyzed.

In particular, this chapter presents:

- the realization of a purely thermal sensor, according to two different fabrication geometries;
- an experimental campaign of thermal cycling involving different sensors, materials, and environmental conditions;
- the development of a dedicated experimental test bench for evaluating the dynamic response of the sensors;
- the application of the acquired expertise to an operational case study in the space sector.

Although the use of FBG sensors for temperature measurement is well established in literature, this activity was fundamental to acquire the necessary expertise to independently develop the entire measurement chain, define installation, acquisition, and data interpretation methodologies, and ultimately proceed with the development of extended sensor networks capable of monitoring complex functions rather than simple physical parameters.

# 4.1 Thermal Probe

The first approach led to the development of a sensor with a geometry very similar to that of a traditional PT100. The adopted strategy consisted in defining a packaging that would make the sensor sensitive only to temperature variations. This packaging was identified as a metallic cylinder inside which the FBG sensor was encapsulated. To validate both the sensor manufacturing process and the obtained results, several sensors featuring different geometric characteristics were produced. Each sensor was encapsulated in an aluminum cylinder with a length of 300 mm. This length was selected as the best compromise between minimal sensor invasiveness and complete mechanical isolation of the FBG. In particular, each cylinder was manufactured in AlSi10Mg using Additive Manufacturing Technique [68]. Furthermore, in order to assess the possible effect of the cylinder geometry on the sensor response, a Design of Experiment (see Appendix A) was carried out in which the following parameters were varied:

- cylinder wall thickness;
- inner diameter;
- one or two through ends;
- fiber insertion method.

Specifically, the cylinder thickness was varied over two levels (1 and 1.5 mm), while the inner diameter was varied over three levels (1.8, 2, and 2.2 mm). In addition, both fully through cylinders and cylinders closed at one end were considered. Finally, the case of bonding the fiber to the metallic cylinder was also investigated.

All specimens were tested through thermal cycling in a climatic chamber over an operating range between −40 °C and +50 °C. The test was conducted by imposing, through the climatic chamber, a stepwise temperature ramp with steps of 10 °C within the considered range. In particular, the maximum transition rate was set, and each temperature level was held constant for 30 minutes. The entire ramp was repeated 10 times for each sensor.

The results were first analyzed in their raw form, namely in terms of wavelength evolution $\lambda(T)$. Subsequently, the wavelength values corresponding to each plateau

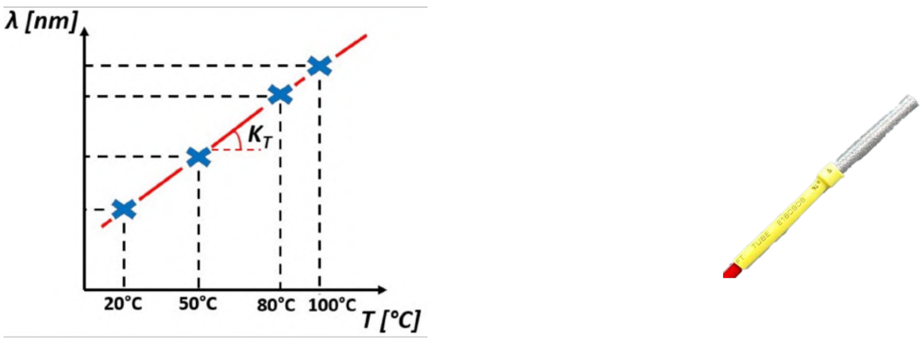


Fig. 4.1 Calibration strategy (left) and developed thermal probe (right).

were condensed into a single point, allowing the pointwise construction of the calibration curve $\lambda(T)$.

From the analysis of the raw data, it was possible to verify the very high stability of the measurement and the complete absence of mechanical interference affecting the data generated by the optical sensors. Given the excellent reliability of the measurements, the subsequent considerations were therefore carried out on the calibration curve $\lambda(T)$.

As expected, two significant conclusions clearly emerge:

- the presence of adhesive significantly alters the sensor calibration;
- the solution in which the fiber does not adhere to any surface and is only held in position by the heat-shrink interface–metallic cylinder is highly repeatable and consistent with literature data.

With regard to the sensors developed by resin casting inside the cylinder, it can be clearly observed that, already above 30 degrees, the degradation of the mechanical properties leads to a loss of linearity in the response. Moreover, even within the linear region, the resulting coefficient exhibits a value approximately 10% higher than the typical $K_T$ reported in the literature. This behavior is not unexpected, considering that the adhesive inside the metallic cylinder generates mechanical continuity between the sensor and the cylinder wall, which is characterized by higher thermal expansion.

Conversely, as expected, the adhesive-free solution yields a linear, reliable, and repeatable calibration curve that is independent of the geometric parameters of the casing. This aspect was confirmed by the numerical results obtained at the end of the DOE analysis.

In Figure 4.2 the calibration of the probe with the adhesive solution is reported; in Figure 4.3, the raw data and the calibration curve for the solution without adhesive are reported.

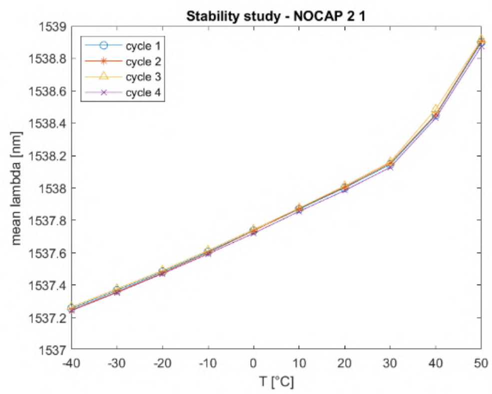


Fig. 4.2 Calibration curve of the probe with adhesive/fiber interface.

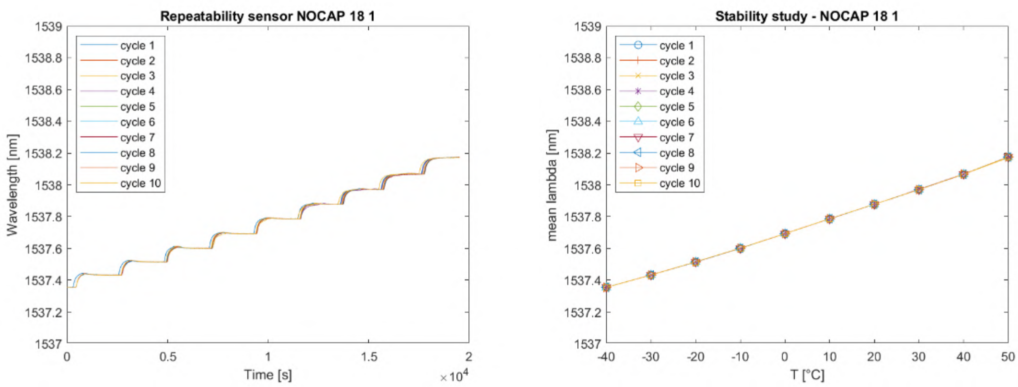


Fig. 4.3 Raw data (left) and calibration curve (right) for probe without resin.

## 4.2 Surface Thermal Sensor

The second approach in the development of a temperature sensor consisted in creating a solution capable of locally measuring temperature on a flat surface, without

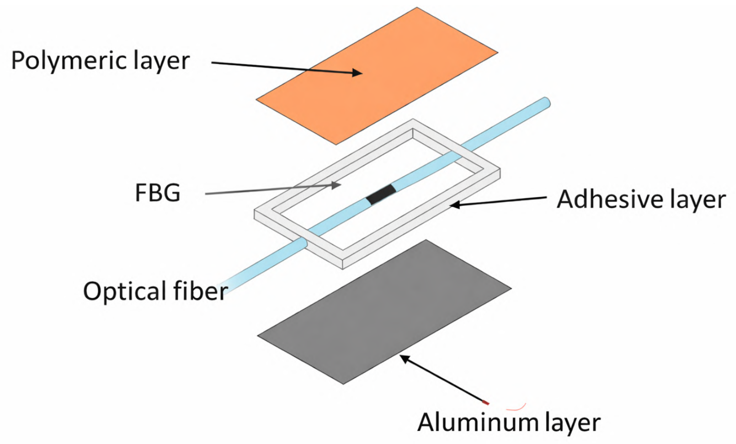


Fig. 4.4 Surface temperature design.

requiring the irreversible integration of the optical fiber with the substrate on which the measurement is to be performed. Figure 4.4 illustrates the concept and functional layout of the considered sensor.

A first thin aluminum layer is placed in contact with the measurement point and, if necessary, bonded or fixed depending on the required operating conditions. This extremely thin metallic layer is highly conductive and does not introduce significant thermal inertia into the measurement system. The FBG sensor is then placed on top of it: it is neither bonded nor mechanically constrained to the metal layer; however, being in contact with it, it is exposed to the same temperature. The absence of bonding allows the Bragg grating to deform due to thermal expansion solely according to the thermo-optical properties of the fiber, which are well known in the literature. This approach therefore greatly simplifies the sensor calibration process. The coefficient $K_T$ can, in fact, be directly assumed from the literature and/or from the sensor datasheet. Moreover, this type of solution allows the sensor to be calibrated prior to its final integration. Finally, the aluminum layer and the sensor resting on it are covered with a second polymeric layer. This polymeric layer fulfills a dual function:

- it mechanically constrains the fiber in the section preceding the sensor;
- it limits environmental thermal disturbances.

As a result, the final integrated solution enables fast, accurate, and repeatable temperature measurements over an extremely small and localized surface area, while minimizing size, installation complexity, and calibration procedures. Furthermore, the complete absence of mechanical constraints acting on the sensor ensures full decoupling between any structural deformation applied to the surface and the optical signal generated by the FBG.

Following the development of the first prototype, an initial testing campaign was conducted to calibrate and verify the sensor functionality based on the proposed design concept. Specifically, Figure 4.5 illustrates the setup used for thermal calibration. The experimental setup included a type-T thermocouple placed in close proximity to the FBG sensor. The testing campaign was carried out in a climatic chamber, subjecting the sensor to repeated thermal cycles consisting of several temperature steps. Each thermal step involved maintaining a constant temperature for 30 minutes, during which the average temperature and the corresponding average wavelength were recorded. The cycles were repeated 10 times in order to evaluate the uncertainty associated with the calibration curve $\lambda(T)$.

The results of the experimental analysis demonstrated a fully linear calibration curve, consistent with what was already discussed in Section 4.1, despite the completely different sensor geometry. In addition, a specific bending test was performed to verify the thermo-mechanical decoupling of the proposed solution. The integrated thermal sensor was placed on a thin and elongated composite specimen. At the same time, in close proximity to the temperature sensor, a second FBG sensor rigidly bonded to the specimen was installed. The entire setup was then subjected to bending load cycles. The results (Fig. 4.6) clearly showed the complete mechanical insensitivity of the proposed solution. This outcome enables the use of this geometry not only for the thermal characterization of a surface, but also, and especially, as an integrated solution for the thermal compensation of mechanical measurements, as will be described in Section 5.3.

Fig. 4.5 Experimental calibration with FBG and thermocouple.

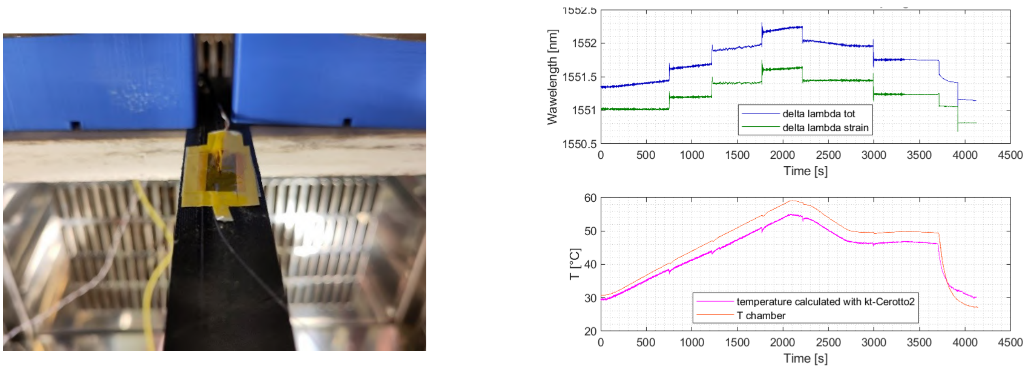


Fig. 4.6 Experimental setup for only FBG configuration validation.

## 4.3 Thermal Characterization of Embedded Sensors

The third approach to the temperature sensitivity of optical fibers no longer focuses on analyzing the performance of an external sensor housed within a specific packaging, but instead considers the sensor as directly integrated onto a given substrate. Initial exploratory tests highlighted a strong dependence of the coefficient $K_T$ on the materials employed. Furthermore, the combination of the optical fiber type (presence or absence of sensor coating, acrylate or polyimide), the selected substrate, and the bonding methodology revealed variations in the overall calibration curve, which under specific conditions exhibited a piecewise linear behavior.

This section therefore examines:

- the initial calibration cycles of integrated sensors;
- a dedicated experimental campaign aimed at comparing the main application solutions;
- the analysis of the observed nonlinearities.

### 4.3.1 Preliminary Analyses

The first calibration tests involved simple specimens, divided as follows:

- two rectangular carbon fiber specimens;
- one metallic plate.

On both carbon fiber specimens, an optical fiber with an FBG sensor was applied by means of epoxy resin bonding. In the first specimen, however, the fiber was simply laid in place and subsequently covered with resin, whereas in the second case it was bonded while subjected to a constant mechanical tension (useful for maintaining a shape as straight as possible). Although characterized by a significant degree of approximation, these two configurations can nonetheless represent two common cases of methodologies required for the development of specific fiber routing solutions. The third specimen consisted of a simple metallic plate on which the FBG sensor was held in position solely by means of Kapton adhesive, widely used in industrial applications and considered a reference standard for thermal testing.

The first test involved analyzing the specimens over an operating temperature range of 20 – 60 °C. The specimens were placed inside a climatic chamber, and the fiber data were compared with both the temperature measured by the chamber and that detected by a dedicated sensor positioned in close proximity to the optical fiber. The temperature was imposed to vary linearly throughout the entire test phase and always in an increasing manner. Figure 4.7 shows the results: the optical fiber exhibited a stable, accurate, precise, and consistent response with respect to the imposed and measured environmental conditions. Thermal inertia remained extremely low, to the extent that the most delayed measurement was found to be that provided by the climatic chamber control sensor.

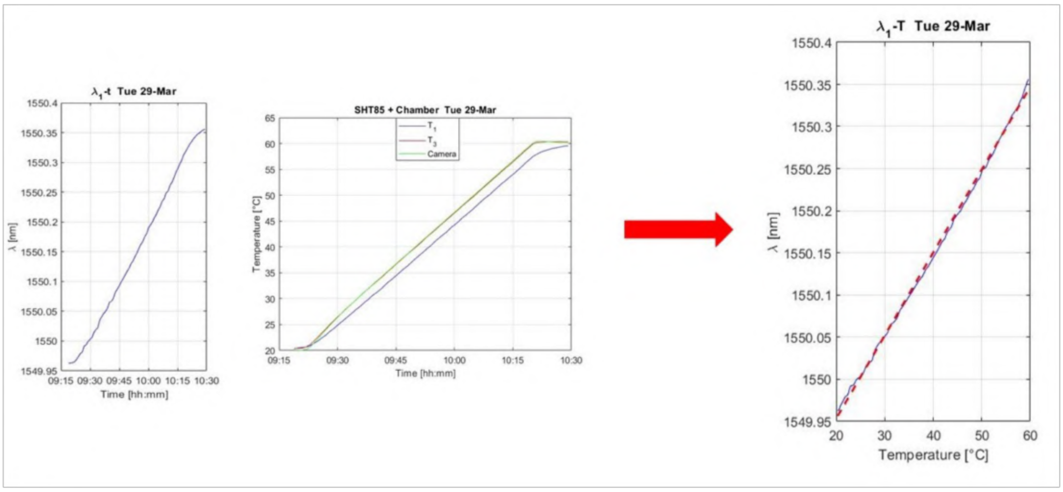


Fig. 4.7 First trial thermal test of surface thermal sensor in bonded bare fiber.

The excellent outcome of these preliminary tests therefore motivated the evaluation of the three proposed configurations over a wider thermal range, from −40 °C to 80 °C. While at higher temperatures the data proved to be fully consistent with a linear calibration, at strongly negative temperatures not all solutions maintained linear behavior, instead exhibiting a sudden increase in the value of $K_T$ (Fig. 4.8). This effect was particularly evident for the fiber bonded with Kapton onto the metallic plate.

A second, more specific test, conducted between −40 °C and 40 °C with a fiber simply laid on the surface of the climatic chamber, once again highlighted a change in the slope of the calibration curve at negative temperatures, thus confirming the presence of a specific contributing factor underlying this phenomenon. The variable results highlighted by these preliminary tests led to the development of a more targeted and specific testing campaign aimed at further investigating the observed scenarios.

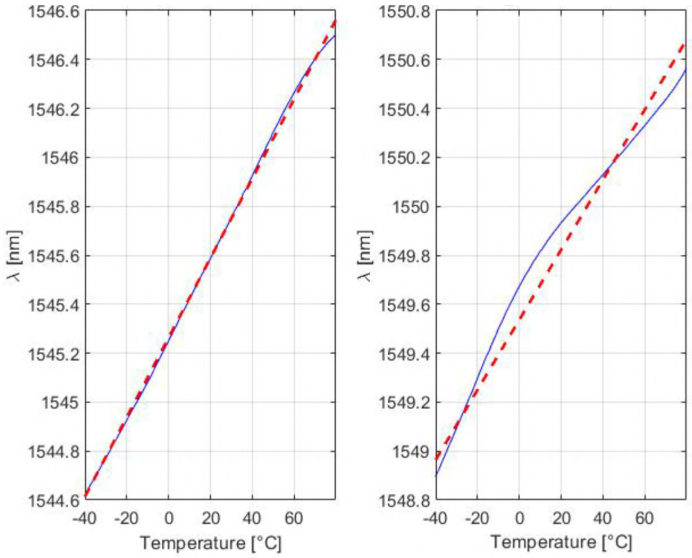


Fig. 4.8 Thermal calibration highlighting nonlinearities.

### 4.3.2 Experimental Campaign

The data presented in Section 4.3.1 highlighted the main reference parameters for a combined study of the thermal response of an FBG sensor integrated with the measurement surface. In particular, the following were identified:

- a metallic or composite/carbon-fiber surface;
- a pre-tensioned or non-pre-tensioned fiber;
- bonding using epoxy resin, cyanoacrylate adhesive, or Kapton.

In order to optimize the available resources, two specimens were manufactured: one with a metallic surface and one made of carbon fiber. Each specimen was instrumented with three integrated sensors: a pre-tensioned fiber bonded with epoxy resin (Fig. 4.10), a non-pre-tensioned fiber bonded with cyanoacrylate adhesive (Fig. 4.11), and a fiber bonded using Kapton (Fig. 4.12). Specifically, for the metallic specimen, a 1000-series aluminum, belonging to the category of continuous casting aluminum alloys, was selected. The physical parameters of the component are reported in Table 4.1. With regard to the carbon fiber specimen, the selected component was a composite material with a Carbowave and Rohacell 51A layup, as shown in Figure 4.9. The choice of this material is particularly significant, as it is typically used in the manufacturing of high-performance UAVs. The technical specifications of the material are reported in Table 4.2.

| **Property** | **Value** | **Unit** |
|---|---|---|
| Length | 25 | cm |
| Width | 5 | cm |
| Thickness | 0.5 | cm |
| Linear thermal expansion coefficient | $21 \cdot 10^{-6}$ | $K^{-1}$ |
| Thermal conductivity (at 20°C) | 130 – 160 | $J\ m^{-1}\ K^{-1}$ |
| Specific heat (at 100°C) | 0.90 | $J\ g^{-1}\ K^{-1}$ |
| Young modulus | 7500 | $kg\ mm^{-2}$ |
| Tensile strength | 240 | MPa |

Table 4.1 Geometric, thermal, and mechanical properties of the aluminum specimen.

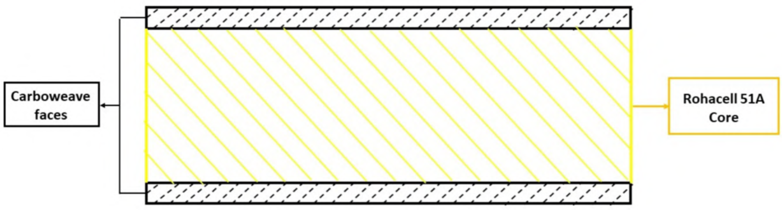


Fig. 4.9 Composite specimen structure.

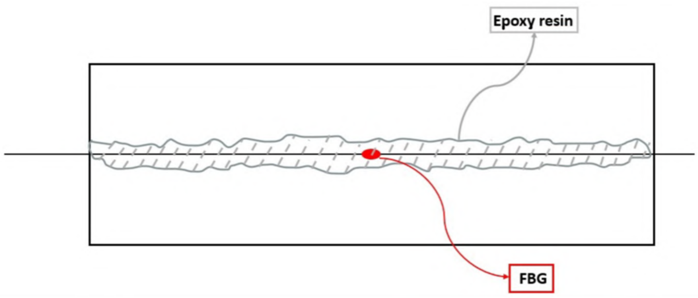


Fig. 4.10 Epoxy resin bonded fiber layout.

| **Property** | **Value** | **Unit** |
|---|---|---|
| Length | 25 | cm |
| Width | 5 | cm |
| Thickness | 0.5 | cm |
| *Carboweave Fabric (Tenax IMS65 24K)* | | |
| Tensile strength | 6000 | MPa |
| Tensile modulus | 290 | MPa |
| Elongation at break | 1.9 | % |
| Surface weight | 30 | $g/m^2$ |
| Fiber orientation | $\pm 45$ | $^\circ$ |
| Laminate thickness | 0.045 | mm |
| *Rohacell 51A (Core)* | | |
| Tensile strength at break | 1.90 | MPa |
| Flexural strength | 1.60 | MPa |
| Compressive strength | 0.900 | MPa |
| Shear strength | 0.800 | MPa |

Table 4.2 Technical Properties of the Composite Specimen.

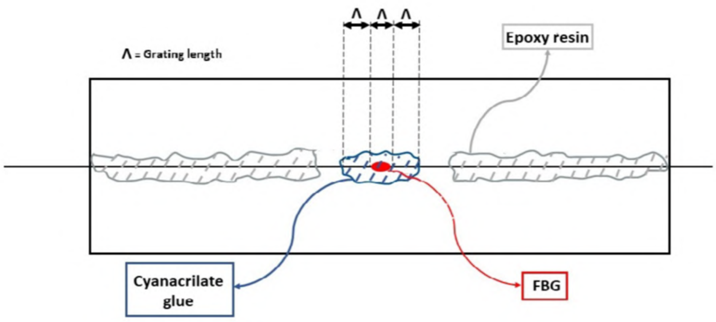


Fig. 4.11 Cyanoacrylate bonded fiber layout.

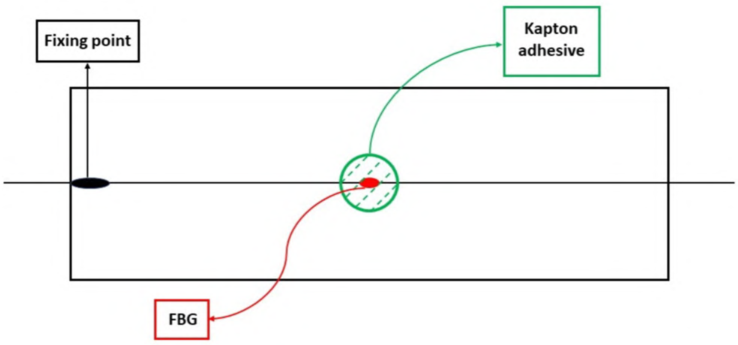


Fig. 4.12 Kapton bonded fiber layout.

All three selected bonding solutions were implemented on both specimens. Bonding with epoxy resin ensures excellent structural strength, good mechanical continuity with the surface, and high stiffness of the final product, which is extremely useful to avoid viscous relaxation or inaccuracies due to slippage and mechanical compliance. Cyanoacrylate adhesive represents the simplest and lowest-cost solution to implement. Bonding using Kapton, on the other hand, provides high versatility in terms of operating temperature range, compliance with industrial standards, and extreme operational simplicity. In addition, one possible condition is the application of a preload to the fiber, mainly for positioning requirements and/or for applications that may operate under compression. It was therefore decided to apply a pre-tension to the resin-bonded fiber, as this bonding technique is best suited for such a solution. Specifically, the fiber was kept under tension using a micro-positioning device and a support plate onto which the free end of the fiber was bonded. At the end of the resin curing process, this free end was removed.

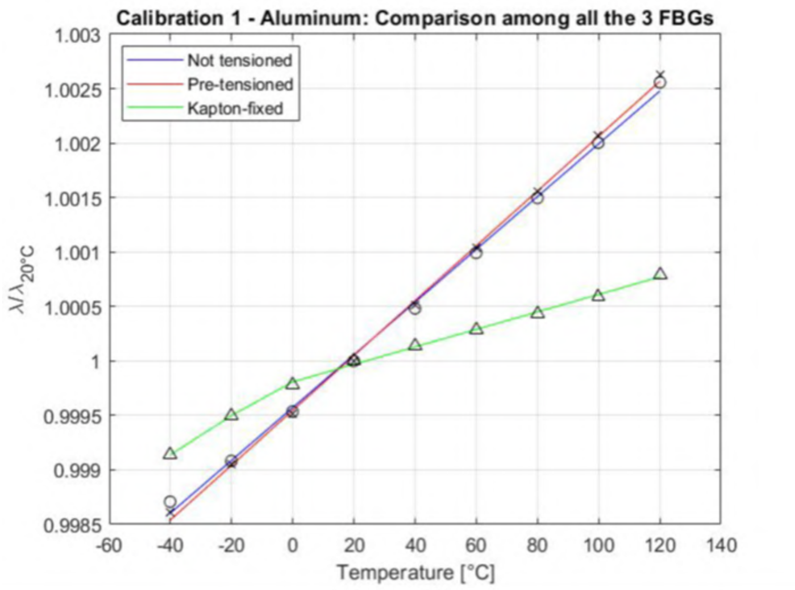


Fig. 4.13 Calibration results for aluminum specimen.

The two manufactured specimens were subjected to five complete test cycles over a temperature range between −40 and +120 °C. Thermal calibration was carried out using the stepwise procedure described in Section 4.1. In particular, nine analysis steps were defined at 20 °C intervals within the considered range. Each step was maintained for 20 minutes, a duration sufficient to ensure that the system reached thermal equilibrium. The relatively high number of points was selected in order to verify the linear nature of the calibration and, if necessary, promptly identify any deviation from this regime. The cycles were performed both from the cold extreme to the hot extreme and vice versa.

The corresponding numerical parameters are reported in Table 4.3.

| | **Epoxy resin** | **Cyanoacrylate** | **Kapton tape** | | |
|---|---|---|---|---|---|
| | *Linear fit* | *Linear fit* | *Linear fit* | *Cold conditions* | *Hot conditions* |
| $K_T$ [nm/°C] | 0.037 | 0.039 | 0.015 | 0.028 | 0.012 |
| $\lambda_0$ [nm] | 1537.35 | 1555.05 | 1541.35 | 1541.62 | 1541.54 |

Table 4.3 Calibration coefficients of aluminum specimen.

The corresponding numerical parameters are reported in Table 4.4.

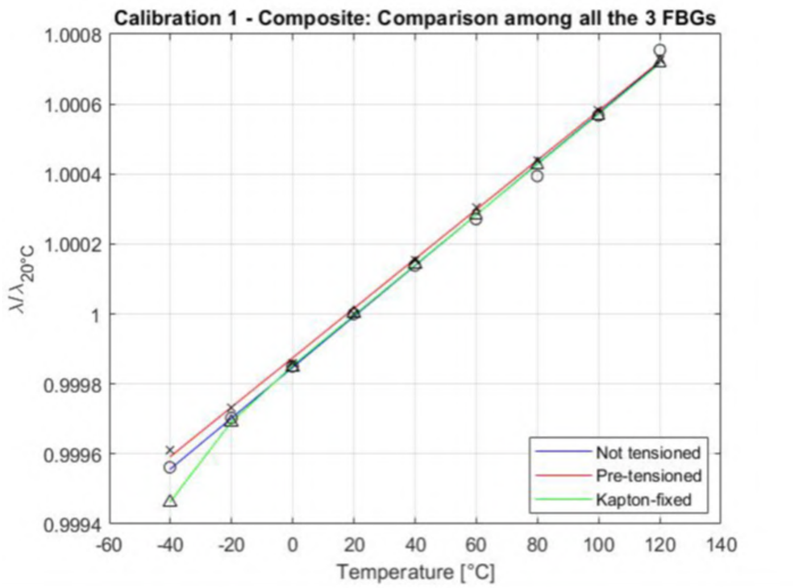


Fig. 4.14 Calibration results for composite specimen.

| | Epoxy resin | Cyanoacrylate | Kapton tape | | |
|---|---|---|---|---|---|
| | *Linear fit* | *Linear fit* | *Linear fit* | *Cold conditions* | *Hot conditions* |
| $K_T$ [nm/°C] | 0.042 | 0.039 | 0.015 | 0.02551 | 0.013 |
| $\lambda_0$ [nm] | 1536.87 | 1555.07 | 1541.49 | 1541.69 | 1541.64 |

Table 4.4 Calibration coefficients of composite specimen.

Overall, these results clearly highlight the significant technical advantage achieved by performing measurements through direct integration of the fiber with the reference structure, thus moving away from the concept of an “applied sensor” and effectively making the measurement surface itself a sensor of its own thermal conditions. The drawback, however, lies in the impossibility of defining a unique calibration curve, as it depends on the materials employed. Furthermore, the integrated approach necessarily requires the development of a well-defined, engineerable, and industrializable procedure in order to optimize the selected materials and minimize measurement errors attributable to the sensorization process.

The same procedure was therefore repeated five additional times in order to provide an initial statistical validation of the process. For the sensors bonded on aluminum, the following observations can be made:

- the resin-bonded and pre-tensioned fiber shows very high and linear measurement repeatability;
- the Kapton-bonded fiber maintains a piecewise linear behavior in all the performed measurement cycles;
- the cyanoacrylate-bonded (non-pre-tensioned) fiber exhibits excellent repeatability at high temperatures and a wider uncertainty range at low temperatures.

Conversely, for sensors bonded on the composite specimen:

- data repeatability is excellent for the Kapton-bonded sensor, but with pronounced variability near the lower extreme of the considered range;
- repeatability is good for the other two configurations, with slightly higher variability at low temperatures.

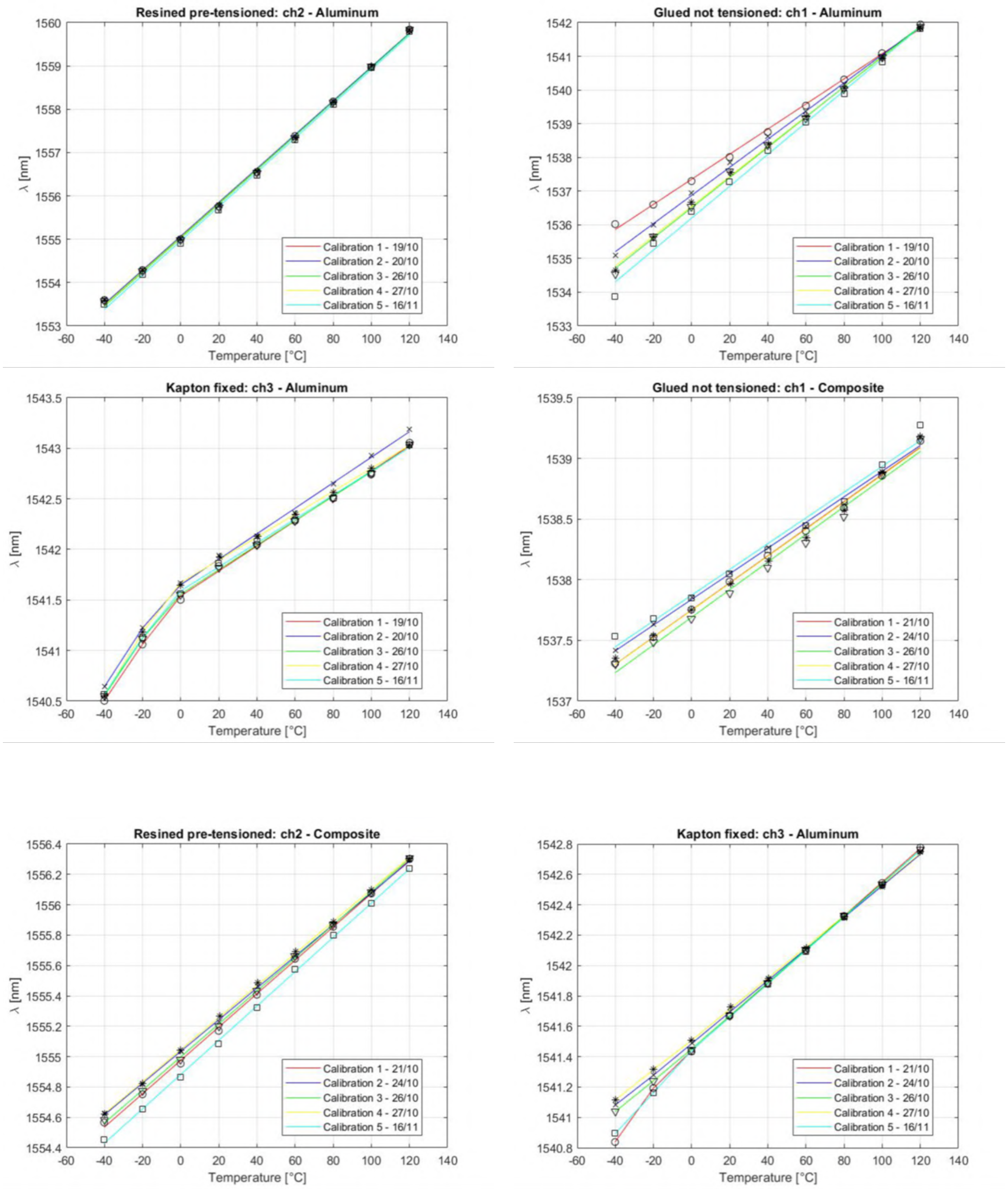


Fig. 4.15 Specimens calibration results.

The results (Figure 4.15) unequivocally demonstrate that the employed material determines the temperature sensitivity of the sensor. FBGs bonded to aluminum exhibit a very high $K_T$ in the two configurations where bonding ensures full adhesion over the entire temperature range. The larger measured optical excursion is therefore entirely attributable to the higher thermal expansion of the substrate. In the case of Kapton bonding, instead, the high thermal expansion of the support, combined with the low adhesive capability of the material, results in a degree of relative sliding between the fiber and the surface, which explains the much lower measured $K_T$. Moreover, this is the only configuration that clearly highlights a change in slope in the calibration curve. FBGs applied to the composite substrate, on the other hand, all measured a significantly lower $K_T$, close to the literature value, further confirming the previously discussed considerations.

### 4.3.3 Non-linearities Analysis

The results shown in the graphs of the previous section do not yet explain the origin of the observed change in slope. Identifying and verifying the cause of this phenomenon is of vital importance for defining a procedure, an industrial standard, and large-scale application of the technology. Recalling the general operating principle of an FBG sensor, it is necessary to assume that the sudden change in slope of the calibration curve is due to a variation in a mechanical property of the material. NASA studies [69] have shown that at very low temperatures the FBG sensor tends to lose its temperature sensitivity, while the application of a mechanical load generates a change in slope similar to that observed here. All the sensors used in the test campaign share a specific characteristic, namely that they are stripped before grating inscription and subsequently recoated. The application of the coating after sensor fabrication therefore introduces a discontinuity in the thermal expansion behavior of the materials.

$$\frac{\Delta\lambda_B}{\lambda_B} = (\alpha_f + \xi)\Delta T + \varepsilon_{induced} \tag{4.3}$$

where:

- $\alpha_f$ is the thermal expansion coefficient (CTE) of the fiber;
- $\xi$ is the thermo-optic coefficient;
- $\varepsilon_{indotto}$ is the mechanical strain transmitted from the coating to the fiber.

The recoating material has a thermal expansion coefficient ($\alpha_c$) that is typically one or two orders of magnitude higher than that of silica ($\alpha_s \approx 0.5 \times 10^{-6}/°\text{C}$).

When the temperature decreases, the polymeric coating tends to contract much more than the fiber. Since the coating is bonded to the fiber, it exerts an axial compressive force on the fiber itself.

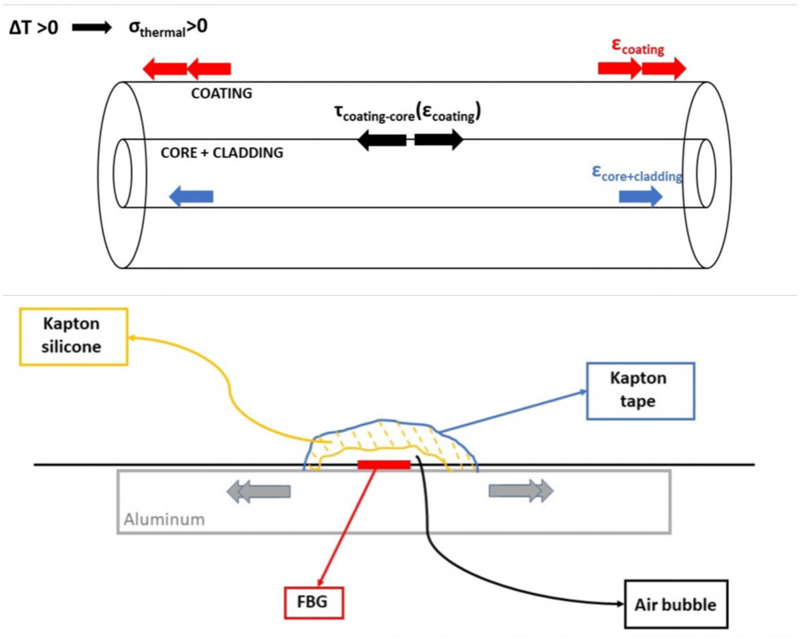


Fig. 4.16 Influence of coating and bonding strategy on the calibration linearity.

The total deformation underwent by the grating therefore becomes a weighted average of the properties of the two materials:

$$\alpha_{eff} \approx \frac{\alpha_f E_f A_f + \alpha_c E_c A_c}{E_f A_f + E_c A_c} \tag{4.4}$$

where $E$ is the Young's modulus and $A$ is the cross-sectional area; the subscripts $f$ and $c$ refer to the fiber (silica) and the coating (acrylate), respectively.

Consequently, the reason why the calibration curve becomes steeper below a certain temperature is related to the mechanical properties of the coating. Many polymers, when approaching cryogenic temperatures or dropping below their glass transition temperature ($T_g$), become significantly stiffer. As $E_c$ increases, the coating exerts a stronger influence on the fiber, transmitting its large thermal contraction more efficiently.

In summary, below a certain temperature, the polymer coating does not merely protect the fiber, but acts as a true mechanical amplifier. The increased stiffness of the polymer at low temperatures, combined with the large thermal expansion mismatch, causes each degree of temperature variation to produce a much more pronounced mechanical strain than at higher temperatures, thereby increasing the slope of the calibration curve.

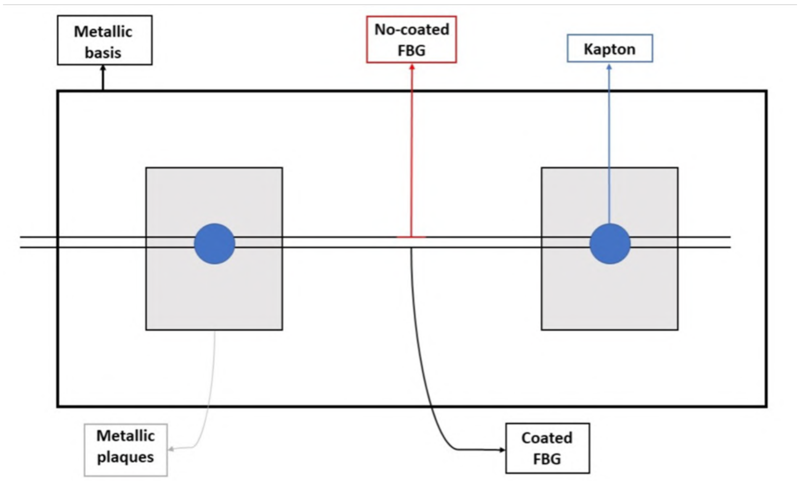


Fig. 4.17 Comparison between coated and uncoated FBG behavior.

In light of these considerations, a simple experimental campaign was set up in which two sensors were placed on a metallic plate: one coated and the other completely stripped. Both were subjected to the calibration process over the temperature range −40 to +50 °C.

The results are shown in Fig. 4.18. First, the absence of hygroscopic materials (or, in any case, materials weakly sensitive to humidity) eliminated offset effects in the calibration. Second, as expected, the uncoated sensor exhibited a perfectly linear response, while the coated sensor showed the characteristic knee in the calibration curve. Moreover, this knee occurred at a consistent temperature across all cycles.

Table 4.5 reports all the measured experimental values, which are fully consistent with the estimates derived from the available information.

| | No-coated FBG | Coated FBG | |
|---|---|---|---|
| | *Linear fit* | *Cold fit* | *Hot fit* |
| $K_T$ [nm/°C] | 0.008677 | 0.01768 | 0.01075 |
| $\lambda_0$ [nm] | 1545.0447 | 1549.7279 | 1549.7212 |

Table 4.5 Experimental data for uncoated and coated FBG sensors.

The proposed hypothesis is therefore strongly validated, together with the operational recommendation to use only stripped sensors or sensors with polyimide coating for cryogenic applications.

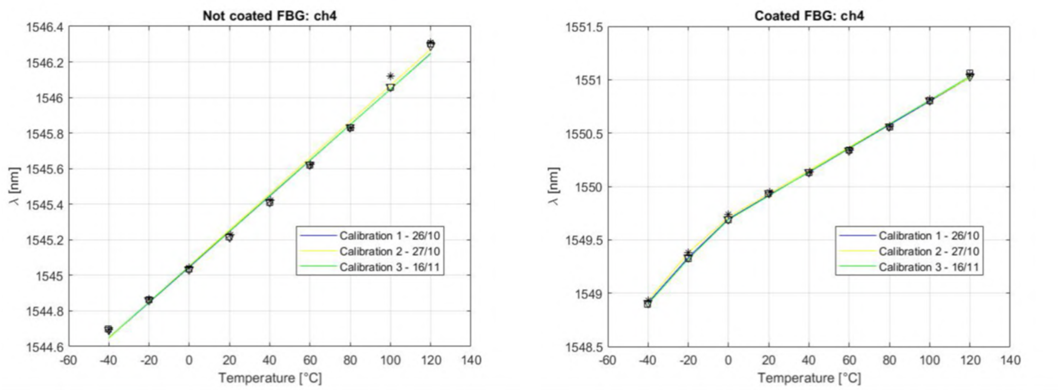


Fig. 4.18 Thermal calibration curves of coated and uncoated FBG sensors.

## 4.4 Dynamic Thermal Response and Performance under Electromagnetic Disturbances

The final aspect investigated concerns the analysis of the thermal response speed of the optical fiber sensor. To this end, a dedicated experimental test bench was developed with the following main features:

- a mechanical support designed to keep a section of fiber with an FBG under tension and in a horizontal configuration;
- a Peltier cell ($1 \times 1$ cm) placed in contact with the sensor;

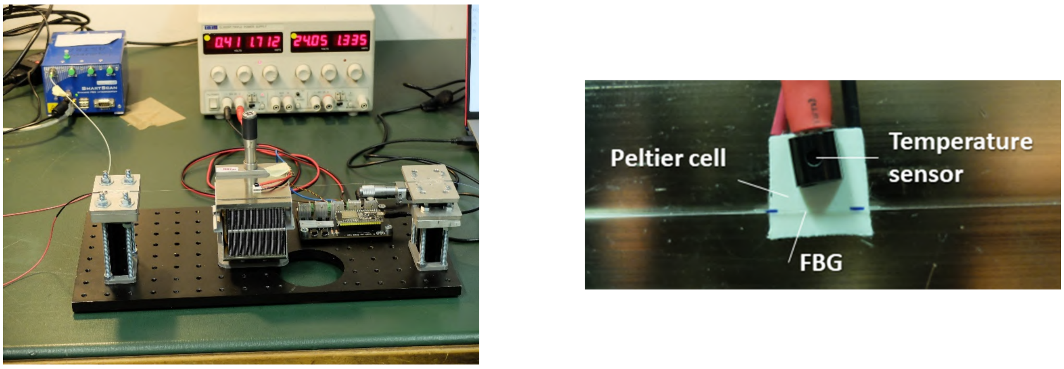


Fig. 4.19 Experimental setup of the Peltier-based test bench (left) and detailed view of the FBG positioning (right).

- an electronic temperature sensor also placed on the Peltier cell (DS18 sensor);
- a control logic for the Peltier cell based on the temperature data provided by the DS18 sensor.

Temperature control of the Peltier cell was implemented through a simple algorithm based on the temperature data supplied by the DS18 sensor. The result is clearly shown in Figure 4.20. The graph superimposes the response of the DS18 sensor with that of the FBG sensor. It is immediately clear how the optical sensor exhibits a significantly faster response than its electronic counterpart. In the reported figure, the Peltier cell is maintained at 10 °C (within an error of approximately 1 °C), followed by a rapid heating to 60 °C, and subsequently held at this temperature.

From the data, it is evident that:

- the rising ramp is detected significantly earlier by the FBG sensor;
- the delay of the DS18 sensor leads the control logic to stabilize the Peltier cell temperature when the FBG indicates that the actual temperature has already exceeded the setpoint imposed by the control algorithm;
- the delay of the DS18 sensor affects the performance of the control logic in all its phases.

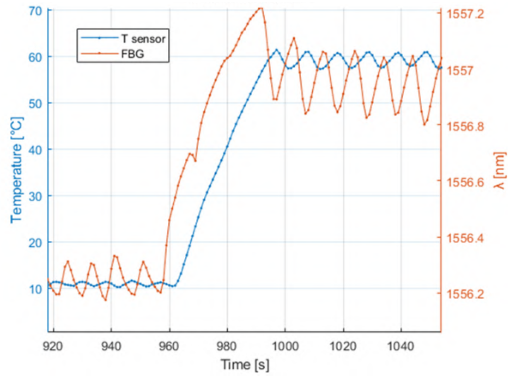


Fig. 4.20 Comparison between the dynamic thermal response of the FBG and a commercial sensor.

Based on these results, and with the aid of the climatic chamber, a further testing campaign was carried out in which the sensors were repeatedly subjected to significant thermal shocks [70]. In all cases, the optical sensor demonstrated a very low time constant, even lower than that of high-performance thermocouples. The results are reported in Table 4.6.

| **Phase** | **Sensor** | **Time constant [s]** |
|---|---|---|
| *Cooling* | FBG 1 | 0,085 |
| | FBG 2 | 0,071 |
| | PT100 | 0,848 |
| *Heating* | FBG 1 | 0,262 |
| | FBG 2 | 0,218 |
| | PT100 | 0,719 |

Table 4.6 Time constant values for cooling and heating phases.

Finally, the capability of FBG sensors to operate without electromagnetic compatibility issues was also verified. In this case as well, a simple experimental validation was performed.

An electric motor was instrumented as shown in Figure 4.21. Specifically, the sensor was placed in the stator region, directly in contact with the metallic structure and in close proximity to the internal windings. Unlike a conventional thermocouple, which in the presence of electromagnetic disturbances and/or when applied to metallic surfaces exhibits significant noise, Figure 4.21 shows that the motor heating was monitored in an extremely accurate, effective, and disturbance-free manner.

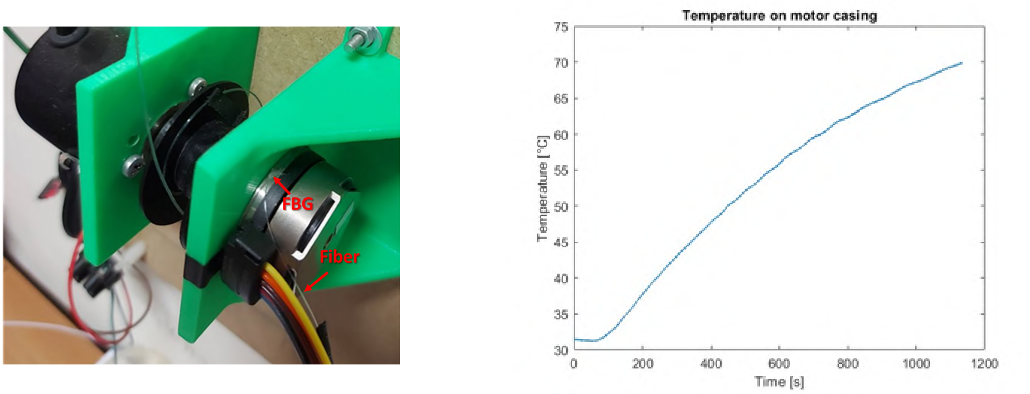


Fig. 4.21 Experimental setup for electromagnetic disturbance testing (left) and measured temperature trend (right).

## 4.5 FBG for Thermal Monitoring of MLI in Space Applications

In this section, the first application case of a Fiber Bragg Grating (FBG) optical sensor network for the thermal monitoring of an industrial project is presented. The activity focused on the design, manufacturing, and testing of a sensor network directly integrated into Multi-Layer Insulation (MLI) systems. The objective of the activity was to assess the capability of the developed network to thermally characterize the performance of the MLI and to compare the obtained measurements with those provided by traditional instrumentation (thermocouples).

In space system engineering, thermal loads represent one of the fundamental aspects to be considered during both the design and testing phases. Operating temperatures can range from a few Kelvin to several hundreds of degrees, depending on exposure to solar radiation. It is therefore mandatory to implement efficient thermal control systems capable of deactivating components when temperature peaks are reached and activating cooling or heating systems, when present onboard. For this reason, sensors capable of guaranteeing high performance even under

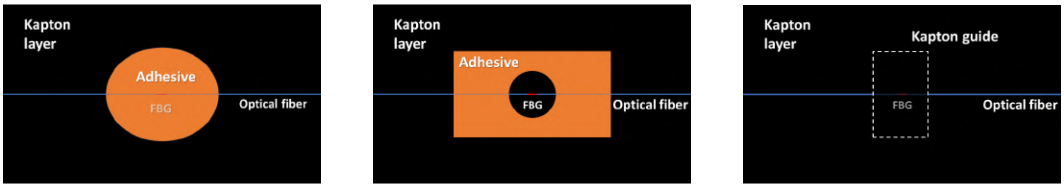


Fig. 4.22 Layout of different bonding strategies, with the adopted one on the right.

harsh conditions (e.g., high temperatures, electromagnetic radiation) are of strategic importance for space applications.

The integration of Fiber Bragg Grating (FBG) sensors into Multi-Layer Insulation (MLI) blankets for space applications offers numerous advantages in terms of monitoring and control of spacecraft environmental conditions. FBG sensors allow pointwise temperature measurements within MLI blankets, which is crucial for optimizing spacecraft thermal management, as temperature fluctuations directly affect the performance and lifetime of onboard components. By monitoring temperature variations at specific locations of the MLI blanket, FBG sensors enable precise closed-loop thermal control, allowing heating systems to be deactivated or radiative mechanisms to be activated when necessary. The integration of FBG sensors into MLI blankets therefore offers several advantages for space applications, not limited solely to thermal monitoring. For instance, the same hardware can be exploited for pressure sensing, structural health monitoring, and impact detection due to hypervelocity debris. These benefits can significantly enhance spacecraft safety, reliability, and performance, ultimately supporting scientific and exploratory missions.

For the test campaign, FBG sensors with polyimide coating (applied to the fiber but not on the sensing region) were employed, as this material is compatible with thermal and outgassing requirements for thermal-vacuum chamber testing in space applications. Ten sensors were distributed over several square samples with a side length of approximately 30 cm. In particular, given the static conditions of the test, no adhesive was applied in proximity to the sensing region in order to avoid mechanical disturbances induced by thermal expansion of the supports. As illustrated in Figure 4.22, the sensors were placed in specific MLI housings made of the same material as the overall substrate.

For all test cycles, the following procedure was adopted:

- the experimental setup was placed inside the thermal-vacuum chamber;
- the measurement system was configured as shown in the figure;
- selected thermal cycles were performed and data were acquired;
- data analysis: sensor calibration, temperature measurement, and comparison with thermocouples.

The applied thermal cycles consisted of temperature steps with variable amplitudes and durations. These cycles enabled, in a first phase, the calibration of the sensors and, subsequently, the verification of their performance. During the calibration phase, the FBG sensors were paired with thermocouples as prescribed by ESA standards for thermal testing. Under vacuum conditions and assuming complete mechanical stability, equation 2.10 can be simplified as:

$$\Delta\lambda/\lambda = K_T \Delta T \tag{4.5}$$

Once the temperature is known from thermocouple measurements, it is straightforward to experimentally determine the value of $K_T$ and, in subsequent tests, compute the temperature as:

$$T_i = (\lambda_i - \lambda_0)/K_T + T_0 \tag{4.6}$$

The test campaign was divided into three specific phases:

- calibration thermal cycle between 0 and 200 °C;
- calibration thermal cycle between -150 and 200 °C;
- verification thermal cycle between -150 and 200 °C.

In all cycles, stable temperature steps of approximately 15 minutes were applied every 20 °C, in order to construct the calibration curve as accurately as possible. Also in light of the aspects discussed previously, the calibration test was divided into two phases: a first phase involving only positive temperatures, followed by a second phase covering the entire test range.

During these initial cycles, each sensor was paired with a reference thermocouple. In the final test cycle, only one sensor per sample was paired with the thermocouple, while for all the others the calibration curve was used to estimate the local temperature.

In Figure 4.23 the results of the first cycle between 0 and 200 °C are reported. It can be clearly observed that the calibration curve is extremely linear and, above all, that performing the measurements under vacuum conditions does not alter either the measurement itself or the calibration values previously obtained in the climatic chamber. The time-domain comparison between the temperature measured by the FBG sensors and that measured by the thermocouple also shows excellent reliability of the optical measurement.

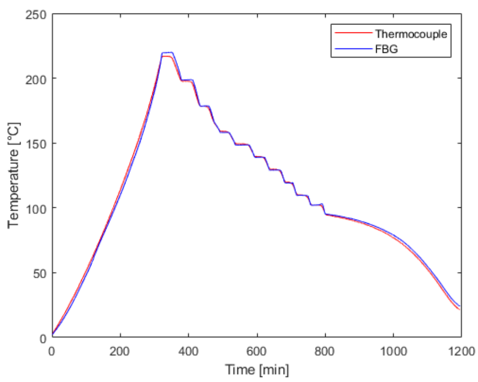


Fig. 4.23 Comparison between FBG and thermocouples for positive temperatures.

The subsequent measurement cycle, from −150 to 200 °C, confirmed the linear trend for positive temperatures. Unlike what was discussed in the previous section, in this case a linear relationship is observed down to approximately −50 °C, followed by a progressive transition leading to a reduction in sensitivity at lower temperatures.

This behavior is opposite to that observed with acrylate coatings at the glass transition temperature $T_g$. While with acrylate coating a variation of the mechanical properties of the fiber is observed near $T_g$, with polyimide only the natural degradation of the physical properties of matter as the temperature approaches absolute zero is observed. In this case, the dominant factor is not mechanical, but optical.

Recalling that the intrinsic thermal sensitivity of the fiber is defined as:

$$K_T = \alpha + \xi \tag{4.7}$$

Table 4.7 Comparison between experimental thermal sensitivity coefficients ($K_T$) for polyimide-coated FBG and typical literature values.

| **Temperature Range** | **Experimental $K_T$** | **Literature $K_T$** |
|---|---|---|
| $T > -50°C$ | 11.4 pm/°C | $10 \div 13$ pm/°C |
| $T < -50°C$ | 6.5 pm/°C | $5 \div 8$ pm/°C |

The thermo-optic coefficient of silica ($\xi$) is not constant. At high temperatures (e.g., +200°C), $\xi$ reaches its maximum value. At cryogenic temperatures (e.g., −150°C), the variation of the refractive index with temperature tends toward zero. Moreover, the thermal expansion coefficient ($\alpha$) of both the fiber and the polyimide decreases as the temperature approaches absolute zero.

For simplicity of conversion, a piecewise linear calibration was adopted, with the discontinuity set at $T = -50$. The conversion of the optical data into temperature demonstrated that this calibration methodology is sufficient to guarantee a conversion error below 1%, which could be further optimized by numerical interpolation of the transition region. Literature data are in good agreement with the experimental results (Table 4.7).

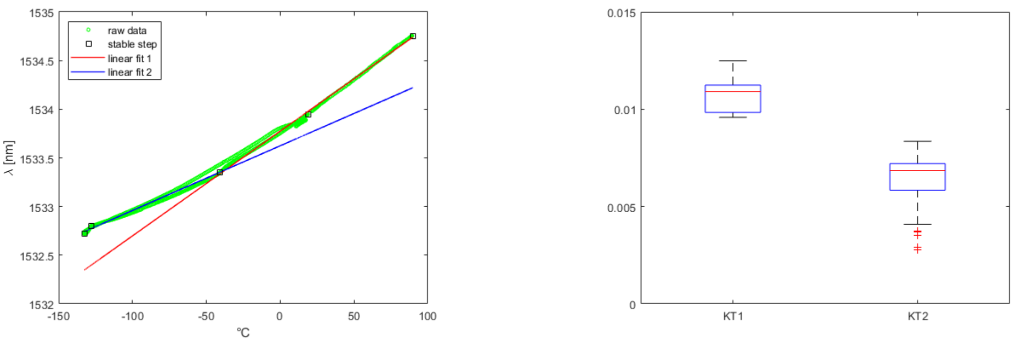


Fig. 4.24 Experimental thermal curve (left) and boxplot analysis of $K_T$.

The final test phase played a crucial role in verifying the repeatability of the FBG sensor measurements. The applied thermal cycle was therefore reproduced in a manner analogous to the previous case, over the entire temperature range of interest. In this last cycle, all thermocouples were removed, except for one sensor per fiber line, which was retained as a spot check to further verify the correct operation of the experimental setup. The optically measured temperature was calculated using the previously developed calibration curves.

In Figure 4.25 the comparison between the sensor output obtained during the two different tests, for the same thermal step, is shown. Despite differences in stabilization time and temperature holding, it is evident that the optical output is essentially identical in both tests.

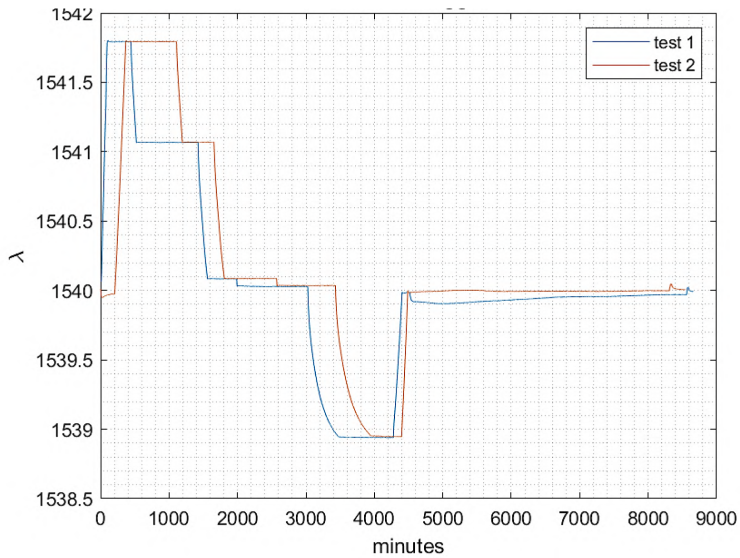


Fig. 4.25 Comparison of FBG data in two different test campaigns.

Finally, compliance with industrial requirements for thermal testing in thermal vacuum chambers (TVC) for space applications was verified. In general, sensor systems are required to demonstrate a thermal stability of at least 0.2°C/hour. In Figure 4.26, the FBG and thermocouple measurements are plotted together with a ±0.1°C band (i.e., a 0.2°C/hour amplitude). The figure shows that the oscillations remain within the tolerance band.

As shown in the graph on the right, the absolute error with respect to the expected mean value is lower than 0.1°C/hour, which is well below the required constraint. Moreover, the absolute difference between FBG and thermocouple measurements always remained below 3 °C and predominantly below 1 °C, with a relative error—when compared to industrial standards—always below 1%.

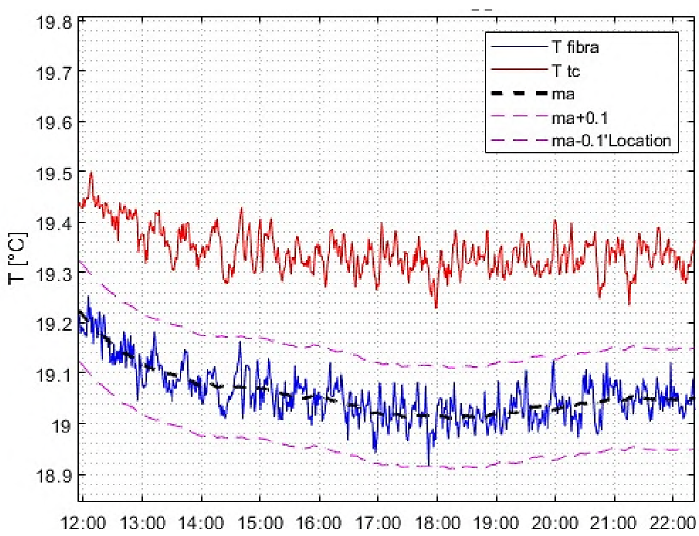


Fig. 4.26 Industrial stability requirements verification.

# Chapter 5

# General Strain Monitoring by Fiber Bragg Gratings

FBG sensors essentially behave as optical strain gauges, providing localized strain measurements at the point they are glued on. Although sensitivity to this parameter is well established in literature, it is essential to perform dedicated tests on laboratory specimens in order to optimize both the installation procedure and the data acquisition process [71]. The aim of this chapter is therefore to verify the strain sensitivity of FBG sensors together with the installation procedures adopted at the Politecnico di Torino. Accordingly, this chapter analyzes:

- the effect of fiber bonding on measurement accuracy;
- the comparison between strain measured by a conventional strain gauge and by an FBG sensor;
- the linearity of the FBG measurement under elastic deformation of the reference substrate;
- thermo-mechanical decoupling strategies for optical measurements.

## 5.1 Effect of Adhesive Application

When FBGs are used as strain sensors, the fiber (or at least the portion containing the sensor) must be bonded to the substrate to be monitored. This section aims to analyze the general effect of the bonding process on strain measurements.

As a first approach, a rectangular geometry was once again considered on a carbon fiber specimen. In particular, two specimens were analyzed, both instrumented with an optical fiber containing an FBG sensor and bonded, in both cases, using epoxy resin. To maintain the fiber in position, a slight mechanical tension was applied during the bonding phase. The main issue associated with the bonding phase is related to the viscous settling of the adhesive. Measurements performed during this phase would be highly inaccurate, as the strain detected by the sensor would not be caused by an actual deformation of the monitored surface, but rather by the resin polymerization process. For this reason, immediately after the fabrication of the second specimen, data acquisition was started. Both samples were left for several days in still air, without mechanical constraints, and were only exposed to unavoidable ambient thermal fluctuations. Data acquisition began as soon as the resin deposition process was completed. After three days, the free end of the fiber connected to the micromanipulator—used to maintain fiber positioning during bonding—was cut.

The measured data were normalized with respect to the mean value measured over the entire period, in order to superimpose the trends independently of the specific $\lambda_B$ of each sensor:

$$\lambda_m = \frac{1}{N}\sum_{i=1}^{N}\lambda_i \tag{5.1}$$

The results are reported in Figure 5.1. It is evident that:

- the influence of daily thermal excursions affects both samples equally;
- an overall stable trend is observed for the already aged sensor (ch2);
- a clear settling trend is visible for the new sensor (ch1) during the bonding phase.

In particular, during the initial resin polymerization phase, a slight downward trend is observed, attributable to the compressive effect induced by resin curing and

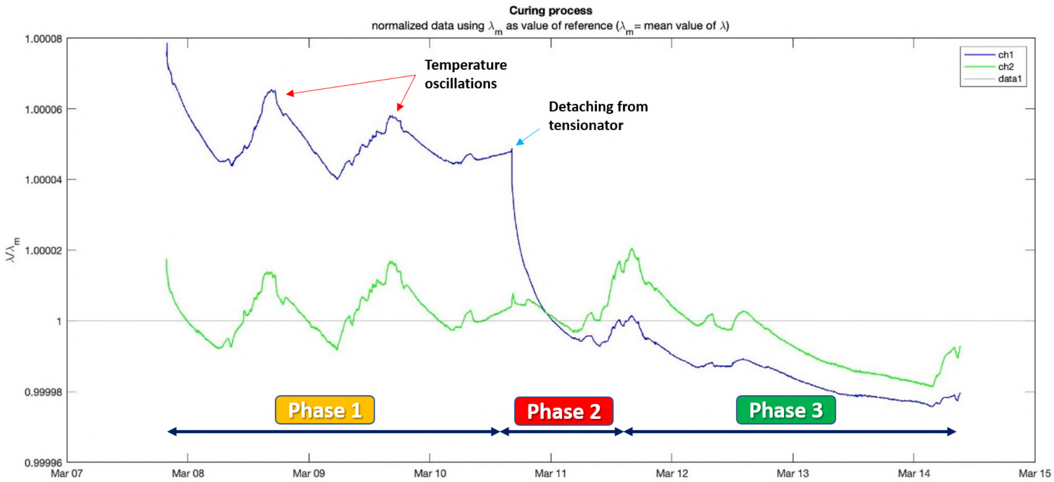


Fig. 5.1 Comparison between data of two specimens.

subsequent stiffening. Subsequently, after removal of the connection to the tensioner, a more pronounced settling phase is observed. At the end of this phase, the difference between the two samples progressively vanishes, indicating that the settling process has been completed.

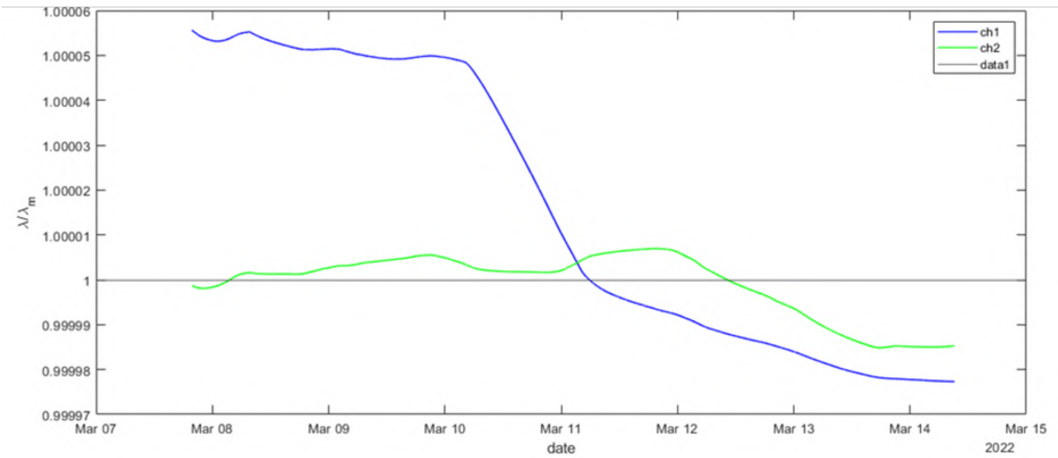


Fig. 5.2 Comparison between filtered trends.

For improved clarity, the same data were filtered using a 24-hour moving average, in order to minimize the effects of thermal excursions induced by the room air-conditioning system:

$$\lambda_m = \frac{1}{N} \sum_{i=N}^{n+N-1} \lambda_{i-\frac{N}{2}} \tag{5.2}$$

The three phases are even more clearly distinguishable. The downward trend observed during the last 36 hours is common to both specimens and can be attributed to the absence of heating during the winter weekend period.

Despite its simplicity, this preliminary test demonstrates the necessity of adopting an installation procedure for the sensors that is as controlled, standardized, and repeatable as possible, in order to guarantee adequate levels of measurement accuracy. In Chapter 7, these aspects will be discussed in detail.

## 5.2 Comparison between Loads, Strains, and FBG data

Once the importance of the bonding phase on the final sensor measurement had been verified (the operational bonding methodology will be analyzed in detail in Chapter 7), the next step was to assess the precision and accuracy of FBGs in measuring mechanical strain.

To this end, a rectangular specimen was again considered (with thickness negligible with respect to the other two dimensions), with an optical fiber placed axially along the specimen and equidistant from its edges. Next to the FBG sensor, a strain gauge was bonded. Even from a purely visual standpoint, the advantage offered by the optical fiber in terms of invasiveness, footprint, and ease of installation is immediately evident. Figure 5.3 shows the experimental setup. The specimen was clamped at one end and mechanically loaded at the opposite end, as shown in the figure. Considering the geometry of the specimen, the shear load can be approximated as being applied at the shear center of the cross-section; therefore, the entire structure is subjected purely to bending. By schematizing the structure as a cantilever beam, a linear variation of the bending moment is obtained, with the maximum value occurring at the clamped end.

When a shear load is applied at the free end of the specimen, a bending moment is generated. The fiber (as well as the strain gauge) measures the strain at the surface to which the sensor is bonded. Such strain, within the elastic regime of the material, is defined by Hooke's law:

$$\sigma = E\varepsilon \tag{5.3}$$

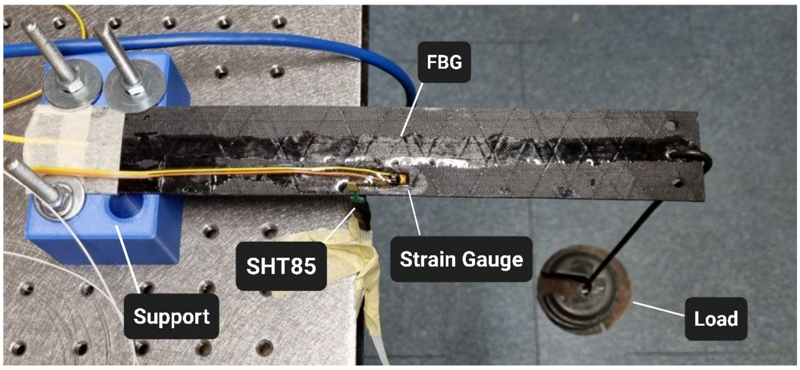


Fig. 5.3 Reference specimen equipped with both FBG and SG.

where $E$ is the elastic modulus of the material and $\varepsilon$ is the strain at the point under consideration.

In turn, for the beam model, the local stress can be defined through Navier's formula:

$$\sigma = \frac{M_z}{I_x} Y \tag{5.4}$$

where $M_z$ is the bending moment at the considered section, $I_x$ is the second moment of area of the cross-section, and $Y$ is the distance of the sensor from the neutral axis of the section.

It follows that the strain $\varepsilon$ is given by:

$$\varepsilon = \frac{M_z}{EI_x} Y \tag{5.5}$$

Recalling again Navier's formulation, the bending moment is simply given by the product $M = F \cdot b$, where in the present case the force $F$ corresponds to the weight force of the mass applied to the specimen. Therefore, the previous relation can be generalized as:

$$\varepsilon = \frac{mg \cdot b}{EI_x} Y = K_C m \tag{5.6}$$

That is, the strain at the considered point is directly proportional to the applied load and, in this specific case, to the weight of the mass applied at the free end of the specimen.

Recalling Eq. 2.15 describing the FBG response, and assuming $T = cost$, it is straightforward to obtain:

$$\Delta\lambda = K_\varepsilon \Delta\varepsilon \tag{5.7}$$

and substituting from Eq. 5.6:

$$\Delta\lambda = Km \tag{5.8}$$

with $K = K_\varepsilon K_C$.

Equation 5.8 therefore demonstrates that the optical sensor response must be linearly dependent on the measured strain and, analogously, linearly dependent on the applied load.

The test campaign was carried out in two distinct phases. In the first phase, the optical measurement was compared with the strain measured by the strain gauge. In the second phase, the relationship between the applied load (both in tension and compression) and the measured wavelength was analyzed, in order to verify the linearity discussed in Eq. 5.8.

The results are reported in Figures 5.4 and 5.5. In both cases, the FBG measurement proved to be extremely precise, repeatable, and consistent with expectations. Measurements were repeated over 20 cycles, both in tension and compression, highlighting both the linearity of the relationship and the validity of coefficient $K$ under both loading conditions.

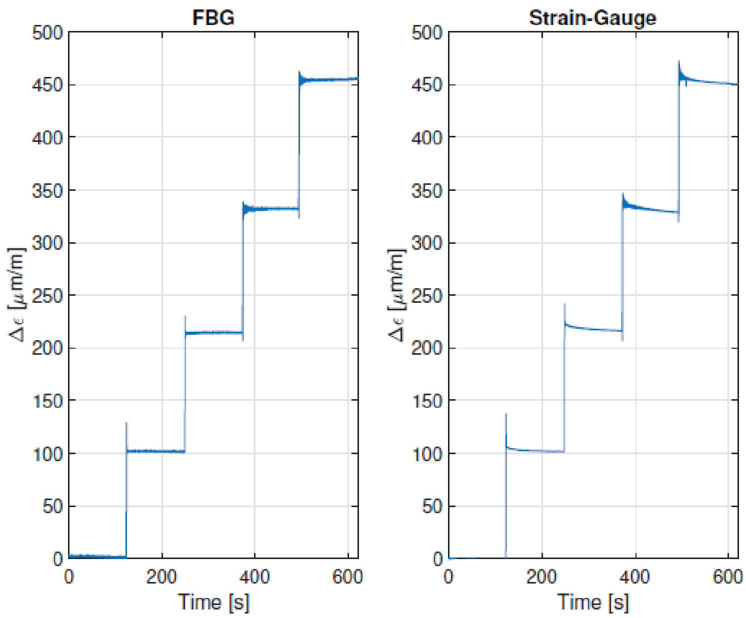


Fig. 5.4 Comparison between FBG and SG output on the same test.

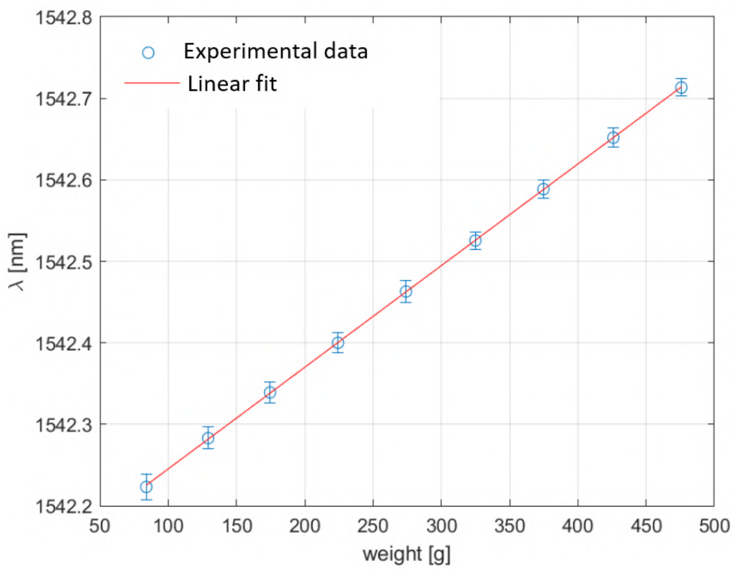


Fig. 5.5 Linear fit between applied load and FBG data.

Although obtained on a highly simplified geometry, this result was of great importance for the continuation of the activity. It demonstrated that, when operating within the elastic regime of a material and applying a sufficiently rigid and durable bonding to the fiber, it is possible to reliably monitor not only instantaneous structural strains, but also to directly correlate the optical output to the load that generated them. This is achieved while ensuring significant savings in terms of weight, footprint, and installation procedures, and with a simple linear calibration. Finally, the simplified geometry of the specimen remains significant, as a flat, slender plate represents the simplest mechanical approximation of the behavior of a semi-wing subjected to aerodynamic loads. More specifically, the test performed is a simplified reproduction of a generic bending test of a wing box. In particular, assuming one or more fiber lines placed along a spar, the sensors will be repeatedly subjected to tension/compression cycles, depending on the variation of the bending moment induced by aerodynamic loads and on their geometric position (i.e., upper surface, lower surface, ...). The precision, accuracy, and repeatability of the obtained results therefore represent a first fundamental step toward the design of distributed FBG sensor networks integrated into much more complex geometries and closer to real application cases.

## 5.3 Thermal Compensation

A particularly critical aspect of measurements performed with FBG sensors is the thermo-mechanical decoupling of the measured optical response. As described by relation 2.10, in the presence of both thermal and mechanical contributions, the simple optical measured response does not allow the nature of each contribution to be distinguished. In order to obtain correct data and perform compensation, it is therefore necessary to consider two fundamental elements:

- the combined use of multiple sensors, suitably arranged to be sensitive to known physical parameters;
- the linear nature of thermal and mechanical calibrations, which allows the application of the superposition principle.

Any thermal compensation process necessarily relies on the combined use of these two considerations. The most immediate and system-level approach consists of using two FBG sensors: one exposed only to temperature variations, and the second exposed to the same thermal variation but also to the mechanical strain of the substrate to which it is bonded.

From a mathematical standpoint, a first sensor (called $FBG_1$) is sensitive only to temperature, while a second sensor $FBG_2$ is sensitive to both thermal and mechanical effects. Their optical responses are therefore given by:

$$\Delta\lambda_1 = K_{T_1}\Delta T \tag{5.9}$$

$$\Delta\lambda_2 = K_{T_2}\Delta T + K_{\varepsilon_2}\Delta\varepsilon \tag{5.10}$$

Sensor $FBG_1$, being exposed only to temperature, does not include the $\Delta\varepsilon$ term. Sensor $FBG_2$, on the other hand, includes both contributions. Moreover, since $FBG_2$ is necessarily mechanically bonded to the measured surface, it follows that $K_{T_1} \neq K_{T_2}$.

From relation 5.9, temperature can be estimated as:

$$\Delta T = \frac{\Delta\lambda_1}{K_{T_1}} \tag{5.11}$$

This expression is then substituted into the equation for sensor $FBG_2$:

$$\Delta\lambda_2 = K_{T_2}\frac{\Delta\lambda_1}{K_{T_1}} + K_{\varepsilon_2}\Delta\varepsilon \tag{5.12}$$

which yields:

$$\Delta\varepsilon = \frac{\Delta\lambda_2 - K_{T_2}\frac{\Delta\lambda_1}{K_{T_1}}}{K_{\varepsilon_2}} \tag{5.13}$$

Relations 5.11 and 5.13 therefore allow the estimation of both $T$ and $\varepsilon$, provided that one sensor is sensitive only to temperature and that a linear superposition of effects applies to the sensor exposed to both contributions.

To verify this principle, a specific laboratory test was carried out. Two thin rectangular carbon-fiber specimens (Figure 5.6), both instrumented with an FBG (as already discussed in previous sections), were placed inside a climatic chamber, where temperature was varied in a controlled manner. The first specimen was simply exposed to the imposed thermal variations. The second specimen, in addition to being subjected to the same environmental conditions, was also loaded with a stepwise increasing mechanical load.

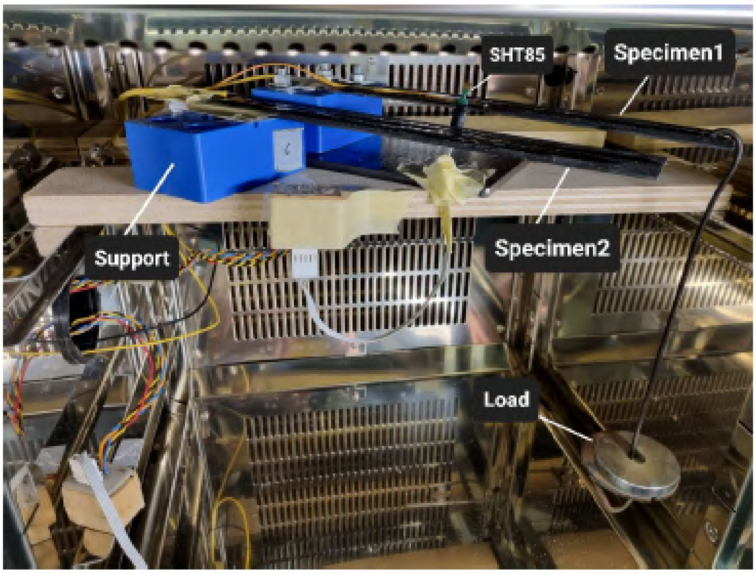


Fig. 5.6 Experimental setup for thermal compensation validation.

Figure 5.7 reports both the applied temperature and load variations (in red) and the response (in blue) of the sensor exposed to both phenomena. It is immediately evident that this response is affected by the superposition of the two effects. By applying relations 5.11 and 5.13, the curve reported in the final graph of Figure 5.7 is obtained, representing the $\Delta\lambda$ variation induced solely by the mechanical load. As can be observed, the optically filtered trend—after removing the temperature contribution—is really well superimposed on the applied load trend, thus validating the superposition principle discussed above.

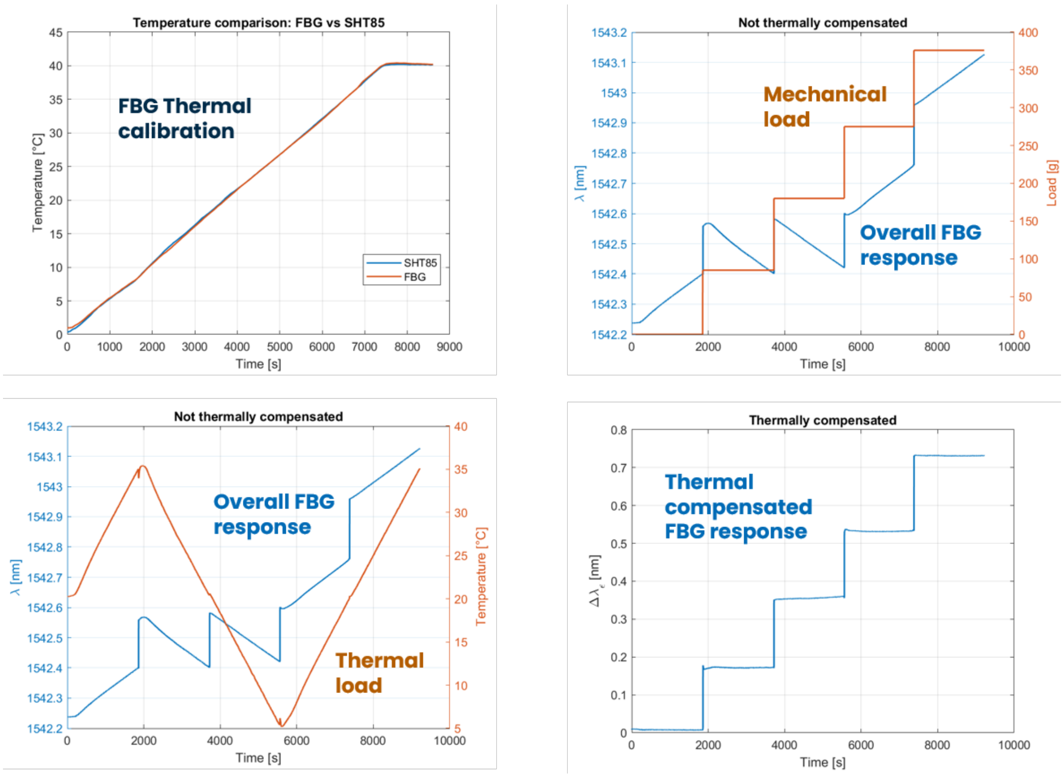


Fig. 5.7 Thermal compensation process.

From a practical standpoint, therefore, to perform a thermally compensated strain measurement at a mechanical point subject to temperature variations, an integrated approach can be adopted (Fig. 5.8). This represents an evolution of the surface thermal sensor previously described in Section 4.3. In this configuration, a first sensor is bonded directly to the surface at the measurement point and is therefore subjected to both thermal and mechanical effects. Above it, a thin metallic layer is placed, on top of which a purely thermal FBG is positioned and finally covered by a protective polymer layer.

The instrumented specimen was then subjected to controlled variations of temperature and mechanical load. By again applying the algorithm described through relations 5.11 and 5.13, the results shown in Figure 5.9 were obtained, further validating the described relationships.

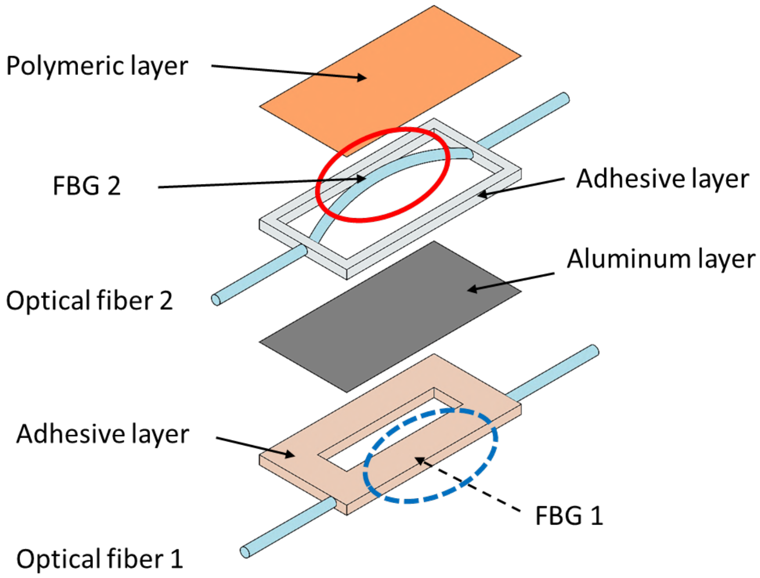


Fig. 5.8 Integrated strain sensor thermal compensated layout.

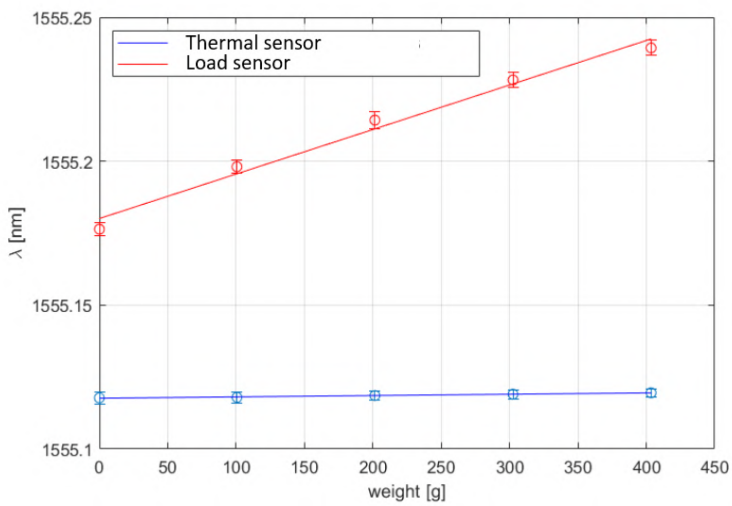


Fig. 5.9 Thermal compensated sensor verification.

## 5.4 Dynamic Loads Monitoring

FBG sensors are characterized by an extremely fast response time. In the mechanical domain, this translates into excellent vibration sensing capability.

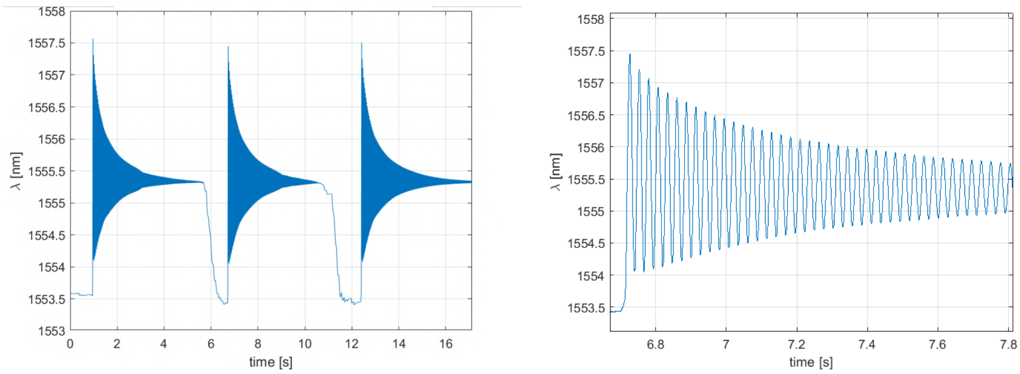


Fig. 5.10 Data of sensor glued on oscillating specimen (left) and detail of acquisition (right).

A first simple test was performed using a specimen with the usual rectangular reference geometry, clamped at one end. Through a dynamometer, an impulsive load was applied at the free end of the specimen, which was then left free to oscillate until returning to rest.

The data log is reported in Figure 5.10. Sampling was performed at high frequency (2.5 kHz), and the resulting curve shows extremely high data precision and an almost complete absence of measurement noise. The large amount and accuracy of the collected data allow both the evaluation of the overall system damping and the precise calculation of the vibration frequency.

Based on these preliminary results, at Politecnico di Torino, an optically instrumented support was developed which, when subjected to vibration testing, demonstrated the ability of FBG sensors to measure mechanical vibrations, in that specific case up to the order of hundreds of Hz [72].

Having obtained precise, reliable, and real-time vibration measurements using FBG sensors, their capability to estimate modal frequencies was also investigated. The use of FBGs for this purpose enables dynamic monitoring of a structure or component with a minimally invasive, integrated system capable of producing large amounts of data even during operational phases, and not only during testing.

The overall experimental approach consisted of performing a classical Hammer test on a composite carbon fiber plate of about 50x60 cm. The specimen was instrumented with both traditional piezoelectric accelerometers and optical sensors. In both tests, the plate was positioned on a highly compliant cylindrical foam support, in order to reproduce as realistically as possible the free–free boundary condition.

Nine measurement points were identified on the surface of the plate for the detection of the natural frequencies, as shown in Fig. 5.12.

FBGs were placed using Kapton tape. In this way, the fiber is able to perceive the accelerations imposed on the structure by the hammer impact. The accelerations of the structure at the points where the fiber is bonded through Kapton induce a stress state that is effectively sensed by the gratings. Operating with highly impulsive loads and very low acceleration levels (as required in a typical hammer test), the Kapton/fiber/composite interface works entirely within the elastic regime, without introducing viscoelastic phenomena that could lead to signal drift over time. Neglecting temperature variations, the entire optical variation measured by the instrumentation can therefore be fully attributed to the mechanical strain experienced by the sensor.

From a mathematical point of view, after the impulse the response can be expressed as a sum of the natural modes:

$$w(x,y,t) = \sum_n \phi_n(x,y) q_n(t) \tag{5.14}$$

where $w$ is the out-of-plane displacement, $\phi_n$ is the shape mode, and $q_n(t)$ is the modal coordinate oscillating with natural frequency $\omega_n$.

Assuming a Kirchhoff-Love plate model, the longitudinal strain on the surface is given by:

$$\varepsilon_p(x,y,t) = -z \frac{\partial^2 w}{\partial x^2} \tag{5.15}$$

where $z = h/2$ is the distance from the neutral axis.

Therefore, the surface of the plate periodically stretches and contracts at the natural frequencies.

Considering the plate–adhesive–fiber system it is characterized by the following parameters:

- $E_f$ = Young's modulus of the fiber;
- $A_f$ = cross-sectional area of the fiber;

- $G_a$ = shear modulus of the adhesive;
- $t_a$ = adhesive thickness;
- $L$ = bonded length.

The plate imposes an axial displacement $u_p(x,t)$ on the surface, while the fiber experiences a displacement $u_f(x,t)$.

The relative displacement generates a shear stress in the adhesive:

$$\tau(x) = \frac{G_a}{t_a}(u_p - u_f) \tag{5.16}$$

The axial force in the fiber is given by:

$$N_f = E_f A_f \frac{du_f}{dx} \tag{5.17}$$

Force equilibrium on a fiber element yields:

$$\frac{dN_f}{dx} = \tau P \tag{5.18}$$

where $P$ is the contact perimeter.

Substituting:

$$\frac{d}{dx}\left(E_f A_f \frac{du_f}{dx}\right) = P\frac{G_a}{t_a}(u_p - u_f) \tag{5.19}$$

which becomes:

$$\frac{d^2 u_f}{dx^2} - k^2(u_p - u_f) = 0 \tag{5.20}$$

with:

$$k^2 = \frac{PG_a}{E_f A_f t_a} \tag{5.21}$$

If the strain in the plate is:

$$\varepsilon_p = \frac{du_p}{dx} \tag{5.22}$$

the solution of the differential equation leads to:

$$\varepsilon_f(x) = \varepsilon_p \left(1 - \frac{\cosh(kx)}{\cosh(kL/2)}\right) \tag{5.23}$$

If the bonded length is sufficiently large ($kL \gg 1$):

$$\varepsilon_f \approx \varepsilon_p \tag{5.24}$$

that is, the strain of the plate is almost completely transferred to the fiber.

Recalling the general equation of FBG:

$$\Delta\lambda_B(t) \propto \varepsilon_f(t) \tag{5.25}$$

Since:

$$\varepsilon_f(t) \approx \varepsilon_p(t) \tag{5.26}$$

the wavelength variation therefore contains the same modal frequencies as the vibrating plate.

Consequently, the frequency analysis of the Bragg wavelength signal is expected to be consistent with the frequency analysis performed on the accelerometer data. Table 5.1 reports the frequencies calculated using accelerometer measurements and those obtained using FBG sensor data. It is immediately evident that the errors are very small, especially for the first natural frequencies of the plate, and remain limited even at higher values on the order of several hundreds of hertz. The experimental results show an excellent agreement between the frequencies identified using FBG sensors and those obtained with accelerometers. In particular, for frequencies below 300 Hz, the discrepancy between the two measurement techniques remains within approximately 2%, demonstrating that FBG sensors are capable of accurately capturing the dynamic response of the structure. The results also highlight the high sensitivity of the optical gratings, which allows the detection of vibration modes that are not clearly identifiable using the reference accelerometric system. Furthermore, the experiments demonstrate that reliable measurements can be obtained even when the optical fiber is simply fixed to the structural surface using industrial adhesive tape (Kapton). This result validates the possibility of implementing FBG sensors in a plug-and-play configuration, significantly simplifying installation procedures and reducing the complexity typically associated with embedded sensing systems.

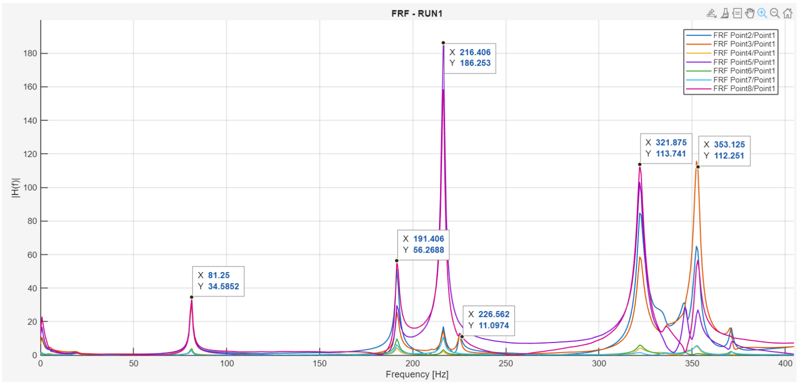


Fig. 5.11 Natural frequencies calculated with accelerometers.

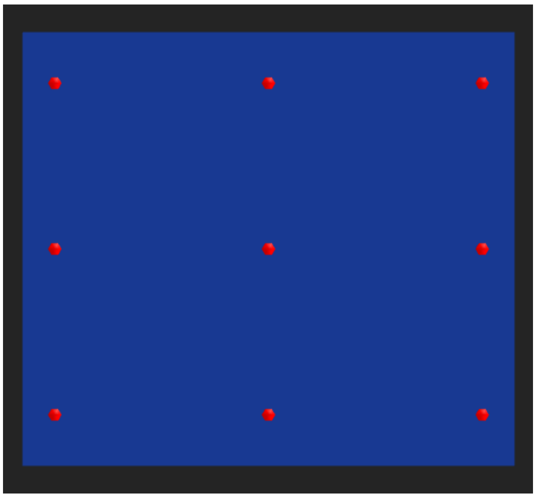

Fig. 5.12 Measurement points on carbon fiber plate specimen.

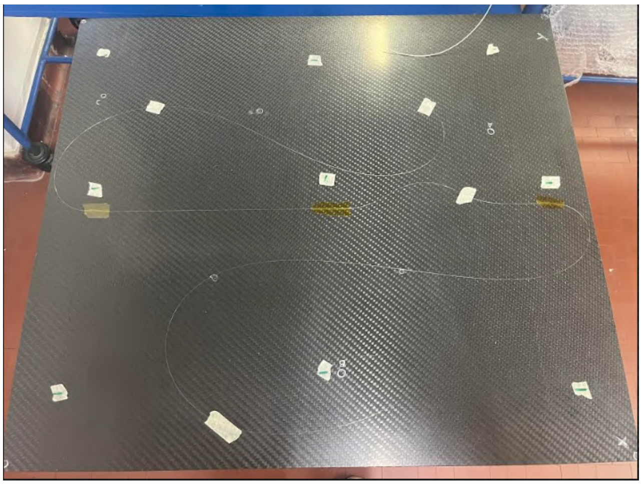

Fig. 5.13 Fiber positioning on the plate.

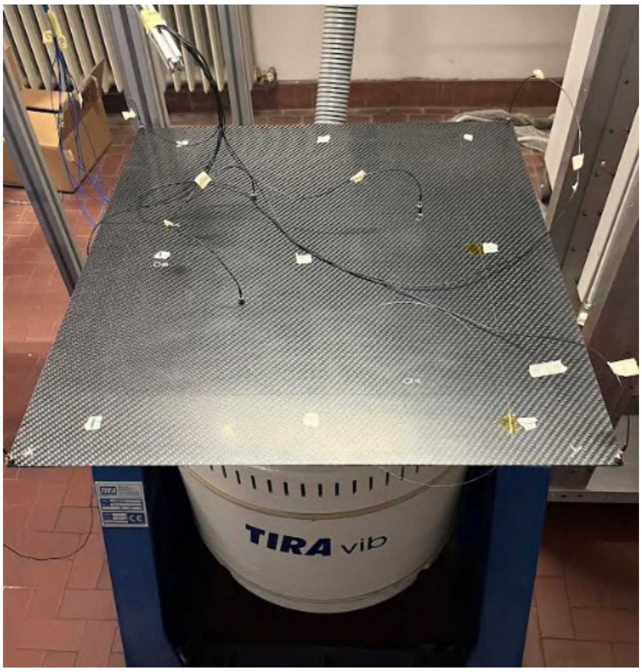


Fig. 5.14 Complete experimental setup with both accelerometers and FBG.

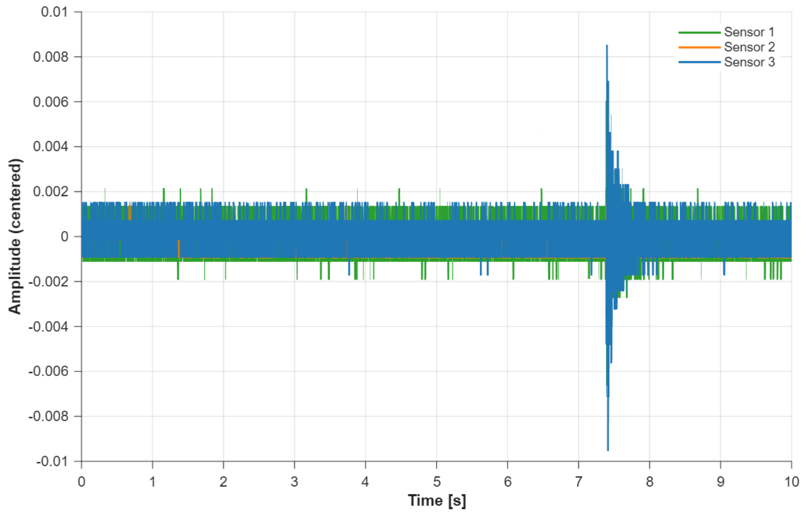


Fig. 5.15 Raw data of FBG during an hammer hit.

Table 5.1 Comparison between the peak frequencies measured in the two methods.

| FBG Frequency [Hz] | Accel. Frequency [Hz] | Error [%] |
|---|---|---|
| 81.6688 | 81.2500 | 0.515 |
| 193.527 | 191.406 | 1.108 |
| 214.709 | 216.406 | 0.784 |
| 221.173 | - | - |
| 229.646 | 226.562 | 1.361 |
| 339.961 | 321.875 | 5.619 |
| 352.469 | 353.125 | 0.186 |

# Chapter 6

# FBG-based Load and Pressure Sensors

The extremely high sensitivity of FBG sensors to mechanical strain enables their use for the measurement of physical parameters that can be directly related to strain. In particular, with reference to aeronautical applications, this chapter investigates the feasibility of developing proof-of-concept devices for two different types of sensors:

- pressure sensor;
- load cell.

Both approaches rely on a common design concept, namely the placement of the optical fiber (and the Bragg grating) within or on the surface of a compliant material that operates within its elastic regime under working conditions. The deformation induced by variations in the physical quantity to be measured can therefore be correlated with the wavelength shift detected by the interrogator. The optical nature of the measurement, combined with operation entirely within the elastic regime of the material, enables the realization of compact sensing systems that are immune to electromagnetic interference and adaptable to different geometries and applications. Moreover, since the final sensor output depends on the strain of the substrate into which the optical fiber is integrated, it is possible to obtain different sensitivity levels, performance characteristics, and application ranges while keeping the sensing hardware unchanged (i.e., FBG sensors and interrogator), and varying only the adopted packaging material. In addition, the combined use of optical sensing and additive manufacturing techniques ensures a high degree of versatility in the design of high-performance, integrated sensing solutions.

## 6.1 Load Cell

The first "complex" sensor developed is a proof-of-concept optical load cell, in which the sensitive element is a Bragg grating. Although load cells are widely available on the market, the development of a fully optical device enables measurements based on innovative materials and operation in harsh environments, where traditional sensing technologies may not provide sufficient precision and accuracy. Furthermore, the capability of optical fibers to support multifunctional measurements allows the serial integration of sensors designed to measure different physical quantities, while maintaining minimal invasiveness.

For the development of the sensor, a cylindrical geometry was selected, with the fiber arranged transversely with respect to the axial direction of the cylinder, along which the load to be measured is applied. The geometric design of the sensor must satisfy two fundamental requirements:

- a linear relationship must exist between the applied load and the strain measured by the FBG;
- the fiber must be positioned such that the applied load does not lead to fiber failure.

Considering these requirements, the fiber (and the sensor) was therefore placed transversely. In this configuration, the fiber is positioned far from the load application point, thus being protected, fully integrated into the system, and potentially usable for serial connections with other optical fiber segments. So, when a load is applied on the upper surface of the cylinder, it undergoes an axial deformation defined as:

$$\varepsilon_l = \Delta L / L_0 \tag{6.1}$$

However, it is well known that a material subjected to longitudinal loading also experiences deformation in the transverse direction. This relationship, which depends on the material properties, is expressed by Poisson's ratio:

$$\nu = \frac{E}{2G} - 1 = \frac{\varepsilon_t}{\varepsilon_l} \tag{6.2}$$

Consequently, assuming $d$ as the diameter of the circular cross-section of the cylinder, it follows that:

$$\Delta d = d \cdot \varepsilon_t \tag{6.3}$$

Substituting $\varepsilon_t$ with the previous expression yields:

$$\Delta d = \nu \cdot d \cdot \varepsilon_l \tag{6.4}$$

Within the elastic regime, the application of an axial load on a cylinder with cross-sectional area $A$ leads to a diameter variation $\Delta d$. By combining Hooke's law with the geometric relations, the following expression can be obtained:

$$F = \frac{E \cdot A}{h} \cdot \varepsilon_l = \frac{E \cdot A}{h} \cdot \frac{\varepsilon_t}{\nu} = K \cdot \varepsilon_t \tag{6.5}$$

This equation demonstrates that, for suitable materials operating in the elastic regime, it is possible to linearly correlate the applied load with the transverse deformation of the cylinder. By embedding the FBG sensor exactly at this location, it directly follows that:

$$F = K \cdot \varepsilon_t = K \cdot \frac{\Delta\lambda}{K_\varepsilon} = K_c \Delta\lambda \tag{6.6}$$

Based on the derived linear relationship, a proof of concept was developed, analyzing the sensor response also as a function of the employed materials. In particular, the sensor was fabricated following these steps:

- fabrication of a hollow mold with cylindrical geometry using additive manufacturing;
- positioning of the optical fiber (by means of suitable external mechanical supports) at the central section of the cylinder;
- casting of the resin into the mold;
- resin curing and mold removal.

The choice of resin was primarily dictated by the possibility of casting the material into the mold after fiber positioning. Moreover, low-cost resins with widely varying stiffness levels are readily available on the market.

Several sensor prototypes were developed, each characterized by specific properties. In particular, three configurations are analyzed here:

- FBG sensor embedded in silicone resin with a first mold geometry;
- FBG sensor embedded in silicone resin with a second mold geometry;
- FBG sensor embedded in epoxy resin with the first mold geometry.

The three developed configurations were tested on a dedicated bench developed at the Politecnico di Torino. In this setup, an electronic load cell was placed in a dedicated flange to assess the overall brake performance in terms of the load applied by the EMA. The optical load cell described in this work was integrated in the same location to evaluate its performance (Figure 6.1).

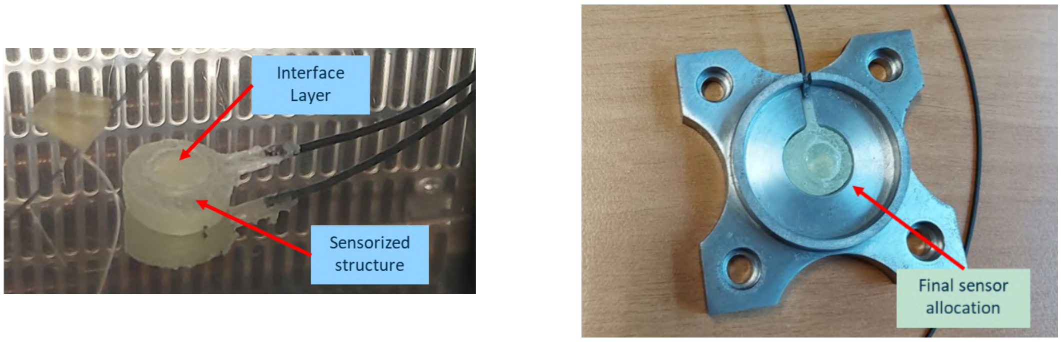


Fig. 6.1 The developed sensor (left) and its integration in the testing flange.

The first prototype was designed with the minimum possible sensor footprint, compatible with sensor placement and manual fabrication. The sensor was manufactured using silicone resin and subjected to stepwise loads ranging from 0 to 50 N. The results exhibit a linear trend, as expected. Furthermore, analysis of the raw data highlights an almost instantaneous response time to load application and, within the considered low-load range, the complete absence of hysteresis in the signal (Figure 6.2).

A second prototype was developed using the same material but with a modified geometry, in order to increase the operating range without altering the sensor sensi-

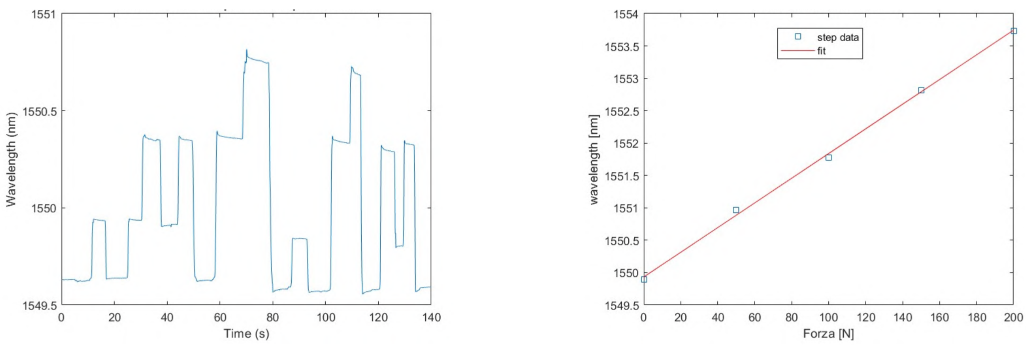


Fig. 6.2 Raw signal generated by the FBG (left) and load calibration curve (right).

tivity. The results confirm the observations made for the previous prototype, with an extended operating range up to 200 N.

Finally, a third proof of concept was realized using epoxy resin and the same geometry as the first prototype. This sensor demonstrated excellent adaptability to housings designed for traditional electronic load cells, showing reliable operation up to 700 N and the potential for extension to higher load ranges. Table 6.1 summarizes the obtained results.

Table 6.1 Comparison between developed Load Cell Sensors.

| **Material** | **Operative range** | **Calibration** |
|---|---|---|
| Silicone resin | 0–50 N | Linear |
| Silicone resin | 0–200 N | Linear |
| Epoxy resin | 0–700 N | Linear |

## 6.2 Pressure Sensor

The pressure sensor exploits the same underlying concept as the load cell, but employs a thin metallic plate uniformly clamped along all its edges as the sensitive structure.

Recalling Kirchhoff plate theory, and assuming small deformations and operation within the elastic regime of the material, the vertical displacement $w$ as a function of the radial coordinate is given by:

$$w(r) = \frac{P}{64D}(R^2 - r^2)^2 \tag{6.7}$$

By bonding the optical fiber to the surface of the plate, the resulting strain is expressed as:

$$\varepsilon(r) = -\frac{t}{2} \cdot \frac{d^2 w}{dr^2} \tag{6.8}$$

Substituting the expression reported in Eq. 6.7 and assuming the sensor is located at $r = 0$, the following expression is obtained:

$$\varepsilon = \frac{PR^2 t}{32D} \tag{6.9}$$

Recalling that $D$ represents the flexural rigidity:

$$D = \frac{Et^3}{12(1-\nu^2)} \tag{6.10}$$

the strain can be rewritten as:

$$\varepsilon = \frac{PR^2 t}{32 \cdot \frac{Et^3}{12(1-\nu^2)}} = \frac{12(1-\nu^2)PR^2 t}{32Et^3} = \frac{3}{8}\frac{PR^2(1-\nu^2)}{Et^2} = K_P \cdot P \tag{6.11}$$

Also in this case, the strain at the sensing point is linearly dependent on the applied pressure. Consequently:

$$P = \frac{\varepsilon}{K_P} = \frac{K_\varepsilon \Delta\lambda}{K_P} = K_S \cdot \Delta\lambda \tag{6.12}$$

A first experimental demonstration was developed to validate the proposed model. The proposed device is particularly suitable for the development and engineering of pressure sensors capable of operating in harsh or chemically aggressive environments, ensuring high performance and accuracy while being completely independent of electrical power. The same physical principle can be applied both to gas pressure measurements and to liquid pressure measurements, for instance for estimating the fuel level in a tank.

The developed prototype was mainly realized by assembling two supports manufactured using additive manufacturing, suitably dimensioned to house the instrumented plate. As with the load cell, the fiber layout was designed to enable flexible and modular integration within complex sensor networks (Fig. 6.3).

The sensor performance was initially evaluated by analyzing its basic optical response. Subsequently, the data distribution corresponding to each load step was carefully examined to validate the statistical behavior. Finally, particular attention was devoted to assessing measurement repeatability. Based on the collected data, the sensor calibration curve was constructed. The calibration curve and the statistical analyses are reported in Fig. 6.3.

The experimental data exhibited a strictly linear trend over the investigated pressure range, with a satisfactory sensitivity level (1 pm/30 mbar). The employed plate has a relatively large thickness (1 mm), and the applied pressure range was extremely low (0–200 mbar), thus ensuring the validity of the small-deformation assumption underlying Kirchhoff plate theory.

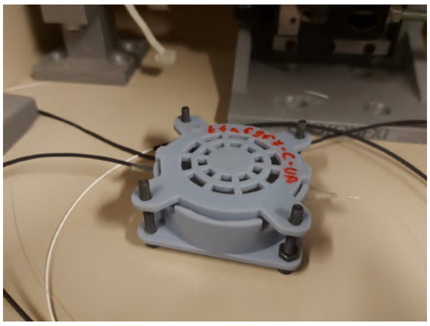

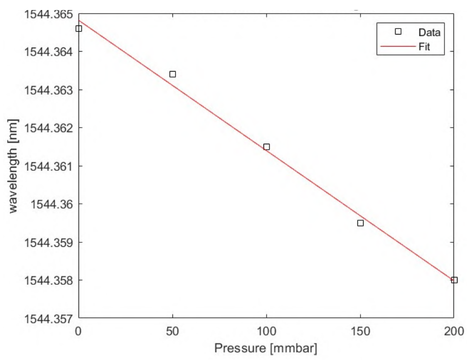


Fig. 6.3 First pressure sensor prototype and calibration curve.

Given the encouraging results, a second prototype was developed. In this case, the plate thickness was reduced to approximately 20 $\mu$m (cite), while the pressure range was increased from 0 to 800 mbar. The corresponding calibration curve is shown in Fig. 6.4.

A clear nonlinear behavior can be observed. Nevertheless, the experimental data demonstrate excellent sensitivity over the entire range (varying from 20 pm/mbar to 4 pm/mbar) and equally excellent repeatability. Due to the extremely small thickness and the extended pressure range, the fundamental assumption of small deformations underlying Eq. 6.7 is no longer valid. The plate thus exhibits a behavior closer to that of a tensioned membrane, which is generally characterized by a nonlinear $P(\varepsilon)$ relationship.

Table 6.2 summarizes the performance of the two developed prototypes.

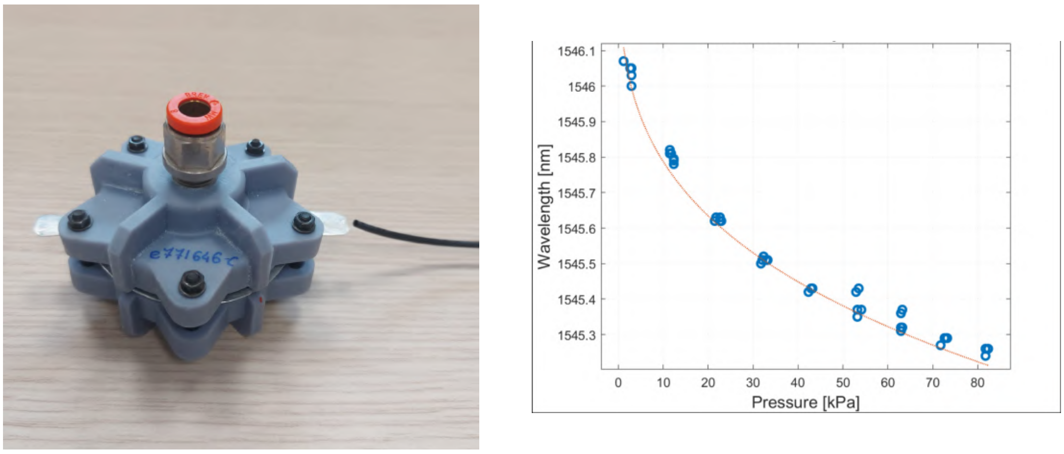


Fig. 6.4 Second pressure sensor prototype and calibration curve.

Table 6.2 Comparison between developed pressure sensors.

| Prototype | Operative range | Sensitivity | Calibration |
|---|---|---|---|
| 1 | 0–200 mbar | 1 pm/30 mbar | Linear |
| 2 | 0–800 mbar | 4–20 pm/mbar | Nonlinear |

# Chapter 7

# Procedure for Integrating FBG Arrays in Complex Systems

The application of sensor networks in the aerospace sector requires compliance with standardized, well-defined, and validated installation methodologies. As already discussed in Chapter 3, there are currently no international standard procedures for the use of optical sensing technologies, nor does a consolidated body of knowledge exist at the national or European level. The aim of this chapter is therefore to propose a methodology for the deployment and application of fiber-optic sensing systems that is versatile, easy to implement, and capable of ensuring repeatability and measurement accuracy.

FBG sensors measure localized strain at the point where they are bonded. They sense the deformation applied to the substrate on which they are mounted, provided that the employed adhesive ensures mechanical continuity. The implementation of a distributed sensor network across multiple components therefore requires routing the optical fiber along a more or less complex path, which may interface with one or more materials. The design of an optical sensing line for monitoring a complex system must therefore take into account several specific operational steps:

- understanding of the physical system to be monitored and the parameters to be measured;
- definition of the correlation between the desired physical parameters and locally measurable strains;

- definition of the measurement locations and of the nature of the information (thermal or mechanical);
- definition of the number of channels to be used;
- definition of the wavelengths to be employed;
- definition of the geometric path of the fiber lines;
- estimation of optical losses and validation of the routing;
- assembly of the sensor line;
- positioning and bonding of the sensing line.

Each of the listed aspects plays a key role in the development of a smart system through the integration of FBG optical sensing technologies.

## 7.1 Understanding of the Physical System

This step does not require physical activities but, from a conceptual standpoint, represents the fundamental transition from using Bragg gratings as simple sensors to adopting them as integrated resources within systems, enabling the development of intelligent components. The activity is based on a simple principle: during the operational phase of any aero-mechanical system, motion conditions, loads, and/or constraints generate localized stresses. These stresses are translated into deformations that, for obvious safety reasons, remain within the elastic regime of the material. The magnitude of these deformations and their spatial distribution depend on the specific operational conditions and on the involved components.

Analogous considerations can be made with respect to the development of localized overheating and, more generally, internal temperature variations within systems. Consequently, a thorough understanding of the operational conditions of the system under investigation—also supported by numerical models and digital twins—allows the identification of the main mechanically compliant regions and enables the determination of the minimum number of sensors required to reconstruct the desired information.

This approach can be adapted to highly diverse applications, provided that a control logic can be developed using temperature or mechanical strain as input parameters. In fact, the optical signal provided by the sensor can be employed within specific control strategies even without being directly converted into a physical parameter (i.e., temperature or strain). Instead, the optical response itself can be used as a raw signal to be compared against suitably defined thresholds and, only at the end of the data processing chain, correlated with a well-defined system performance metric.

## 7.2 Definition of the Correlation between desired final Physical Parameters and locally Measurable Parameters

It is not possible to define a universal high-level correlation between local strain and system-level quantities for every type of system. However, the approach becomes clearer when considering practical examples. As already discussed in the development of the pressure sensor and the load cell, the calibration curve of the sensor was not correlated to the micro-strain measured at the sensing point, but rather to the overall load applied to the entire sensor. The same concept can be applied, for instance, to constraint regions within kinematic supports. The motion of arms, links, or similar components generates reaction forces in the supporting structures. Through appropriate calibration procedures, it is possible to obtain a correlation between the wavelength shift measured by the sensors and the physical motion that generated it.

Another possible approach consists in the development of control logics based on the combination of multiple measurement points, where the logic produces an "on/off" output. The extremely fast response of the optical fiber is particularly suitable for this type of data interpretation. This approach is especially useful for the qualitative description of system parameters that do not require an output expressed in physical units. Examples include the detection of an impact on a panel or the identification of thermal hot-spots within a control volume. In such cases, the absolute value measured by a single sensor is not relevant; instead, the relative variation between different sensing points is of primary importance.

This type of monitoring becomes increasingly meaningful as the number of sensing points increases, while the overall mass, volume, and installed hardware remain nearly unchanged. Another application adopting this logic is the determination of the "in-flight" or "on-ground" state of a UAV. By properly positioning an FBG sensor (for example, on the landing gear structure), it is possible to identify with high accuracy a range of optical responses characterizing the ground state, and another range corresponding to flight conditions.

By applying this concept at scale to individual components, it becomes possible to develop a comprehensive mapping of system performance through an integrated, versatile, and lightweight solution capable of generating data without relying on electromagnetic phenomena. Finally, the possibility of multiplexing different sensors on the same optical line enables the simultaneous management of thermal and mechanical measurements and their interpretation, whether as direct sensor readings or as threshold-based inputs within more complex control logics.

## 7.3 Definition of the Number of Sensors, Channels, and Fiber Geometric Path

The design of a distributed FBG sensor network for the integrated monitoring of a specific system, at different levels of complexity, requires the definition of specific requirements:

- the number of measurement points required to characterize the behavior of interest;
- the relative placement of the different sensing points;
- an estimate of the expected range of values for each measurement point;

These three requirements represent the key parameters around which the design choices for the optical sensor network are developed.

The number of required measurement points is a determining factor in the overall definition of the sensing line configuration. This aspect is directly linked to the performance of the employed interrogator. As is well known, each type of interrogator operates by sending a specific wavelength spectrum into the optical fiber.

Bragg gratings must therefore be designed such that, independently of the operational conditions, they reflect wavelengths that lie within the working spectrum of the interrogator. For this reason, it is essential to obtain an accurate estimate of the amplitude of the wavelength variations at each measurement point under all operational conditions, while also ensuring a suitable margin for off-nominal scenarios. Depending on the confidence level of the estimate, appropriate safety factors must be adopted. As a rule of thumb, for mixed thermal and/or mechanical sensing applications, a margin of ±2 nm for each measurement point represents a good compromise. This value ensures a margin of approximately ±200 °C assuming purely thermal measurements, and about ±2000 $\mu\varepsilon$ in purely mechanical applications. Moreover, it generally prevents overlap between measured signals while maximizing the multiplexing capability of the instrumentation, which typically supports up to 16 measurement points per communication line, with an interrogation spectrum of approximately 40 nm. In addition, it is essential to ensure that the signals do not overlap. The interrogator, in fact, orders the sensors according to increasing detected wavelengths, without providing any spatial information. The correlation between wavelength and physical sensor location is always performed during post-processing. It is therefore evident that, on each optical line, the operational wavelength ranges of each sensor should ideally be completely disjoint or, alternatively, the sensors should be arranged such that their relative wavelength order does not change (for example, all points experience heating, all experience cooling, or only compression or only tension). In Figure 7.1 a schematic representation of this concept is reported.

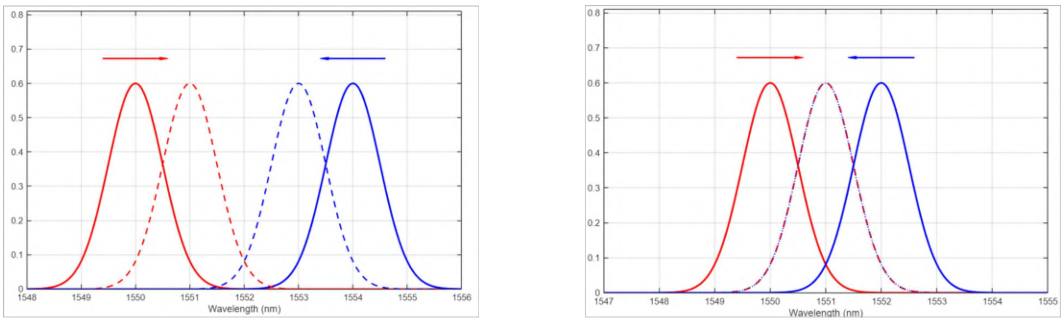


Fig. 7.1 Example of wavelength selection strategy.

Once the measurement points, the reference wavelengths for each sensor, and the number of lines have been defined, the geometric routing of the fiber must be determined. This routing must satisfy specific requirements:

- the fiber must have a bending radius not smaller than 3 cm, in order to avoid excessive optical transmission losses;
- two consecutive sensors placed on the same optical line must be spaced by at least 10 cm to allow for proper physical assembly;
- the fiber must not be subjected to shear stresses, either during system operation or during assembly and maintenance phases.

As an example, the following hypothetical operational case is provided. Let us assume that an FBG sensor network is to be installed on a panel as depicted in the figure, where the points highlighted in red represent those identified—through an appropriate feasibility analysis—as the most significant ones to be monitored. One possible sensing strategy is shown in Figure 7.2, where four fibers with three sensors each are employed. This solution, for instance, enables linear routing paths, sufficient spacing between wavelengths, reduced multiplexing losses, and optimized data handling.

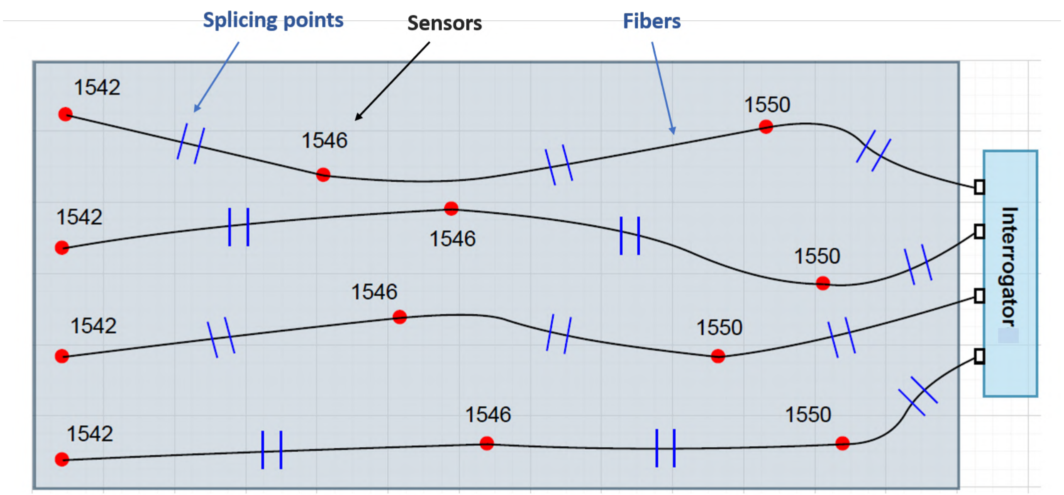


Fig. 7.2 Example of sensors network project.

## 7.4 Optical losses estimation

The definition of the number of sensors and of the geometric routing of the optical fiber does not conclude the design phase of the measurement line. Indeed, it is necessary to consider that every bend, every sensor, and, more generally, every element composing the optical communication line contributes to a progressive attenuation of the optical signal. Since the data generated by each sensor consist of a reflected wavelength peak within the reference optical spectrum, it is essential to maintain a sufficiently high signal intensity level (typically above 20%) in order to clearly distinguish a sensor-generated peak from background noise.

To estimate the final signal intensity produced by the sensors under operational conditions, it is therefore necessary to consider both the optical power generated by the interrogator and all elements within the transmission line that may introduce optical losses. More specifically, the main sources of optical loss include:

- intrinsic attenuation of the optical fiber;
- presence of mechanical connections (connectors, feedthroughs, ...);
- splices performed using a fusion splicer, necessary to multiplex different sensors or to connect fiber sections and connectors;
- bending radius of the fiber routing, resulting in local variations of propagation conditions;
- sensor insertion losses.

In this section, each of the main optical signal loss mechanisms is analyzed and quantified based on data available in the literature and validated through dedicated laboratory tests. Furthermore, simplified formulations are derived in order to develop a functional and scalable algorithm for predicting optical power losses once the geometry of a specific system is known. This tool is intended as a practical support for the standardized and integrated design of large-scale sensor networks deployed over complex geometries.

### 7.4.1 Optical Losses Estimation Model

In order to develop a tool capable of estimating the overall optical power loss during the design phase of a measurement line, it is necessary to define an appropriate computational model. The total optical loss measured by the instrumentation results from the combination of the physical properties of the materials used and the geometric characteristics of the designed optical path. In its most general form, the model allows the overall optical power loss to be expressed as:

$$L_{tot} = 2(L_f + L_b + L_c + L_s) \tag{7.1}$$

where:

- $L_f$ represents the optical loss induced by the material properties of the fiber;
- $L_b$ accounts for the losses due to macrobending, i.e., the geometric curvatures imposed on the fiber;
- $L_c$ refers to losses induced by optical connections (splices, feedthroughs, connectors);
- $L_s$ represents the losses introduced by the FBG sensors located upstream of the considered measurement point.

The contribution $L_f$ depends on the physical characteristics of the optical fiber. It is typically expressed as attenuation in [dB/km], a value generally provided by the fiber manufacturer. This total attenuation includes two main components:

- intrinsic attenuation of the fiber material;
- losses due to microbending effects.

Material absorption losses $L_f$ arise from the intrinsic absorption of light by the fiber material, as well as from impurity-related absorption caused by metallic ions and $OH^-$ ions within the fiber. Additionally, scattering losses originate from the diffusion of the optical signal within the fiber medium [73–75]. The combined effect of these mechanisms defines the intrinsic attenuation of the fiber, typically expressed in dB/km, and can be determined from manufacturer specifications [76]. Microbending losses result from microscopic bends in the fiber that induce local variations in propagation conditions.

The term $L_c$ depends on the optical connections present along the fiber line and is calculated as the sum of:

- losses due to connector insertion;

- losses from fusion splicing between fiber segments;
- losses due to feedthroughs along the optical path.

Each of these losses is quantified based on manufacturer data, while splicing losses are measured directly by the fusion splicer at the end of each joining process.

The term $L_s$ represents the loss introduced by each FBG sensor located upstream of the considered point along the optical network. In this case as well, the optical loss generated during sensor fabrication is generally standardized and provided in the manufacturer datasheet.

The term $L_b$ accounts for attenuation due to macrobending, i.e., the power loss induced by the geometric path imposed on the fiber. Estimating the variation of optical properties as a function of the bending radius is a complex task due to the interaction between the spectral characteristics of the incident light and the mechanical and optical properties of the fiber (core and cladding). Using the simplified Marcuse model [77], the attenuation coefficient can be expressed as:

$$2\alpha = \frac{\sqrt{\pi}k^2 e^{-\frac{2\gamma^3 R_{eff}}{3\beta^2}}}{2\sqrt{\gamma^3 R_{eff}}V^2 K_{m-1}(\gamma a)} \tag{7.2}$$

where:

- $a$ is the core radius;
- $V = 2\pi a/\lambda\sqrt{n_1^2 - n_2^2}$ is the normalized frequency of the optical fiber, with $n_1$ and $n_2$ being the refractive indices of the core and cladding, respectively, and $\lambda$ the incident wavelength;
- $\beta = k_0 n_{eff}$ with $k_0 = 2\pi/\lambda$ and $n_{eff}$ the effective refractive index;
- $\gamma = \sqrt{\beta^2 - k_0^2 n_2^2}$ describes the exponential decay of the field in the cladding region;
- $k = \sqrt{k_0^2 n_1^2 - \beta^2}$ represents the radial oscillation rate within the core;
- $K_\nu$ denotes the modified Hankel function of order $\nu$;

- $R_{eff} = 1.28R$ is the Schermer and Cole relation [78], which accounts for elasto-optic effects and refractive index deformation induced by curvature $R$.

Considering $R_{eff}$ as the only geometry-dependent parameter of the optical system (since all other parameters are fixed by the fiber material and light source), the model was simplified for implementation in the overall loss estimation as:

$$\alpha = \frac{A}{\sqrt{R_{eff}} e^{BR_{eff}}} \tag{7.3}$$

where parameters $A$ and $B$ are calculated from relation 7.2.

Finally, from the same relation it is also possible to estimate the bending loss induced by a specific number $N$ of complete circular windings:

$$L_N = \eta N \tag{7.4}$$

where $\eta$ is the loss of a single winding calculated using Eq. 7.2.

### 7.4.2 Test Campaign

A laboratory test campaign was conducted to validate the proposed model and it was structured into three main phases. First, the effect of fiber curvature on signal transmission was analyzed. Subsequently, point losses at optical connections were investigated. Finally, the influence of individual sensors on signal intensity during transmission was evaluated.

The first phase consisted of an experimental campaign in which, by modifying the fiber bending radius and measuring the corresponding signal loss, it was possible to estimate the trend of the attenuation coefficient $\alpha$ $[dB/mm]$. This allowed verification of the consistency between the theoretical model and experimental data. To reproduce the desired bending conditions, a series of small cylindrical molds were designed using CAD and fabricated via 3D printing in resin. Each cylinder had a height of 1 cm and a different radius, around which the optical fiber was wrapped. Adhesive tape was used to maintain the fiber position and prevent excessive tension or oscillations in the signal. A range of curvature radii between 4 mm and 15 mm was selected to encompass the most relevant cases. The results confirmed that the implemented model is in good agreement with laboratory data (Figure 7.4). The only notable discrepancy was observed for very small bending radii (below approximately 6 mm), where the model becomes less accurate due to oscillatory phenomena. These effects would require more advanced modeling approaches, such as perturbation theory. However, such extreme bending conditions are typically avoided in practical applications due to excessive signal attenuation. The experimental results also showed good agreement for multiple winding configurations.

The second phase focused on losses due to optical connections. Increasing the number of interconnections leads to cumulative attenuation of the signal. Measurements performed using FC/APC connectors showed an average loss per connector pair of approximately 0.24 dB, in close agreement with the datasheet value of 0.25 dB. Slight variations between individual measurements highlighted the importance of connector cleanliness and alignment. The final phase examined losses associated with the presence of sensors along the fiber. By analyzing the reflected signal from downstream sensors, losses of 0.15–0.18 dB were observed, confirming consistency with manufacturer specifications ($\leq 0.25$ dB).

For the development of the software interface, a dedicated Python code was implemented using the Tkinter GUI toolkit. The interface collects input parameters such as intrinsic fiber attenuation, microbending losses, connector losses, and FBG insertion losses. Users can define the sequence of elements along the optical path and their characteristics. Specific assumptions were introduced to simplify user input. For connectors and FBG sensors, default loss values are used, while splice losses must be manually entered due to their dependence on alignment quality. A dedicated section allows the evaluation of bending losses, based on the simplified Marcuse model. Depending on the selected configuration, the user inputs:

- number of windings and bending radius;
- bending radius and winding angle;
- number of windings and ellipse semi-axes.

For elliptical configurations, a numerical integration approach was implemented due to the variable bending radius. A warning is provided when small radii may reduce accuracy. Finally, the interface computes total losses and provides a graphical representation of the signal spectrum and reflected peaks, similar to that obtained from an optical interrogator (Figure 7.5).

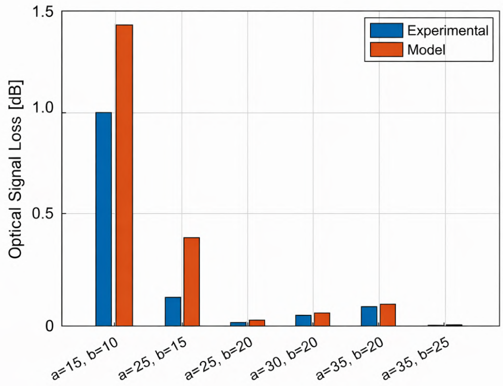


Fig. 7.3 Comparison between numerical model and experimental data on elliptical losses.

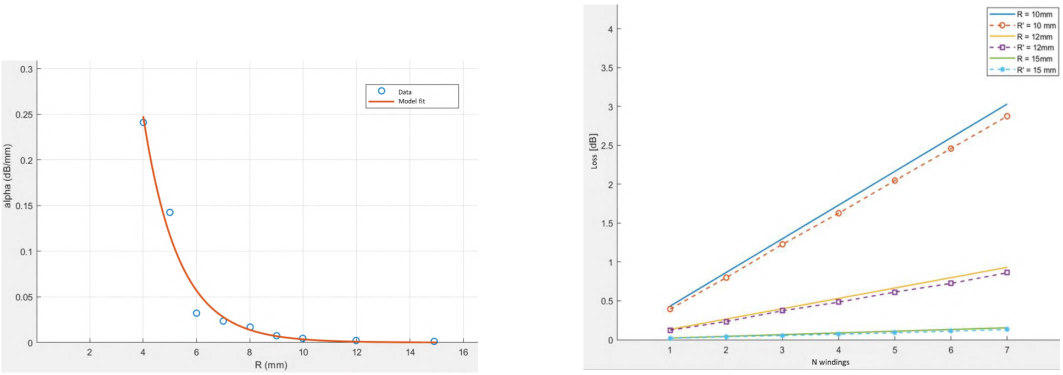


Fig. 7.4 Comparison between experimental data and the simplified model fit for different bending radii (left) and comparison between experimental data and the simplified mathematical model for different bending radii and number of windings (right).

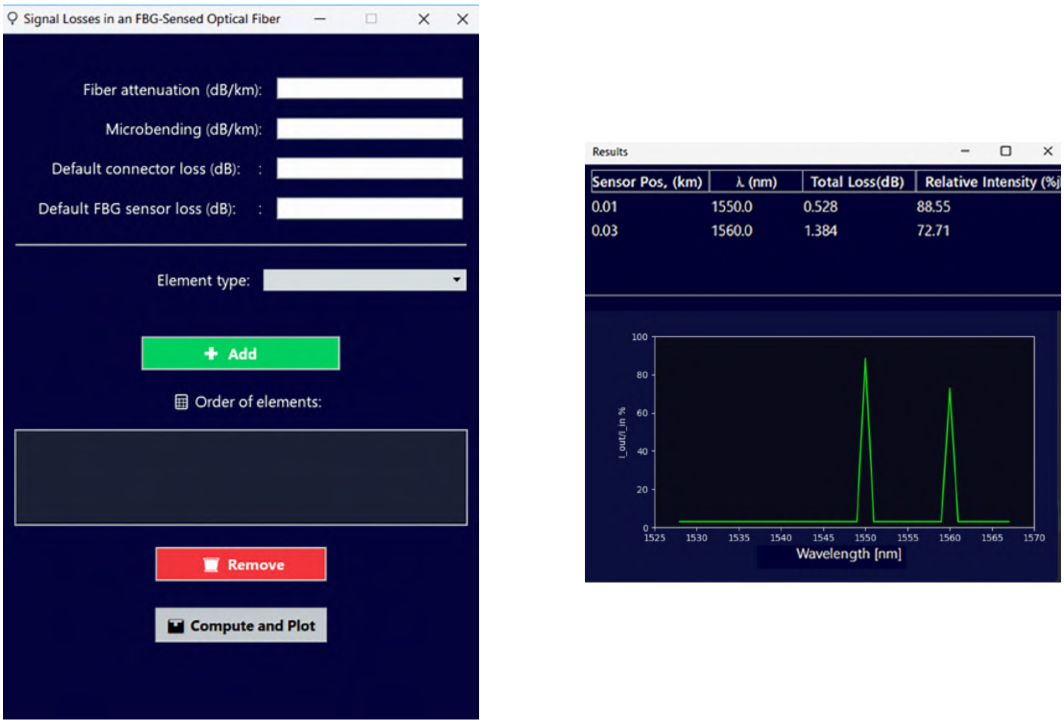


Fig. 7.5 Graphical interface of model results.

## 7.5 Assembly of the Measurement Line

Once the number of sensors, their distribution across the available optical channels, the reference wavelengths assigned to each of them, and the geometric routing of the optical fibers have been defined, it is possible to proceed to the assembly phase of the measurement line. This phase can be further subdivided into several key steps:

- Selection of the fiber coating;
- Calculation of the required fiber length;
- Splicing of the individual fiber segments;
- Final positioning and bonding of the fiber.

Each of these aspects requires specific considerations, whose complexity depends on the intended application.

### 7.5.1 Selection of the Fiber Coating

Although the coating does not perform any data transmission function, it plays a crucial role in ensuring the integrity and functionality of the fiber, given the extreme fragility of the inner core and cladding layers responsible for optical signal propagation. Considering the most common application domains and the availability of raw materials on the market, two primary selection parameters can be identified:

- material;
- diameter.

With regard to the material, two main coating types are typically considered:

- acrylate coating;
- polyimide coating.

Regarding diameter, the coating may lead to a final fiber diameter of:

- 125 $\mu m$;
- 250 $\mu m$.

In general, polyimide coating is preferable for applications involving harsh environments—particularly in the space sector—since it withstands higher temperatures and provides improved mechanical resistance. Conversely, a smaller diameter enhances the minimal invasiveness of the sensing system, whereas a larger diameter increases robustness and facilitates handling during installation. Given the still limited scientific literature concerning low-level operational procedures for FBG fiber implementation—especially with regard to comparative analyses under different application methodologies—a dedicated experimental campaign was conducted to quantitatively evaluate the performance of the various configurations. Table 7.1 summarizes the main features of polymide and acrylate based coatings.

| Property | Acrylate | Polyimide |
|---|---|---|
| Max temperature | $\sim 100°C$ | $\sim 300°C$ |
| Mechanical resistance | Medium | High |
| Handling ease | Medium | High |
| Humidity sensitivity | Low | High |
| Suitability for space | Low | High |
| Diameter availability | 125-250 $\mu$m | 125–250 $\mu$m |

Table 7.1 General comparison between acrylate and polyimide fiber coatings.

### 7.5.2 Calculation of the Required Fiber Length and Splicing of Individual Segments

The splicing procedure between two fiber segments is performed using high-precision equipment and follows a well-defined process. The joint is obtained through localized fusion of the two fiber ends using a high-intensity electric arc. The splicing procedure consists of three distinct steps:

- stripping phase;
- cleaving phase;
- splicing phase.

The stripping phase involves removing the coating from the two fiber ends to be joined. This step is essential because the fusion process must act exclusively on the core and cladding. The cleaving phase consists of a high-precision cut of the fiber ends. In order to ensure proper fusion through the electric arc, the two contact surfaces must be orthogonal to the fiber axis, with an angular tolerance typically not exceeding 1°. The splicing phase involves the application of the electric arc, the physical fusion of the fiber ends, and—if required—the recoating of the spliced section. In order to perform a geometrically precise splice, it is necessary to properly dimension the two fiber pigtails to be joined. After completion of the process, the spliced region typically extends over several centimeters. Moreover,

variability associated with stripping, cleaving, and splicing operations may introduce a length uncertainty of approximately 5–10 cm if not properly managed. While such uncertainty may be negligible for large geometries, it becomes unacceptable in many applications, where tolerances are typically on the order of 1–2 cm. To drastically reduce this uncertainty, a careful analysis of the stripping and cleaving phases is required. Stripping is generally performed manually using dedicated pliers (see Fig. 7.6). The procedure lacks a precise spatial reference: the coating is removed from the first fiber–blade contact point to the free end. Since this operation requires applying a controlled axial force to avoid fiber breakage, stripping is typically limited to 5–7 cm.
Cleaving, on the other hand, is performed using a mechanized blade (see Fig. 7.6) that allows positioning the cut with micrometric precision relative to the end of the coated section. As a result, at the moment of arc application (which does not significantly alter the total length of the pigtails), the configuration corresponds to that shown in Fig. 7.6.

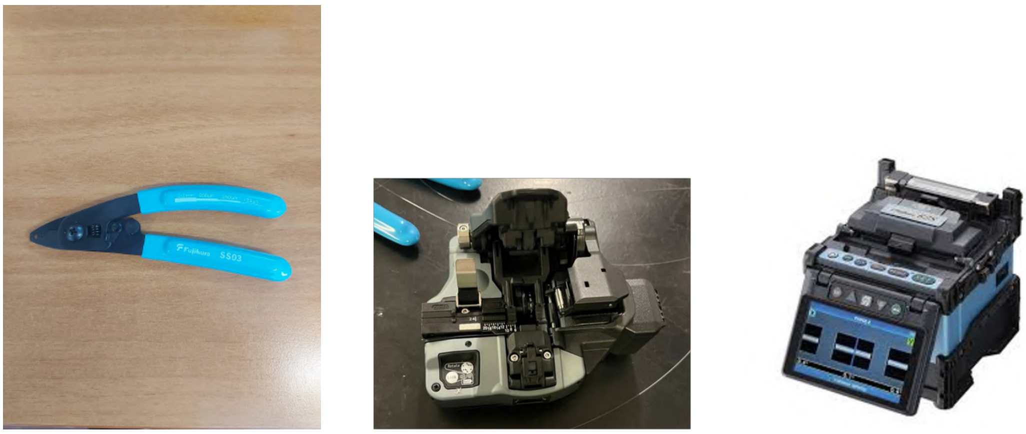

Fig. 7.6 Fromn left to right: stripper, cleaver and splicer.

Let $x$ denote the distance between the splice point and the origin of the measurement reference (typically the upstream sensor). Let $a$ represent the stripped section extending from the end of the coating to the cleaving point, and $b$ the additional free length required for proper positioning during cleaving. From the schematic representation (Fig. 7.7), segment $a$ lies upstream of the splice, whereas segment $b$ lies downstream. Given the desired distance $x$, the fiber must first be manually cut at position $x+b$ (using a simple cutter) for both pigtails. After this initial cut, stripping should begin at position $x - a$ (or, more practically, at a distance $c = a + b$ from the manual cut).

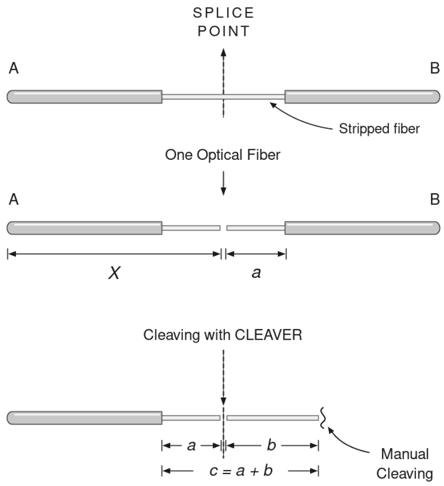


Fig. 7.7 Scheme of fusion splicing process.

Once stripping is completed, the fiber is positioned inside the cleaver. The beginning of the stripped region must be aligned with the graduated reference corresponding to distance $a$. After stripping and cleaving, the fiber ends can be placed near the electrodes of the fusion splicer, where alignment and fusion are automatically performed. There are no strict universal values for $a$ and $b$; however, practical experience allows defining reference values. Parameter $a$ represents the stripped portion that remains exposed after splicing. This section significantly weakens the fiber and reduces its mechanical robustness. Therefore, especially in long and complex sensor networks with multiple splices, $a$ should be minimized. However, the fusion splicer requires a sufficient stripped length to correctly align the fiber cores and reduce splice failure probability. Although the automated process can technically start with any value of $a$, lengths below 5 mm frequently lead to alignment errors due to coating discontinuity. A good compromise is therefore $a = 10$ mm (with $a > 5$ mm). Regarding parameter $b$, its value depends on the specific cleaver used. Since cleaving is a mechanical process, precision improves when the fiber is firmly supported and slightly tensioned. For most commercial cleavers, a value of $b = 5$ cm provides adequate cutting precision and manageable handling. This description highlights that, in case of splice failure, repeating the operation while preserving the original geometric references is often impossible. Two main failure mechanisms may occur:

- contact surface misalignment beyond geometric tolerance;
- defective fusion due to contamination.

In the first case, the improperly cleaved end must be re-cut. In the second case, the fiber must be manually cut at the defective splice and the entire process repeated. However, repeating the process implies having only the residual stripped length $a$, which is often insufficient for proper cleaving and positioning. Consequently, a new stripping operation upstream becomes necessary, shifting the original reference position $x-a$ and reducing the final distance $x$. While the optimal strategy remains the proper initial dimensioning of $a$ and $b$, several compensatory strategies may be adopted:

- slightly oversize $a$ and $b$;
- accept reduced support during re-cleaving;
- perform operations sequentially on the two pigtails;
- minimize unnecessary multiplexing;
- carefully clean fiber ends using ethyl alcohol and dedicated tools.

### 7.5.3 Positioning and Bonding of the Optical Fiber

Once the optical line has been fabricated, the most appropriate strategy for fiber positioning must be selected. Depending on the application, several techniques can be adopted:

- mechanized jig for high-precision bonding;
- additive-manufactured mask for controlled adhesive deposition;
- cellulose matrix pre-impregnated with adhesive;
- direct adhesive application;

- Kapton/industrial adhesive tape covering;
- protective coating without direct adhesive contact.

In practical applications, multiple approaches are often combined. It is essential to distinguish between sensored and non-sensored fiber segments. The bonding strategy of the sensored section directly affects measurement accuracy and must therefore be carefully selected. Conversely, non-sensored sections mainly require mechanical protection, allowing simpler solutions. For strain measurements, bonding is mandatory. Typically, cyanoacrylate or epoxy resin is used. A detailed analysis is provided in Section 7.6. Manual adhesive application is generally sufficient, although masks can improve precision and aesthetics. For high-precision applications, a dedicated mechanized tool was developed (Fig. 7.8). The system ensures repeatable bonding thickness and geometry.

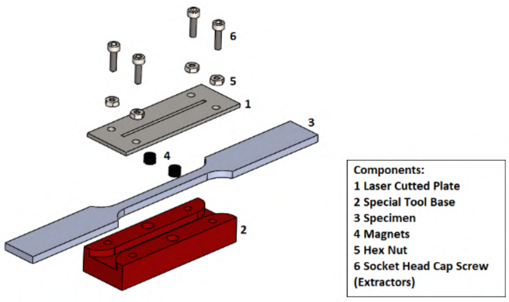


Fig. 7.8 Example of localized standard bonding method.

The standardized bonding procedure is:

- place the specimen and position the fiber;
- apply release agent to the calibrated plate;
- align and fix the plate;
- inject resin;
- allow curing and remove the tool.

This method guarantees repeatability and enables comparative studies. An alternative approach uses a pre-impregnated porous matrix (Fig. 7.9), ensuring uniform bonding and protection.

Fig. 7.9 Example of diffused standard bonded method.

Finally, Kapton tape represents a simple and versatile solution. It is suitable for low-strain applications or as protection for non-sensored sections, but less reliable for high-load or dynamic measurements due to viscoelastic effects.

| **Application** | **Recommended Coating** | **Bonding Strategy** | **Notes** |
|---|---|---|---|
| High-temperature / space | Polyimide | Epoxy resin | High thermal stability, low outgassing |
| Structural strain measurement | Acrylate / Polyimide | Epoxy or cyanoacrylate | Ensure strong mechanical coupling |
| Low-strain / temporary installation | Acrylate | Kapton tape | Fast installation, lower accuracy in case of high loads |
| Dynamic measurements | Polyimide | Epoxy resin | Avoid viscoelastic effects |
| Distributed sensing (large networks) | Acrylate / Polyimide | Mixed strategies | Balance between robustness and flexibility |
| Protected routing (non-sensored fiber) | Acrylate or Polyimide | Tape / External jacket | Only mechanical protection |

Table 7.2 General guidelines for selecting coating and bonding strategy for FBG sensor integration.

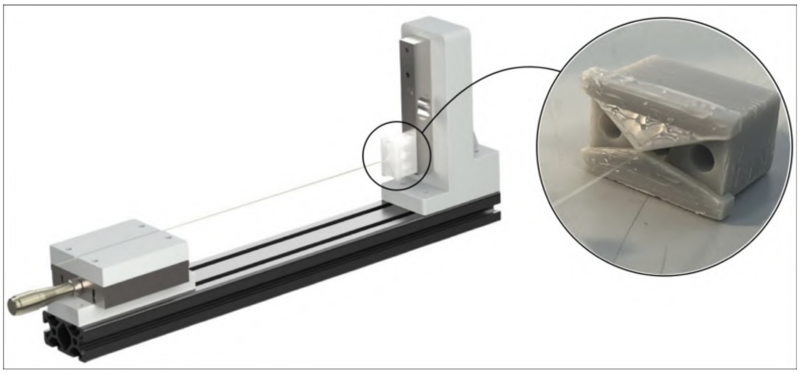

Fig. 7.10 Experimental test bench for comparative analysis of bonding solutions.

## 7.6 Experimental Comparison of Application Solutions

The methodological framework for optical sensor network implementation is completed through a dedicated experimental campaign aimed at comparing the main optical fiber configurations and bonding strategies previously discussed. An experimental test bench was designed based on a structural frame consisting of a double linear guide, selected to ensure high stability and precision during the application of mechanical loads. Several functional supports were integrated into this structure, each specifically designed to house and correctly position the main components of the setup, namely the micro-displacement actuator, the load cell, and the optical fiber. The physical components were manufactured using Additive Manufacturing techniques. In particular, Fused Deposition Modeling (FDM) with PLA material was adopted for non-critical elements, due to its adequate mechanical strength and rapid fabrication capability. In order to evaluate the influence of multiple parameters on the optimal integration methodology, a simplified Design of Experiments (DoE) approach was developed, considering the following variables:

- External diameter of the optical fiber ($125\,\mu m$ and $250\,\mu m$)
- Coating material (polyimide and polyacrylate)
- Type of adhesive used for bonding

Following the selection of materials and adhesives, the experimental procedure for mechanical testing was defined as follows:

1. *Specimen preparation:* Each test began with fiber selection and adhesive application at one end. In the case of epoxy resin, specimens were cured for at least 24 hours at room temperature to ensure complete polymerization.

2. *Specimen installation:* After curing, the specimen was mounted between the fixed support (connected to the load cell) and the micro-displacement actuator, which acted as the loading system.

3. *Test execution:* Incremental displacements of 0.1 mm were applied. At each step, the force transmitted to the fiber was measured by the load cell. The electrical signal was amplified and digitized using an HX711 module and acquired through an Arduino platform.

4. *Data acquisition and storage:* Data were collected in real time using custom MATLAB software. The program computed the average force over five measurements at each step and recorded it together with the corresponding elongation.

The collected datasets were initially analyzed to provide a preliminary comparison between configurations. This first analysis clearly showed that, for identical fiber characteristics (same diameter and coating), silicone adhesive exhibited a mechanical response not comparable with the other bonding solutions. As shown in Fig.7.11, silicone adhesive presented a significantly different behavior. While epoxy resin and cyanoacrylate exhibited a linear force–elongation relationship, silicone showed irregular behavior with force levels approximately one order of magnitude lower (around 0.5 N compared to 25–30 N). This difference indicates a fundamentally different load transfer mechanism, and therefore silicone adhesive was excluded from further analysis.

### 7.6.1 Factorial Analysis – Linear Elastic Regime

The independent variables influencing the system response were defined at two or three levels:

- Fiber diameter: 2 levels (125 $\mu m$ and 250 $\mu m$)
- Fiber coating: 2 levels (polyimide = 1; polyacrylate = 2)

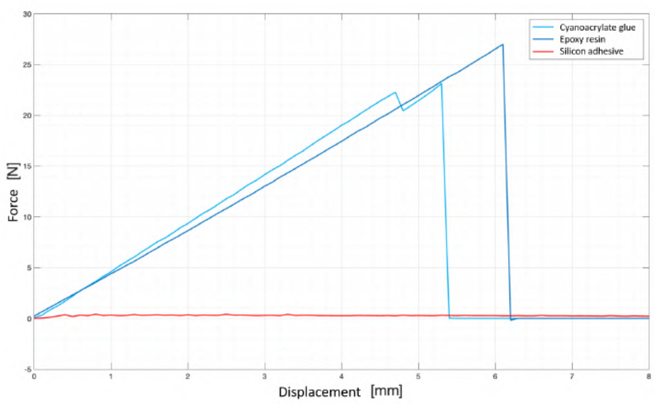


Fig. 7.11 Comparison of adhesive performance: silicone vs structural adhesives.

- Adhesive type: 2 levels (epoxy resin = 1; cyanoacrylate = 2)
- Fiber elongation: initially 3 levels (0.5 mm, 1.0 mm, 1.5 mm)

The analysis was first limited to the linear elastic regime, where the force–elongation relationship is proportional and reversible. Probability plots indicate that the measured forces do not strictly follow a normal distribution. This behavior is consistent with the deterministic nature of the system, governed by physical and technological parameters rather than stochastic variability. The Pareto analysis identified fiber diameter as the dominant factor, followed by displacement. Interaction effects were negligible, and the adhesive type remained below the statistical significance threshold, confirming its marginal influence in the linear regime.

Detailed factor analysis highlighted that:

- *Diameter:* Fibers with larger diameter (250 $\mu m$) showed higher force values, due to increased bonding area and improved load transfer.
- *Coating:* Polyimide-coated fibers sustained higher loads. Although median values were comparable, polyimide exhibited larger dispersion, indicating increased compliance.
- *Adhesive:* No significant differences were observed between epoxy and cyanoacrylate.
- *Displacement:* A linear increase of force with displacement was observed, as expected.


Fig. 7.12 Effect of diameter and coating in linear regime.


Fig. 7.13 Effect of adhesive and displacement in linear regime.

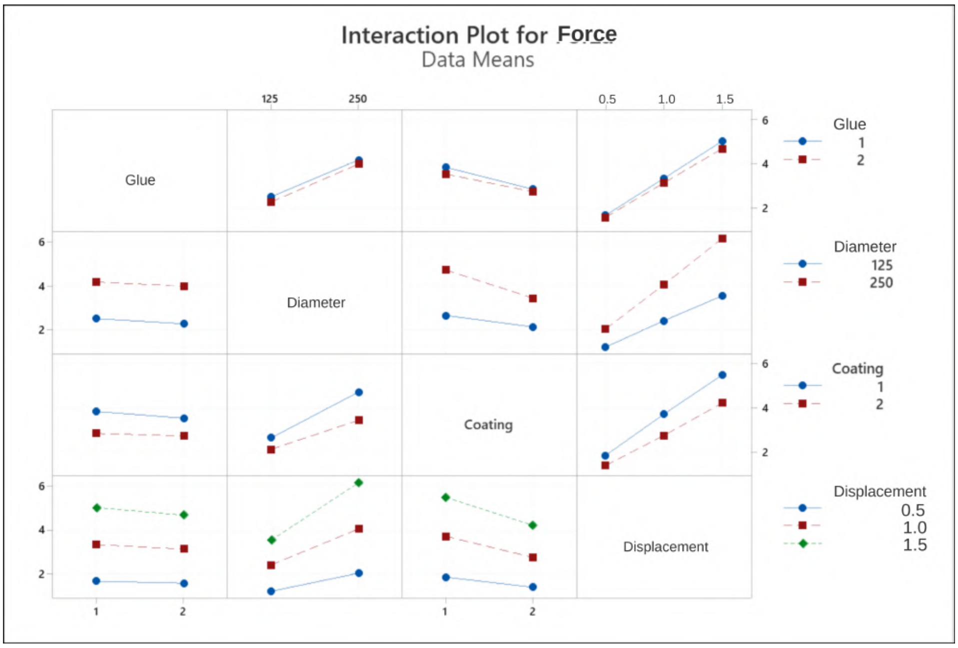


Fig. 7.14 Interaction effects in linear regime.

### 7.6.2 Non linear Regime Analysis

The analysis was extended to higher displacement levels (up to 3 mm) in order to investigate nonlinear effects. The results showed that fiber diameter and coating became the dominant factors, while displacement lost relative importance. Higher-order interactions also became significant, indicating increased system complexity. Key observations include:

- *Diameter:* The 250 $\mu m$ fibers maintained superior performance.
- *Coating:* Polyimide maintained a quasi-linear behavior, whereas polyacrylate exhibited a clear loss of load transfer capability beyond 1.5–2 mm due to delamination.
- *Adhesive:* Still negligible.
- *Displacement:* Increased dispersion beyond 2 mm indicates nonlinear behavior.


Fig. 7.15 Effect of diameter and coating in nonlinear regime.

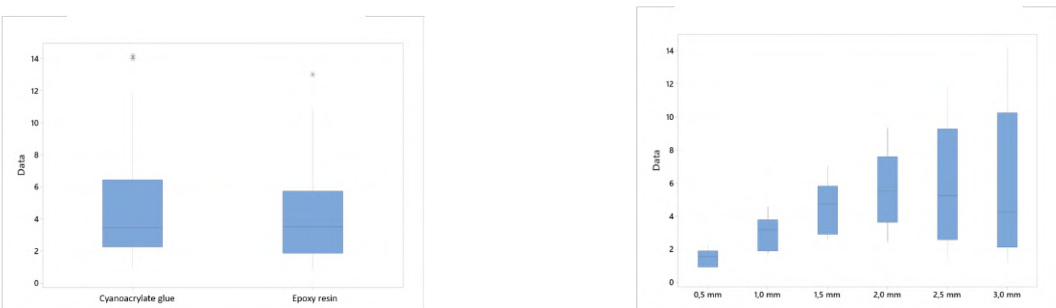


Fig. 7.16 Effect of adhesive and displacement in nonlinear regime.

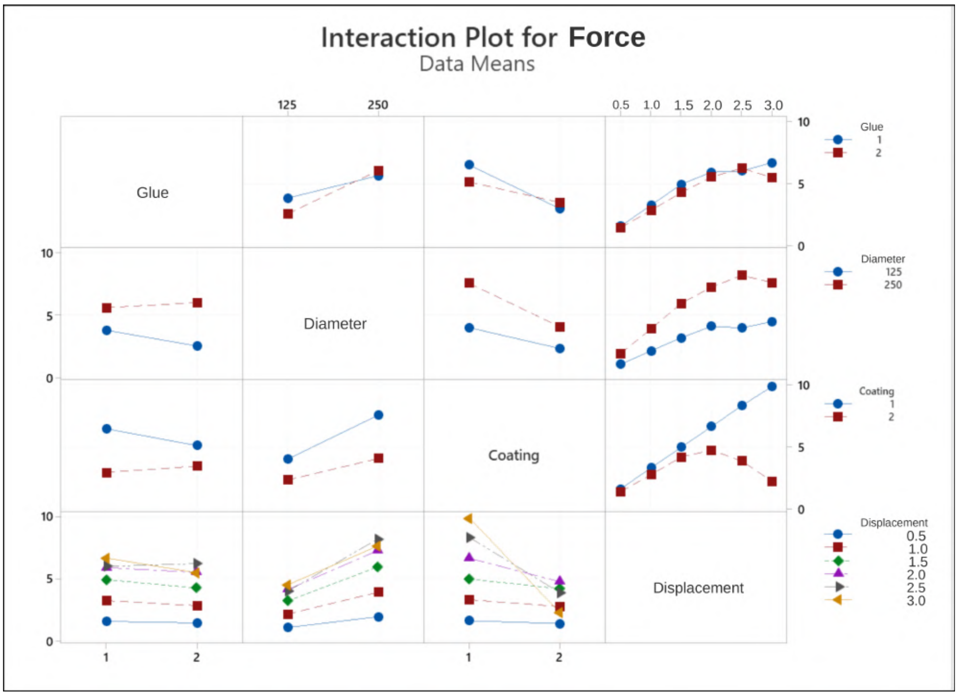


Fig. 7.17 Interaction effects in nonlinear regime.

### 7.6.3 Results and Discussion

The experimental and statistical analyses consistently demonstrate that the combination of 250 $\mu m$ diameter fiber with polyimide coating provides the most robust and reliable configuration. This result is attributed to the larger bonding surface and the superior mechanical stability of polyimide, which prevents delamination even under high deformation. Regarding the adhesive, no statistically significant differences were observed between epoxy resin and cyanoacrylate. However, epoxy resin was selected for subsequent applications, in accordance with ECSS recommendations [79], due to its higher reliability in aerospace environments.

Table 7.3 summarizes the main results obtained from the DoE approach.

| Factor | Levels Tested | Effect (Linear Regime) | Effect (Nonlinear Regime) |
|---|---|---|---|
| Fiber diameter | 125 $\mu$m / 250 $\mu$m | Dominant factor – higher load for 250 $\mu$m | Remains dominant – improved load transfer and stability |
| Coating material | Polyimide / Polyacrylate | Moderate influence – similar median, higher variability for polyimide | Strong influence – polyimide stable, polyacrylate shows delamination |
| Adhesive type | Epoxy / Cyanoacrylate | Negligible effect | Negligible effect |
| Displacement | 0.5–1.5 mm | Linear response | Nonlinear behavior beyond 2 mm |

Table 7.3 Summary of DoE results for FBG bonding configurations.

# Chapter 8

# Smart Components with Embedded FBG

The minimal invasiveness of FBG-based sensing systems enables the design of smart components with optical fiber sensors directly integrated within their structure. This approach allows any component—independently of its primary function—to provide, in real time and at high acquisition rates, either basic thermo-mechanical parameters or more complex information derived from the integration of multiple sensing points and processed through dedicated control logics.

In this chapter, two specifically designed and experimentally validated applications are presented:

- integration of FBG sensors into composite panels;
- integration of FBG sensors into structural components manufactured using lunar regolith simulant.

Despite the significant differences in mechanical properties, operational conditions, and intended applications, both solutions represent proof-of-concept implementations for the development of structural elements conceived as smart platforms. These platforms are capable of simultaneously fulfilling both structural and sensing functions. The design of such components—conceived to be flexible, modular, and scalable—represents a fundamental step toward the development of intelligent systems in which optical sensing is fully integrated during manufacturing and becomes indistinguishable from the structure during operation.

## 8.1 Composite Structures with Embedded FBG Sensors

The increasing use of fiber-reinforced composite materials is driven by their superior specific strength and stiffness compared to conventional metallic materials. This makes them essential for weight reduction and, consequently, for improving aircraft efficiency and reducing operational costs. Composite structures have become a key enabling technology for reducing fuel consumption, emissions, and lifecycle costs in modern aerospace systems. However, their use introduces significant challenges compared to metallic materials. These include limited repairability, anisotropic mechanical behavior, progressive degradation over time, high initial manufacturing costs, and complex failure mechanisms. Typical failure modes—such as transverse cracking, delamination, and debonding—can be induced by static and dynamic loads, vibrations, and impact events. Due to these critical aspects, composite structures require continuous monitoring. In this context, Fiber Bragg Grating (FBG) sensors represent an effective solution for Structural Health Monitoring (SHM). The extensive use of FBG technology enables the development of distributed sensing networks capable of monitoring large structural areas. Thanks to multiplexing capabilities and high interrogation performance, it is possible to design "neural-like" sensing networks over complex structures such as fuselage sections and control surfaces. The Bragg wavelength shift can be exploited for multiple monitoring purposes:

- identification of localized thermal gradients;
- detection of internal damage mechanisms (delamination, debonding, cracking);
- measurement of static and dynamic strain fields;
- monitoring of residual stresses during curing.
- detection and localization of impact events;

To fully exploit these advantages, proper embedding of the optical fiber within the composite laminate is required. In this section, the manufacturing process of two composite panels embedding FBG sensors is described, together with the experimental campaign carried out to evaluate their performance.

### 8.1.1 Smart Composite Specimen Production Process

Preliminary experimental activities highlighted that a thin adhesive layer could not be sufficient to guarantee adequate protection of optical fibers, especially during handling and integration into structural systems. For this reason, it was decided to embed the sensors directly within the composite laminate. Due to the small diameter of the optical fiber, it can be placed between carbon fiber plies without significantly affecting the structural integrity of the laminate. A rectangular geometry has been selected as reference for the first proof-of-concept specimen development. The selected reinforcement material is a 2x2 twill carbon fiber fabric (200 g/m$^2$, 3K), commonly used for prototyping activities. This fabric allows the realization of quasi-isotropic laminates with limited thickness. The resin system adopted is Epoxy Resin L with EPH 161 hardener (R&G), selected for its low curing temperature and suitable mechanical performance. The curing process requires approximately 24 hours at room temperature. Without post-curing, the maximum operating temperature is approximately 70°C, which can be increased up to 120°C with thermal treatment. In this study, post-curing was not performed, as the objective was to evaluate the thermal response of the embedded sensors. A laminate composed of approximately 20 plies was manufactured, with the FBG sensor positioned between the fifth and sixth ply (Figure 8.1). This configuration was selected to allow both thermal and mechanical measurements, avoiding placement at the neutral axis where strain would be negligible. The specimen dimensions were set to 80×320 mm, consistent with standard dimensions used within the research group. The manufacturing process consisted of the following steps:

- Cutting of carbon fiber plies (100×360 mm) to allow trimming after curing;
- Preparation of the working surface using a stainless-steel plate to ensure flatness;
- Protection of the mold using plastic layers and release materials;
- Impregnation of each ply using a roller and manual layup;
- Sequential stacking of plies up to the fifth layer;
- Placement of the FBG sensor and routing of the optical fiber;
- Completion of the stacking process up to 20 plies;

- Application of peel ply, perforated film, and breather layers;
- Vacuum bagging and leak checking;
- Controlled vacuum application and curing.

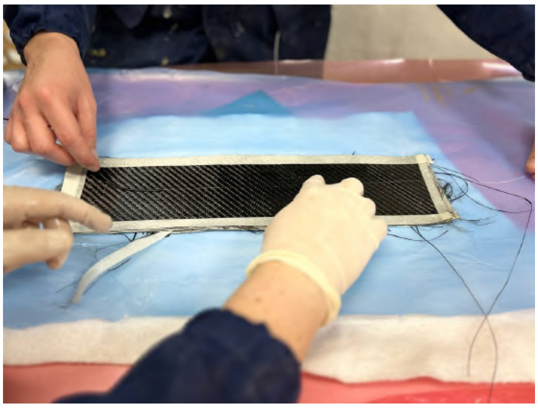

Fig. 8.1 Placement of the FBG sensor within the laminate.

To protect the fiber exit point, a heat-shrink tube was applied. This prevents stress concentration at the interface between the rigid composite and the optical fiber. The inclusion does not significantly affect the laminate integrity due to its small size. After curing under vacuum for approximately 24 hours, the specimen was removed from the bag and left to stabilize under ambient conditions. The laminate was then trimmed to final dimensions using a rotary tool with a diamond tip (Fig. 8.2. Particular care was taken at the fiber exit region to avoid damage and ensure a gradual stress transition. Final finishing operations included edge sanding and dimensional (Fig. 8.3). Table 8.1 summarizes the main specimen features.

Fig. 8.2 Cured specimen after vacuum bagging.

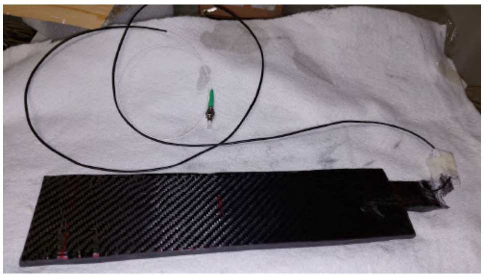

Fig. 8.3 Final composite specimen with embedded FBG sensor.

| Category | Parameter | Value |
|---|---|---|
| **Geometry** | Length | 320 mm |
| | Width | 80 mm |
| | Number of plies | 20 |
| | Layup type | Quasi-isotropic (2x2 twill) |
| **Materials** | Fiber reinforcement | Carbon fiber 2x2 twill, 200 $g/m^2$, 3K |
| | Resin system | Epoxy Resin L + EPH 161 hardener |
| | Curing condition | 24 h at room temperature |
| | Post-curing | Not applied |
| **FBG Integration** | Sensor type | Fiber Bragg Grating (FBG) |
| | Sensor position | Between 5th and 6th ply |
| | Fiber routing | Embedded with external exit protection |
| | Exit protection | Heat-shrink tube |
| **Manufacturing** | Process | Manual layup + vacuum bagging |
| | Mold type | Flat stainless-steel plate |
| | Compaction method | Vacuum pressure |
| | Finishing | Cutting and edge sanding |

Table 8.1 Summary of composite specimen configuration and manufacturing parameters.

### 8.1.2 Thermal Characterization

The thermal characterization was structured through repeated thermal cycles between 10 and 80 °C. Each temperature step was maintained for 30 minutes in order to verify measurement accuracy, statistically validate the results, and assess signal stability. Two sensors were employed: a first FBG placed on the surface of the component but mechanically decoupled from it, and a second sensor directly laminated within the composite specimen. The test enabled the definition of the calibration curves for both sensors, the evaluation of the sensitivity of the embedded FBG, and the estimation of the thermal flux inside the component using only optical data. The acquired data were crucial for validating the use of optical fiber sensors in the development of intelligent components capable of autonomously providing information regarding their operational status. Starting from thermal aspects, two main activities were performed:

- thermal calibration of FBG sensors;
- estimation of heat flux within the component.

A climatic chamber was used for both activities. For the thermal calibration, repeated thermal cycles were performed, each consisting of 8 temperature steps ranging from 10 to 90 °C. Data acquisition was carried out under steady-state conditions at each temperature level, following the settings imposed by the climatic chamber. The repetition of measurements enabled statistical validation of the results. The calibration curves obtained exhibit excellent linearity and are fully comparable with those obtained from the reference FBG sensor placed on the specimen surface. This result enables a simple and accurate estimation of the internal temperature of the specimen. Recalling the operating principle of an FBG, the linear correlation between wavelength shift and temperature allows the temperature to be computed as:

$$T_i = (\lambda_i - \lambda_0)/K_T \tag{8.1}$$

The calibration results for both sensors are reported in Fig. 8.4 and Fig. 8.5, showing excellent linearity and repeatability.

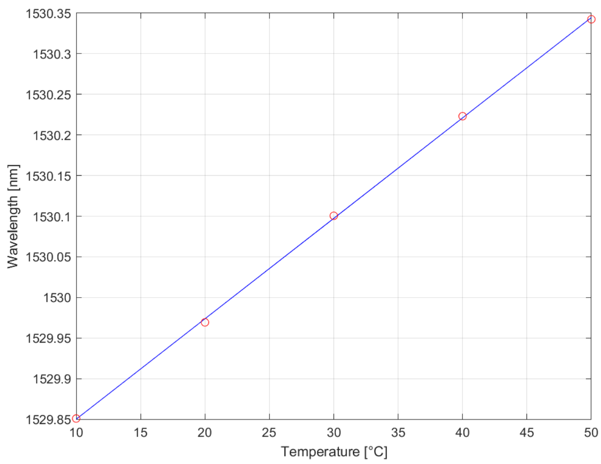


Fig. 8.4 Thermal calibration curve of surface-mounted FBG sensor.

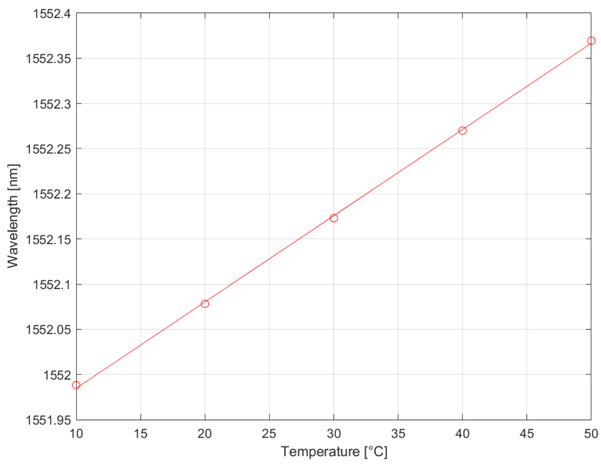


Fig. 8.5 Thermal calibration curve of embedded FBG sensor.

Once the temperatures measured by the two sensors were determined, it was possible to calculate the internal thermal flux within the specimen as:

$$Q = K \cdot (T_2 - T_1)/d \tag{8.2}$$

where $K$ is the average thermal conductivity of carbon fibers and matrix ($K_{\text{carbon}} = 800\ \text{W}/(\text{m}\cdot\text{K})$, $K_{\text{matrix}} = 1.37\ \text{W}/(\text{m}\cdot\text{K})$), resulting in $K = 400.685\ \text{W}/(\text{m}\cdot\text{K})$; $T_1$

and $T_2$ are the temperatures measured by the FBG sensors, and $d$ is the specimen thickness ($d = 0.0014$ m).

The resulting thermal flux is reported in Fig. 8.6.

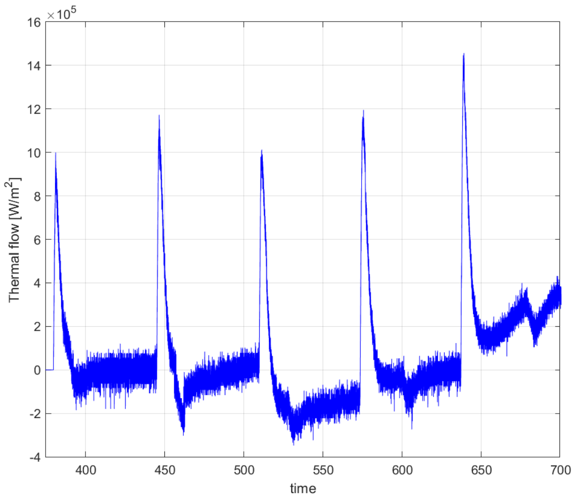


Fig. 8.6 Thermal flux estimated using embedded and surface FBG sensors.

The experimental results demonstrate high sensitivity and a highly linear calibration response for both sensors. Minor disturbances, likely caused by mechanical relaxation effects during transient phases, were observed but do not significantly affect measurement accuracy. The thermal calibration proved to be precise, reliable, and repeatable. This enabled the repetition of the thermal cycle while simultaneously measuring both surface and internal temperatures, allowing for the computation of the thermal flux across the specimen. The obtained data were found to be fully consistent with the environmental conditions imposed by the climatic chamber. In addition, the FBG sensors exhibited high sensitivity to mechanical strain. This opens the possibility of implementing non-destructive monitoring techniques for real-time structural assessment and maintenance support, including fatigue life estimation. However, due to the complexity of mechanical testing and data interpretation, this work focuses exclusively on thermal aspects. Table 8.2 summarizes the main results achieved.

| Parameter | Surface FBG | Embedded FBG |
|---|---|---|
| Temperature range [°C] | 10–90 | 10–90 |
| Step duration [min] | 30 | 30 |
| Calibration behavior | Linear | Linear |
| Sensitivity $K_T$ | $\approx 10 pm/°C$ | $\approx 10 pm/°C$ |
| Repeatability | High | High |
| Hysteresis | Negligible | Negligible |
| Noise sensitivity | Low | Low |

Table 8.2 Summary of thermal calibration performance for surface-mounted and embedded FBG sensors.

### 8.1.3 Development of Fully Integrated Panels

The manufacturing of the first specimen yielded extremely positive results in terms of sensitivity, precision, accuracy, and repeatability of the acquired measurements. However, the developed geometry still presented a significant limitation. All sensors were connected to a single optical fiber exiting the specimen, and the fiber outlet represented the most critical point of the entire component. The mechanical discontinuity at this location significantly reduced handling robustness and, more importantly, in the event of fiber breakage at the exit point, no repair strategy could be applied to recover the embedded sensors. This limitation demonstrated that the adopted solution was not sufficiently mature to ensure reliable and repeatable implementation. The main issue lies in the transition of the optical fiber from the interior of the composite laminate to the external environment. This transition introduces stress concentrations and weak points due to the interface between the free optical fiber and the rigid CFRP structure, effectively nullifying part of the advantages provided by embedding the fiber within the laminate. To address this limitation, a new routing strategy was developed with the objective of minimizing unnecessary interfaces with the external environment. After curing, the probability of fiber failure inside the laminate is negligible, whereas damage is far more likely to occur in exposed sections due to handling. Therefore, improving the robustness of the fiber exit region became a key design requirement.

A viable solution was identified in the use of an optical connector coupled with a female–female adapter, housed within a dedicated protective structure. This configuration protects the fiber exit and redistributes mechanical loads acting on the connector interface. Preliminary tests demonstrated that the lamination resin could not be used to directly bond the connector to the structure. Due to its low viscosity, the resin penetrates the micro-gaps of the connector threads, compromising its functionality (Fig. 8.7).

Fig. 8.7 Effect of resin infiltration on the optical connector during lamination.

To overcome this issue, the connector was physically isolated from the resin during the entire lamination process by enclosing it within a resin-tight protective bag. In this configuration, the optical fiber exits the connector and remains unprotected only for a few millimeters before entering the laminate, while the connector support and adapter are installed after curing. The lamination process was performed following standard procedures. The protective bag was positioned as close as possible to the fiber exit point, and resin was applied up to the final ply. Microperforated films and breather layers were arranged around the connector to prevent resin infiltration and ensure proper vacuum distribution. After curing, the vacuum bag was opened and the protective layers were removed. The protective bag remained intact and the optical fiber was undamaged. Upon opening the bag, the connector was found to be completely free of resin contamination and fully functional. Once the connector was extracted, the female adapter and the 3D-printed protective housing were installed. The resulting configuration exhibited high signal quality and improved mechanical robustness (Fig. 8.8).

Based on these results, a second specimen was developed. This component integrates the sensors within the laminate while providing a fully accessible and protected optical interface. The laminate consisted of five plies, with the sensors

Fig. 8.8 Integrated connector housing and protective structure after assembly.

embedded between the third and fourth plies, enabling both thermal and mechanical measurements. Two FBG sensors were positioned with a relative orientation of 90° in order to enhance sensitivity along the principal directions. The layout of the smart panel is shown in Fig. 8.9.

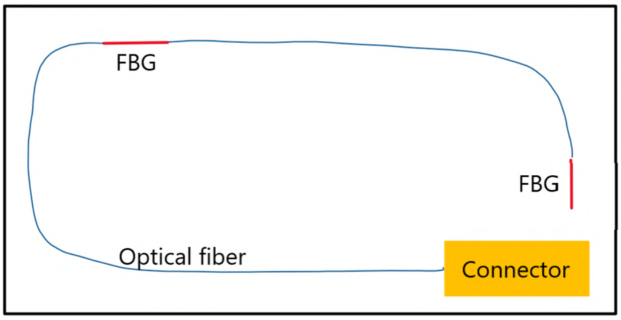


Fig. 8.9 Design of the smart composite panel with embedded FBG sensors.

The optical measurement line was assembled by splicing the two FBG sensors along the same fiber. The carbon fiber fabric and auxiliary materials were prepared according to the same procedure used for previous specimens. During the lamination process, particular attention was paid to fiber routing. The fiber was arranged using smooth curvature paths in order to avoid sharp bends and stress concentrations. The first sensor was positioned along the longitudinal direction, while the second was placed near the outlet and aligned with the transverse direction. After curing, the vacuum bag was removed and the component was extracted. The connector region was identified as the most critical area; however, the protective layers were easily removed and the connector remained fully functional and free from contamination. The component was then connected to the optical interrogator using a standard jumper. Both sensors were correctly detected, and their response under mechanical loading confirmed the proper functionality of the system. Finally, the connector housing was permanently fixed to the laminate using cyanoacrylate adhesive. The resulting configuration proved to be highly effective and reliable. Compared to previous solutions, this approach provides several advantages:

- improved mechanical robustness at the fiber exit;
- protection of exposed fiber segments;
- elimination of critical shear stress concentrations;
- scalability toward more complex sensor networks;
- modularity through connector-based integration.

This solution represents the most advanced and reliable configuration developed within this work, enabling the realization of fully integrated smart composite components.

| **Feature** | **First Prototype** | **Improved Prototype** |
|---|---|---|
| Number of plies | 20 | 5 |
| Number of sensors | 1 | 2 |
| Fiber exit strategy | Direct | Connector-based |
| Repairability | None | Modular |
| Risk of failure at exit | High | Low |
| Integration level | Partial | Fully integrated |

Table 8.3 Comparison between initial and improved smart panel configurations.

### 8.1.4 Smart Panel for Impact Detection and Localization

The tests described in Section 8.3 demonstrated high sensitivity to both thermal and mechanical effects, together with excellent repeatability and negligible hysteresis phenomena. These results allow the developed specimens to be considered as proof-of-concept solutions for lightweight, modular, and scalable smart panels. The integration of optical fibers within composite structures, combined with the modular approach described in the previous section, enables the realization of sensing systems with negligible impact in terms of mass and volume. The adopted configuration allows multiple instrumented panels to be connected in series through optical jumpers, enabling large-scale data acquisition suitable for advanced monitoring and control algorithms. Moreover, despite the serial architecture, the embedded fiber is intrinsically protected by the laminate and can only be damaged in case of structural failure of the panel itself. In addition, the modular design enables easy replacement of individual panels without affecting the entire sensing network. Based on the previously obtained calibration results, a dedicated experimental campaign was carried out to investigate the following aspects:

- measurement of static loads applied at different locations;
- statistical evaluation of repeatability and hysteresis;
- detection of dynamic impact events.

Two specimens were tested under static loading conditions by applying a concentrated load of 1 kg at predefined coordinates on the panel surface. Each test was repeated multiple times in order to assess repeatability.

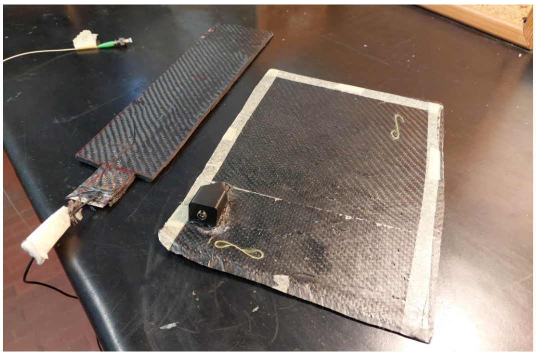

Fig. 8.10 Manufactured composite specimens used for static and dynamic testing.

The results obtained from the first specimen (Fig. 8.11) show excellent sensitivity, high repeatability, and very low data dispersion. The comparison between pre-loading and post-loading conditions confirms the absence of hysteresis effects, as the measured wavelength returns to its initial value after load removal.

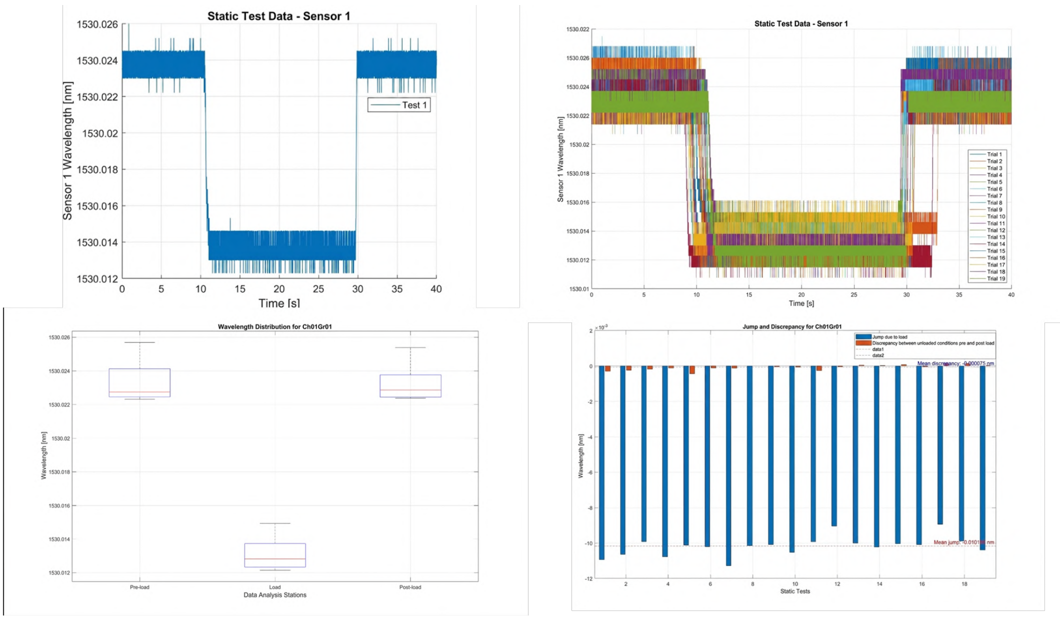


Fig. 8.11 Static test results for single-sensor specimen: repeatability and hysteresis analysis.

A slightly higher dispersion was observed when the load was applied directly above the sensor location. This behavior is attributed to experimental uncertainty associated with manual load application and remains within acceptable limits. Similar results were obtained for the specimen equipped with two sensors. In this case, the simultaneous response of both sensors provides additional information on load distribution and spatial sensitivity. The experimental data clearly show that the sensor response depends on both the magnitude of the applied load and its distance from the sensing location (Fig. 8.12).

Subsequently, dynamic impact tests were performed using a small spherical mass of $m = 1$ g released from a height of $h = 780$ mm. The corresponding impact velocity can be estimated as $v = \sqrt{2gh}$, leading to a momentum on the order of $10^{-3}$ $\mathrm{kg\,m\,s^{-1}}$. The recorded signals clearly show both the impact peak and the subsequent oscillatory transient response (Fig. 8.13). The FBG sensors demonstrated excellent capability in detecting rapid events and very small deformations.

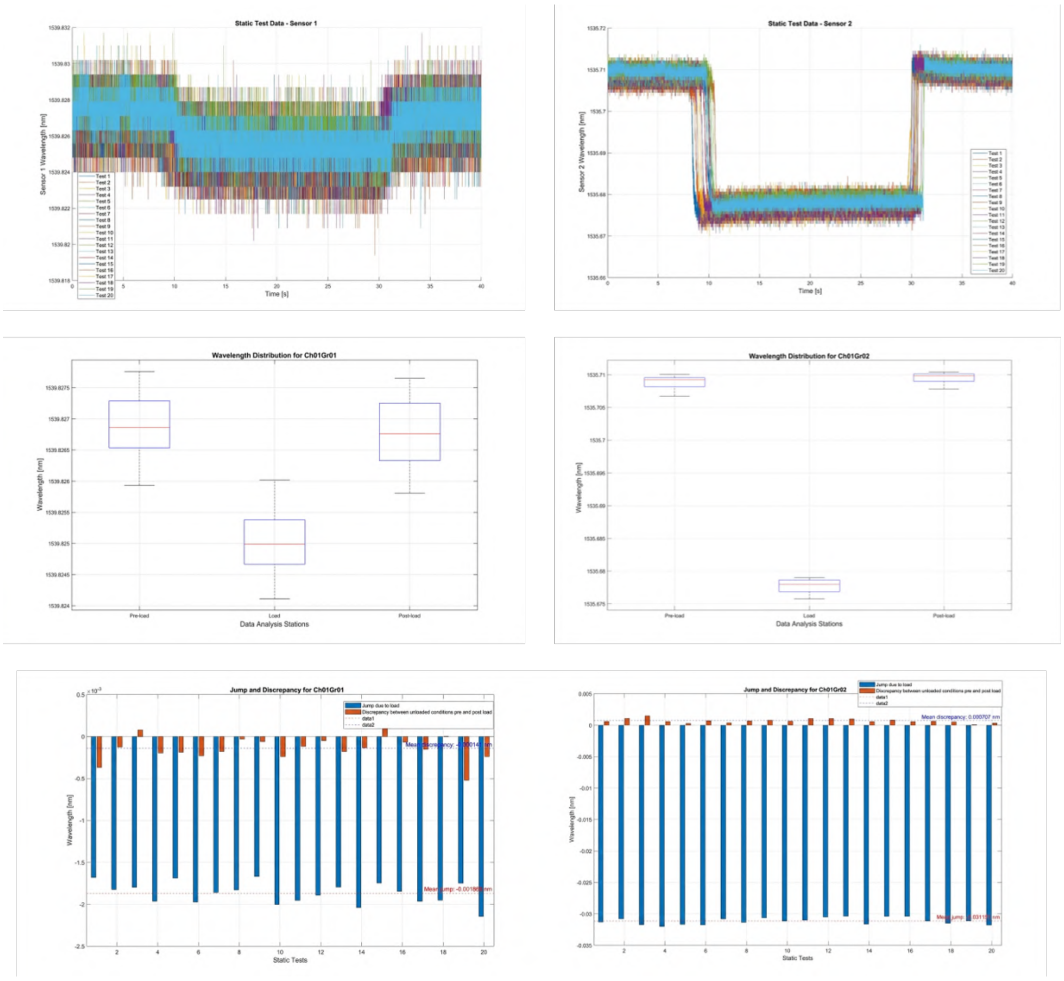


Fig. 8.12 Static response of dual-sensor specimen for different load positions.

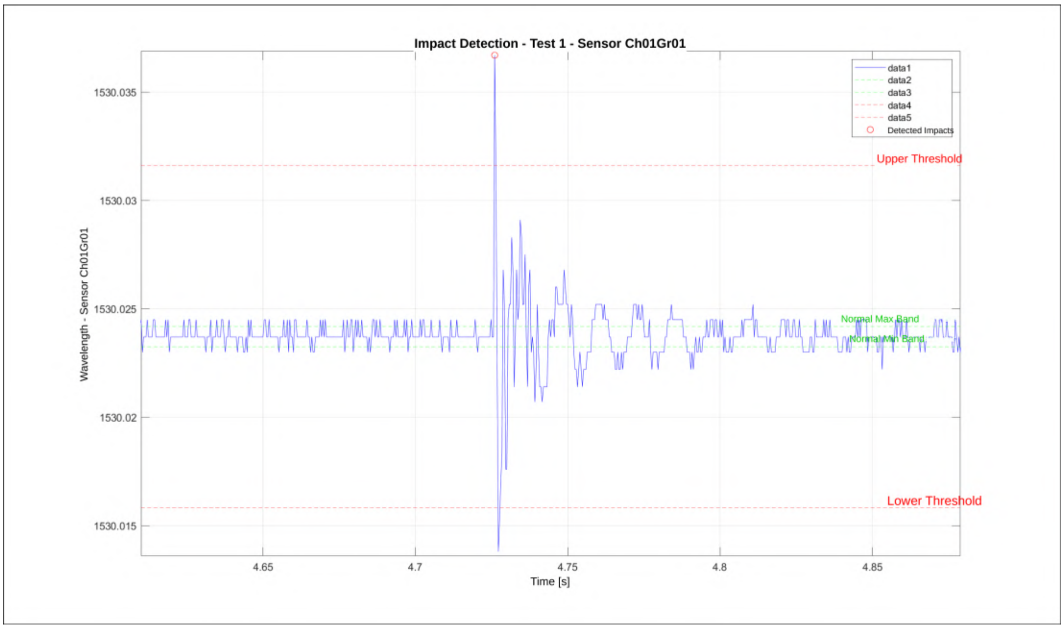


Fig. 8.13 FBG response to dynamic impact: peak detection and transient oscillations.

The signal-to-noise ratio between the impact-induced peak and the background noise was consistently greater than 3, even under unfavorable conditions. Both specimens exhibited high sensitivity, confirming the robustness of the sensing approach. Finally, the combined use of multiple sensors at different locations enables the development of smart panels capable of estimating both the position and intensity of impact events in real time. This represents a key step toward the implementation of advanced structural health monitoring systems based on embedded optical sensing.

| Parameter | Single-sensor specimen | Dual-sensor specimen |
|---|---|---|
| Number of sensors | 1 | 2 |
| Laminate thickness | High (20 plies) | Low (5 plies) |
| *Static behavior* | | |
| Sensitivity | High | High |
| Repeatability | Excellent | Excellent |
| Hysteresis | Negligible | Negligible |
| Spatial information | Not available | Available |
| *Dynamic behavior (impact)* | | |
| Peak detection | Clear | Clear |
| Signal-to-noise ratio | $> 8$ | $> 3$ |
| Oscillatory response | Present | Present |
| Sensitivity to impact position | Limited | High |
| *Monitoring capability* | | |
| Load localization | Not possible | Possible |
| Impact localization | Not possible | Potentially achievable |
| System redundancy | None | Partial |

Table 8.4 Comparison between single-sensor and dual-sensor smart composite specimens under static and dynamic testing.

## 8.2 Regolith-based Specimens

The same approach of embedding optical fibers directly within structural components was also explored, in a fully preliminary and exploratory manner, for the development of simple structural units manufactured through the sintering of lunar regolith simulant. This activity becomes particularly relevant in light of the growing interest in returning humans to the Moon, which is driving the development of increasingly complex and ambitious mission scenarios [80]. Future lunar missions aim at establishing self-sustaining outposts capable of supporting long-duration operations. One of the major challenges in this context is the availability of resources, since transporting materials from Earth is economically and logistically prohibitive. For this reason, significant efforts are currently devoted to the development of *In Situ Resource Utilization* (ISRU) strategies, focusing in particular on the use of lunar regolith for the fabrication of structural elements. However, the realization of large-scale infrastructures under extreme environmental conditions also requires the development of smart structures, capable of monitoring their operational status and providing real-time feedback to ensure both structural integrity and mission safety. Among the measurable parameters, temperature plays a fundamental role due to the extreme thermal excursions experienced on the lunar surface. Thermal gradients can induce significant internal stresses, potentially compromising the structural stability of regolith-based elements. In this context, Fiber Bragg Grating (FBG) sensors represent an ideal solution, enabling the measurement of internal temperature, thermal gradients, and potentially thermo-mechanical stresses within the structure. The objective of this activity is therefore to assess the feasibility of embedding optical fibers within regolith-based bricks during the manufacturing process, in order to enable internal temperature monitoring. This work was carried out within an international collaboration between Politecnico di Torino, with expertise in optical sensing for space applications, and ESA-EAC, specialized in the development of regolith-based materials [81].

### 8.2.1 Manufacturing Process

The manufacturing process is based on a composite approach, combining lunar regolith simulant (EAC-1A) with a thermoplastic binder (polylactic acid, PLA) in powder form. The process begins with a drying phase aimed at removing residual moisture from both materials. The regolith is dried at 250°C for two hours, while PLA is dried at 50°C for twelve hours to mitigate its hygroscopic behavior. Subsequently, both materials are sieved to obtain a controlled and uniform particle size distribution, which directly affects the final mechanical properties of the specimen. The powders are then weighed according to the desired regolith-to-binder ratio and manually mixed to ensure a homogeneous distribution of the phases. The resulting mixture is transferred into a mold, whose internal surfaces are pre-treated (using Kapton tape or PTFE spray) to prevent adhesion and facilitate demolding. A dedicated mold was designed to enable the insertion and alignment of the optical fiber along the longitudinal axis of the specimen. The powder mixture is then compacted using a toggle press equipped with a 2 kN load sensor, increasing the density and mechanical integrity of the final component. Following compaction, the specimen undergoes a thermal treatment at approximately 220°C for 20 minutes. During this phase, the PLA melts and encapsulates both the regolith particles and the optical fiber, forming a cohesive structure upon cooling. The cooling process is performed under ambient conditions, allowing full consolidation of the composite material. The most relevant materials and processing steps are shown in Figure 8.14, while the final specimen with the embedded optical fiber is reported in Figure 8.15.

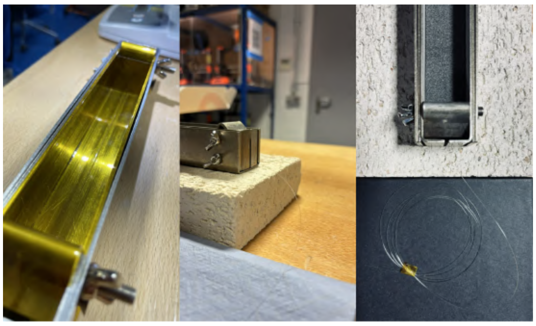

Fig. 8.14 Main matherials for regolith-based specimen fabrication.

Fig. 8.15 Regolith-based specimen with embedded optical fiber.

### 8.2.2 Thermal Characterization

The fabricated specimen was subjected to a standard thermal calibration procedure, analogous to the one adopted for previous test campaigns. The calibration results are reported in Figure 8.16.

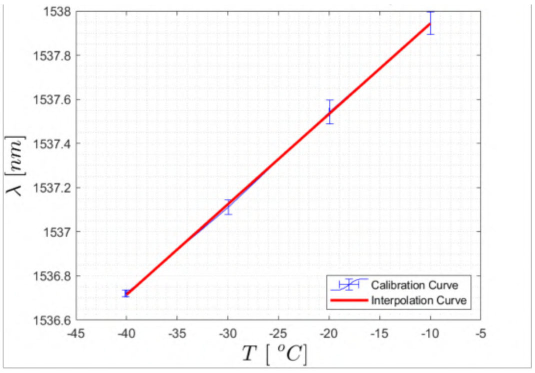


Fig. 8.16 Thermal calibration of the embedded FBG sensor.

The thermal response of the FBG-integrated specimens showed a behavior consistent with the expected trend under cyclic temperature variations. The sensors demonstrated stable and repeatable performance across multiple thermal cycles, confirming the feasibility of the proposed sensing approach. However, a significant limitation was identified. The interaction between the fiber coating and the regolith-based matrix leads to a non-ideal mechanical coupling, which affects the linearity of the sensor response. In particular, the calibration curve exhibits a reduced linear operating range, currently limited to negative temperatures and, preferably, below $-10$°C. This limitation is mainly attributed to the complex physicochemical interaction between the fiber coating and the regolith–polymer composite. As a consequence, further developments are required to improve the integration strategy, including:

- optimization of fiber coating materials;
- development of dedicated protective packaging;
- improvement of fiber–matrix adhesion mechanisms.

Despite these limitations, the results obtained represent a promising proof of concept for the development of smart regolith-based structures capable of internal temperature monitoring. Future work will focus on extending the operational temperature range and improving measurement reliability, with the goal of enabling fully integrated sensing systems for lunar infrastructure applications.

# Chapter 9

# Integrated Sensor Networks for Multifunctional Monitoring

The design, development, and integration of FBG-based sensing systems enable the implementation of a dedicated hardware platform capable of providing key parameters for integrated multifunctional monitoring of complex systems. Fiber Bragg Grating technology, in fact, introduces a paradigm shift in the way sensing architectures are conceived and deployed. Traditional sensing methodologies based on electronic measurements typically distinguish three fundamental elements:

- the substrate on which the measurement is performed;
- the sensing device responsible for generating the signal;
- a communication cable used to transmit the information.

When optical fiber sensing is employed, this paradigm is fundamentally redefined. The optical fiber simultaneously acts as both sensing element and signal transmission medium. Furthermore, due to its extremely low invasiveness, once integrated, the fiber becomes practically indistinguishable from the structure itself. This capability enables the realization of intelligent systems, defined as the physical and functional integration of sensing elements within structural components, capable of autonomously providing real-time information about their operational state. The design, assembly, and integration procedures described in Chapter 7 therefore represent the operational foundation for implementing such systems. In particular, this chapter focuses on exploiting the intrinsic advantages of optical fiber sensing in order to maximize the amount of physical information extracted from a single hardware platform. A representative case study is presented, characterized by a complex geometry and multiple interacting subsystems. The selected reference system consists of a portion of a UAV semi-wing, in which dedicated compartments were created to host and simulate the presence of typical onboard subsystems.

## 9.1 Integration of Fibers on a UAV Wing Box

The selected case study is a wing box belonging to a large UAV platform. Multiple optical fiber lines were designed and integrated in order to address the following monitoring objectives:

- distributed strain measurements on the upper and lower skins of the wing box;
- thermal monitoring within a control volume potentially subject to overheating;
- deformation monitoring within an electromechanical actuation system.

The fibers installed on the upper and lower skins are intended to provide localized strain measurements. These sensors detect structural deformations induced by aerodynamic loads during flight conditions and can therefore supply valuable information regarding the operational state of the aircraft. Additionally, the distributed sensing capability enables the detection of higher-frequency phenomena, such as structural vibrations or fuel-induced oscillations within the wing. The wing box also includes three internal compartments used to simulate different onboard subsystems:

- an empty compartment, representing a cargo bay potentially subject to overheating (e.g., fire scenarios);
- a compartment containing a flexible fuel bladder, used to simulate sloshing phenomena;
- a compartment housing an electric motor and mechanical support, representing a simplified servo actuator for flight control.

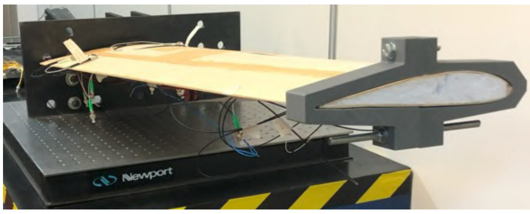


Fig. 9.1 Experimental setup of the instrumented UAV wing box.

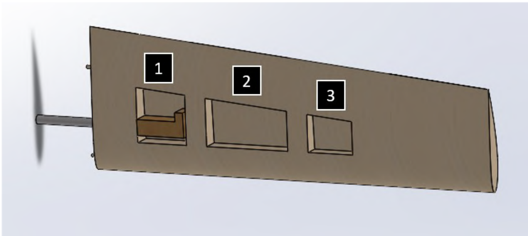


Fig. 9.2 CAD model of the UAV wing box and internal compartments.

The experimental setup was realized using a semi-wing extracted from a UAV platform with a total wingspan of approximately 2 m. The section closest to the fuselage attachment was selected, and a dedicated mechanical support was designed to reproduce the clamped boundary condition at the wing root. The wing box structure is characterized by a shell-based configuration. Details regarding specimen preparation and structural modifications are reported in [82]. Based on the defined monitoring objectives, three distinct families of optical fibers were designed and integrated using different approaches. The external skins were instrumented with eight FBG sensors distributed along four fiber lines: two on the upper surface and two on the lower surface. For each surface, one fiber was positioned near the leading edge and one near the trailing edge. These fibers were bonded using the technique described in Chapter 7, based on a thin porous cellulose layer impregnated with epoxy resin. This solution ensures:

- full mechanical coupling between fiber and structure;
- protection against accidental mechanical damage;
- negligible alteration of the aerodynamic profile;
- minimal added mass.

The compartment dedicated to overheating detection was equipped with an electrical resistor capable of generating rapid temperature variations. Three FBG sensors were positioned along the principal axes of the compartment. In this case, the sensors were mechanically constrained but not bonded, in order to measure the local air temperature without structural coupling effects.

The most complex subsystem is represented by the electromechanical actuator. A dedicated support was designed and manufactured using additive manufacturing techniques. When the motor applies torque, a reaction torque is generated at the interface between the motor and its support. This reaction induces a localized deformation, which is intentionally amplified through geometric compliance. This configuration enables an optimal balance between measurable strain and practical feasibility of fiber routing. The system operates entirely within the elastic regime, ensuring a linear relationship between applied load, induced deformation, and FBG wavelength shift. The capability of the proposed system of generating significative data could cover a crucial role for prognostics and diagnostics in aircraft flight controls [83–85]. In the following sections, each group of sensors is analyzed in detail, with particular focus on sensor distribution, integration methodology, experimental testing, and data interpretation.

## 9.2 Surface Bonded Fibers

As previously discussed in Section 7.2, the minimally invasive bonding technique represents an effective solution for monitoring the structural stress state of the wing. By knowing both the spatial distribution of the FBG sensors and the applied load conditions, it is possible to reconstruct the deformation patterns underwent by the structure and estimate the corresponding load factors during operation. As described earlier, eight sensors were distributed over the wing surfaces, as shown in Figure 9.3.

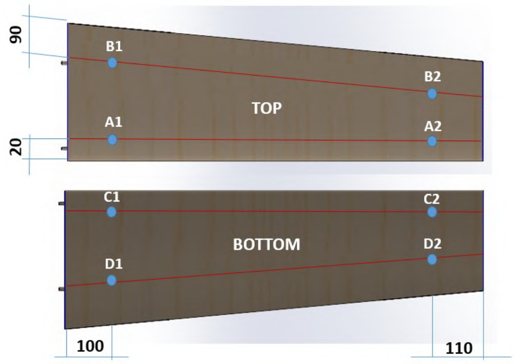


Fig. 9.3 Layout of FBG sensors bonded on the wing skins.

A static load test was performed using a stepwise pyramidal loading profile. The load was progressively increased up to a predefined maximum value and then decreased following the same sequence. The loads were applied directly on the end rib, with particular care taken to minimize impulsive effects.

The test sequence was defined as follows:

- Step 1: application of a 1 kg load;
- Step 2: addition of 0.5 kg (total 1.5 kg);
- Step 3: addition of another 0.5 kg (maximum load 2 kg);
- Unloading: sequential removal of the applied weights.

Each load condition was maintained for approximately 15 seconds, allowing both the transient response and the stabilized structural deformation to be observed. To ensure statistical robustness, the entire test was repeated five times. During each acquisition, all eight sensors were interrogated simultaneously. The experimental objective was to verify:

- the proportionality between applied load and measured deformation;
- the consistency of sensor responses at different structural locations;
- the repeatability of the measurement system.

Figures 9.4 and 9.5 show the wavelength variation measured during a representative test. Blue curves correspond to sensors placed on the dorsal (upper) surface, while red curves refer to sensors on the ventral (lower) surface. Figure 9.4 reports the sensors located near the wing root, whereas Figure 9.5 refers to those near the wing tip.

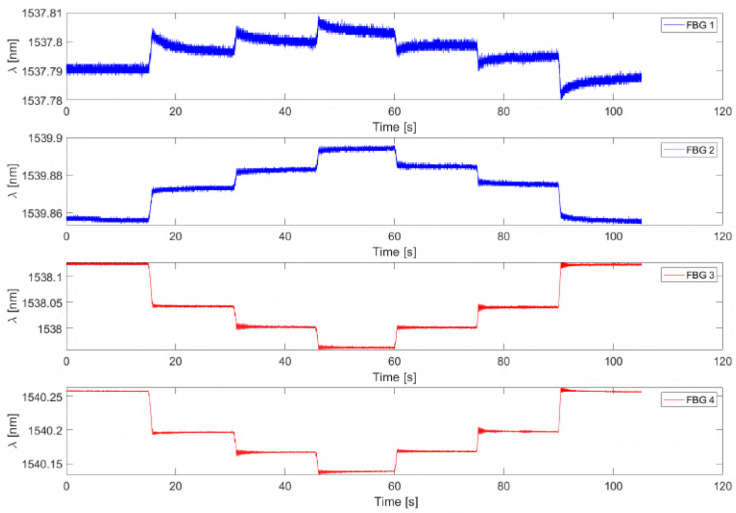


Fig. 9.4 Wavelength response of FBG sensors located near the wing root.

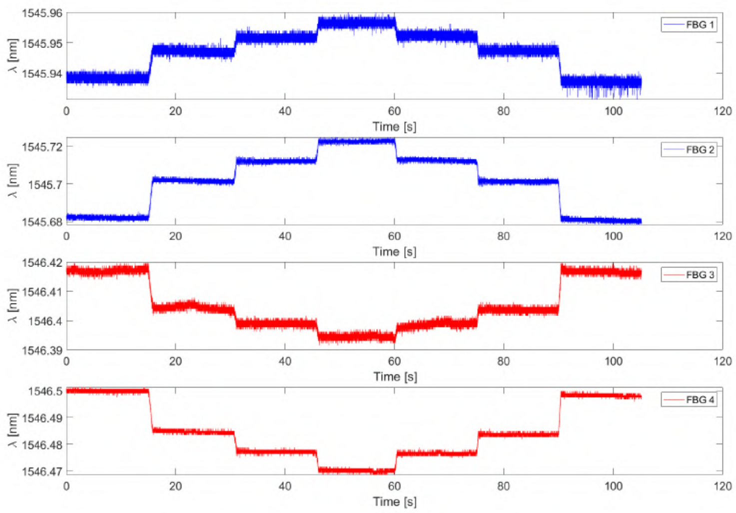


Fig. 9.5 Wavelength response of FBG sensors located near the wing tip.

The measured trends clearly reflect the expected structural behavior. Under bending conditions, the dorsal surface is subjected to tensile stress, resulting in an increase in the reflected wavelength, whereas the ventral surface experiences compressive stress, leading to a decrease in $\lambda$. This behavior is fully consistent with the response of a clamped beam under bending loads. A significant difference in $\Delta\lambda$ can be observed between sensors located near the root and those near the tip, even under identical loading conditions. This reflects the non-uniform distribution of bending moments along the span of the wing. The measured signals closely follow the imposed loading cycles, showing a high degree of symmetry between loading and unloading phases. This confirms the elastic behavior of the structure within the tested load range. Some differences in signal quality are observed depending on sensor placement. Sensors positioned near the leading edge exhibit higher noise levels, likely due to the increased local stiffness caused by structural reinforcements. The sensor located on the dorsal side near the root and leading edge shows a distinct transient response characterized by higher initial peaks, followed by a stabilization phase within approximately 2–3 seconds. This behavior can be attributed to the combined effect of boundary constraints and local stiffness variations. It should also be noted that several structural modifications were introduced during the preparation of the test specimen. These interventions may have altered the local stiffness distribution, contributing to the observed variability among sensor responses. To evaluate repeatability, the response of a single sensor across five repeated tests is shown in Figure 9.6.

The results demonstrate excellent repeatability, with overlapping curves and stabilized values contained within a variation range of approximately 0.1 nm. This level of dispersion is fully acceptable and confirms the reliability of the measurement system. Moreover, the proportionality between load increments and wavelength variation is clearly evident. Since the second and third load increments correspond to half of the initial load, the resulting wavelength steps exhibit the same proportional relationship. This confirms the linear sensitivity of the system to applied loads, as expected from the theoretical model. The transient response following each load application also reveals the capability of the system to detect rapid events and short-duration peaks. Even impulsive responses lasting only fractions of a second are clearly identifiable.

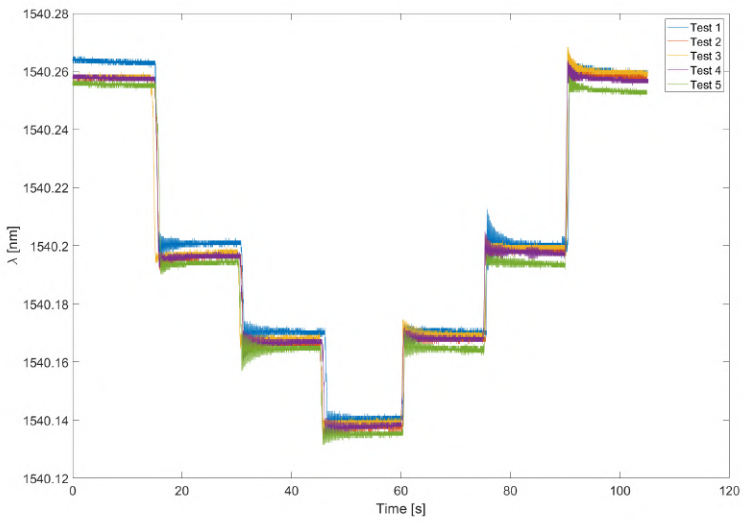


Fig. 9.6 Repeatability analysis of a representative FBG sensor over multiple tests.

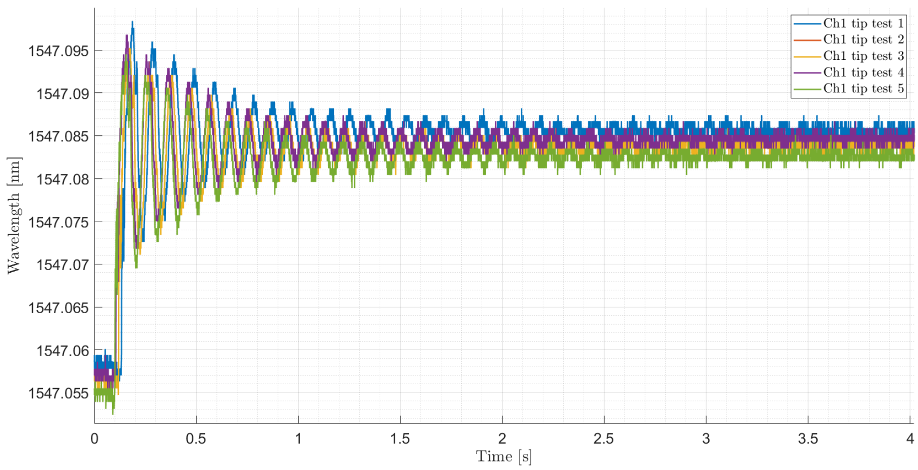


Fig. 9.7 Detection of transient oscillations and comparison between repeated tests.

This capability is particularly relevant for structural health monitoring applications, as it enables the detection of load peaks and dynamic events experienced by critical structural regions. Such information can be used to assess structural degradation and support condition-based maintenance strategies. Overall, the results validate the effectiveness of the proposed sensing approach, demonstrating high sensitivity, excellent repeatability, and the ability to capture both steady-state and transient structural responses.

## 9.3 Fibers for Hot-spot Detection

The thermal monitoring subsystem required a different experimental approach compared to the structural tests. The objective was to activate a localized heat source—represented by an electrical resistor—and, through real-time analysis of the FBG signals, detect and spatially localize the thermal anomaly within the monitored volume. The experimental set-up was so arranged as reported in Figure 9.8: three sensors were put in three different vertices of the volume considered, in correspondence of the three reference axes.

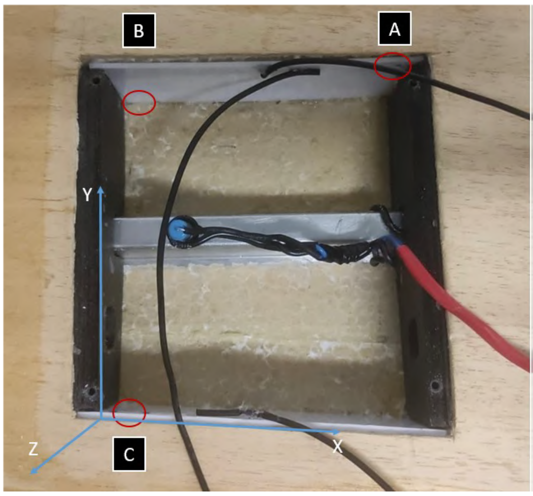


Fig. 9.8 Experimental setup for heat source detection using FBG sensors.

### 9.3.1 Preliminary Sector-based Identification

An initial experimental phase was conducted by placing the resistor in five predefined positions within the compartment (the four corners and the center). For each configuration, data were acquired for one minute starting from the activation of the heat source.

By comparing the relative wavelength variation among the sensors, it was possible to construct a preliminary sector-based map of the heat source location. To quantify the thermal response, a parameter $m$ was introduced, representing the heating rate of each sensor:

$$m = \frac{\Delta\lambda}{\Delta t} \tag{9.1}$$

The comparison of the parameters $m_1, m_2, m_3$ associated with each sensor allowed for the identification of the region in which the heat source was located.

### 9.3.2 Distance Estimation Model

To generalize this approach, an extended experimental campaign was performed. For each sensor, measurements were conducted at 10 different positions of the heat source, with each test repeated 10 times. For each configuration, the parameter $m$ was calculated and correlated with the distance between the sensor and the heat source.

From the experimental data, an empirical relationship was derived:

$$r_i = \left(\frac{m_i}{a}\right)^{-\frac{1}{b}} \tag{9.2}$$

where:

- $r_i$ is the distance between the heat source and the $i$-th sensor;
- $m_i$ is the measured heating rate;
- $a$ and $b$ are empirically determined calibration parameters.

### 9.3.3 Localization Algorithm

Based on this model, a localization algorithm was implemented in MATLAB. The logic is based on the following steps:

- Detection: a non-zero value of $m$ for at least one sensor indicates the presence of a thermal anomaly;
- Distance estimation: each sensor provides an estimate of the distance $r_i$ from the heat source using Eq. 9.2;
- Spatial reconstruction: each distance defines a circumference centered on the sensor position;

- Localization: the intersection of the circumferences identifies the position of the heat source.

Due to experimental uncertainties, the three circumferences do not intersect in a single point but rather define a small region. The estimated position of the heat source is therefore obtained as the centroid of the intersection region, while the uncertainty is defined as the spatial dispersion of the intersection points.

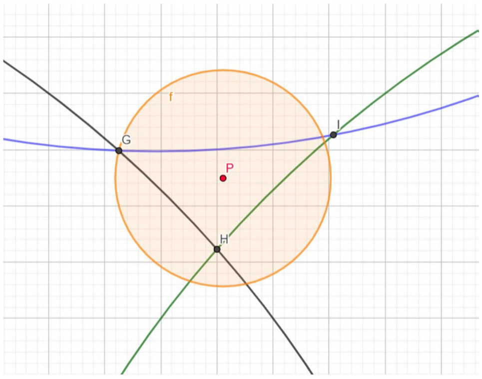


Fig. 9.9 Trilateration-based localization of the thermal source.

A graphical interface was developed to provide real-time visualization of the detected anomaly. The estimated position is marked by a red point, while the uncertainty region is represented by a surrounding circular area.

Fig. 9.10 Real-time graphical interface for heat source localization.

### 9.3.4 Results and Discussion

Figure 9.11 shows a representative example of the sensor response during the heating phase, while Figure 9.12 reports the experimental correlation between the parameter $m$ and the sensor–source distance.

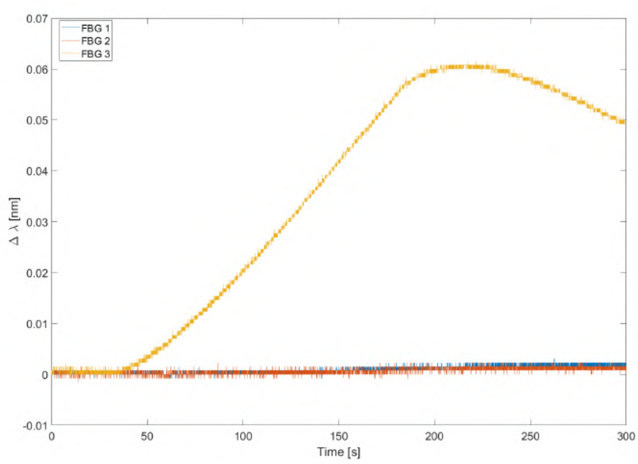


Fig. 9.11 Example of FBG response during heat source activation.

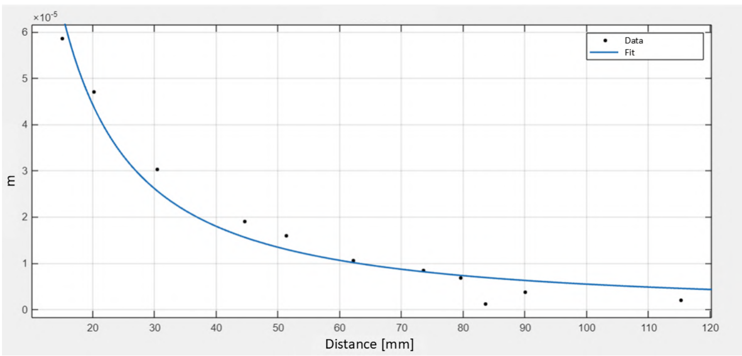


Fig. 9.12 Experimental correlation between heating rate $m$ and sensor–source distance.

The results demonstrate a clear dependence of the measured heating rate on the distance from the heat source, confirming the validity of the proposed model. The relationship assumed during the design phase is therefore supported by experimental evidence. The system showed excellent repeatability across all calibration and validation tests. The sensor network proved capable of detecting thermal anomalies even under relatively small temperature variations and within a simplified geometric configuration. The maximum localization uncertainty was approximately 2 cm, which is considered highly satisfactory given the simplicity and minimal invasiveness of the system.

These results validate the proposed sensing approach and highlight its potential for real-time thermal diagnostics in aerospace applications. In particular, the system is inherently immune to electromagnetic interference and can be deployed in critical areas where traditional electronic sensors may be less reliable. This approach can therefore represent the basis for the development of integrated diagnostic systems capable of detecting and localizing thermal anomalies in real time, supporting both safety monitoring and predictive maintenance strategies.

Table 9.1 Performance summary of the FBG-based hot-spot detection system.

| **Parameter** | **Value / Observation** |
|---|---|
| Number of sensors | 3 |
| Localization method | Trilateration (based on $m$ parameter) |
| Measured parameter | Heating rate $m = \Delta\lambda/\Delta t$ |
| Calibration approach | Empirical ($m$ vs distance correlation) |
| Number of calibration positions | 10 |
| Repetitions per position | 10 |
| Total calibration tests | 100 |
| Maximum localization error | $\approx 2$ cm |
| Repeatability | High (consistent over all tests) |
| Sensitivity to heat source | Clearly detectable even for small $\Delta T$ |
| Response time | Few seconds (transient phase detection) |
| Minimum detectable event | Short transient thermal peaks |
| Environmental robustness | Immune to electromagnetic interference |
| System invasiveness | Minimal |
| Scalability | High (extendable to larger sensor networks) |
| Real-time capability | Confirmed (MATLAB implementation) |

## 9.4 Fiber for Servo-mechanism Monitoring

The instrumentation for monitoring the motion of the servo motor arm was designed based on the control logic required to reconstruct the desired information. The actuator (a DiyMore 8120MG digital servo motor controlled via an Arduino Due board) generates a torque on its mechanical arm, which is transmitted to the final user system. The adopted concept consists in housing and securing the servo motor within a custom-designed support. This support becomes the location where the reaction forces generated by the arm motion are transferred. These forces induce localized stresses in the material, which can be measured by FBG sensors in terms of strain. The supports were designed using CAD models and iteratively refined through prototypes manufactured via additive manufacturing. An initial prototype made of PLA was discarded due to excessive flexibility and sensitivity to environmental conditions, which could compromise measurement accuracy. The final version was realized using UV-cured resin, ensuring higher stiffness and dimensional stability.

The geometry of the support was specifically optimized to:

- maximize deformation in the sensing regions;
- maintain operation within the elastic regime;
- ensure safe and reliable routing of the optical fibers.

Dedicated grooves were introduced to host the optical fibers and protect them during operation. Particular attention was paid to fiber pre-tensioning during bonding, in order to avoid measurement errors associated with residual compressive stresses induced during resin curing.

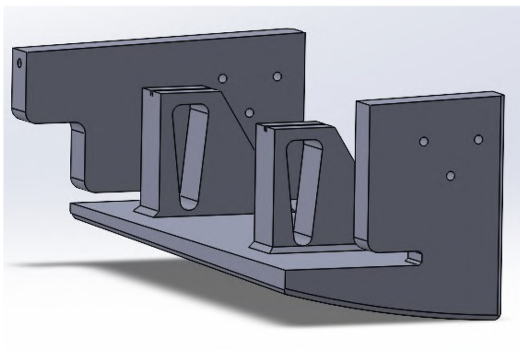

Fig. 9.13 CAD model of the servo support with integrated sensing regions.

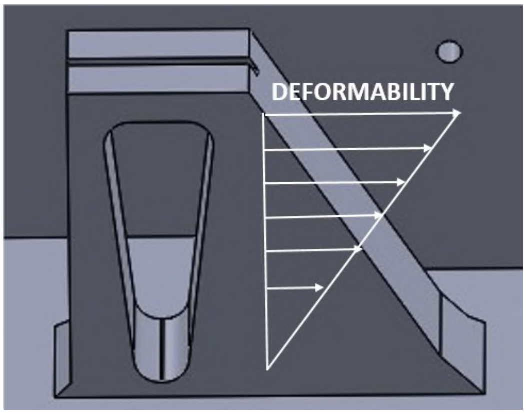


Fig. 9.14 Deformation field of the support under applied torque.


Fig. 9.15 Final prototype of the servo support with embedded optical fibers.

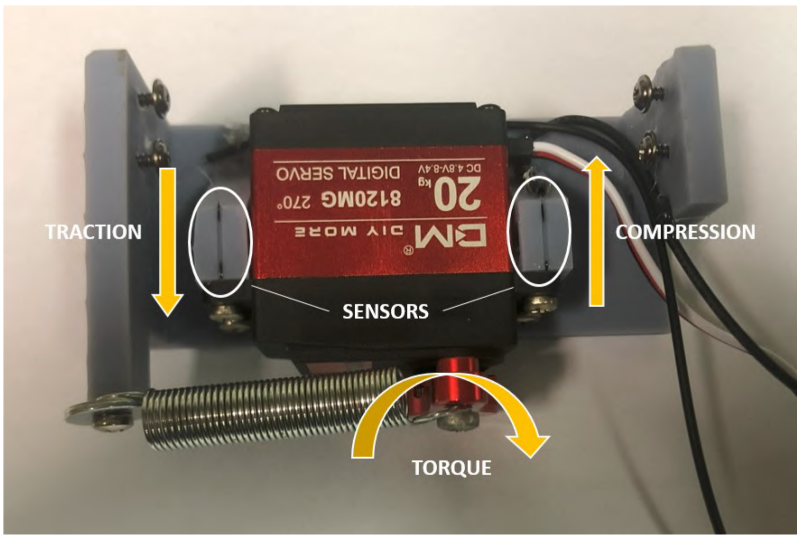


Fig. 9.16 Conceptual scheme of force transmission and sensing principle.

### 9.4.1 Servomotor Actuation Monitoring

The sensors were positioned to measure the deformation induced by the reaction forces generated by the applied torque. As shown in Fig. 9.16, the arm motion produces alternating tensile and compressive stresses on opposite sides of the support. This configuration exploits the intrinsic compliance of the structure as a sensing mechanism, enabling the correlation between local deformation and the macroscopic actuation behavior. The servo motor was programmed to oscillate harmonically between two angular limits (60°–120°), simulating repeated actuation cycles. Additionally, the motor arm was connected to a constrained spring to reproduce realistic loading conditions.

The raw optical data exhibited excellent qualitative agreement with the imposed physical behavior. In particular:

- The two sensor signals are in phase opposition;
- The amplitudes differ due to geometric asymmetry.

These observations are consistent with the sensor layout. The FBGs are positioned on opposite sides of the support, but not symmetrically, leading to different local stress levels under the same applied torque. From a theoretical standpoint, the optical response can be expressed as:

$$\Delta\lambda = K_\varepsilon \Delta\varepsilon \tag{9.3}$$

Assuming linear elastic behavior:

$$\varepsilon = \frac{\sigma}{E}, \quad \sigma = \frac{F_V}{S} \tag{9.4}$$

which leads to:

$$\Delta\lambda = \frac{K_\varepsilon \Delta F_V}{ES} \tag{9.5}$$

Since the reaction force $F_V$ is directly related to the motor torque $T_V$, and therefore to the angular position $\Delta\vartheta$, an experimental correlation was established:

$$\Delta\lambda = k\Delta\vartheta \tag{9.6}$$

This relation enables direct reconstruction of the actuator angular position from optical measurements.

The use of two sensors provides:

- redundancy in position estimation;
- detection of asymmetries and misalignments;
- improved robustness for control applications.

The results clearly demonstrate a strong correlation between the optical signals and the imposed actuator motion (Fig. 9.17). The periodic behavior of the wavelength variation closely follows the commanded angular trajectory, confirming the validity of the proposed sensing approach. Furthermore, the phase opposition between the two sensors is clearly visible, reflecting the alternating tensile and compressive stress states induced in the support during actuation.

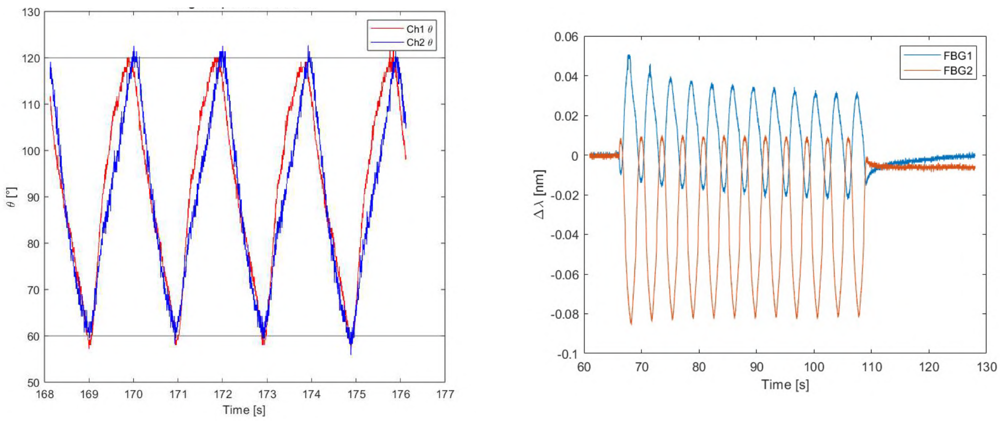


Fig. 9.17 Servo mechanism excursion estimation by FBG sensors and raw data.

Table 9.2 Performance summary of the FBG-based servo monitoring system.

| Parameter | Value / Observation |
|---|---|
| Actuator type | Digital servo motor (DiyMore 8120MG) |
| Control system | Arduino Due |
| Angular range | $60^\circ$ – $120^\circ$ |
| Motion type | Harmonic oscillation |
| Load condition | Spring-constrained arm |
| Number of FBG sensors | 2 |
| Sensor configuration | Opposite sides of support |
| Measured parameter | Strain-induced wavelength shift $\Delta\lambda$ |
| Derived quantity | Angular position $\Delta\vartheta$ |
| Calibration law | $\Delta\lambda = k \cdot \Delta\vartheta$ |
| Signal behavior | Periodic and stable |
| Phase relation | Phase opposition between sensors |
| Amplitude behavior | Asymmetric (geometry-dependent) |
| Response time | Real-time (high-frequency acquisition) |
| Sensitivity | High (clear detection of small deformations) |
| Repeatability | Excellent (consistent cycles) |
| Noise level | Low compared to signal amplitude |
| Transient detection | Enabled (peaks and oscillations captured) |
| Diagnostic capability | Misalignment detection (dual-sensor comparison) |
| Redundancy | Yes (dual-sensor configuration) |
| Control integration | Possible (direct $\vartheta$ reconstruction) |
| Scalability | High (extendable to multiple actuators) |

## 9.5 FBG Data for Dynamic Loads Monitoring

As described in Section 9.1, no additional sensors were specifically installed to monitor fluid-induced vibrations. Instead, the same eight FBG sensors integrated on the wing surface were used, in order to validate the multifunctional capability of the embedded sensing network. To reproduce the sloshing phenomenon, impulsive structural excitations were required. A flexural loading condition similar to that adopted for structural tests was applied. A 1 kg mass was suspended from the wingtip rib using a cable. The weight was initially stabilized to eliminate oscillations and ensure a steady pre-load condition. Once data acquisition started, the cable was suddenly cut, allowing the weight to fall freely and inducing a transient dynamic response in the structure. The test was performed both with and without the fuel tank installed, enabling comparison between the bare structural response and the fluid-structure interaction case.

Once the time-domain data were collected, frequency-domain analysis was performed by applying the Fast Fourier Transform (FFT). This allowed the computation of amplitude and phase as functions of frequency, generating Bode diagrams for each sensor and tank configuration. Figures 9.18 and 9.19 show representative results for a single sensor in two configurations: empty tank and 60% fill level. The spectra exhibit the expected behavior, with dominant low-frequency components associated with the initial transient excitation and higher-frequency structural modes clearly identifiable. A key step in the analysis was the identification of the natural frequencies of the structure. The reference configuration without the tank was used for this purpose. The dominant peaks in the Bode diagrams were identified and compared across all sensors. Peaks consistently present in all measurements were considered as the natural frequencies of the system. Particular attention was given to sensors located near the wingtip, as their higher displacement amplitudes enhance modal visibility. The five most significant natural frequencies are reported in Table 9.3. The comparison between different configurations highlighted that the presence of the fluid significantly affects the dynamic response of the structure. In particular:

- Increasing the liquid level leads to a reduction in oscillation amplitude;
- The effect is more pronounced at lower fill levels and tends to stabilize at higher levels;

- No monotonic trend in frequency shift was clearly identified.

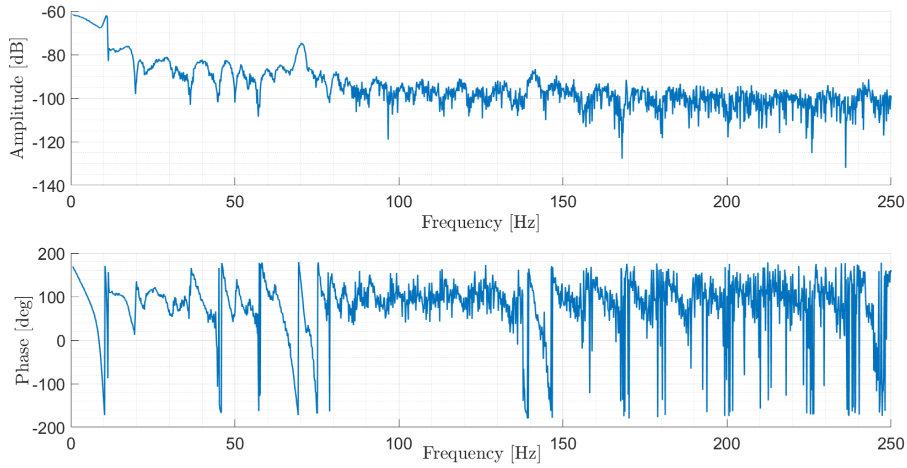


Fig. 9.18 Results of Fast-Fourier transform for oscillations with empty tank.

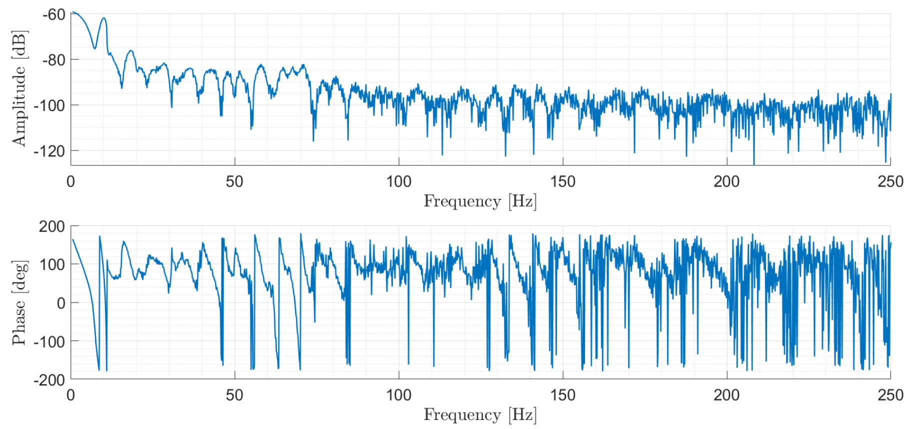


Fig. 9.19 Results of Fast-Fourier transform for oscillations with 60% tank fill level.

This behavior can be explained by the combined effect of increased structural mass and additional damping introduced by the fluid. The added mass modifies the dynamic response of the structure, while the sloshing motion dissipates energy, reducing oscillation amplitudes. Figure 9.20 clearly illustrates the correlation between peak amplitude and tank fill level. These results clearly demonstrate the capability of FBG sensor networks to provide multifunctional monitoring using a single embedded sensing infrastructure, significantly reducing system complexity, weight, and installation effort. Table 9.4 summarizes the key results for dynamic

| Natural frequencies | |
|---|---|
| $f_1$ | 10.14 Hz |
| $f_2$ | 17.86 Hz |
| $f_3$ | 41.57 Hz |
| $f_4$ | 47.14 Hz |
| $f_5$ | 70.14 Hz |

Table 9.3 System natural frequencies.

loads and fuel sloshing monitoring. In conclusion, table 9.5 clearly highlights the versatility of the proposed FBG-based sensing architecture, demonstrating its capability to provide multiple independent measurements using a single embedded sensor network. This approach significantly reduces system complexity while enabling advanced monitoring functionalities.

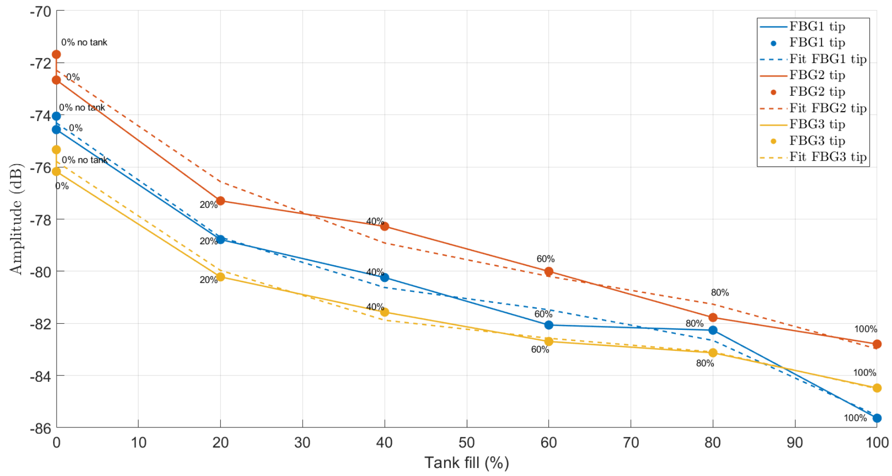


Fig. 9.20 Correlation between amplitude of oscillations detected by FBGs and tank fill level.

Table 9.4 Summary of dynamic monitoring results using FBG sensors.

| **Parameter** | **Observation** |
|---|---|
| Number of sensors | 8 (shared with structural monitoring) |
| Measurement domain | Time + Frequency (FFT analysis) |
| Excitation type | Impulsive (weight release) |
| Repeatability | High (consistent overlap of signals) |
| Identified natural frequencies | 10.14, 17.86, 41.57, 47.14, 70.14 Hz |
| Dominant frequency region | Low-frequency transient + structural modes |
| Effect of fluid presence | Significant modification of response |
| Effect of increasing fill level | Decrease in oscillation amplitude |
| Damping behavior | Increased with fluid presence |
| Resonance condition | Not clearly observed |
| Sensitivity | High (clear detection of dynamic response) |
| Multifunction capability | Confirmed (same sensors used for multiple tasks) |

Table 9.5 Multifunctional capabilities of the integrated FBG sensing network.

| **Application** | **Measurement / Method** | **Key result** |
|---|---|---|
| Structural monitoring | Strain ($\Delta\lambda \rightarrow \varepsilon$) | Linear response, high repeatability |
| Hot-spot detection | Temperature localization ($m = \Delta\lambda/\Delta t$) | Position error $\sim$ 2 cm |
| Servo monitoring | Angular position ($\Delta\lambda = k \cdot \Delta\vartheta$) | Real-time motion reconstruction |
| Dynamic loads / sloshing | Frequency analysis (FFT + Bode) | Natural frequencies and damping identified |

# Chapter 10

# Optical Data Visualization for Systems Monitoring: The PhotoNext Project

An essential aspect in the management and monitoring of systems instrumented through distributed Fiber Bragg Grating (FBG) sensing concerns data visualization and the software environment responsible for data handling. This aspect becomes increasingly relevant as distributed FBG sensing establishes itself as a key enabling technology for the development of intelligent systems capable of autonomously providing information about their operational state. The data visualization and management system developed within this work, in collaboration with the DAUIN Department, is based on a modular architecture structured into three distinct levels:

- basic data reading in post-processing;
- near real-time data acquisition and visualization;
- near real-time data acquisition integrated with control algorithms.

Another fundamental aspect concerns the connection modality between the interrogator and the data processing unit. The interrogator available for the present activities (and, more generally, most commercially available interrogators) is designed to be connected via a LAN interface to a PC responsible for data management.

Such a configuration represents a significant limitation for the deployment of FBG-based sensing systems in complex geometries or onboard platforms such as UAVs. Although some of the most recent interrogators available on the market provide direct data storage capabilities (e.g., database integration), the instrumentation employed in this work does not include this functionality. Therefore, it becomes necessary to develop a dedicated software and communication architecture tailored to the specific interrogator used in this study.

## 10.1 Basic Monitoring through an Interrogator–LAN–PC Architecture

The reference interrogator employed in this work is the SmartScan device manufactured by SmartSoft. The standard data acquisition procedure relies on proprietary software provided by the manufacturer, which generates output files in `.log` format (readable as plain text files). These files contain all acquired samples recorded sequentially over time. The most straightforward and immediate analysis approach consists of performing data acquisition directly through the manufacturer's software and subsequently importing the generated `.log` files into a post-processing environment (e.g., MATLAB), where the data are visualized using dedicated scripts. As discussed in previous chapters, the interrogator acquisition frequency can be set to very high values. Moreover, the device updates the `.log` file each time its internal memory buffer is filled. This buffer corresponds to approximately 500 samples. Consequently, when operating at the maximum acquisition frequency over the full optical spectrum (2500 Hz), the file is updated approximately every 200 ms. This behavior implies that data can be accessed and processed with a latency that is, in practice, comparable to near real-time applications, even when using a post-processing workflow. This first level of implementation represents the baseline architecture upon which more advanced real-time and control-oriented solutions are developed in the following sections.

## 10.2 Near Real-Time Data Acquisition, Wireless Transmission, and Data Management

In order to fully exploit the advantages offered by fiber-optic sensing technologies, it is necessary to develop a dedicated telemetry system capable of supporting not only complex ground-based applications, but also—and especially—airborne platforms. As demonstrated in the previous chapter, the true added value of FBG-based sensing does not lie solely in the conversion of optical measurements into physical parameters, but rather in the extraction of higher-level information through the fusion of data acquired at multiple sensing locations. This requirement naturally leads to the need for a control-oriented architecture capable of continuously acquiring sensor data while simultaneously processing their content in near real time. Such functionality cannot be achieved using only the proprietary software provided by the interrogator manufacturer. Instead, it requires the development of a modular and flexible data acquisition framework that can be seamlessly integrated with custom analysis and control algorithms. As described in Chapter 2, the manufacturer-provided software offers the following functionalities:

- LAN-based communication between interrogator and PC;
- visualization of the reflected optical spectrum;
- visualization of the temporal evolution of individual sensor signals;
- storage of acquired data in time-resolved log files.

However, this configuration presents several critical limitations:

- lack of integration with control logic and data fusion algorithms;
- limited capability to associate measurements with the physical geometry of the system;
- absence of a scalable and comprehensive near real-time monitoring environment.

For these reasons, it is necessary to develop a dedicated data handling process capable of automatically acquiring, storing, and processing optical data within a computational environment that overcomes these limitations. The solution proposed in this work is designed to be lightweight, modular, and easily deployable, making it suitable for both laboratory testing and flight applications (as discussed in Chapters 12-13). The interrogator used in this work (SmartScan) communicates externally exclusively through a LAN interface. This constraint imposes the need for an intermediate hardware layer capable of interfacing with the interrogator, extracting the data stream, and managing its transmission toward external systems. From a system engineering perspective, the overall architecture can be decomposed into four main elements:

- *Physical system.* The instrumented platform (e.g., UAV) including all structural components and embedded FBG sensor networks.
- *Middleware (onboard hardware).* The interrogator and an additional processing unit (e.g., Raspberry Pi or mini-PC), connected via LAN, responsible for data acquisition, buffering, and transmission.
- *Cloud database.* A remote storage system acting as an interface between onboard instrumentation and ground-based monitoring systems.
- *Viewer.* The software environment responsible for data retrieval, processing (including control logic and data fusion), and visualization through user interfaces.

The functional architecture of the proposed system is illustrated in Fig. 10.1. The proposed architecture enables scalable deployment of FBG sensing systems, allowing the same hardware platform to support monitoring, diagnostics, and control-oriented applications.

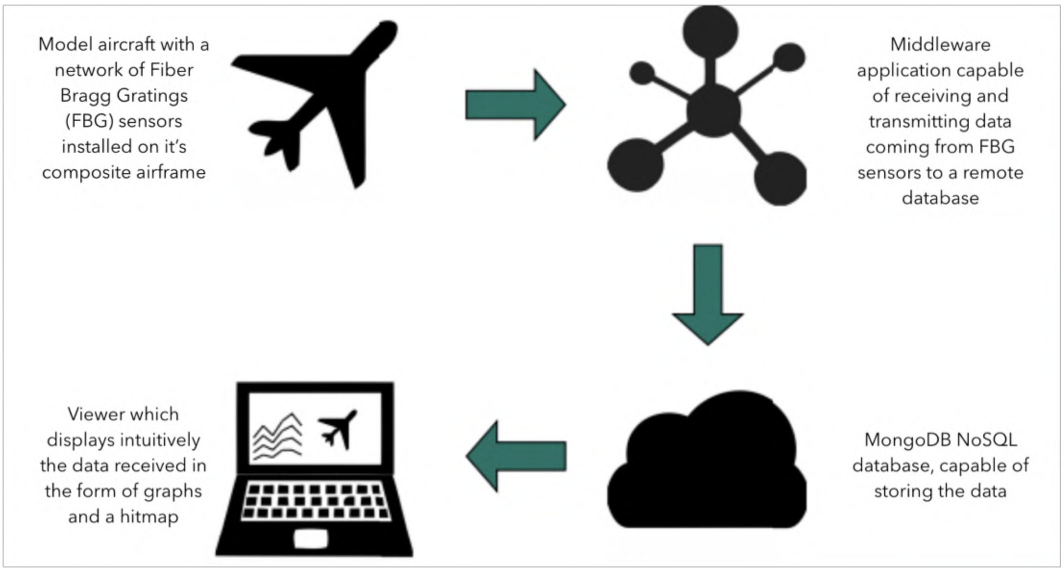


Fig. 10.1 Functional architecture of the proposed FBG-based telemetry and data management system.

## 10.3 Raspberry Pi–Based Architecture

The first developed architecture is based on the following main components:

- a Raspberry Pi connected to the interrogator via LAN;
- a dedicated C++ application developed to retrieve data from the interrogator;
- Internet connectivity provided through a 4G/4G+ USB modem;
- data upload to a cloud-based MongoDB database;
- a desktop viewer;
- a data analyzer.

This configuration offers several significant advantages:

- simplicity of installation;
- low overall cost;

- the possibility of avoiding the use of the manufacturer's proprietary software, thus enabling fully customized data visualization;
- reduced size and footprint.

In this architecture, the interrogator is connected to the Raspberry Pi via a LAN interface. Through a specifically developed application, the data generated by the interrogator are retrieved and stored in a MongoDB database. However, this solution also presents several limitations at the application level:

- limited achievable sampling frequency;
- difficulties in establishing and maintaining a stable connection with the interrogator;
- limited data processing capabilities.

Additional details regarding this architecture are provided in the following sections, while Figure 10.2 illustrates its functional block diagram.

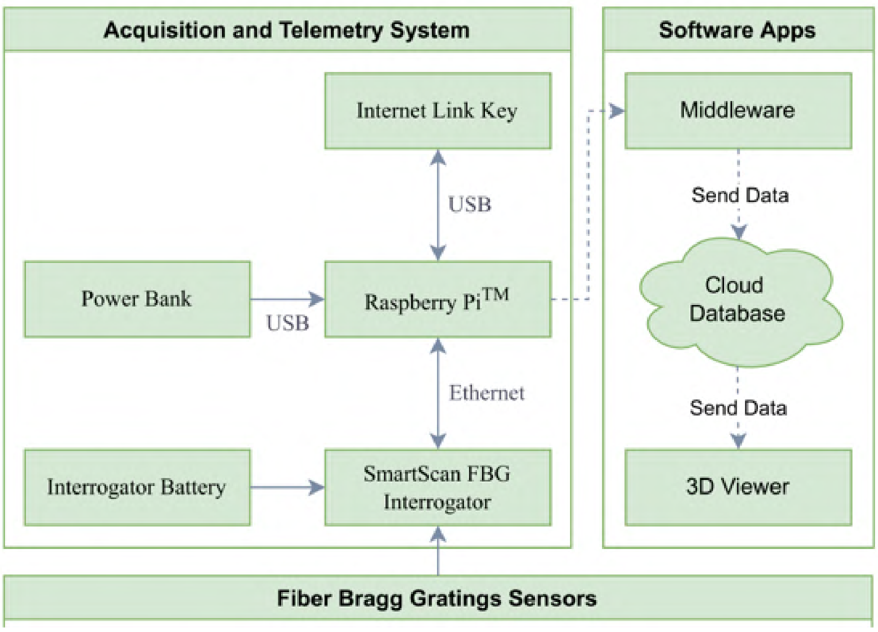


Fig. 10.2 Functional architecture of the Raspberry Pi–based data acquisition system.

### 10.3.1 Middleware

The middleware is based on a Raspberry Pi™ 3 Model B+ System-on-Chip (SoC), running a Linux operating system and executing a dedicated C/C++ application. This software enables the connection to the interrogator and the retrieval of the main parameters typically provided in the acquisition `.log` file, namely the sensor ID, the measured value, and the associated timestamp.

The application was developed at the Department of Control and Computer Engineering of the Politecnico di Torino [86], and an example of its operation is shown in Figure 10.3. As anticipated, this solution completely decouples the data acquisition process from the manufacturer's proprietary software, enabling direct use of the acquired data either within a custom visualization environment or as input for more complex control algorithms. In addition, the application allows both local storage of the acquired data on the Raspberry Pi memory and real-time transmission to the cloud database during measurement operations [87].

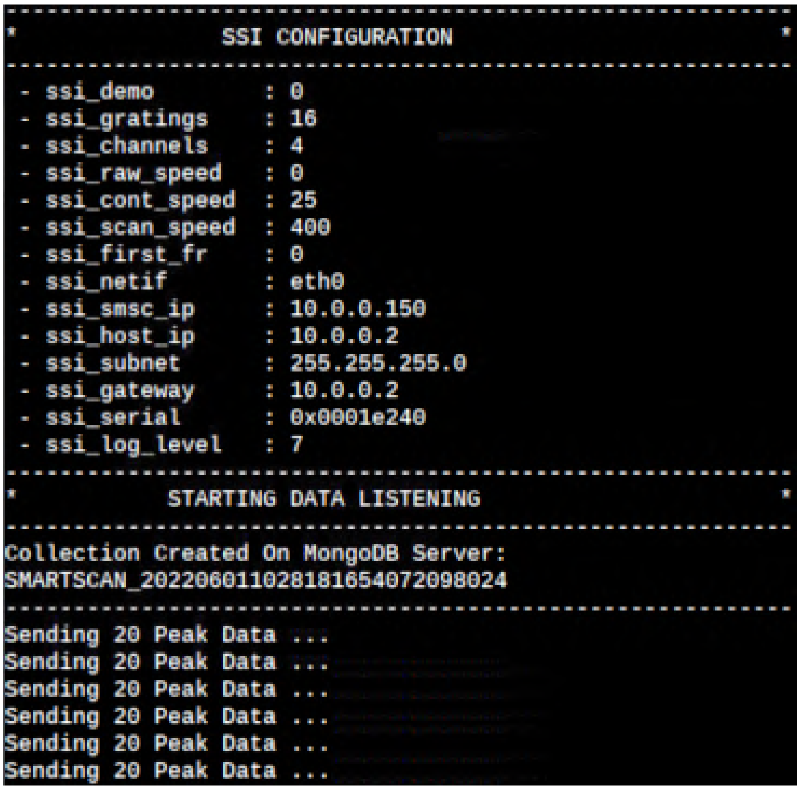


Fig. 10.3 Middleware interface for real-time data acquisition and upload.

### 10.3.2 Cloud Database

The project requires fast storage and retrieval of sensor data within a cloud-based environment. For this reason, a NoSQL database was selected, as its capability to handle unstructured data eliminates the need for strict schema validation, thus enabling faster write operations [88]. Following a comparative analysis of available NoSQL solutions, *MongoDB®* was selected. One of its most relevant features is the use of *collections*, which represent containers for storing similar data records. Upon connection, the middleware automatically creates a new collection, named according to the convention SMARTSCAN_<timestamp>. In MongoDB terminology, each individual uploaded data record is defined as a *document*. The rationale behind this approach was to maintain a simple data structure in order to maximize upload efficiency and achieve high data transmission rates. However, this strategy proved to be suboptimal in practice. While associating a single document with each data sample enables fast write operations, it severely limits the achievable sampling frequency to the order of a few hertz. Such performance is insufficient for the characterization of even moderately complex dynamic phenomena, which typically require higher acquisition rates.

### 10.3.3 Viewer

The primary purpose of the viewer is to represent the sensor data acquired by the interrogator. Two complementary visualization modalities are implemented:

- a graph showing the difference between the nominal Bragg wavelength and the measured value, commonly referred to as $\Delta\lambda$, which varies as a function of strain and temperature;
- a heat-map-based visualization, representing sensor data through variations in color and intensity around each sensor location.

While graphical plots provide higher quantitative accuracy, the heat-map visualization offers a more intuitive and immediate interpretation of the system state. Users can load arbitrary 3D models into the software [89]. Once connected to the cloud database, the viewer automatically retrieves the sensor configuration and displays their positions as interactive elements (red spheres). These can be manually adjusted through a drag-and-drop interface, allowing accurate alignment with the physical system geometry. After configuration, real-time data visualization can be initiated.

### 10.3.4 Data Analyzer

In addition to basic visualization, a dedicated application named *PhotoNext FBG Data Analyzer* was developed in collaboration with DAUIN. Its purpose is to combine:

- remote data management without direct connection to the interrogator;
- advanced data visualization and integration within control and analysis algorithms.

The software was developed in C++ using the Qt framework [90] and is structured into multiple views, each designed for specific analysis tasks [91].

The *Main view* displays both instantaneous wavelength values and their temporal evolution. It includes:

- a sensor list with selection and color customization options;
- a real-time spectral visualization graph;
- a time-history plot of the measured signals.

The *Measures view* allows the visualization of temperature or strain values derived from the optical signals. Users can configure calibration coefficients and define reference sensors for temperature compensation.

The *FFT view* provides frequency-domain analysis using Fast Fourier Transform (FFT). To optimize performance, FFT calculations are performed on batches of $n$ samples rather than continuously.

The *Table view* presents real-time numerical data in tabular format, offering a precise and immediate overview of sensor measurements.

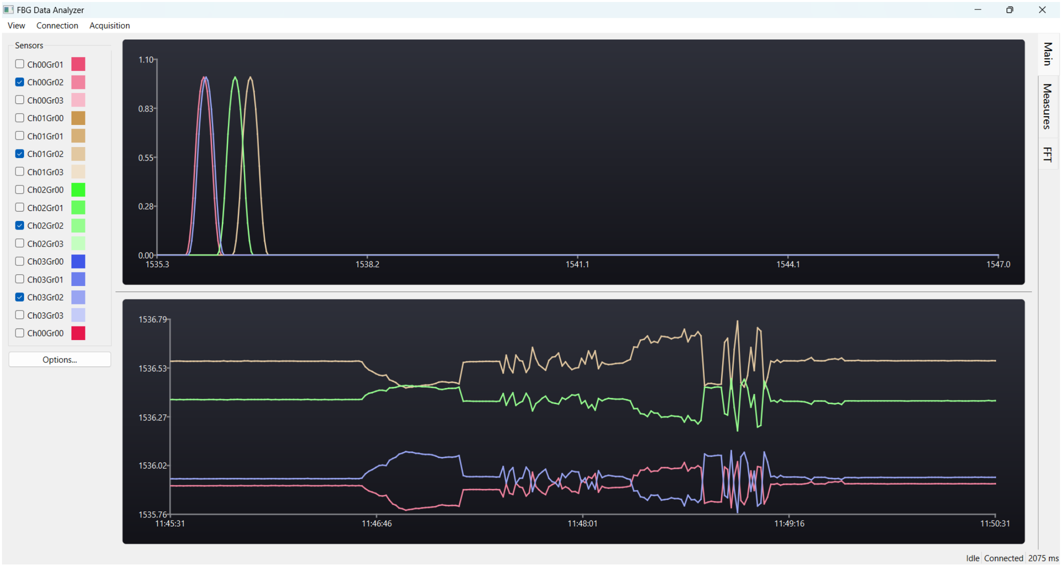


Fig. 10.4 A screenshot of the *Main* view of the *PhotoNext FBG Data Analyzer*.

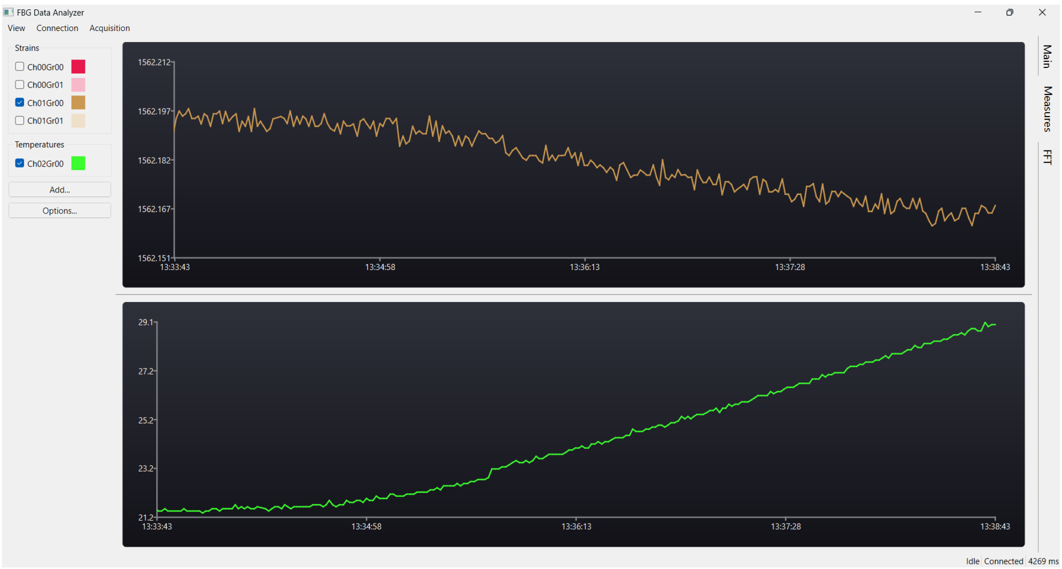


Fig. 10.5 A screenshot of the *Measures* view of the *PhotoNext FBG Data Analyzer*.

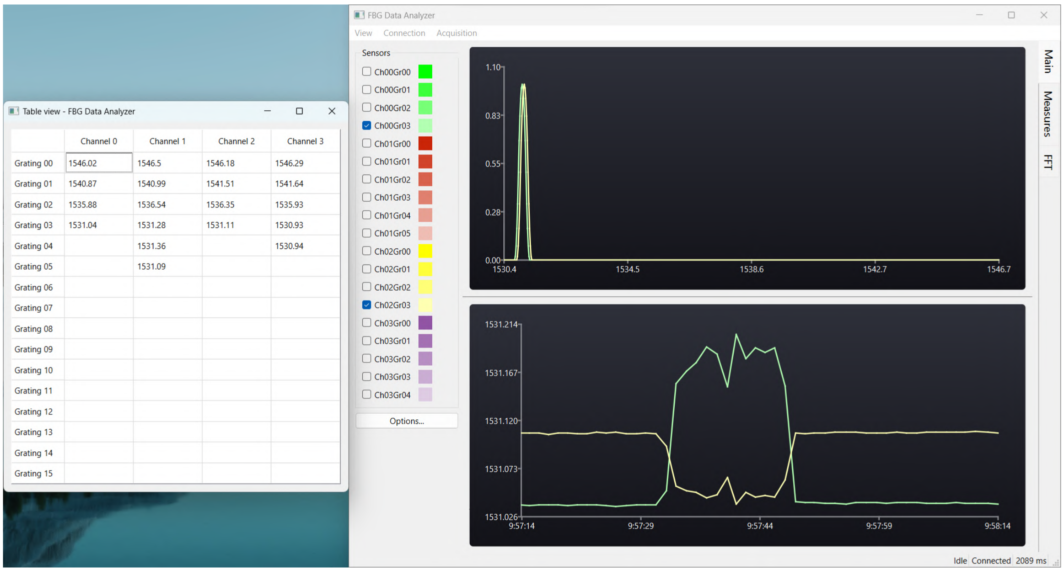


Fig. 10.6 A screenshot of the *Table* view of the *PhotoNext FBG Data Analyzer*.

The application also includes data logging functionalities and customizable acquisition parameters such as sampling rate and duration.

All user-defined settings are stored in a `settings.json` file, enabling configuration reuse across multiple experimental campaigns.

As previously mentioned, the *PhotoNext FBG Data Analyzer* is distributed as an open-source solution [91], allowing further customization according to specific application needs.

Table 10.1 Components and functionalities of the Raspberry Pi–based architecture.

| **Component** | **Role** | **Key Features** |
|---|---|---|
| Interrogator | Optical data acquisition | High-frequency FBG interrogation, LAN output |
| Raspberry Pi (Middleware) | Data retrieval and transmission | C/C++ application, local storage, cloud upload |
| 4G Modem | Internet connectivity | Wireless communication for onboard applications |
| MongoDB Cloud Database | Data storage | NoSQL structure, fast write operations, collections |
| Viewer (3D + Graphs) | Data visualization | $\Delta\lambda$ plots, heat-map representation, 3D model integration |
| PhotoNext Data Analyzer | Advanced processing | Real-time plots, FFT, strain/temperature conversion, logging |

Table 10.2 Advantages and limitations of the Raspberry Pi–based architecture.

| **Advantages** | **Limitations** |
|---|---|
| Low cost | Limited sampling frequency |
| Compact and lightweight | Connection instability issues |
| Easy deployment | Limited processing capability |
| Full customization | Not suitable for high-frequency dynamics |

## 10.4 Mini-PC–Based Architecture

The solution presented in the previous section is well suited for quasi-static phenomena or systems characterized by very slow dynamics (below 1 Hz). However, in order to accurately characterize complex systems—such as an unmanned aerial vehicle (UAV) in flight, which represents the primary objective of this work—a sampling frequency of only a few hertz is clearly inadequate. Since more advanced commercial solutions (featuring compact dimensions and direct database integration) were not readily available at the time of development, a new architecture was designed, building upon the experience gained from the system presented in Section 9.3.

Conceptually, the new system preserves the same overall structure shown in the functional diagram in Figure 10.1, while replacing several key components. In particular, the main modifications include:

- the adoption of a mini-PC instead of a Raspberry Pi;
- the use of the original *Smart Soft* software on the onboard mini-PC;
- the development of a dedicated application (*Uploader*) for database upload starting from *Smart Soft* output files;
- a redesigned data organization strategy within the database;
- the development of a dedicated *Downloader* application for the ground station;
- the integration of the *Downloader* within the MATLAB environment to enable near real-time data processing through dedicated control algorithms.

The physical architecture of the system is shown in Figure 10.7.

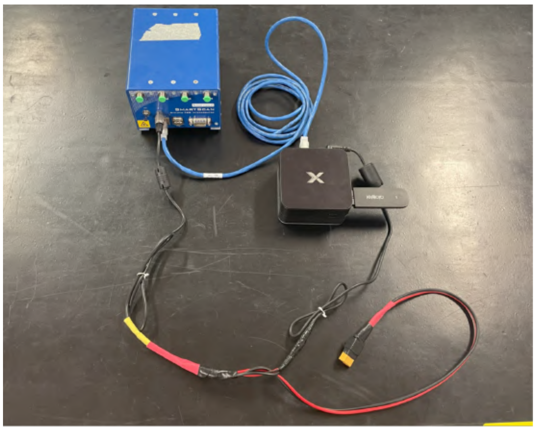

Fig. 10.7 Mini-PC–based architecture for high-frequency data acquisition and transmission.

### 10.4.1 Mini-PC and Smart Soft

Among the various mini-PC solutions available on the market, the T9 Pro model was selected [92]. This choice represents a balanced compromise in terms of cost, computational performance, physical dimensions, and availability. The mini-PC operates under a Windows 10 environment, enabling the direct use of the proprietary *Smart Soft* software. This allows replication of the standard data acquisition workflow already described in previous sections, ensuring compatibility with the interrogator and eliminating the need for low-level communication management.

### 10.4.2 Database

The selected database remains MongoDB, as described in Section 10.3. However, in this architecture, the strategy for data organization and storage is significantly revised. In the previous solution, each individual sample was stored as a separate document. While this approach ensured minimal latency and simple data management, it limited the achievable sampling frequency to only a few hertz. In the new architecture, the data source is the `.log` file periodically updated by the interrogator through the *Smart Soft* software. The interrogator writes data in batches corresponding to its internal buffer size (approximately 500 samples). When operating at the maximum sampling frequency (2.5 kHz), the file is updated approximately every 200 ms. This high-frequency data stream enables a more efficient storage strategy, in which multiple samples are grouped into a single document. This significantly reduces the overhead associated with database operations and enables an effective sampling frequency of approximately 300 Hz during transmission. To minimize latency, the interrogator continues operating at its maximum sampling rate, while the upload process applies a subsampling strategy to match the bandwidth and processing limitations of the system.

Each database collection corresponds to a single measurement campaign and consists of multiple documents. Each document includes:

- a reference timestamp $t_0$;
- multiple samples for each sensor.

The temporal reference of each sample within a document is defined as:

$$\Delta t = t_0 + i \cdot \frac{1}{f} \tag{10.1}$$

where $f$ is the effective sampling frequency and $i$ is the sample index within the document.

This structure allows efficient storage and retrieval while preserving temporal coherence across sensors.

### 10.4.3 Uploader

A dedicated application for data upload was developed in Python. The application reads data from the `.log` file and organizes them into structured documents, each containing multiple samples over a defined time interval $\Delta T$. These documents are then uploaded to the database. The process is repeated iteratively until no new data are detected for a specified time interval, at which point the acquisition is considered complete.

The main configurable parameters are:

- *rowsPerDocument*: number of samples stored per document;
- *bufferDocuments*: number of documents uploaded per batch;
- *waitTime*: delay for new data availability;

- *maxWaitTime*: timeout for acquisition termination;
- *subsampling*: reduction factor applied to raw data.

Increasing *rowsPerDocument* improves upload efficiency but may increase latency. Conversely, smaller documents reduce latency but increase overhead. Therefore, an optimal balance must be achieved depending on system constraints. Similarly, *subsampling* allows adapting the effective sampling frequency to the capabilities of the communication channel and database.

From an operational perspective, the workflow consists of:

1. launching the *Smart Soft* software;
2. starting acquisition and generating the `.log` file;
3. launching the Python script `DynamicUploader.py`;
4. selecting the `.log` file;
5. stopping acquisition, after which the upload process automatically terminates.

### 10.4.4 Visualizer

The final component of the architecture is the data download and visualization system, implemented in MATLAB. This environment was selected due to its strong capabilities in data processing, visualization, and database connectivity. The MATLAB code retrieves data from the MongoDB database in near real time and reconstructs the measurement matrix in the same format as the original `.log` file (samples $\times$ sensors). Once the connection is established and a dataset is selected, the code continuously updates the data matrix as new documents become available.

This enables:

- real-time visualization of sensor data;
- post-processing and signal analysis;
- integration with control algorithms.

Different visualization modes are included in the software, such as tabular representation, time evolution of wavelength variations, and graphical mapping of sensor data onto the system geometry (Figure 10.8). This tool represents a fundamental step toward the management of large datasets and the fusion of heterogeneous sensor information (e.g., IMU, GPS, etc.). In conclusion, Table 10.3 highlights the significant performance improvement achieved by the Mini-PC–based architecture, particularly in terms of sampling frequency, stability, and suitability for dynamic system monitoring.

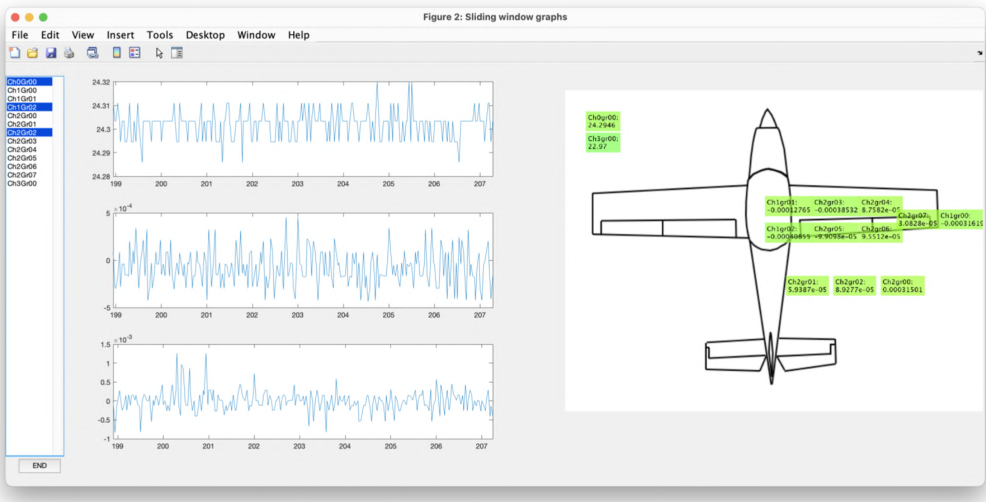


Fig. 10.8 Example of MATLAB-based visualization interface.

Table 10.3 Comparison between Raspberry Pi–based and Mini-PC–based Architectures.

| **Parameter** | **Raspberry Pi** | **Mini-PC** |
|---|---|---|
| Sampling frequency | ∼1–5 Hz | ∼300 Hz (effective) |
| Interrogator interface | Custom C++ code | Native Smart Soft software |
| Data source | Direct stream | `.log` file buffering |
| Database structure | 1 sample / document | Multiple samples / document |
| Latency | Low | Moderate (∼200 ms) |
| Connection stability | Limited | High |
| Processing capability | Low | High |
| System complexity | Low | Moderate |
| Customization | High | High |
| Suitability | Quasi-static systems | Dynamic systems (UAV) |

# Chapter 11

# Augmented Reality for Optical Data Management

The management of complex systems, together with the evaluation of their performance and the associated levels of safety, precision, and reliability, is strictly related to the quality of the human–machine interface. This aspect plays a key role in determining the level of situational awareness of the human operator interacting with the aero-electro-mechanical system under consideration, or with a system of systems. Regardless of the application domain (aeronautics, space, unmanned aerial vehicles) or the operational phase (testing, operation, or maintenance), human factors represent a critical contribution to overall system reliability and safety. In this context, the way in which data are visualized and presented to the end user becomes strategically important in minimizing human-related errors and improving decision-making processes. Moreover, advanced visualization techniques can provide access to information that would otherwise be difficult to interpret or entirely unavailable. The use of Extended Reality (XR) technologies in the aerospace sector is widely recognized as a promising approach to address these challenges. Although XR technologies have historically undergone alternating phases of enthusiasm and disillusionment, recent technological advancements have led to the development of highly mature commercial devices. These include the Meta Quest 3 and HTC Vive Pro 2 for Virtual Reality (VR), the Apple Vision Pro for Mixed Reality (MR), and the Microsoft HoloLens 1 and 2 for Augmented Reality (AR). This evolution has enabled applications that would have been impractical or impossible only a few decades ago.

XR technologies enable the development of applications that can:

- fully replace the physical environment with a virtual one (VR);
- integrate real-world data to contextualize virtual content (MR);
- superimpose digital information directly onto the physical world (AR).

These technologies are currently employed in a wide range of applications. VR is widely used for education [93, 94], training [95, 96], and gaming [97, 98]. AR, on the other hand, is particularly suited for data visualization [99, 100], maintenance and diagnostics [101, 102], and training activities [103, 104]. Mixed Reality, due to its hybrid nature, encompasses use cases overlapping both VR and AR domains [105–107]. In this chapter, the focus is specifically placed on Augmented Reality as a tool for enhancing human perception. The objective is to develop a demonstrative prototype for the visualization of data acquired through Fiber Bragg Grating (FBG) sensors using an AR headset. The combination of these technologies allows the advantages of distributed fiber-optic sensing networks to be fully exploited. As discussed in previous chapters, FBG technology enables the realization of "smart" components capable of providing multiparametric information through a single, minimally invasive sensing system. However, conventional desktop-based visualization—typically limited to near real-time plots—may not provide sufficiently intuitive or actionable information for human operators. The reference application considered in this work concerns advanced in-flight performance monitoring of an unmanned aerial vehicle (UAV). This should be interpreted as a demonstrative case study rather than a limitation of the proposed approach. The activity was carried out in collaboration with the Department of Control and Computer Engineering of the Politecnico di Torino, which contributed to both the hardware setup and the software development.

The reference hardware platform selected for this study is the Microsoft HoloLens 2, which represents one of the most advanced AR headsets currently available. The physical acquisition setup remains identical to that of a conventional FBG measurement system. The innovation introduced by the proposed approach lies in the direct connection between the HoloLens device and the MongoDB database described in the previous chapter. This architecture eliminates the need for additional hardware components for visualization. Instead, the key element is the application running on

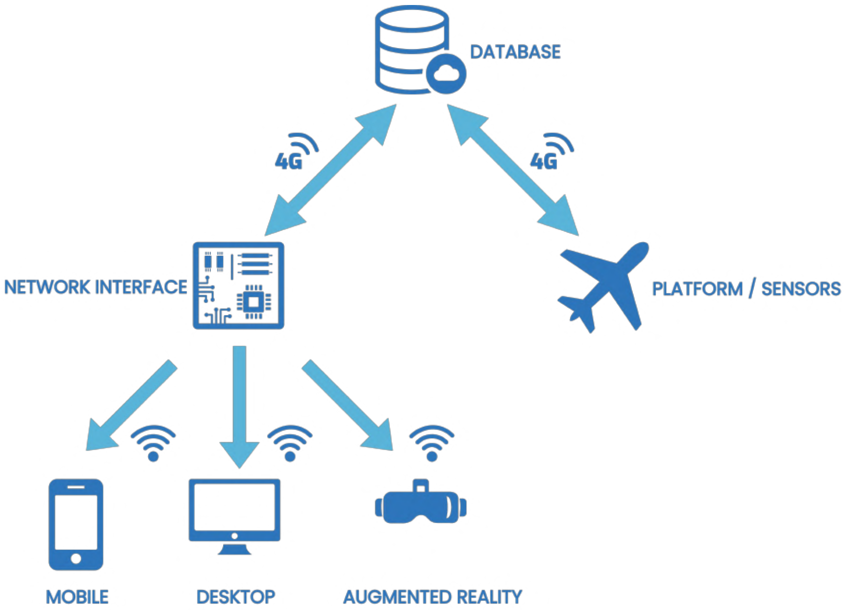


Fig. 11.1 Augmented Reality visualization of FBG-based sensor data on an instrumented system.

the headset, which retrieves data from the database and converts them into meaningful visual information tailored to the user's task. A demonstrative application was developed with the following functionalities:

- import of a three-dimensional model of the instrumented system;
- manual positioning of sensors within the model, including specification of the measured quantity (thermal or mechanical);
- visualization of real-time sensor data through dedicated dialog windows;
- implementation of a heat-map representation, highlighting the spatial distribution of sensor variations.

The developed system is particularly suited for scenarios in which complex information must be derived from distributed sensor networks and communicated to a human operator in an immediate and intuitive manner. A representative application is ground-based UAV piloting, where critical information—such as thermal anomalies, structural loads, or system performance parameters—can be directly visualized while observing the physical system. Augmented Reality thus represents a highly effective medium for integrating and communicating heterogeneous sensor data. Within this framework, the FBG sensor network provides access to physical quantities that are otherwise difficult to measure, while AR enables their intuitive interpretation. Figure 11.2 shows an example of the initial configuration phase, where sensors are positioned within the 3D model. The user interface allows enabling or disabling different visualization modes and selecting whether visual elements are anchored to the user's viewpoint or to the physical environment. To ensure smooth operation and responsiveness, the acquired data are subjected to a subsampling process, reducing the update frequency of the graphical interface. This represents a necessary compromise between visualization performance and system responsiveness.


Fig. 11.2 Sensor configuration and visualization setup within the AR environment.

## 11.1 Laboratory Tests

The experimental activities presented in this section aim to demonstrate the practical applicability of the developed visualization software within a laboratory environment. In particular, the tests highlight both the conventional graphical visualization and the proposed heat-map-based representation. The instrumented *Anubi* UAV platform (see Chapter 12) was used as the reference system. The platform is equipped with the following sensors:

- nine strain FBG sensors distributed across the upper and lower surfaces of the right wing;

- one temperature FBG sensor located on the upper part of the right wing, near the root, used for thermal compensation;
- one temperature FBG sensor positioned on the fuselage, close to its center, used to measure the external temperature.

For clarity, and due to the limited field of view (FOV) of the HoloLens device, only a subset of sensors is displayed in the figures reported below. In the strain tests, two sensors positioned on the upper and lower wing surfaces (Ch3Gr3 and Ch3Gr4) were selected to emphasize tensile and compressive effects. In the combined strain–temperature tests, the temperature sensor located on the fuselage (Ch1Gr1) was also included in the visualization.

### 11.1.1 Strain Test

The strain test focused on evaluating the software response under purely mechanical loading conditions. In the initial configuration, two weights of 1 kg each were applied to the wings of the *Anubi* platform using dedicated sliding supports. This configuration induced compressive strain on the lower surface of the wing and tensile strain on the upper surface. Following the removal of the weights, the structure returned to its unloaded condition. The subsequent reapplication of the weights restored the initial stress state, enabling the observation of repeatable loading–unloading cycles. Figure 11.3 shows representative snapshots of the test. The evolution of the strain field is clearly captured by the visualization system, both in terms of temporal trends and spatial distribution through the heat-map representation.

### 11.1.2 Strain and Temperature Test

The second test investigated the system response under combined mechanical and thermal loading conditions. The initial configuration was identical to the previous test, with two 1 kg weights applied to the wings. During the test, lasting approximately 6 minutes, the following operations were performed:

- the temperature sensor was locally heated using a lighter for approximately 15 seconds, inducing a rapid increase in the measured wavelength due to thermal expansion effects;

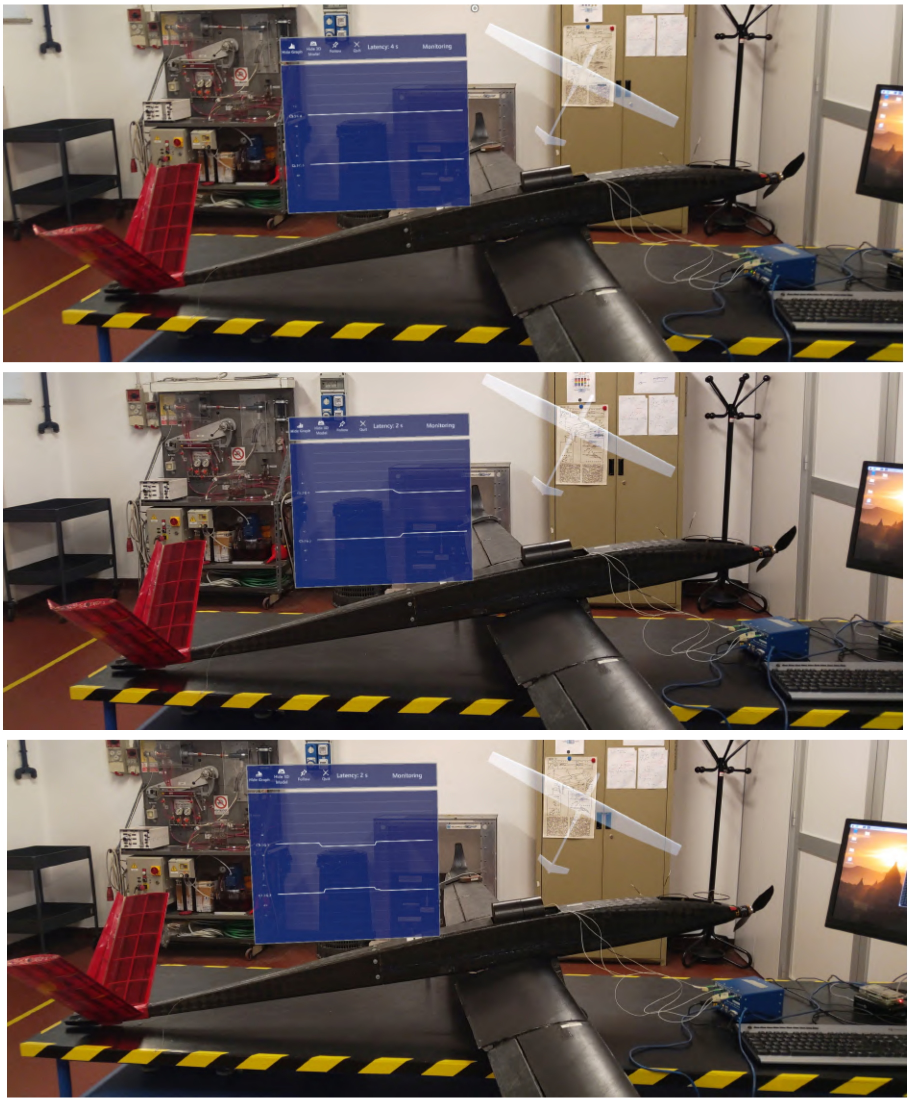

Fig. 11.3 Visualization of different phases of the strain test, highlighting the variation of tensile and compressive states in the wing structure.

- the weight applied to the right wing was removed, allowing the structure to return to its unloaded condition.

The thermal excitation produced a clear transient response, followed by a gradual return to equilibrium as the sensor cooled down. At the same time, the mechanical unloading produced a distinct variation in the strain-related measurements. Figure 11.4 shows representative frames of the test. The combined effect of strain and temperature variations is clearly distinguishable, demonstrating the capability of the system to simultaneously handle multiphysical phenomena.

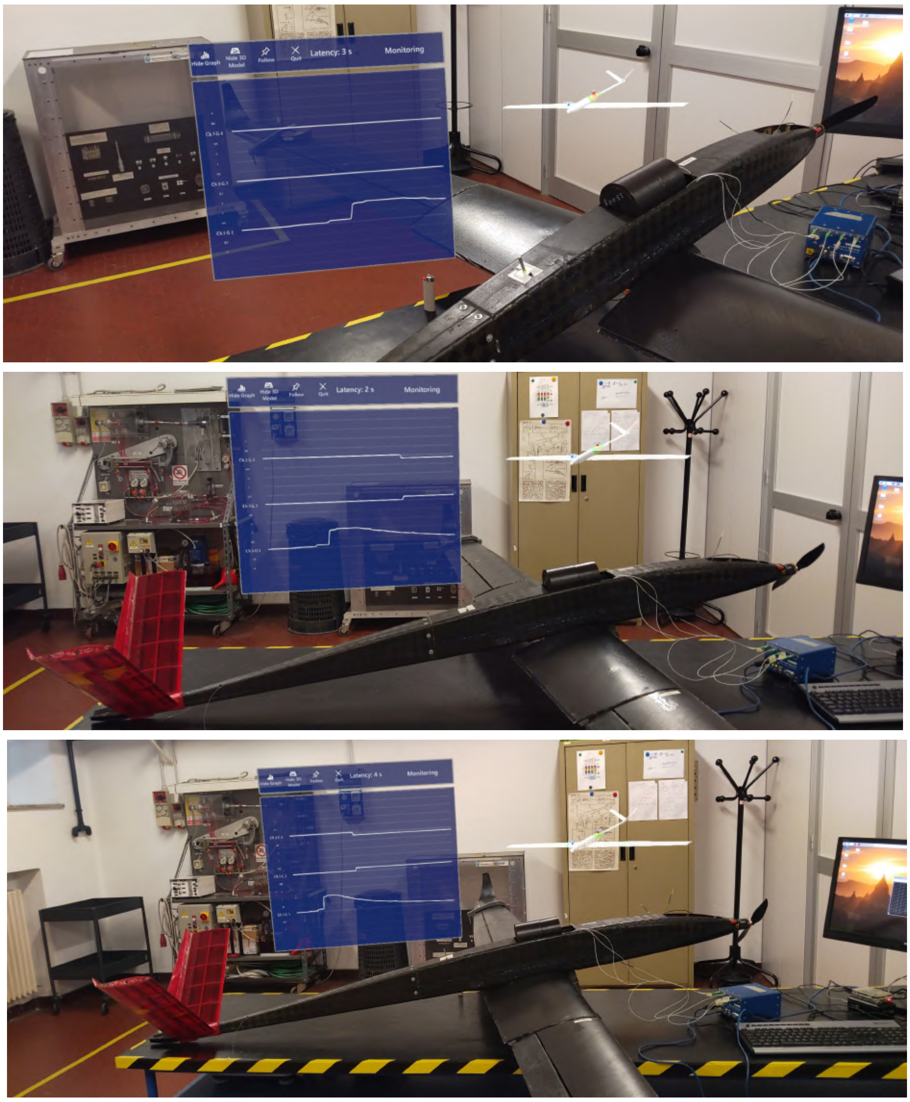

Fig. 11.4 Visualization of the combined strain and temperature test, showing the simultaneous influence of thermal excitation and mechanical unloading.

### 11.1.3 Tests with Other Geometries

To provide a first generalization of the proposed approach, additional tests were performed on different instrumented geometries, including composite laminates with embedded optical fibers and specimens manufactured using regolith simulant material. The test conducted on the composite specimen lasted approximately 40 minutes. The specimen was placed inside a climatic chamber and subjected to a temperature decrease from ambient conditions (approximately 25 °C) down to −30 °C. Before reaching thermal equilibrium, the temperature was abruptly increased to 75 °C, generating a rapid thermal transient clearly detectable by the embedded sensor. The regolith specimen was tested over a duration of approximately 20 minutes. Starting from an ambient temperature of 25 °C, the temperature was reduced to 0 °C and subsequently increased to 30 °C and then to 50 °C. The corresponding sensor responses demonstrate the capability of the system to capture thermal variations even in unconventional materials.

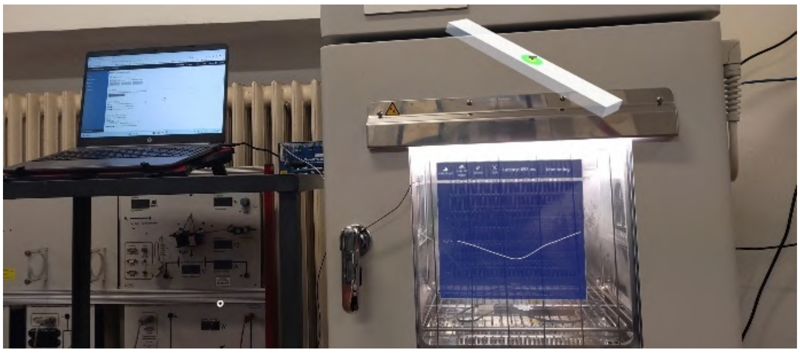

Fig. 11.5 Augmented Reality visualization of thermal variations in a regolith-based specimen during climatic chamber testing.


Fig. 11.6 Augmented Reality visualization of thermal response in a composite laminate with embedded FBG sensor.

| Test | Phenomenon | Key Outcome |
|---|---|---|
| Strain test | Mechanical strain | Clear detection of tension/compression and high repeatability |
| Strain + temperature test | Coupled thermo-mechanical | Simultaneous discrimination of thermal and mechanical effects |
| Composite specimen | Thermal transient | Accurate detection of rapid temperature variations in laminate |
| Regolith specimen | Thermal variation (limited range) | Feasibility demonstrated, with reduced linear range |

Table 11.1 Summary of Augmented Reality validation tests performed on different instrumented systems.

## 11.2 Future Trends

The experimental results presented in this chapter highlight the significant potential of integrating fiber-optic sensing systems with augmented reality technologies. This combination enables not only the generation of complex, multiparametric information but also its intuitive and immediate visualization through an advanced human–machine interface. The laboratory tests validated the entire data chain—from acquisition to transmission and visualization—within a representative operational scenario. These results demonstrate the feasibility of extending the proposed approach to real-world applications, such as in-flight monitoring of UAV systems. Future developments may focus on improving data fusion capabilities, enhancing real-time performance, and extending the visualization framework to support more complex control and decision-making processes.

# Chapter 12

# FBG for UAV Testing: General In-Flight Systems Monitoring

In the previous chapters, the application of the methodologies and technologies developed throughout this work has been presented through controlled laboratory activities. The final part of the work extends such developments to a complete operational case study, tested within a relevant environment, namely in-flight conditions.

The objective of this final phase is to design, integrate, and validate an FBG-based sensing network—characterized by variable complexity—for monitoring the performance of an unmanned aerial vehicle (UAV) during flight, with near real-time data availability. To enable the transition from laboratory experiments to flight testing, the system was designed to satisfy the following key requirements:

- the data acquisition system must be capable of operating onboard the UAV;
- the sensor integration must ensure sufficient robustness and compatibility with manual handling during pre-flight and post-flight operations;
- the sensor positioning, fiber routing, and wavelength allocation must be consistent with both the aircraft geometry and the physical constraints of optical fibers;
- the acquisition system must autonomously store data for post-flight analysis;
- the system must provide a reliable telemetry solution to enable in-flight monitoring.

The flight testing activities followed a modular and system-level approach, with parallel development of sensing, integration, and data management aspects. These activities were conducted within the framework of the *PhotoNext* project (introduced in Chapter 10), in collaboration with the DAUIN Department [108] and the Icarus Polito student team. In particular, DAUIN contributed to the development of the telemetry architecture, enabling near real-time monitoring through both desktop-based applications and augmented reality visualization tools. The Icarus team provided the UAV platforms and supported the experimental campaigns by implementing the required modifications for onboard optical instrumentation.

The overall flight testing campaign extended over more than one year and involved two different aircraft platforms. The first aircraft, named *Anubi*, represented an initial technological demonstrator. The experimental activities conducted with this platform enabled the achievement of the following results:

- monitoring of strain on both upper and lower wing surfaces, with correlation between optical measurements and flight maneuvers through comparison with inertial measurement unit (IMU) data;
- monitoring of airflow temperature and wing skin temperature;
- monitoring of the battery temperature of the propulsion system;
- monitoring of landing gear deformation and identification of the *on-ground/in-flight* state;
- development of a telemetry system for near real-time data visualization through a desktop interface;
- implementation of augmented reality visualization for real-time representation of sensor data.

The flight campaign conducted with *Anubi* clearly demonstrated the potential of embedded optical sensing systems in UAV applications. In particular, it validated the concept of smart structures, where sensing elements are fully integrated within the structure, becoming effectively indistinguishable from it and enabling the structure itself to act as a sensor of its operational state. Furthermore, the experimental results highlighted the possibility of estimating complex flight parameters—such as flight attitude—through strain measurements. This represents a significant step toward the use of optical fibers as a multifunctional sensing platform capable of simultaneously providing thermal and mechanical information. The overall data acquired could represent a fundamental tool for supporting monitoring activities and PHM algorithms for several safety critical components [109, 110]. The informational content is obtained through the fusion of data from distributed optical sensors and traditional onboard instrumentation.

However, the *Anubi* platform also revealed two main limitations of the initial implementation:

- the sensor layout was not fully optimized, limiting the accuracy of attitude estimation;
- the fiber routing was not adequately designed, resulting in complex handling procedures and increased vulnerability of critical components, particularly at fiber–structure interfaces.

To address these limitations, a second platform, named *Sirius "2.0 – photonic"* (to distinguish it from the original non-instrumented version developed by the Icarus team), was designed and implemented. This new configuration introduced several key improvements:

- optimization of sensor number and placement, reducing installation complexity while increasing the amount of extractable information;
- capability to estimate, in real time, vertical acceleration and angular rates (pitch and roll);
- monitoring of aileron deflection during flight maneuvers;
- monitoring of the actuation mechanism of the flight control system, extending the methodology previously demonstrated in Chapter 9 to in-flight conditions.

In the following sections, the ground and flight testing campaigns conducted with the *Anubi* platform are described in detail.

## 12.1 Anubi UAV: Main General Characteristics

The *Anubi* UAV was the first aircraft developed by the Icarus Team for the 2017 edition of the Air Cargo Challenge. The aircraft features a wingspan of approximately 4 m, electric propulsion, and an empty weight of 2 kg. Its main characteristics are summarized below:

- maximum payload capacity of 6 kg;
- high dynamic stability;
- excellent controllability;
- large static margin.

These characteristics enable the aircraft to safely perform moderate acrobatic maneuvers under a wide range of loading conditions. For these reasons, *Anubi* proved to be an ideal platform for experimental research activities. Its high stability and wide flight envelope allow significant variations in flight attitude while minimizing the risk of stall or structural failure—an essential requirement considering the presence of delicate optical instrumentation onboard. As shown in Figure 12.1, the aircraft is predominantly constructed using composite materials, with the exception of the tail section, which follows a more traditional design based on ribs, spars, and stringers made of balsa wood and poplar plywood. The wing is a sandwich structure composed of unidirectional carbon fiber skins and Rohacell foam. A wooden spar reinforced with resin-impregnated Kevlar filaments provides additional structural stiffness. The main geometric characteristics of the aircraft are reported in Table 12.1.

The aircraft features a rectangular fuselage cross-section with rounded edges and a tapered high-aspect-ratio wing equipped with Fowler flaps and winglets. The aerodynamic configuration, combined with the V-tail design, minimizes induced drag while maximizing lift efficiency.

| Property | Value |
|---|---|
| Wingspan | 409 *cm* |
| Wingspan (without winglets) | 383 *cm* |
| Root chord (flap retracted) | 27.5 *cm* |
| Fuselage length | 200 *cm* |
| Maximum height from ground | 32.5 *cm* |
| Aspect ratio | 18.5 |
| Wing surface | 0.829 $m^2$ |

Table 12.1 Main geometrical characteristics of the Anubi UAV.


Fig. 12.1 Anubi UAV platform used for in-flight testing activities.

## 12.2 Fiber Positioning

The sensorization of the *Anubi* platform was carried out in multiple phases, following the progressive development of the project. The first phase of integration was performed during the manufacturing of the wing structure. All sensors were positioned along the main spar, with optical fibers placed at the interface between the spar and the wing skin, as shown in Figure 12.2.

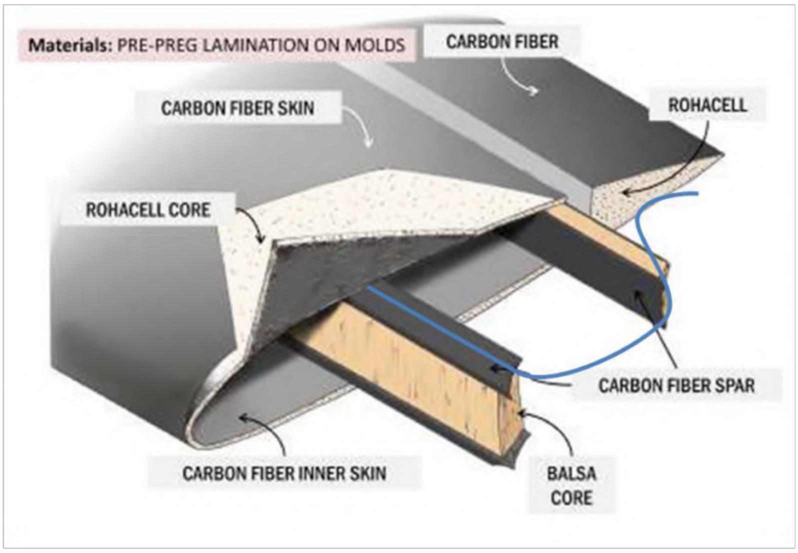


Fig. 12.2 Optical fiber positioning along the main spar of the wing structure.

This configuration offers several advantages. The fiber follows a linear path along a structurally stiff element, minimizing routing complexity. Moreover, the axial deformation of the spar during flight is aligned with the fiber direction, ensuring optimal strain transfer to the FBG sensors. Each semi-wing is composed of two sections: a root section permanently connected to the fuselage and a detachable outer section extending to the wing tip. Sensorization was implemented only on the right semi-wing, including both sections.

In the root section, two optical fibers were bonded to the spar:

- one on the dorsal side (upper surface);
- one on the ventral side (lower surface).

The dorsal fiber was extended to the outer wing section to enable full-span sensorization. At the end of the sensing section, an FC-APC connector was installed and interfaced with a female–female bulkhead adapter. This solution allowed external access to the optical line after wing closure. A mating fiber pigtail was prepared on the outer wing section, enabling connection during assembly. Despite its practicality, the connector region represented the most critical point of the optical system. Once embedded, the fiber cannot be repaired, and any failure near the connector results in the loss of the entire sensing line. The relatively high mass of the connector compared to the fiber introduces additional risks: under vibration or accidental impacts, oscillations may induce shear stress and lead to fiber breakage. Although no failures occurred during the experimental campaign, this configuration highlighted the need for improved mechanical protection and routing strategies, especially in areas exposed to handling or interaction with other onboard systems. In this initial phase, three optical fiber lines were installed:

- one fiber on the dorsal side, equipped with 3 FBG sensors in the root section and 5 additional sensors extending to the tip;
- one fiber on the ventral side, equipped with 3 FBG sensors;
- one fiber dedicated to temperature compensation.

A second phase of sensor integration introduced four additional sensing elements:

- an air temperature sensor developed during laboratory activities;
- a strain sensor bonded to the landing gear;
- a temperature sensor installed on the propulsion battery;
- a temperature sensor integrated into the electronic speed controller (ESC).

This second phase was less invasive, as it relied on already-developed and calibrated sensors. Fiber routing was performed using jacketed patch cords, ensuring mechanical protection and simplifying installation. The landing gear strain sensor was bonded using cyanoacrylate adhesive. The fiber was then protected and routed toward the interrogator using the same approach adopted for temperature sensors.

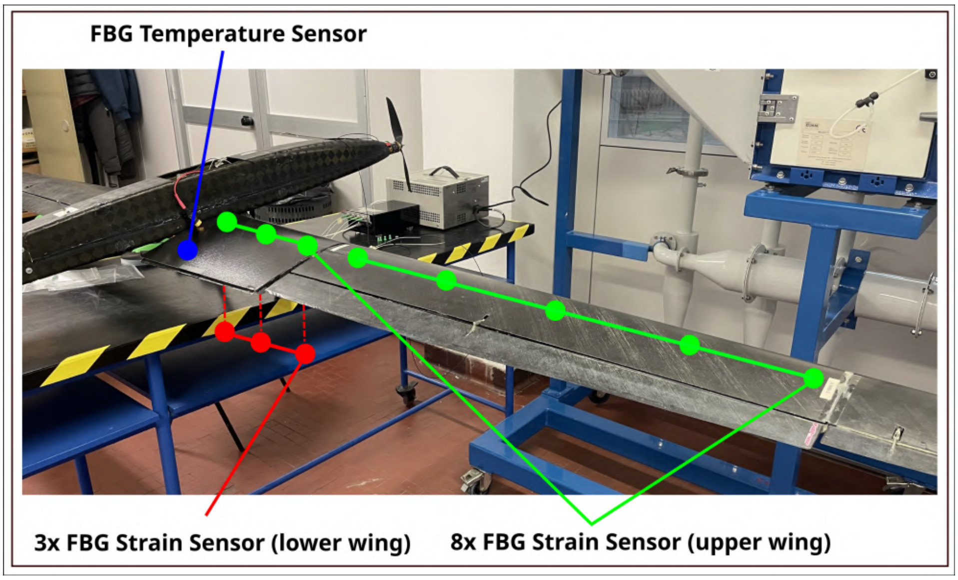


Fig. 12.3 Strain sensor installed on the landing gear structure.

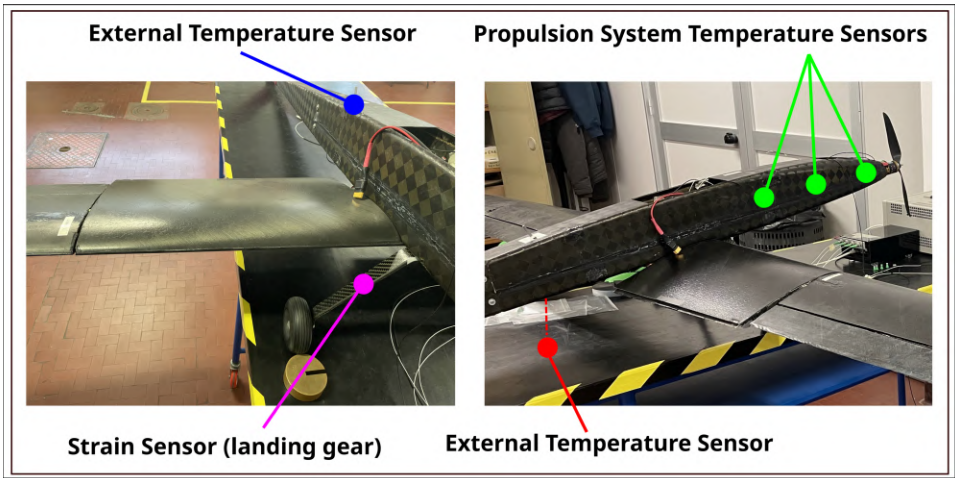


Fig. 12.4 Temperature sensors integrated within the UAV subsystems.

| **Sensor Type** | **Location** | **Quantity** | **Measured Parameter** |
|---|---|---|---|
| FBG strain sensors (dorsal spar) | Upper spar (root + tip section) | 8 | Axial strain (tension) |
| FBG strain sensors (ventral spar) | Lower spar (root section) | 3 | Axial strain (compression) |
| FBG temperature (compensation) | Wing structure | 1 | Temperature (reference for strain compensation) |
| FBG temperature (air) | External airflow | 1 | Air temperature |
| FBG strain (landing gear) | Landing gear leg | 1 | Structural deformation / load state |
| FBG temperature (battery) | Propulsion battery | 1 | Battery temperature |
| FBG temperature (ESC) | Electronic speed controller | 1 | ESC temperature |

Table 12.2 Summary of the FBG sensor network integrated into the Anubi UAV.

## 12.3 Ground Tests

After the aircraft assembly and sensor integration were completed, a dedicated ground testing campaign was carried out to verify the correct operation of all the involved subsystems. For the sake of clarity, this section reports only the tests related to sensor functionality and to the development of monitoring algorithms used for data analysis. However, it is worth noting that the overall campaign also included the verification of the telemetry system performance and of the augmented reality data visualization tools described in the previous chapters. The ground tests performed can therefore be summarized as follows:

- sensitivity tests of the landing gear sensor for the identification of the “on ground / in flight” condition;
- sensitivity tests of the FBG sensors laminated in the wing, aimed at correlating the measured strain with the applied loads;

- tests on the temperature sensors used to compensate the thermal effects affecting the mechanical sensors installed in the wing;
- tests on the temperature sensors integrated into the propulsion system components.

### 12.3.1 Landing Gear

The strain measurement on the landing gear structure was exploited to implement a WoW (Weight-on-Wheels) system capable of determining whether the aircraft is on the ground or in flight. Figure 12.6 shows the measured $\varepsilon$ during a laboratory ground test, in which the UAV was repeatedly lifted and placed back on the ground. As visible in the graph, $\varepsilon$ clearly represents a reliable indicator of the landing gear state (“in flight” or “on ground”). When the aircraft takes off, the strain decreases and reaches a negative peak before stabilizing at a quasi-steady value. The observed delay is most likely due to the sensor installation method: the sensor is attached to the gear leg through an adhesive patch, which introduces a slight viscoelastic effect. Conversely, when the UAV is placed back on the ground, $\Delta\varepsilon$ increases and the signal is dominated by oscillations related to the structural dynamics of the system, including landing gear deformation, tire elasticity, and wing structural response. A first monitoring approach therefore led to the definition of a strain threshold band: within this range the aircraft is identified as “in flight”, whereas values above the threshold correspond to the “on ground” condition (Figure 12.6). As shown in Figure 12.6, a simple function can convert the measured strain directly into the corresponding flight state variable once the threshold values are known. However, considering a sequence of repeated lift–drop maneuvers during ground tests, it becomes evident that the landing dynamics—such as bouncing effects or oscillations induced by wheel–ground interaction—can lead to two possible analysis approaches:

- a highly detailed approach, capable of identifying individual rebounds during landing;
- a global approach, where the system simply detects the transition from “in flight” to “on ground”, regardless of the detailed landing dynamics.

Transitioning from the first approach to the second can be achieved by implementing a counter-based logic. Instead of applying the strain-to-flight-state conversion directly to instantaneous data, the algorithm computes an average over a predefined time window before determining the flight state. As clearly shown in Figure 12.6, this solution effectively filters out the individual bouncing dynamics during landing while still allowing the correct detection of take-off, landing, and potential touch-and-go maneuvers. Naturally, the introduction of a counter-based logic increases the data processing latency, although the delay remains compatible with near real-time operation (typically between 0.1 and 1 s).

Fig. 12.5 Strain signal measured on the landing gear during repeated lift–drop tests.

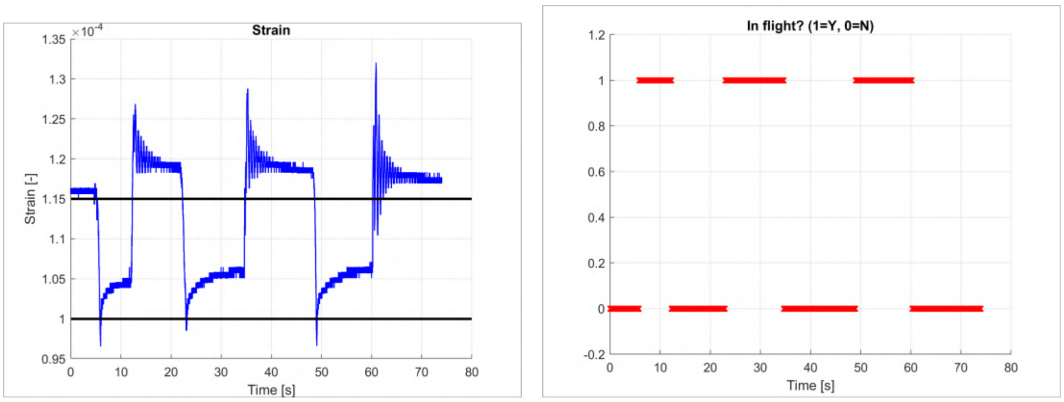


Fig. 12.6 WoW calibration (left) and corresponding binary flight-state output (right).

### 12.3.2 FBG Strain Sensitivity

The second part of the ground testing campaign focused on evaluating the sensitivity of the FBG strain sensors directly integrated into the instrumented semi-wing. The first test phase consisted of repeatedly lifting and lowering the UAV over a period of approximately 20 seconds, initially lifting the aircraft only from the fuselage and allowing it to bounce on the landing gear. Around 40 seconds into the test, Anubi was lifted again, this time by holding the wings instead of the fuselage. The measured trends are shown in Figures 12.9 and 12.10, where the raw FBG signals are normalized in terms of strain. As visible in the plots, the FBG strain sensors integrated in the wing clearly detected the structural dynamics induced by these operations. Both phases are clearly observable: first, the transient associated with the aircraft falling back onto the landing gear, and subsequently the significant deformation induced when the UAV was lifted directly from the wings. As expected, the three sensors installed on the lower wing surface measured tensile strain, while the eight sensors located on the upper wing surface measured compressive strain.

The measured data demonstrate the extremely high sensitivity of the sensors to structural deformation, with an almost instantaneous mechanical response time and the absence of disturbance or hysteresis effects. For this reason, it was possible to quantify the correlation between the measured strain and the vertical load acting on the semi-wing. Assuming that the structure operates entirely within the elastic regime, where loads and deformations are directly proportional, let $\varepsilon \in \mathbb{R}^n$ be the vector of measured strains and $\mathbf{L} \in \mathbb{R}^k$ the vector of load entities. The structural direct model can be written as:

$$\varepsilon = A\mathbf{L} \tag{12.1}$$

where $A \in \mathbb{R}^{n \times k}$ is the influence matrix describing the strain distribution generated by each unit load entity.

When the number of measurements is at least equal to the number of independent loads ($n \geq k$) and matrix $A$ has full rank, the loads can be estimated through the inverse model obtained via least-squares inversion:

$$\mathbf{L} = (A^T A)^{-1} A^T \varepsilon. \tag{12.2}$$

If the only load entity considered is the vertical load $F_v$, the model simplifies to:

$$\varepsilon = \mathbf{a}F_v \tag{12.3}$$

with $\mathbf{a} \in \mathbb{R}^n$.

If $n \geq 1$ and the structure has been properly calibrated, the load value can be estimated through least-squares inversion:

$$F_v = (\mathbf{a}^T\mathbf{a})^{-1}\mathbf{a}^T\varepsilon. \tag{12.4}$$

For the experimental calibration, the UAV was positioned on a flat support (Figure 12.7) with the wings turned upside down. After recording the baseline strain values in the unloaded configuration, two load steps were applied symmetrically to both semi-wings, and the resulting strain values were acquired. By iteratively repeating the procedure, it was possible to empirically determine the numerical correlation between the measured strain and the applied load. To verify the validity of this approach, the UAV was lifted again from the wings while recording the strain data and converting them into vertical force (lift). The estimated lift resulted in approximately 37 N total (18.5 N per semi-wing), corresponding to a mass of 3.8 kg. The actual UAV mass measured with an electronic scale was 3.9 kg. To summarize, the empirical coefficients used for the load–strain correlation allowed an accurate estimation of the aircraft total weight, supporting the hypothesis that the same methodology could be applied during flight.

Fig. 12.7 Experimental setup for load–strain calibration.

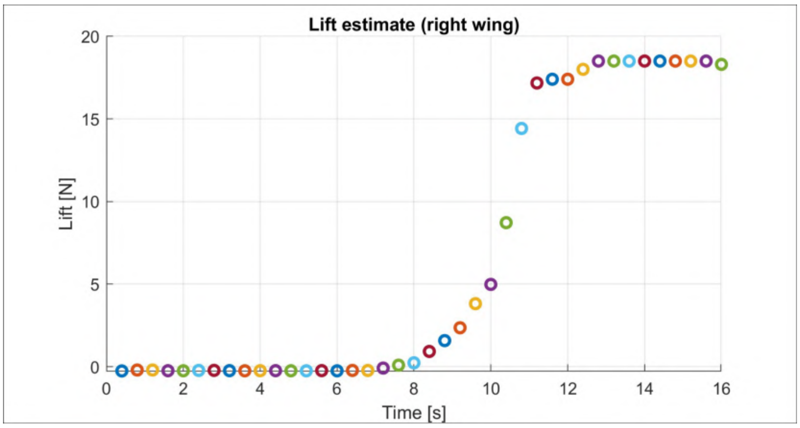


Fig. 12.8 Lift estimation based on FBG measurements.

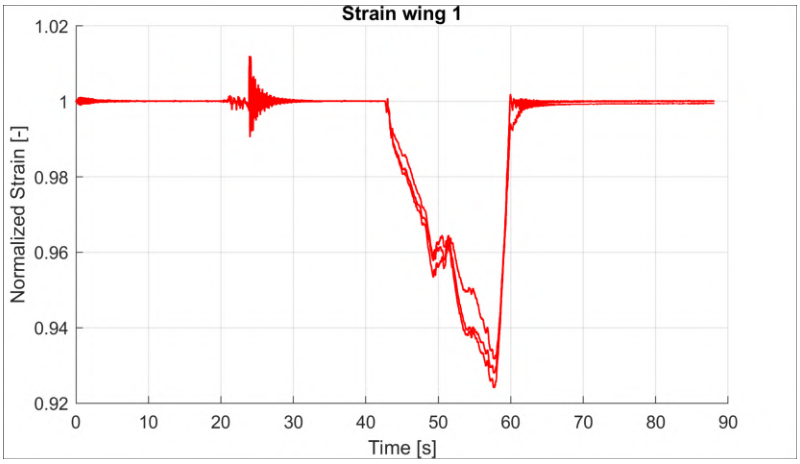


Fig. 12.9 Strain measurements – upper wing surface.

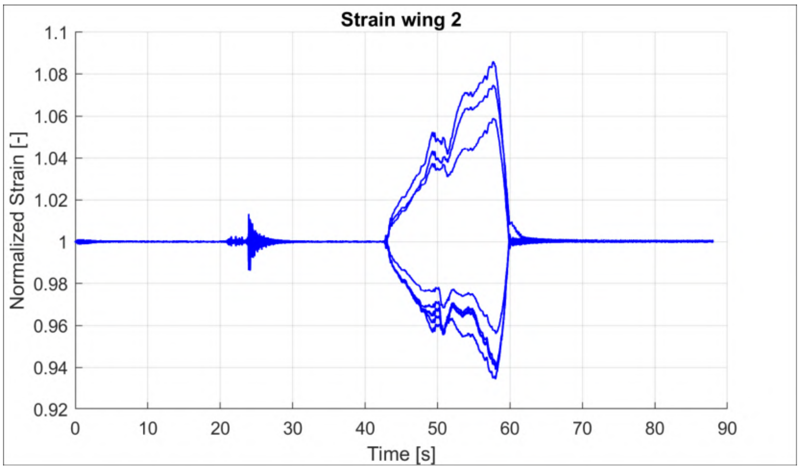


Fig. 12.10 Strain measurements – lower wing surface.

### 12.3.3 Thermal Tests

The Anubi structure was also instrumented with several sensors dedicated exclusively to temperature measurement. In particular, the following sensors were installed:

- a temperature sensor integrated inside the wing;
- a temperature sensor installed externally on the fuselage;
- a temperature sensor mounted on the Electronic Speed Control (ESC) of the propulsion system;

- a temperature sensor mounted on the propulsion battery.

The sensor integrated inside the wing structure was verified to operate correctly under ambient conditions and, more importantly, to exhibit an almost constant value during the mechanical tests described in the previous section. Its implementation is extremely simple, as the sensing section is neither bonded nor mechanically constrained to the structure. The external fuselage temperature sensor corresponds exactly to the sensor designed, developed, and tested in Chapter 4. Therefore, no additional activity was required apart from verifying its correct operation after routing the fiber inside the fuselage. The two temperature sensors installed on the battery and the ESC were realized following the procedure described in Chapter 4. Before describing the test results, it is important to recall that the propulsion system of Anubi represents the most critical subsystem from a thermal monitoring perspective. Since the propulsion is entirely electric, uncontrolled overheating phenomena may represent precursors of safety-critical failures capable of compromising the control of the aircraft. The proposed sensing approach offers significant advantages compared to traditional technologies. Optical fibers can be placed directly in contact with the battery surface and integrated onto the ESC without introducing electromagnetic interference or disturbances. This enables accurate, stable, and reliable temperature measurements, even in proximity to safety-critical components.

Figure 12.11 illustrates the functional scheme of the instrumented propulsion system. The main components are:

- AXI 2826/10 GOLD LINE V3 electrical motor: a brushless motor with neodymium magnets and a rotating case, designed to provide extremely high torque and allowing large-diameter propellers to be driven without the need for a gearbox;
- FullPower PRO 85A SBEC Electronic Speed Control (ESC): an electronic circuit that regulates the speed of an electric motor by controlling the current flowing through the motor windings. It may also provide reversing capability and dynamic braking;
- WELLPOWER LiPo ULTIMA 5200 mAh / 11.1 V 3S 35/70C supply battery pack: a lithium-polymer rechargeable battery providing electrical energy to the ESC. LiPo batteries offer higher specific energy compared to other lithium

technologies and are widely used in applications where weight is a critical constraint.

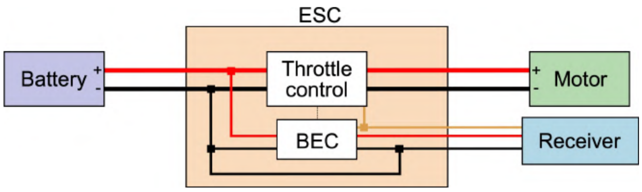


Fig. 12.11 Scheme of Anubi Propulsion System.

It is immediately evident that all three components are safety-critical subsystems. For each of them, continuous and localized temperature monitoring can be extremely valuable for the development of more advanced, reliable, and safe UAV systems. In the present work, only the battery and ESC were instrumented for safety reasons. In both cases, sensor integration can be performed in a minimally invasive manner by simply placing the optical sensor in contact with the component surface. Instrumenting the motor would instead require integrating the optical fiber directly inside the motor housing. Since the propulsion system uses a commercial off-the-shelf motor and this motor represents the only propulsion source of the UAV, it was considered unsafe to modify it for sensor integration during the flight campaign. The integration procedure for motor instrumentation requires the development of dedicated integration, testing, and data analysis procedures. These activities were partially investigated through the development of a dedicated test bench but have not yet reached the maturity level required for flight integration. The thermal sensors installed on the ESC and the battery were realized according to the procedure previously described in Chapter 4 and bonded to the respective component surfaces. The test was conducted by anchoring the UAV to the ground and commanding the propulsion system using throttle profiles similar to those typically experienced during flight. In particular, throttle peaks of approximately $80-90\%$ — representative of take-off, go-around, or demanding maneuvers—were alternated with throttle levels around $50-60\%$, typical of standard cruise conditions. The results of the tests are shown in Figure 12.12. The following observations can be made:

- within a few minutes, the ESC temperature increases by approximately 35°C;
- during the same time interval, the battery temperature increases by approximately 5°C;

- the cooling phases are dominated by the thermal inertia of the individual components.

A particularly interesting aspect emerges when comparing ESC and battery temperatures not only in terms of absolute temperature increase but also in terms of relative overheating with respect to the expected maximum values. Comparing the results of the three tests performed, a consistent repeatability of the maximum temperature values can be observed under equivalent operating conditions. Furthermore, both monitored components reach their maximum temperature at approximately the same rate.

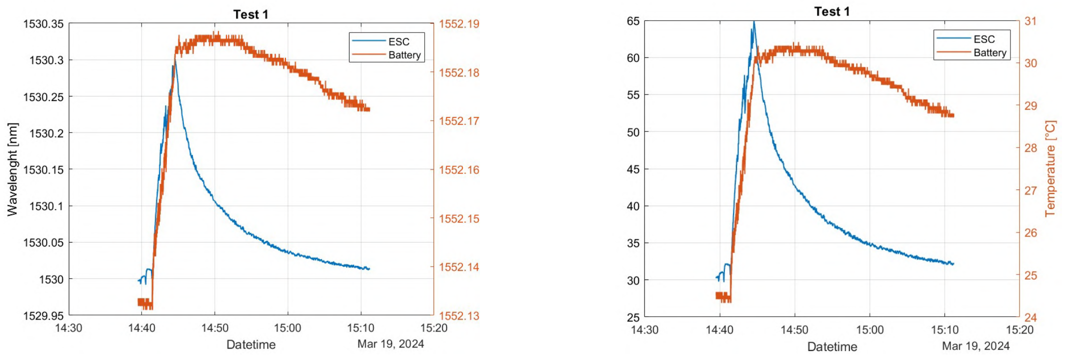


Fig. 12.12 Thermal response of ESC and battery under controlled throttle conditions.

This behavior is consistent with the architecture of the propulsion system, where ESC and battery are connected in series and therefore subjected to the same current $I$. In both components, the temperature increase measured by the sensors is proportional to the dissipated power:

$$P = I^2 R_{int} \tag{12.5}$$

where $R_{int}$ represents the internal resistance of the component.

The performed tests therefore demonstrate the strong potential of the proposed approach: a simple, integrated monitoring system based on optical sensing principles, capable of providing real-time information on the thermal behavior and potential degradation of critical propulsion system components, provided that appropriate datasets are available for interpretation.

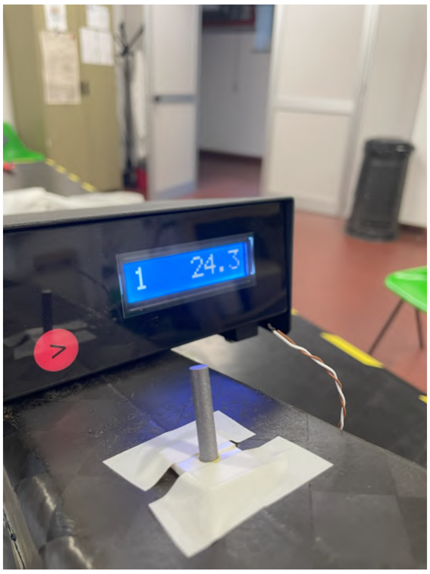


Fig. 12.13 External temperature sensor installation.

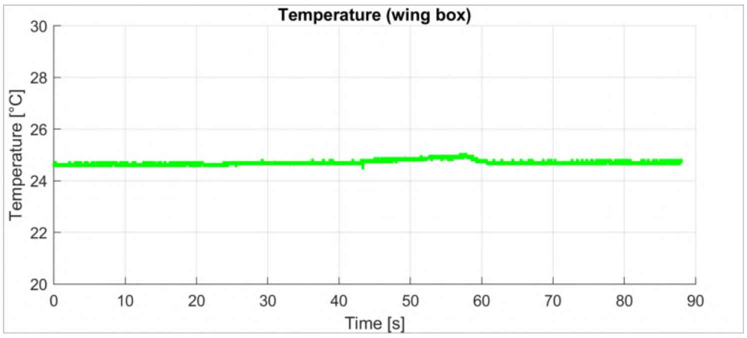


Fig. 12.14 Wing temperature sensor calibration.

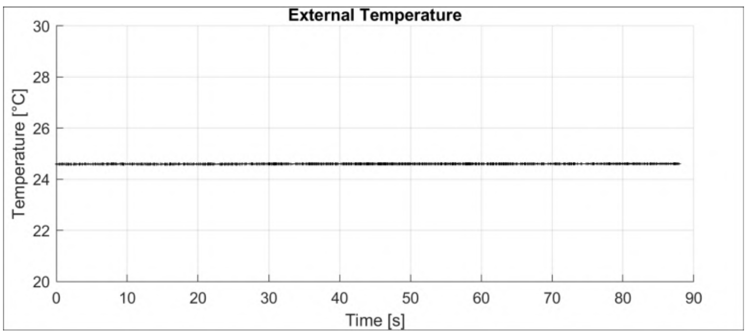


Fig. 12.15 External temperature calibration.

| **Test Category** | **Objective** | **Method** | **Key Outcome** |
|---|---|---|---|
| Landing gear (WoW) | Detect flight state (ground / air) | Repeated lift–drop cycles, strain threshold + averaging | Reliable WoW detection; filtering reduces bounce-induced noise |
| Wing strain sensitivity | Correlate strain to applied load | Manual lifting (fuselage / wings) + calibrated load steps | Linear strain–load relation; lift estimated with ∼3% error |
| Load reconstruction model | Estimate vertical load from strain vector | Least-squares inversion of $\varepsilon = A\mathbf{L}$ | Robust load estimation enabled by distributed sensing |
| Thermal compensation (wing) | Validate temperature reference stability | Monitoring during mechanical tests | Stable signal; negligible thermal drift on strain measurements |
| External temperature sensor | Validate environmental measurement | Ambient testing after installation | Correct operation; ready for in-flight monitoring |
| ESC thermal test | Evaluate propulsion overheating behavior | Controlled throttle cycles (50–90%) | Rapid heating (+35°C); repeatable trends |
| Battery thermal test | Assess battery thermal response | Same throttle profile as ESC | Moderate heating (+5°C); consistent behavior |
| Propulsion system analysis | Correlate thermal response to electrical load | Comparison ESC vs battery | Consistent with $P = I^2R$ dissipation model |

Table 12.3 Summary of ground testing activities and main results for the Anubi UAV.

## 12.4 Final System Arrangement before Flight Testing

The core of this study is represented by the flight testing activities, which include all operations ranging from the preparation and transportation of the required equipment to the flight field, up to the disassembly and storage of the instrumentation at the end of the testing campaign. The operations are organized into several phases following a well-defined sequence, progressively refined and validated throughout the development of the experimental campaign.

A flight test can be considered correct and valid only if all procedures are properly executed and the resulting data are consistent and reliable. The procedures described below are the result of an iterative process of optimization and standardization, aimed at improving both time efficiency and operational effectiveness. Before reaching the flight field—especially when complex experimental activities are planned—it is advisable to prepare a checklist including all the materials required to complete the operations. In particular, it is essential to bring equipment for possible repairs, as well as spare components for the parts of the aircraft most subject to wear. In the present case, the required equipment included toolboxes, multimeters, various types of electrical batteries, soldering equipment, computers and related cables, monitors, and additional support devices. This preparation phase is essential to ensure the safety and reliability of the operations. Before starting the assembly procedure, a visual inspection must be performed on each structural component of the aircraft—such as wing sections and tail surfaces—which are transported disassembled. This inspection aims to identify possible structural irregularities or damage prior to assembly. The assembly phase consists of connecting the wing sections and attaching the tail surfaces to the fuselage. The joints between structural elements are sealed using adhesive tape, which serves a dual function: preventing separation of the components and smoothing the junction edges by sealing small gaps, thereby improving aerodynamic performance. The cables controlling the tail control surfaces and the extension connectors for the servo motors are then connected and secured using adhesive tape or dedicated locking systems. At this stage, the propulsion battery can be installed in the front compartment of the fuselage, immediately behind the firewall bulkhead where the motor is mounted.

The loading procedure of the *payload* (i.e., the monitoring system) must be carried out carefully due to the limited space available inside the fuselage. First, the battery supplying power to the monitoring system is inserted into the fuselage section located ahead of the wing leading edge. A Y-shaped cable is connected to the battery to simultaneously power both the onboard computer and the interrogator. The interrogator is then placed inside the central payload compartment. Particular care must be taken to position it on a soft support base—in this case, a custom-shaped foam padding was used. The interrogator power cable and the Ethernet cable required for communication with the onboard computer are then connected. Due to its dimensions, the onboard computer must be installed on the dorsal side of the fuselage, approximately at the wing trailing edge location. A generous amount of adhesive tape is used to secure the device and prevent movement or accidental detachment during flight.

Once the aircraft is fully assembled and the *payload* installed, the power-up sequence can begin. Together with the SmartScan interrogator, the onboard computer is powered on. To start the required software applications, the onboard computer must temporarily be connected to a monitor, keyboard, and mouse. This procedure allows the operator to launch the data acquisition software, establish the connection with the remote server at the Politecnico, and verify that all optical fibers correctly transmit signals from the installed sensors.

Once the monitoring system is active, the aircraft control system can be powered on. In this phase, it is mandatory to first switch on the radio transmitter and only afterwards power the onboard electronics, in order to prevent unintended motor activation or abnormal servo behavior. Before activating the onboard electronics, the calibration of the flight control system must be performed. After calibration, it is verified that all control surfaces move correctly and that the motor is properly armed and operational. If required, one or more *action cameras* can be installed on the aircraft to provide visual feedback of the flight operations, with a reference aligned to the aircraft body axes. These cameras are generally positioned as close as possible to the aircraft center of gravity, although they may also be mounted on the tail boom. This flexibility is allowed because most of the payload is concentrated in the front section of the fuselage.

Before moving the aircraft to the runway, the ground station must be activated. On a separate ground computer, the secondary receiver and the Arduino-based system are powered on to record control input signals, and data acquisition is started using the *PLX-DAQ* software. At this point, the aircraft can be moved to the runway. Once the aircraft is positioned at one of the runway thresholds, the recording of the *action cameras* is started and the pilot moves to the designated pilot area beside the runway.

The flight tests were conducted at the A.S.D. “Volare su Tetti” flying field in Tetti Neirotti. The facility includes two parallel runways of different lengths; the one used for the experiments is described below. The runway is approximately 150 m long—of which about 120 m are usable for take-off and landing—and its width varies between 20 and 35 m. The surface is entirely grass-covered and oriented along heading 03/21. It also presents a slight slope of approximately 1–1.5 m along the direction of runway heading 03. At the threshold corresponding to runway 03 there is a perimeter fence, as well as along the side of the runway adjacent to the parking area. The facility also includes a covered structure equipped with photovoltaic panels connected to a 12/24 VDC power system. This infrastructure enables the use of dedicated Li-Po battery chargers. An inverter was required to convert the 12 V direct current into 230 V alternating current to power the laptops used in the ground control station.

Fig. 12.16 Pre-flight preparation and payload integration of the Anubi UAV.

## 12.5 Telemetry and Data Acquisition System

The telemetry systems employed during the flight testing campaigns correspond to those described in Chapter 10. In summary, two different configurations were developed:

1. a telemetry system based on a Raspberry Pi and a dedicated *middleware* software;
2. a telemetry system based on a mini-PC, with data acquisition performed through the *Smart Soft* software.

The first configuration was adopted during the initial flight tests in order to acquire the raw optical response of the FBG sensors under flight conditions. Moreover, this solution enabled a simpler integration with the augmented reality visualization system. The second configuration, on the other hand, was employed in more advanced flight tests involving integrated functional monitoring of multiple subsystems, including the wing semi-span structure, the propulsion system, and the landing gear.

In order to fully characterize the sensor response during flight operations, it was considered essential to record the control inputs provided by the pilot during flight maneuvers. The collaboration with the Icarus team and, in particular, with the UAV pilot, enabled the development of a prototype system for tracking pilot control commands. Since the UAV used in this study is a radio-controlled aircraft, the pilot's control system does not natively provide any means of recording the control inputs applied through the transmitter sticks. This limitation is particularly critical for commands associated with control surface deflections and propulsion throttle. The developed acquisition system was designed to operate without any modification to the aircraft and without increasing its onboard mass or volume. The system is based on an *Arduino UNO* microcontroller and acquires six radio channels corresponding to the ailerons, the V-tail control surfaces, and the motor throttle. The signals received from the radio receiver consist of standard PWM pulses, whose width is proportional to the stick position. However, due to hardware limitations of the microcontroller, it was not possible to accurately read all channels simultaneously using direct digital measurements. To overcome this limitation, an analog acquisition strategy was implemented. Each PWM signal is filtered through an RC circuit, converting the pulse-width modulation into a continuous voltage proportional to the duty cycle. This approach allows the Arduino to acquire six analog voltage signals with reduced computational load and improved stability. To avoid any onboard installation, a secondary radio receiver was placed on the ground and connected to the acquisition system. This receiver was configured in broadcast mode so as not to interfere with the primary receiver used for UAV control. The acquired signals are transmitted via serial communication to a ground computer and recorded in real time in `.csv` format, with a sampling frequency of approximately 28 Hz. Since the analog readings depend on the supply voltage, a preliminary calibration procedure was required in order to correlate the measured voltage levels with the actual angular deflections of the control surfaces.

## 12.6 Flight Testing Data

The flight testing campaign was carried out over several experimental sessions at the "Volare su Tetti" flying field located in Tetti Neirotti. The facility includes two parallel runways of different lengths; the one used for the experimental activities is described below.

The runway is approximately 150 meters long—of which about 120 meters are effectively usable—and its width varies between 20 and 35 meters. The surface is entirely grass-covered and oriented along heading $03/21$. The runway also features a slight slope of approximately one to one and a half meters when moving in the direction of runway 03. At the threshold corresponding to runway 03 there is a perimeter fence, as well as along the side of the runway adjacent to the parking area.

The facility also includes a covered structure equipped with photovoltaic panels connected to a $12/24VDC$ power system. This infrastructure enables the use of dedicated chargers for Li-Po batteries, such as those installed onboard the UAV. An inverter was required to convert the $12V$ direct current into $230V$ alternating current in order to recharge the computers used in the ground control station.

In this section, the results obtained from the flight tests are presented according to the following logical structure:

- sensitivity and significance of the raw strain data measured by the sensors;

- capability of the system to provide near real-time telemetry, including augmented reality visualization;
- capability of the landing gear sensor to determine the “in flight” and “on ground” states;
- capability of the system to perform thermal monitoring of the propulsion battery and ESC during flight.

Fig. 12.17 Anubi UAV during steady flight.

Fig. 12.18 Touch-and-go maneuver during flight testing.

Fig. 12.19 Landing phase of the UAV.

Fig. 12.20 Onboard camera view during flight.

### 12.6.1 Raw Data Acquisition from Laminated Sensors

Figure 12.21 shows a typical signal trend measured during a flight test. Even a qualitative inspection of the raw data highlights both the richness of the information content and the high quality of the acquired measurements.

The most evident feature is the identification of the flight phase, which clearly appears as a step variation in the optical signal associated with the generation of aerodynamic lift. It is also possible to distinguish between the sensors installed on the upper wing surface (dorsal side), which experience compressive strain, and those installed on the lower surface (ventral side), which experience tensile strain. This behavior is consistent with the expected bending response of the wing and is further emphasized by the symmetric placement of the sensors.

Moreover, the distribution of sensors along the wing spar enables a detailed observation of the strain variation as a function of the distance from the wing root. This level of spatial resolution, combined with the high measurement accuracy, allows the sensing system to be interpreted as a distributed and continuous source of structural information.

Such datasets can therefore be used to feed advanced algorithms for data fusion, virtual sensing, and continuous comparison with expected deformation fields derived from numerical structural models.

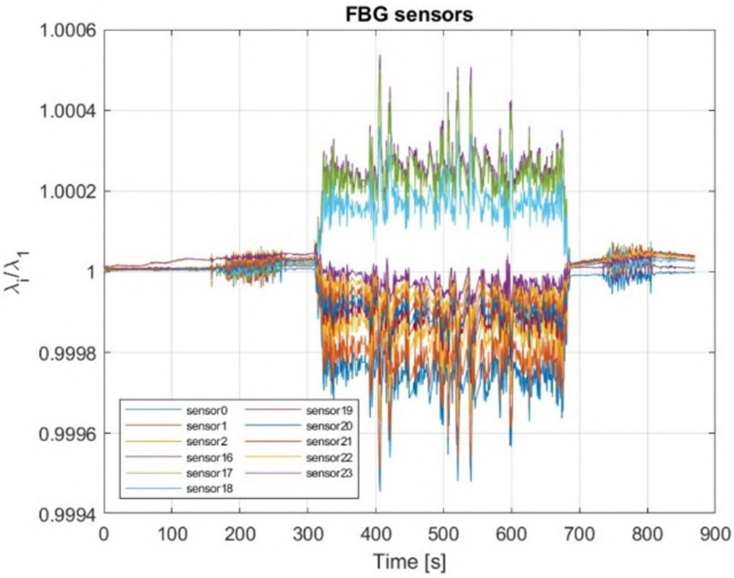


Fig. 12.21 Example of raw strain data acquired during flight.

## 12.6.2 Near Real-Time Data Visualization

In parallel with the assessment of data quality, the flight tests performed with Anubi allowed the validation of the implemented telemetry systems. Both configurations demonstrated their capability to operate in real flight conditions, as described in Chapter 10.

The HoloLens headset was used by a co-pilot observing the UAV operations and enabled near real-time visualization of the sensor wavelength signals, with a latency ranging between 200 and 1000 ms. For practical purposes, the displayed signal corresponded to a filtered version of the raw optical data.

The use of augmented reality enabled the validation of a first proof-of-concept of the proposed monitoring approach. On one side, embedded optical sensors allow the UAV structure itself to act as a sensing system capable of measuring its own operational conditions. On the other side, the AR interface introduces a novel paradigm for human–machine interaction directly integrated into the operator's field of view.

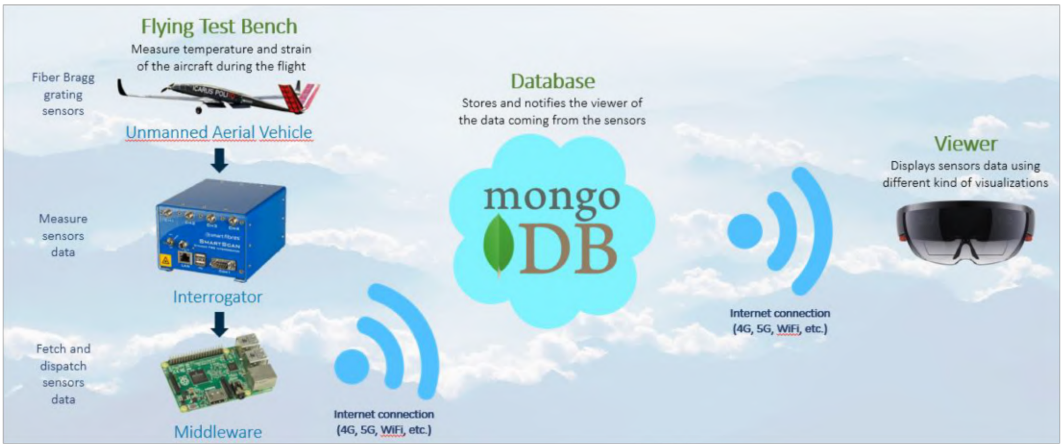


Fig. 12.22 Augmented reality telemetry visualization.

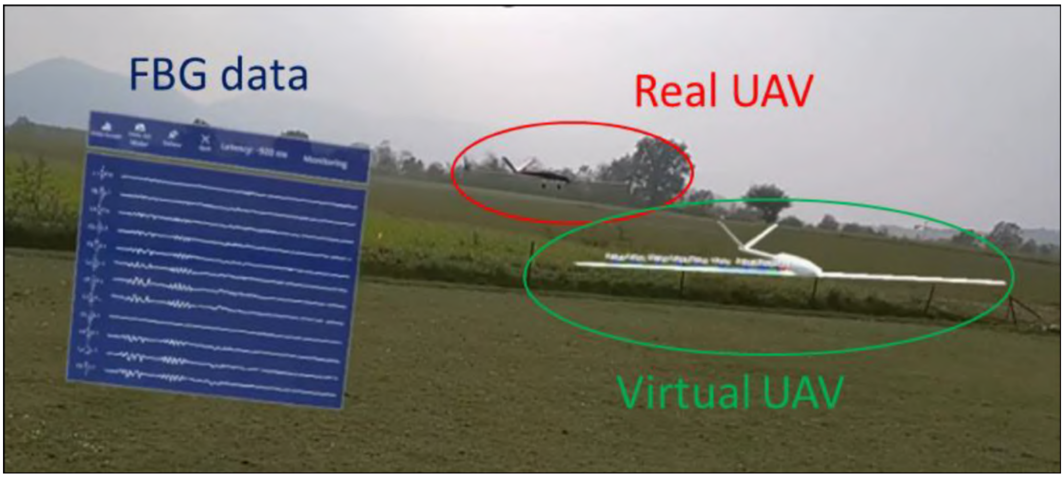


Fig. 12.23 Example of AR-based visualization during flight operations.

The availability of large amounts of data enables the monitoring of complex systems, whose performance parameters—once properly processed—can be presented to the operator in an intuitive and immediately interpretable form. This approach has the potential to significantly improve situational awareness and operational safety, particularly in demanding scenarios such as low-visibility conditions or safety-critical missions.

The tests successfully validated the entire measurement chain, including data acquisition, wireless transmission, and visualization. Further developments are required to transition toward industrial applications, particularly in the design of advanced data fusion algorithms and user-oriented visualization interfaces.

### 12.6.3 Data Sensor Fusion for UAV Monitoring

Since the sensors were installed only on one semi-wing, a complete reconstruction of the global aerodynamic behavior of the aircraft is not possible. Nevertheless, the reliable estimation of the load acting on the instrumented semi-wing, combined with onboard avionics data, enables a first meaningful validation of the proposed monitoring methodology.

Figure 12.24 reports the following monitored quantities:

- ambient temperature;
- ESC temperature;
- battery temperature;
- flight state.

The analysis of the collected data shows a strong consistency with the results obtained during the ground testing campaign. In particular, the ambient temperature is correctly detected both by the external sensor and by the sensor embedded within the wing structure. Minor discrepancies between sensors are attributable to different irradiation and exposure conditions.

The temperatures measured on the ESC and on the battery are also consistent with the ground test results, confirming the reliability of the thermal monitoring approach. This opens the possibility of future developments, such as indirect estimation of current consumption and battery state-of-charge based on thermal measurements.

The landing gear sensor also confirmed its capability to correctly identify “on ground” and “in flight” states during dynamic flight conditions, including touch-and-go maneuvers.

Finally, the most relevant result is represented by the data fusion between the strain measurements and the onboard inertial platform. The adopted control logic includes the following steps:

- acquisition and storage of raw IMU and FBG data;
- filtering of IMU signals to remove background noise;

- filtering of optical data and conversion into vertical load estimation;
- estimation of the load factor through normalization with respect to aircraft weight;
- fusion of the two signals through a complementary filter to improve robustness.

The resulting fused signal is shown in Figure 12.26.

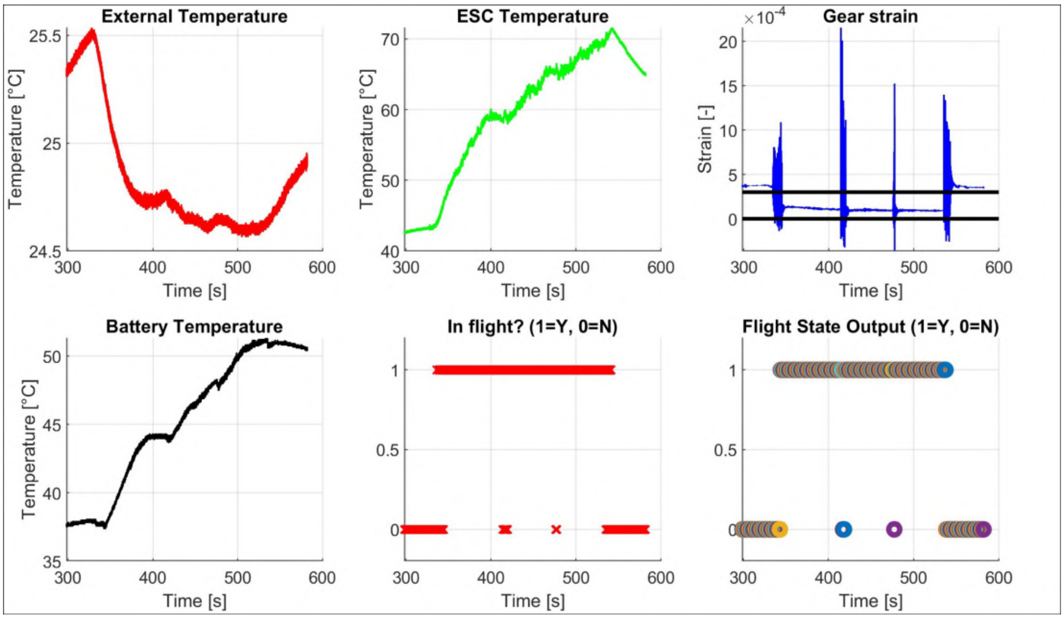


Fig. 12.24 In-flight monitoring of thermal parameters and flight state.

Overall, the results obtained during the flight testing campaign demonstrate the strong potential of the proposed approach. The integration of fiber-optic sensing within the UAV structure enabled the acquisition of high-quality, distributed and multi-functional systems measurements under real operational conditions, confirming both the robustness of the sensing technology and its compatibility with flight environments.

The capability to combine optical measurements with onboard avionics data through sensor fusion techniques further highlights the possibility of extracting meaningful and operationally relevant information from the system. In particular, the estimation of structural loads, the identification of flight states, and the monitoring of thermal conditions represent a significant step toward the development of intelligent, self-monitoring aerospace structures. These results validate the feasibility of the

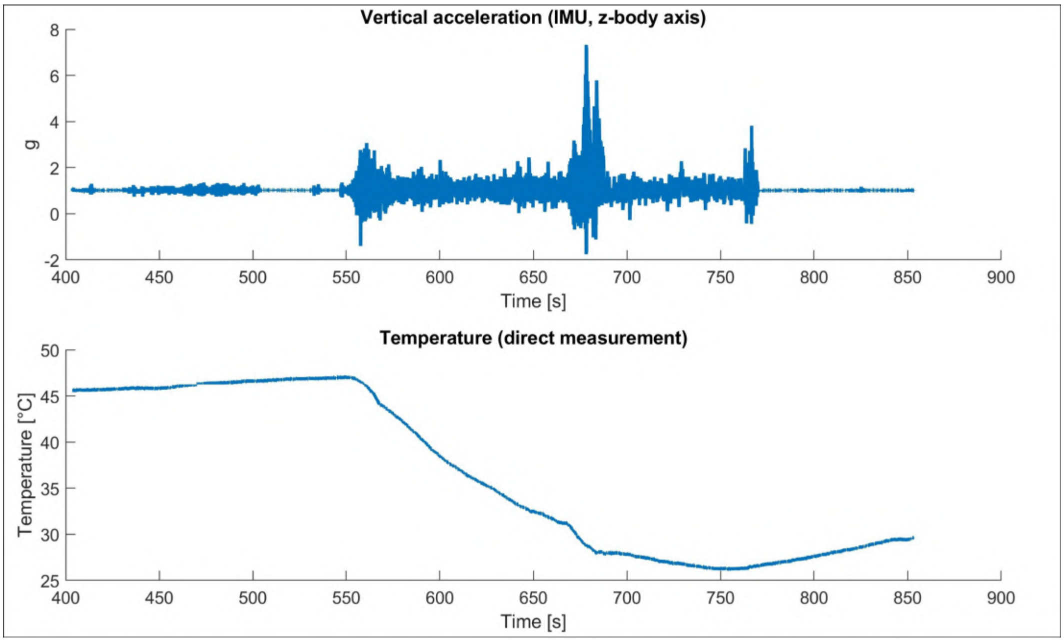


Fig. 12.25 IMU data acquired during flight.

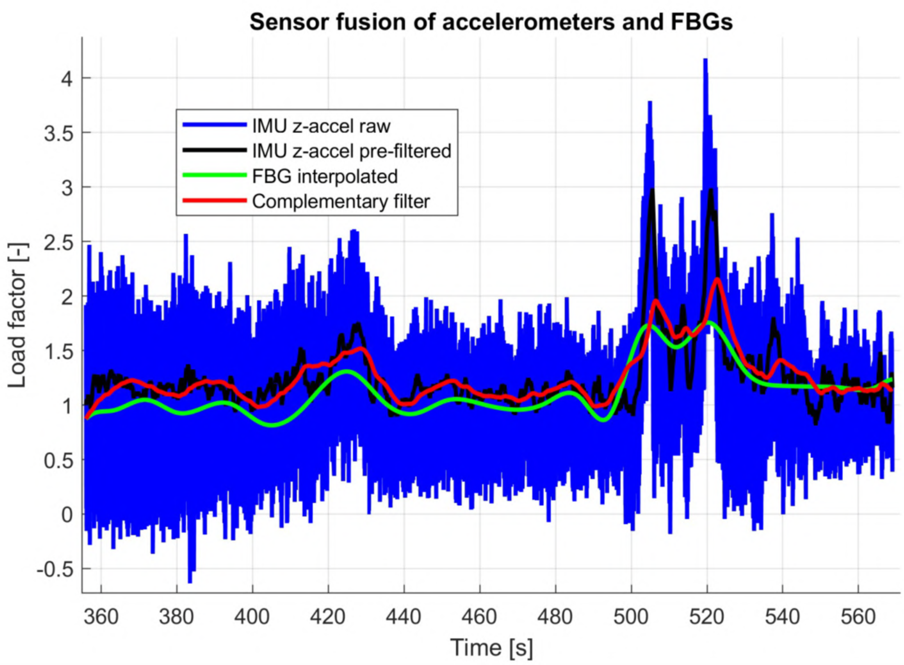


Fig. 12.26 Result of sensor fusion between IMU and FBG data.

proposed methodology as a foundation for next-generation monitoring systems, while also providing clear indications on the aspects that require further improvement and optimization.

## 12.7 Limitations of Anubi and Requirements for Sirius

Despite the promising results obtained during the flight testing campaign, several limitations and open issues were identified, providing important guidelines for future developments. A first limitation concerns the spatial distribution of the sensors along the wing. The adopted layout is inherently asymmetric, as sensors were installed only on one semi-wing. Moreover, the positioning was not fully optimized in terms of redundancy and spatial coverage. This configuration limits the possibility of reconstructing the complete aerodynamic and structural behavior of the aircraft and reduces the robustness of the estimation algorithms in the presence of local disturbances or sensor faults. A second critical aspect is related to the accessibility of the onboard systems. The integration of the optical fibers and of the associated instrumentation resulted in a complex internal layout, making pre-flight and post-flight operations time-consuming and increasing the risk of accidental damage during handling. This issue is particularly relevant for connectors and fiber routing within confined fuselage compartments. Furthermore, the overall structure and sensorization strategy lack modularity. The integration process was strongly dependent on the specific geometry of the aircraft and required invasive installation procedures, especially for the sensors embedded within the wing structure. As a consequence, maintenance, replacement, or reconfiguration of the sensing system is not straightforward. Finally, from a methodological perspective, a key open point is the need to explicitly estimate critical flight parameters directly from the optical measurements. While the current approach demonstrates the feasibility of correlating strain measurements with flight conditions through data fusion with onboard avionics, a fully autonomous estimation based solely on fiber-optic data has not yet been achieved. The development of dedicated algorithms capable of extracting quantities such as load factor, attitude, or aerodynamic states directly from FBG measurements represents a fundamental step toward the realization of fully self-sensing structures. Addressing these limitations will be essential for the transition from a proof-of-concept demonstrator to a robust and scalable monitoring system suitable for real-world aeronautical applications.

| **Identified limitation (Anubi)** | **Proposed improvement (Sirius)** |
|---|---|
| Asymmetric and non-optimized sensor distribution limited to a single semi-wing | Optimized and symmetric sensor layout, designed to maximize spatial coverage and redundancy, enabling improved load reconstruction and robustness |
| Limited correlation between different sensors and overall logic control for system monitoring | Fibers and sensors placement fulfill a mechanical logic for high-level performance monitoring |
| Difficult access to onboard systems and fragile fiber routing | Redesign of fiber routing and connector interfaces to improve accessibility, robustness, and ease of maintenance |
| Low modularity of the sensing architecture and invasive integration procedures | Development of a modular sensor integration strategy allowing easier installation, replacement, and scalability across different platforms |
| Dependence on external avionics for flight parameter estimation (sensor fusion required) | Development of dedicated algorithms for direct estimation of flight parameters (e.g., load factor, attitude) using only FBG measurements |

Table 12.4 Summary of limitations identified in the Anubi platform and corresponding improvements targeted in the Sirius “2.0 – photonic” development.

# Chapter 13

# FBG for Flight Testing: Smart Structures for Navigation Control

The positive—although still not fully mature—results obtained during the flight testing campaign with the Anubi platform highlighted the need for a new UAV specifically designed to support the integration of a fully distributed optical sensing network. Building upon the experience gained, a second platform was therefore identified and adapted to overcome the limitations previously observed.

The close collaboration with the ICARUS PoliTO team, together with their consolidated expertise in the design and operation of high-performance model aircraft, led to the selection of their latest UAV platform as the reference system for this phase of the work.

The selected aircraft, named *Sirius* (Figure 13.1), was developed for the 2024 edition of the Air Cargo Challenge, held in Aachen in July of the same year. The Air Cargo Challenge is a biennial international competition involving university teams worldwide, focused on the design, manufacturing, and flight testing of radio-controlled aircraft for payload transport missions. Each edition introduces a new mission profile and a dedicated set of constraints, requiring the development of a completely new aircraft configuration. Performance is evaluated based on transported payload, energy efficiency, mission execution time, and take-off distance, under strict limitations on propulsion system current consumption.

Sirius was designed as a fixed-wing composite UAV, with extensive use of carbon fiber materials, optimized to maximize payload capacity while complying with the imposed current limit of 30 A. The 2024 competition mission required the transport of billiard balls, with scoring based on payload mass, execution speed, and overall efficiency, including a bonus for take-offs shorter than 40 m.

From a geometric and aerodynamic standpoint, Sirius is a low-wing UAV configuration, a choice driven by the need to facilitate payload loading and unloading operations within the cargo bay. The aircraft features an aspect ratio of approximately 11, selected as a compromise between aerodynamic efficiency and structural constraints. It is equipped with slotted flaps, enabling take-off within 60 m under the propulsion conditions adopted during the competition. The propulsion system consists of a single nose-mounted electric motor (T-Motor AT2826 900KV), powered by a three-cell lithium-polymer (LiPo) battery with a nominal voltage of 11.1 V. The system is completed by a tractor propeller with an 11-inch diameter and 7-inch pitch, capable of delivering approximately 12.5 N of static thrust. During operation, the motor was current-limited to ensure compliance with the 30 A constraint. The aircraft adopts a T-tail configuration and is equipped with a fixed tricycle landing gear, complemented by a tail wheel located near the vertical stabilizer. The structure is entirely realized using composite materials, primarily carbon fiber laminates. The wing is manufactured using a semi-monocoque configuration with skins produced in negative molds, while the fuselage is fabricated using a similar process based on molds obtained through additive manufacturing.

Fig. 13.1 Sirius UAV platform.

The excellent results achieved with the original Sirius platform enabled the development of a second, enhanced configuration named *Sirius II – photonic*. This new platform preserves the aerodynamic and structural characteristics of the competition aircraft while integrating a distributed network of Fiber Bragg Grating sensors directly within the structure, in order to obtain a full smart UAV. The activities described in this chapter are therefore focused on the following aspects:

- identification and optimization of the measurement points;
- definition of the fiber routing strategy to reach the selected sensing locations;
- selection of the fiber integration and bonding methodology, ensuring compatibility with the manufacturing and assembly processes;
- ground validation of the sensing system;
- execution of flight testing activities;
- comparative analysis between FBG-based measurements and data provided by the onboard inertial platform.

| **Sirius UAV – Main Characteristics** | |
|---|---|
| **Configuration** | Fixed-wing, low-wing |
| **Structure** | Carbon fiber composite |
| **Fuselage manufacturing** | Negative molds (AM-based) |
| **Aspect ratio** | $\sim 11$ |
| **High-lift devices** | Slotted flaps |
| **Tail configuration** | T-tail |
| **Landing gear** | Fixed tricycle + tail wheel |
| **Motor** | T-Motor AT2826 900KV |
| **Battery** | LiPo 3S (11.1 V) |
| **Max current (limited)** | 30 A |
| **Static thrust** | $\sim 12.5$ N |

Table 13.1 Main characteristics of the Sirius UAV platform.

## 13.1 Definition of Measurement Points

The design of the sensor positioning and fiber routing strategy was directly based on the experience gained from the Anubi platform. In particular, the primary objective was to define a configuration capable of minimizing the risk of failure of the sensing network during all operational phases, including assembly, disassembly, system activation, and shutdown before and after flight operations.

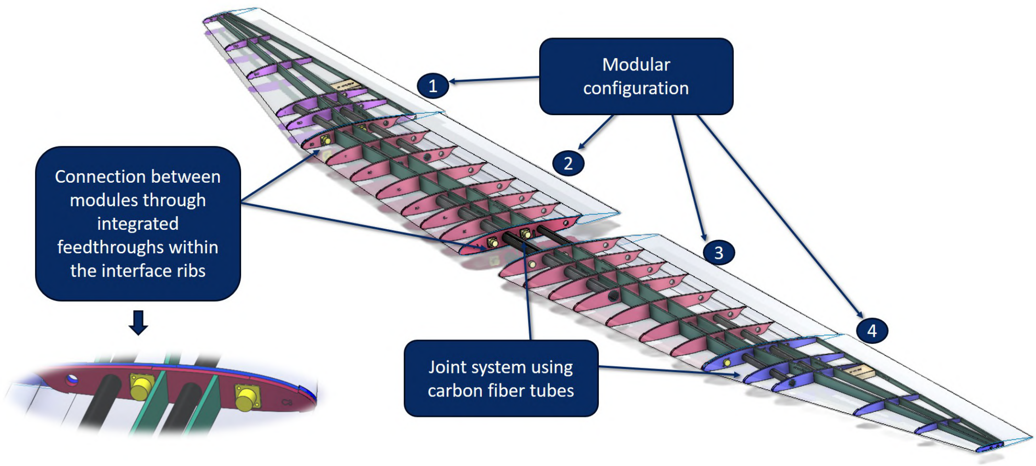


Fig. 13.2 Modular wing configuration and structural interfaces.

A key design requirement was to achieve a fully integrated sensing solution, in which the structure itself acts as a sensing element. For this reason, particular attention was devoted to avoiding exposed fiber segments and connectors that could be subject to direct handling. The most critical interfaces were identified as the wing–fuselage joint and the interface between the root and tip sections, for each semi-wing. In the root section, the fiber was terminated within the interface ribs using bulkhead feed-through connectors. At the wing tip, a short fiber pigtail was initially retained. However, unlike the Anubi configuration, the reduced wingspan of Sirius does not require the separation of the tip and root sections during transport and assembly. Separation is only required during manufacturing, as the components are laminated independently. Once the integration process is completed, the two sections remain permanently assembled. As a result, the connector associated with the tip section—although directly connected to the sensors located in the tip—is fixed within the bulkhead feed-through of the interface rib (Figure 13.2), preventing any accidental manipulation. Consequently, the only critical phase remains the initial assembly process.

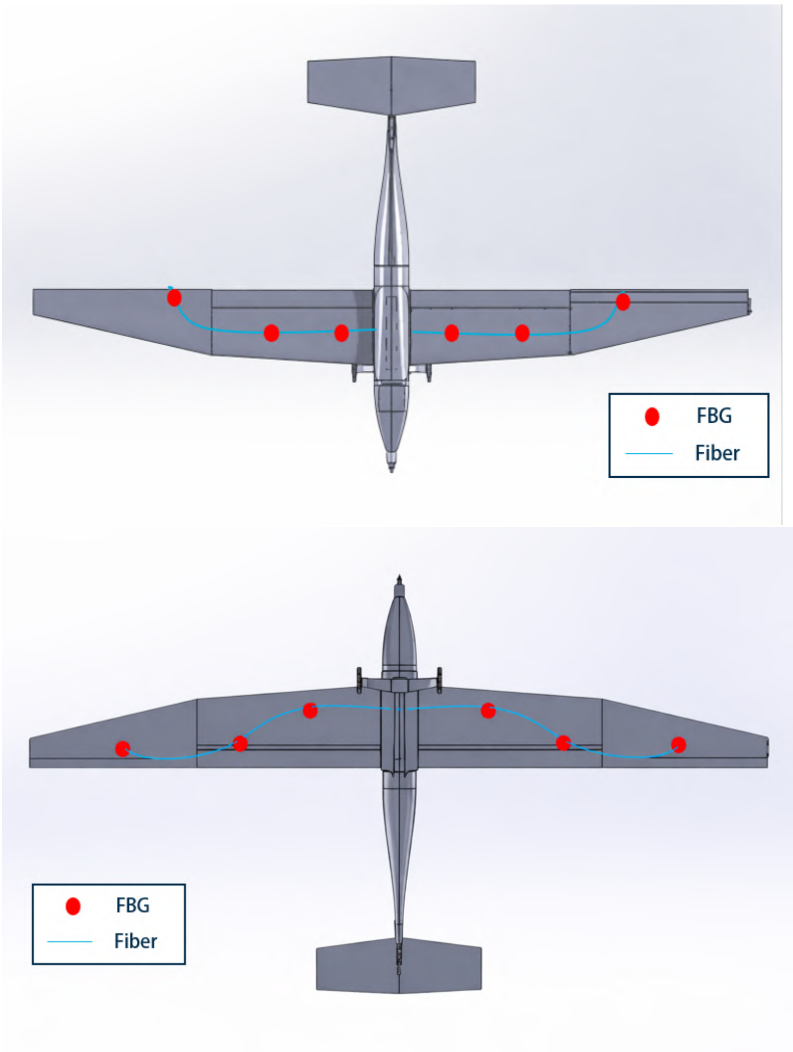


Fig. 13.3 Fiber routing layout on dorsal and ventral surfaces of the wing.

The fundamental idea behind the fiber routing design is the possibility of reconstructing the UAV flight attitude by measuring, in real time, the aerodynamic loads acting on the wing structure. By integrating optical fibers in both semi-wings, the system aims to estimate:

- the roll rate;
- the pitch rate;

- the load factor.

As shown in Figure 13.3, the fibers are routed along the aircraft $y$-axis, extending from the wing root toward the tip. Considering the optical fiber as a one-dimensional sensing element, the sensors laminated on the wing skins are primarily sensitive to strain components induced by the bending moment acting on each semi-wing. The *roll rate* is associated with an antisymmetric distribution of lift between the two semi-wings, resulting in a differential bending moment. To capture this effect, one sensing line was positioned on each semi-wing as close as possible to the torsional center, in order to isolate the strain contribution due to bending. A similar approach applies to the estimation of the *load factor*, which is directly related to the vertical aerodynamic load acting on the aircraft. In this case as well, sensor placement near the torsional center allows a more direct correlation with bending-induced strain. The estimation of the *pitch rate* requires a different strategy. The pitching moment is associated with torsional loads acting on the wing. Since it is not possible to directly align the fiber with the torsional deformation field, a second sensing line was introduced on the lower (ventral) surface of each semi-wing, positioned at a significant distance from the torsional axis. In this configuration, torsional loads generate measurable longitudinal strain components through flexural–torsional coupling. The mathematical formulation of these relationships is presented in Section 13.4. Based on these considerations—and taking into account the structural geometry, manufacturing constraints, and sensor integration requirements—the final sensor layout was defined as shown in Figure 13.4.

In each semi-wing root section, two fiber lines were installed: one on the dorsal surface and one on the ventral surface, each equipped with two FBG sensors connected in series. The dorsal fiber line was positioned at approximately $c/2$, within the region between the two spars. This location corresponds to a structurally stiff area, close to the torsional center, allowing the sensors to predominantly capture bending-induced strain while minimizing flexural–torsional coupling effects. Conversely, the ventral fiber line was designed to maximize sensitivity to torsional effects. The sensors were positioned at the same spanwise locations as the dorsal sensors but placed as far as possible from the torsional axis, namely near the leading and trailing edges of the airfoil. Finally, four additional sensors were installed in the tip sections, each connected as an extension of the dorsal and ventral fiber lines. In particular, the ventral line was extended toward the servo housing region, while the dorsal line

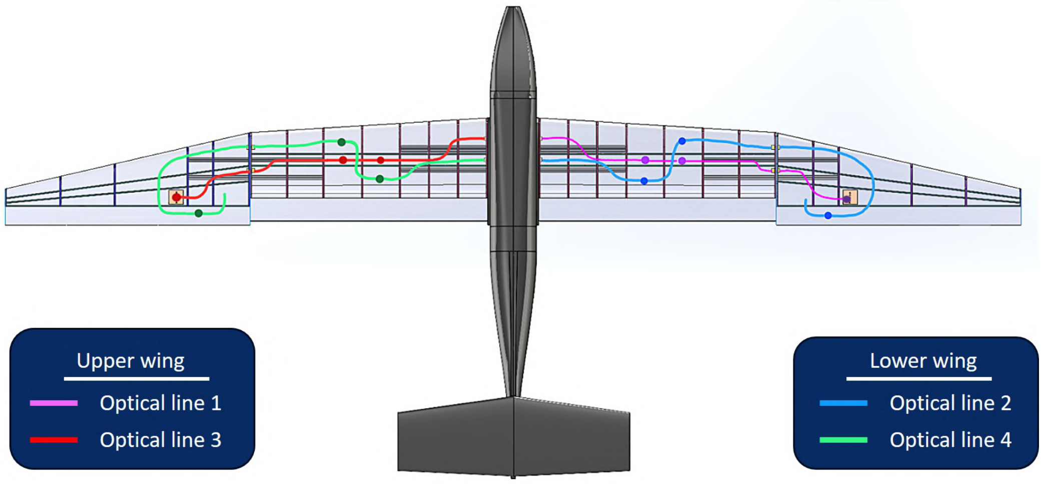


Fig. 13.4 Final sensor layout and fiber routing configuration.

was extended along the aileron. The final positioning of the sensors was defined by combining the results of the FEM structural analyses performed by the ICARUS team with the practical constraints imposed by the manufacturing process and the integration of onboard subsystems.

| **Sensor group** | **Position** | **Structural role** | **Measured quantity** |
|---|---|---|---|
| Dorsal sensors | Mid-chord $(c/2)$, near torsional center | Bending-dominated region | Wing bending $\rightarrow$ Load factor and roll rate |
| Ventral sensors | Near leading and trailing edge | Far from torsional axis | Torsion + bending coupling $\rightarrow$ Pitch contribution |
| Dorsal sensors (tip) | Onside the aileron | High aileron excursion sensitivity | Local load variation $\rightarrow$ flight control monitoring |
| Ventral sensors (tip) | Near servo housing | High deformation region | Local deformation $\rightarrow$ flight control actuation monitoring |

Table 13.2 Summary of FBG sensor positioning and associated measured physical quantities.

## 13.2 Fiber Integration Process within the Structure

The fibers installed in the root section, both on the dorsal and ventral sides, were integrated following the same operational procedure:

- detailed definition of the fiber routing;
- assembly of the optical line;
- definition of the bonding region;
- application of the bonding layer on the inner surface of the skin.

The fibers were bonded to the inner surface of the wing skins, both on the dorsal and ventral sides. For practical reasons and in order to preserve the structural integrity of the wing, the fibers were not positioned directly on the spar surfaces but rather on the skin. This choice was driven by the geometric complexity of the internal structure (ribs and spars) and by the need to minimize the risk of damaging the instrumentation during manufacturing and assembly. For each skin panel, the fiber was initially positioned using adhesive tape in order to define the routing directly on the structure and to evaluate the curvature radii imposed by the selected path. Subsequently, the internal wing structure was temporarily assembled on the skin. This step proved to be essential, as during the autoclave integration phase the balsa structure required local recesses at each point where the fiber intersected structural elements. As a consequence, the number of rib and spar crossings along the fiber routing was minimized and their locations were carefully optimized. In particular, crossings near the spar–fuselage attachment regions were avoided. When crossings were unavoidable, the fiber was arranged as orthogonally as possible with respect to the main structural deformation direction of the crossed element. Once the routing had been finalized, the optical line was assembled according to the procedure described in Chapter 7. The fiber was then repositioned along the defined path and bonded using epoxy resin (Figure 13.5). At this stage, it was also necessary to define the exact endpoint of the bonded region. The optimal bonding termination point was identified between the first and second ribs. This solution ensured that the fiber pigtail, including the connector, remained sufficiently free to allow manual handling during the installation of the bulkhead feed-through and the assembly of the interface rib. This configuration represents a compromise between the required maneuverability of the unbonded fiber segment and the curvature imposed by the final positioning of the connector, which is located further inside the structure than the initial assembly position.

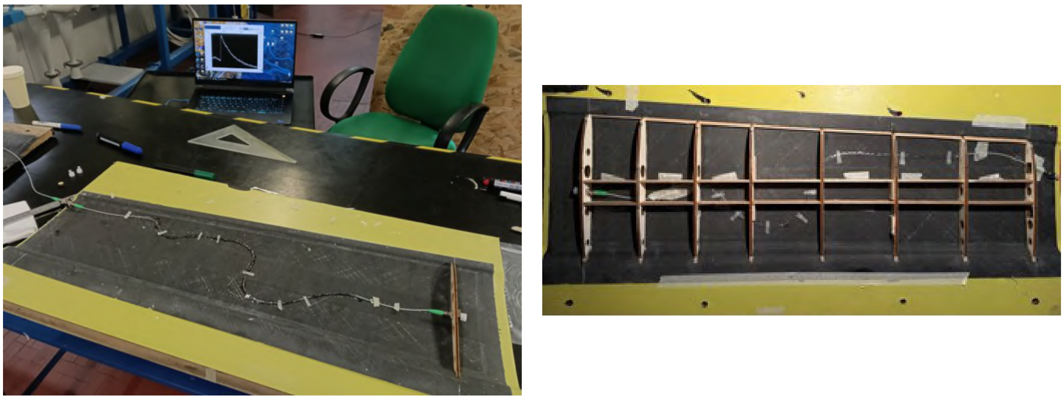

Fig. 13.5 Fiber bonding process on the inner surface of the wing skin.

Once the bonding length had been defined and the epoxy resin applied, the fiber integration process for the root section was completed. The integration procedure for the tip sections differed from that adopted for the root sections. The two fibers installed in the wing tips were integrated according to two distinct configurations. The dorsal fiber installed in the tip section was dedicated to monitoring the deflection of the servo motor arm controlling the aileron. The fiber was bonded along its routing path to the inner dorsal skin, while the sensing section was bonded to the rear side of the servo housing, replicating the approach described in Section 7. The remaining portion of the fiber was integrated using the same procedure adopted for the root section. Conversely, the ventral fiber was designed to extend onto the aileron surface. The transition from the internal structure to the external surface was achieved through a small hole in the skin. Particular care was taken to minimize the curvature imposed during this transition. The external fiber segment was protected using Kapton tape, ensuring both mechanical fixation and protection against impacts or accidental damage during handling. During aileron actuation, the fiber is subjected to a tensile strain proportional to the control surface deflection. This strain is transferred to the FBG grating, resulting in a measurable wavelength variation. Figure 13.6 shows the wing–fuselage interface and the first laboratory assembly with the interrogator. Figure 13.7 shows the complete semi-wing, while Figure 13.8 illustrates the connection between the interrogator and the integrated fibers. Finally, Figure 13.9 shows the assembly detail of the two semi-wing sections.

This integration strategy ensured a robust, minimally invasive, and operationally reliable sensor network, suitable for repeated assembly cycles and flight testing conditions.

Fig. 13.6 Wing–fuselage interface and first system integration with interrogator.

Fig. 13.7 Complete semi-wing after fiber integration.

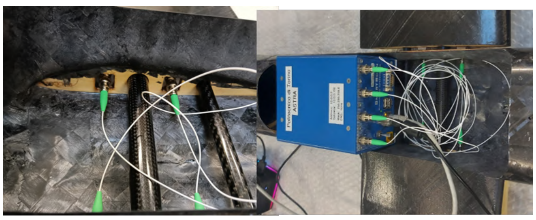

Fig. 13.8 Connection between interrogator and wing-integrated fibers.

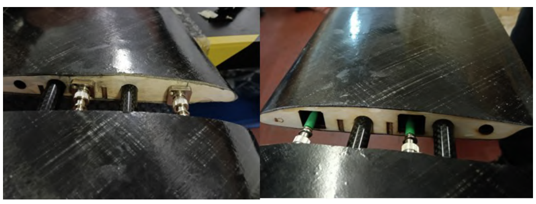

Fig. 13.9 Detail of semi-wing assembly and fiber routing at the interface.

## 13.3 Ground Tests

The functionality of each sensor was verified through a dedicated ground testing campaign. The instrumented sections were first tested individually and subsequently in an integrated configuration, progressively reproducing the sensor network layout intended for flight operations. The ground tests were conducted in order to verify the following requirements:

- correct operation of all integrated sensors;
- sufficient bonding stiffness to ensure measurable responses unaffected by drift phenomena;
- sensitivity of the sensors to bending and torsion, as expected from the design;
- capability to detect the motion of the servo mechanical arm;
- capability to measure the deflection of the aileron.

The results obtained for the structural sensors installed in the two root sections were highly satisfactory. The measurements exhibited extremely fast response, high sensitivity, excellent repeatability, and a clear and unambiguous distinction between equilibrium and loaded conditions. These results were consistently validated for all sensors installed in both semi-wings. Regarding the sensors installed in the tip sections, the bonding process between the skins and the internal structure performed in the autoclave led to partial damage of the optical fibers, resulting in the loss of signal from the two sensors of the right wing. Nevertheless, the left wing tip still allowed verification of the correct operation of the sensing system. In particular, both the sensor installed in contact with the servo housing and the one positioned on the aileron successfully detected the applied deflections, both of the control surface and of the servo housing itself. These results confirm the robustness of the proposed integration approach and its suitability for subsequent flight testing activities.

## 13.4 Structural Model and Relationship Between Strain Measurements and Aircraft Kinematics

The sensor layout (summarized in Figure 13.10) was designed to enable the estimation of aircraft angular rates and accelerations through FBG sensors embedded within the UAV structure. The ultimate objective is to relate the locally measured strains to inertial measurements obtained from the IMU, thereby introducing an alternative physical principle for the generation of flight state information. For this phase of the analysis, attention is restricted to the eight sensors laminated in the root sections of the two semi-wings. In particular, the following sensor pairs are considered:

- *Sensor pair (1):* two sensors located on the upper wing surface (dorsal side), symmetrically placed at a spanwise distance $y_0$ from the fuselage and positioned close to the wing elastic axis, where torsional sensitivity is minimal;
- *Sensor pair (2):* two sensors located on the lower wing surface (ventral side), also at spanwise distance $y_0$, but offset by a distance $x_0$ from the spar axis, thus maximizing sensitivity to torsional effects.

The selected sensor configuration enables the estimation of:

- vertical acceleration (and therefore load factor);
- roll rate;
- pitch rate.

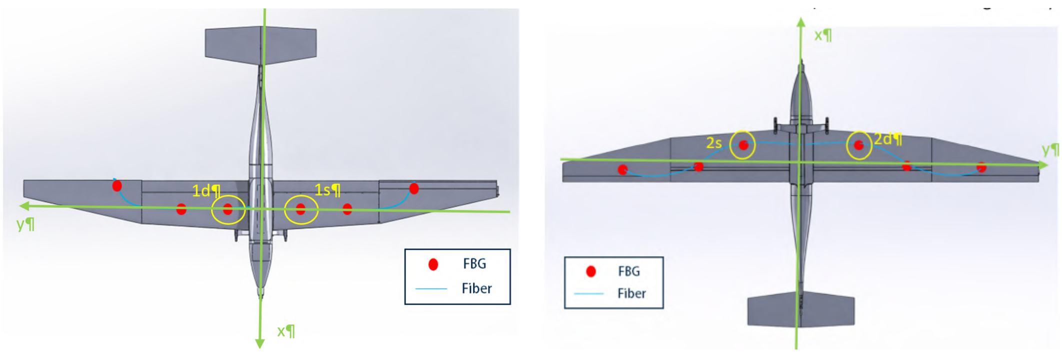


Fig. 13.10 Simplified structural model and sensor positioning used for kinematic estimation.

Due to limitations related to interrogator channels and optical losses associated with complex fiber routing, the tail surfaces were not instrumented. As a consequence, yaw rate estimation is not addressed. However, the purpose of this work is to demonstrate the feasibility of estimating the primary flight dynamics parameters using embedded optical sensing.

## 13.4.1 Model for Load Factor Estimation

The estimation of the load factor is based on sensor pair (1), shown in Figure 13.10. These sensors are aligned with the spar axis and located at the same spanwise position $y_0$, making them primarily sensitive to bending strains induced by vertical loads, while minimizing torsional contributions. Variations in the vertical loads acting on the semi-wings may generate:

- a roll rate, in the presence of antisymmetric lift distributions;
- a variation of the load factor, associated with a global vertical acceleration of the aircraft.

The strain measured on the right semi-wing can therefore be expressed as:

$$\varepsilon_{1,r} = \varepsilon_p + \varepsilon_n \tag{13.1}$$

where $\varepsilon_n$ is the strain contribution due to load factor variation and $\varepsilon_p$ is the contribution associated with roll dynamics. Due to symmetry, the strain measured on the left semi-wing becomes:

$$\varepsilon_{1,l} = -\varepsilon_p + \varepsilon_n \tag{13.2}$$

Summing the two contributions eliminates the antisymmetric component:

$$\varepsilon_{1,r} + \varepsilon_{1,l} = 2\varepsilon_n \tag{13.3}$$

Thus, the symmetric strain component is directly related to the load factor. Recalling the FBG sensing principle, the same proportionality holds for wavelength shifts:

$$\Delta\lambda_{1,r} + \Delta\lambda_{1,l} \propto \varepsilon_{1,r} + \varepsilon_{1,l} \propto n \tag{13.4}$$

The vertical equation of motion of the aircraft is:

$$\sum F_z = ma_z \tag{13.5}$$

The total lift is:

$$L_{tot} = L_r + L_l \tag{13.6}$$

Under quasi-steady conditions:

$$L_{tot} = m(g + a_z) \tag{13.7}$$

Defining the load factor:

$$n = \frac{L_{tot}}{mg} \tag{13.8}$$

which yields:

$$L_{tot} = n \cdot mg \tag{13.9}$$

The bending moment at a section located at distance $y_0$ from the root is:

$$M(y_0) = \int_{y_0}^{b/2} (s - y_0) q(s)\, ds \tag{13.10}$$

which can be linearized as:

$$M(y_0) = K(y_0) L_{tot} \tag{13.11}$$

According to Euler–Bernoulli beam theory, the strain at a distance $c$ from the neutral axis is:

$$\varepsilon = \frac{c}{\rho} \tag{13.12}$$

and the bending moment is related to curvature by:

$$M = \frac{EI}{\rho} \tag{13.13}$$

Combining these expressions:

$$\varepsilon(y_0) = \frac{M(y_0)c}{EI} \tag{13.14}$$

Substituting:

$$\varepsilon_{r,l}(y_0) = \frac{c}{EI} K(y_0) \frac{L_{tot}}{2} \tag{13.15}$$

Summing the contributions from both semi-wings:

$$\varepsilon_r + \varepsilon_l = \frac{c}{EI} K(y_0) L_{tot} \tag{13.16}$$

Substituting Eq. 13.9:

$$\varepsilon_r + \varepsilon_l = \frac{c}{EI} K(y_0) m(g + a_z) \tag{13.17}$$

From which:

$$a_z = \frac{EI}{cK(y_0)m} (\varepsilon_r + \varepsilon_l) - g \tag{13.18}$$

and, in terms of load factor:

$$n = K_\Sigma (\varepsilon_r + \varepsilon_l) \tag{13.19}$$

where:

$$K_n = \frac{EI}{cK(y_0)mg} \tag{13.20}$$

is a calibration coefficient.

Finally, recalling the FBG relationship:

$$\Delta\lambda_{1,r} + \Delta\lambda_{1,l} = K_\varepsilon(\varepsilon_{1,r} + \varepsilon_{1,l}) = K_\varepsilon \cdot \frac{n}{K_n} \tag{13.21}$$

From which:

$$n = \frac{K_\Sigma}{K_\varepsilon}(\Delta\lambda_{1,r} + \Delta\lambda_{1,l}) \tag{13.22}$$

This model demonstrates that the selected sensor placement and bonding methodology enable a direct correlation between the raw FBG measurements and the aircraft load factor. This result represents a key step toward the development of fully optical-based flight state estimation systems.

### 13.4.2 Roll Rate Estimation Model

As introduced in the previous section, the same sensor pair (1) can be used to estimate the roll rate by considering the difference between the measured strains, i.e., by exploiting the differential signal provided by the two sensors. The underlying physical principle is that the rolling moment is generated by an antisymmetric variation of lift between the two semi-wings. This produces an antisymmetric variation of the bending load and, consequently, of the measured strain. The roll rate can therefore be estimated from the differential strain between the two semi-wings.

Recalling that:

$$\varepsilon_{1,r} = \varepsilon_p + \varepsilon_n \tag{13.23}$$

$$\varepsilon_{1,l} = -\varepsilon_p + \varepsilon_n \tag{13.24}$$

the difference between the two measurements eliminates the symmetric contribution associated with the load factor:

$$\varepsilon_{1,r} - \varepsilon_{1,l} = 2\varepsilon_p \tag{13.25}$$

Thus, the differential strain is directly related to the roll-induced deformation. The objective of the following derivation is to demonstrate the relationship between the measured strain difference and the roll rate $p = \dot{\phi}$. Similarly to the previous section, the bending moment at a section located at a distance $y_0$ from the root is:

$$M(y_0) = \int_{y_0}^{b/2} (s - y_0)\, q(s)\, ds \tag{13.26}$$

and the corresponding strain is:

$$\varepsilon(y_0) = \frac{M(y_0)c}{EI} \tag{13.27}$$

Under symmetric flight conditions:

$$L_r = L_l = \frac{L_{tot}}{2} \tag{13.28}$$

which implies:

$$\varepsilon_r(y_0) = \varepsilon_l(y_0) \tag{13.29}$$

In the presence of a non-zero roll rate ($p \neq 0$), generated for instance by differential aileron deflection, an antisymmetric lift variation arises:

$$\Delta L = L_r - L_l \tag{13.30}$$

This induces a differential variation of the bending moment:

$$\Delta M(y_0) = M_r(y_0) - M_l(y_0) \tag{13.31}$$

Since:

$$\varepsilon(y_0) = \frac{M(y_0)c}{EI} \tag{13.32}$$

it follows that:

$$\Delta\varepsilon(y_0) = \frac{\Delta M(y_0)c}{EI} \tag{13.33}$$

The rolling moment is defined as:

$$L_{roll} = \int_{-b/2}^{b/2} y\, dL(y) \tag{13.34}$$

Under quasi-steady assumptions:

$$L_{roll} \approx \Delta L \cdot \frac{b}{2} \tag{13.35}$$

Thus, the variation of the bending moment can be expressed as:

$$\Delta M(y_0) = K(y_0)\,\Delta L \tag{13.36}$$

where $K(y_0)$ depends on the sensor location.

Therefore:

$$\Delta\varepsilon(y_0) = \frac{K(y_0)c}{EI}\Delta L \tag{13.37}$$

which implies:

$$\Delta\varepsilon(y_0) \propto L_{roll} \tag{13.38}$$

To relate this quantity to the roll rate, the rotational dynamics equation is considered:

$$I_x\dot{p} = L_{roll} \tag{13.39}$$

where $I_x$ is the moment of inertia about the longitudinal axis.

Under quasi-steady conditions (or for slowly varying motions), the rolling moment can be approximated as:

$$L_{roll} \approx C_p \, p \tag{13.40}$$

which leads to:

$$\Delta\varepsilon(y_0) \propto p \tag{13.41}$$

A linear relationship can therefore be established:

$$p = K_\Sigma \Delta\varepsilon(y_0) \tag{13.42}$$

where:

$$K_p = \frac{EI}{c\,K(y_0)\,C_p} \tag{13.43}$$

is a calibration coefficient.

Finally, recalling the FBG sensing principle:

$$\Delta\lambda_r - \Delta\lambda_l = K_\varepsilon \Delta\varepsilon(y_0) = K_\varepsilon \frac{p}{K_p} \tag{13.44}$$

From which:

$$p = \frac{K_\Sigma}{K_\varepsilon}(\Delta\lambda_r - \Delta\lambda_l) \tag{13.45}$$

This demonstrates the direct correlation between the differential optical measurement and the aircraft roll rate.

### 13.4.3 Pitch Rate Estimation Model

To estimate the pitch rate, sensor pair (2) must be considered. Unlike sensor pair (1), these sensors are located on the lower wing surface at a spanwise distance $y_0$ from the fuselage and at a chordwise distance $x_0$ from the spar, toward the leading edge. This configuration maximizes the distance between the sensing location and the torsional center of the wing section. Although the sensors are still oriented along the aircraft $y$-axis, the offset $x_0$ makes them highly sensitive to bending–torsion coupling. Furthermore, being laminated on the skin and located away from the spar, they operate in a region characterized by lower stiffness. This reduces the contribution of pure bending deformation while enhancing the strain component induced by torsional moments. The objective of this section is to formalize the relationship between the strain measured by sensors (2) and the pitch rate $q = \dot{\theta}$. In the presence of bending–torsion coupling, the measured strain can be expressed as:

$$\varepsilon = \varepsilon_f + \varepsilon_t \tag{13.46}$$

where $\varepsilon_f$ is the bending contribution and $\varepsilon_t$ is the torsional contribution. The bending strain is given by:

$$\varepsilon_f = \frac{c}{EI} M_f \tag{13.47}$$

where the bending moment is proportional to the vertical load:

$$M_f = K_f L_{semi} \tag{13.48}$$

The vertical load consists of:

- a symmetric component (associated with vertical acceleration);
- an antisymmetric component (associated with roll motion).

The torsional contribution induces a rotation of the wing section:

$$\theta = \frac{M_t}{GJ} \tag{13.49}$$

which produces a longitudinal strain at a distance $x$ from the torsional center:

$$\varepsilon_t = x\theta = \frac{x}{GJ} M_t \tag{13.50}$$

Introducing the pitch dynamics:

$$I_y \dot{q} = M_{pitch} \tag{13.51}$$

where $I_y$ is the moment of inertia about the lateral axis.

Assuming linear behavior around equilibrium:

$$M_{pitch} = C_q q \tag{13.52}$$

The pitching moment induces a symmetric variation of the angle of attack and, consequently, a symmetric torsional moment distribution along the wings. The local torsional moment can therefore be expressed as:

$$M_t(x_0, y_0) = K_t(x_0, y_0) C_q q \tag{13.53}$$

Substituting:

$$\varepsilon_t = \frac{x_0}{GJ} K_t C_q q \tag{13.54}$$

Defining:

$$k_q = \frac{x_0}{GJ} K_t C_q \tag{13.55}$$

it follows that:

$$\varepsilon_t \propto q \tag{13.56}$$

However, sensors (2) also measure bending-induced strain. Therefore, the total strain at each sensor can be expressed as:

$$\varepsilon_{r,l} = k'_z a_z + k'_p p + k_q q \tag{13.57}$$

where:

- $k'_z$ is the sensitivity to vertical acceleration;
- $k'_p$ is the sensitivity to roll rate;
- $k_q$ is the sensitivity to pitch rate.

Since pitch and vertical acceleration generate symmetric effects, while roll produces an antisymmetric contribution, summing the strains measured on the two semi-wings yields:

$$\varepsilon_r + \varepsilon_l = 2k'_z a_z + 2k_q q \tag{13.58}$$

The roll contribution cancels automatically. To isolate the pitch contribution, the vertical acceleration term must be removed. From sensor pair (1), which is insensitive to torsion:

$$\varepsilon_r^{(1)} + \varepsilon_l^{(1)} = 2k_z a_z \tag{13.59}$$

thus:

$$a_z = \frac{\varepsilon_r^{(1)} + \varepsilon_l^{(1)}}{2k_z} \tag{13.60}$$

Substituting:

$$\varepsilon_r + \varepsilon_l = 2k'_z \frac{\varepsilon_r^{(1)} + \varepsilon_l^{(1)}}{2k_z} + 2k_q q \tag{13.61}$$

from which:

$$q = \frac{1}{2k_q} \left[ (\varepsilon_r + \varepsilon_l) - \frac{k'_z}{k_z} (\varepsilon_r^{(1)} + \varepsilon_l^{(1)}) \right] \tag{13.62}$$

This expression shows that the pitch rate can be obtained from the symmetric strain component measured in the torsion-sensitive region once the bending contribution has been removed. As a first approximation, if the sensors are placed in a region weakly sensitive to pure bending ($k'_z \ll k_z$), the equation simplifies to:

$$q \approx \frac{1}{2k_q} (\varepsilon_r + \varepsilon_l) \tag{13.63}$$

Finally, recalling the FBG relationship:

$$q \approx \frac{1}{2k_q K_\varepsilon}(\Delta\lambda_{2,r} + \Delta\lambda_{2,l}) \tag{13.64}$$

### 13.4.4 Compact Formulation of the Complete Model

Having established the relationships between the wavelength shifts $\Delta\lambda_i$ measured by sensor pairs (1) and (2), the overall model can be expressed in a compact matrix form. This formulation provides a rigorous framework for integrating optical measurements within a control-oriented estimation architecture, enabling the real-time reconstruction of aircraft kinematic quantities during flight.

The state vector is defined as:

$$\mathbf{x} = \begin{bmatrix} a_z \\ p \\ q \end{bmatrix} \tag{13.65}$$

where $a_z$ is the vertical acceleration, $p$ is the roll rate, and $q$ is the pitch rate.

As previously discussed, the different dynamic contributions generate distinct structural responses:

- vertical acceleration produces a symmetric lift contribution:

$$L_{sym} = m(g + a_z) \tag{13.66}$$

- roll motion produces an antisymmetric lift variation:

$$L_{roll} = C_p p \tag{13.67}$$

- pitch motion generates a torsional moment:

$$M_{pitch} = C_q q \tag{13.68}$$

Considering a generic point located at $(x_0, y_0)$, the resulting strain due to bending–torsion coupling can be expressed as:

$$\varepsilon = \frac{c}{EI} M_f + \frac{x_0}{GJ} M_t \tag{13.69}$$

where:

$$M_f = K_f L_{semi}, \qquad M_t = K_t M_{pitch} \tag{13.70}$$

Sensors (1) are located near the torsional center ($x \approx 0$), thus minimizing torsional effects. The measured strain is therefore:

$$\varepsilon_r^{(1)} = k_z a_z + k_p p \tag{13.71}$$

$$\varepsilon_l^{(1)} = k_z a_z - k_p p \tag{13.72}$$

Sensors (2), located at $x_0 \neq 0$, are sensitive to bending–torsion coupling:

$$\varepsilon_{r,l}^{(2)} = k_z' a_z \pm k_p' p + k_q q \tag{13.73}$$

where $k_z'$, $k_p'$, and $k_q$ are sensitivity coefficients.

The measurement vector is defined as:

$$\mathbf{y} = \begin{bmatrix} \varepsilon_r^{(1)} \\ \varepsilon_l^{(1)} \\ \varepsilon_r^{(2)} \\ \varepsilon_l^{(2)} \end{bmatrix} \tag{13.74}$$

which leads to the linear measurement model:

$$\mathbf{y} = \mathbf{H}\mathbf{x} \tag{13.75}$$

with:

$$\mathbf{H} = \begin{bmatrix} k_z & k_p & 0 \\ k_z & -k_p & 0 \\ k'_z & k'_p & k_q \\ k'_z & -k'_p & k_q \end{bmatrix} \tag{13.76}$$

Recalling the fundamental FBG relation (assuming thermal compensation):

$$\Delta\lambda = K_\varepsilon \Delta\varepsilon \tag{13.77}$$

the measurement vector can be expressed directly in terms of wavelength shifts:

$$\Delta\lambda = \begin{bmatrix} \Delta\lambda_r^{(1)} \\ \Delta\lambda_l^{(1)} \\ \Delta\lambda_r^{(2)} \\ \Delta\lambda_l^{(2)} \end{bmatrix} \tag{13.78}$$

leading to the final compact form:

$$\Delta\lambda = K_\varepsilon \mathbf{H}\mathbf{x} \tag{13.79}$$

This formulation highlights that the structural response of the aircraft, measured through FBG sensors, can be directly mapped into a state estimation problem. Consequently, the proposed sensing architecture enables the reconstruction of key flight dynamics variables without relying exclusively on traditional inertial sensors, opening the way to structurally integrated navigation and control systems.

## 13.5 Flight Testing

The preparation of the flight configuration proved to be significantly simpler compared to the setup previously adopted for the Anubi platform. In particular, the fuselage geometry ensured stable positioning of the interrogator, straightforward access to the acquisition channels, and safe handling of all optical fiber connections, minimizing the risk of damage during installation.
The system layout is conceptually analogous to that previously described for the

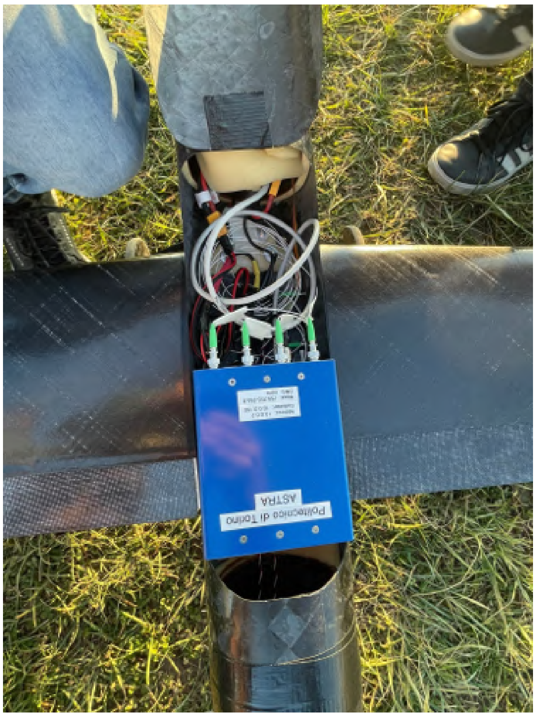


Fig. 13.11 Pre-flight integration of the onboard instrumentation within the fuselage.

Anubi tests. However, the internal arrangement of the onboard systems was optimized such that the payload—consisting of the interrogator, the mini-PC, and the optical patch cords—could be installed as the final step of the integration procedure. Figure 13.11 shows the fuselage configuration before and after the installation of the interrogator.

A total of five flight tests were performed with the Sirius configuration, following an initial reference flight without instrumentation. The first three flights were dedicated to verifying the correct operation of the optical sensor network, while the last two included the acquisition of IMU data (angular rates and accelerations along the three axes). Each flight lasted approximately five minutes.
The experimental results presented in this section are aimed at validating the theoretical framework introduced in the previous section by comparing the quantities derived from the FBG sensors with the corresponding measurements provided by the onboard inertial unit.

### 13.5.1 Raw Data

Figures 13.12, 13.13, and 13.14 report the raw data acquired from the ten sensors installed onboard. Several key features can be immediately identified:

- The transition between on-ground and in-flight conditions is clearly distinguishable;
- The sensor installed on the aileron exhibits rapid oscillations consistent with control surface actuation;
- Similar oscillatory behavior is observed in the sensor bonded to the servo housing, although affected by a drift phenomenon occurring during a specific flight.

Figures 13.12 and 13.13 show the full dataset acquired on the right and left semi-wings, respectively, while Figure 13.14 focuses on the signal measured by a single sensor located on the upper wing surface. During the flight phase, the generation of aerodynamic lift induces an upward bending of the wing, resulting in compressive strain at the measurement location. Despite the dynamic oscillations associated with flight maneuvers, two distinct regimes can be clearly identified: a baseline level corresponding to the on-ground condition and a deformation band associated with in-flight operation.

The raw signals exhibit a relatively high level of background noise, primarily due to structural vibrations induced by the propulsion system. In addition, under unfavorable environmental conditions (e.g., strong solar irradiation or significant humidity gradients), low-frequency drift phenomena can be observed, likely associated with thermal effects and hygroscopic behavior of the materials. To address these issues, the acquired signals were processed using a band-pass filter, allowing the removal of both high-frequency vibration components and low-frequency drift effects. Finally, the comparison between different flight tests demonstrated a high level of repeatability of the measurement system, confirming the robustness of the adopted sensing approach under real flight conditions.

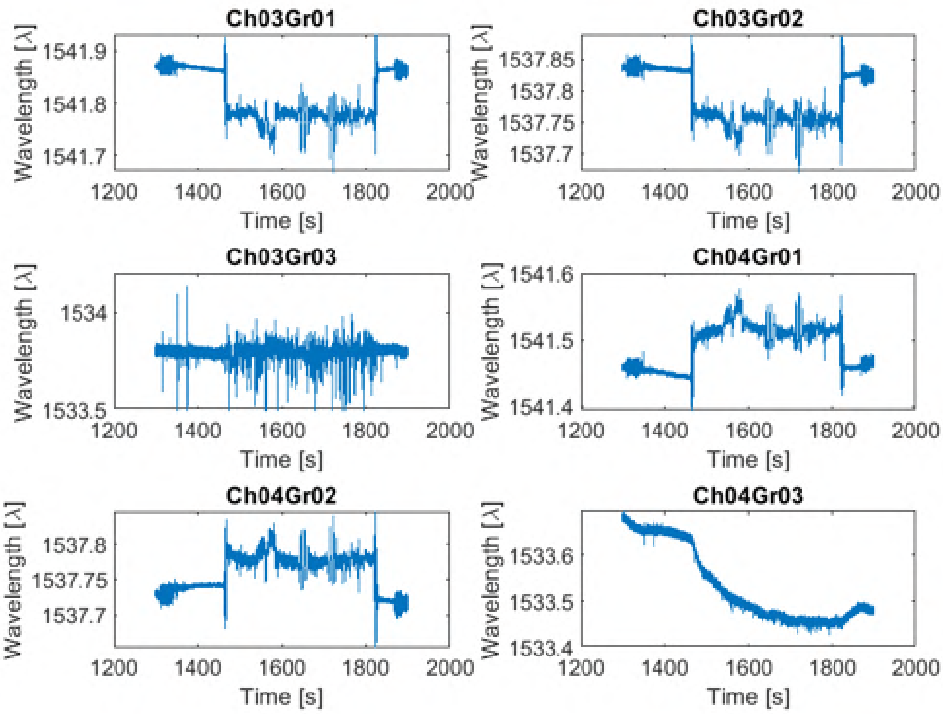


Fig. 13.12 Raw wavelength data acquired from the sensors installed on the right semi-wing.

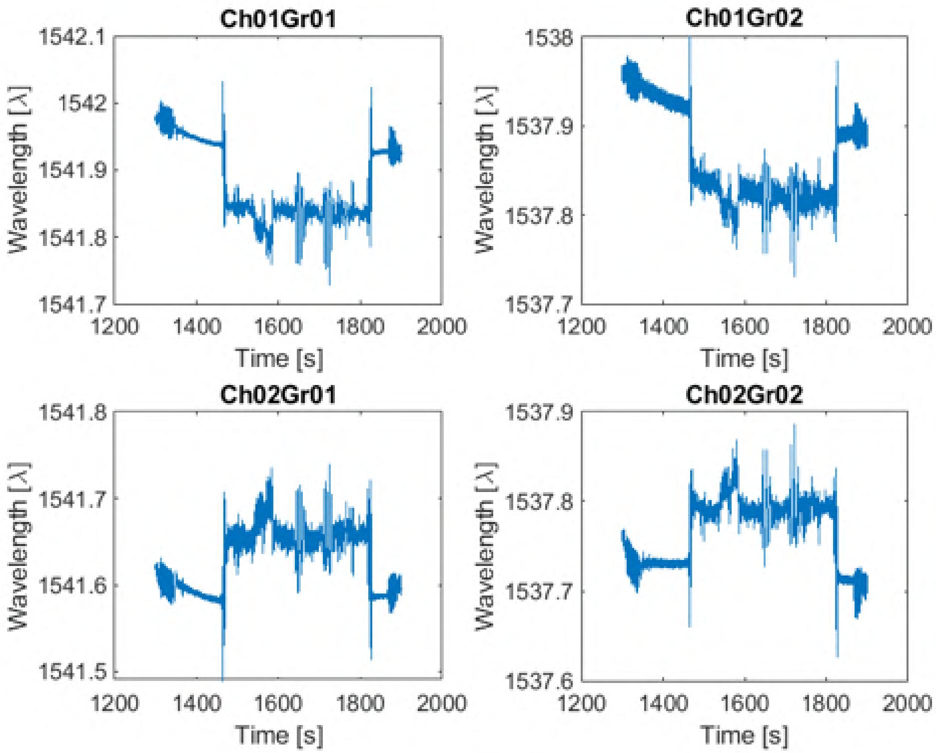


Fig. 13.13 Raw wavelength data acquired from the sensors installed on the left semi-wing.

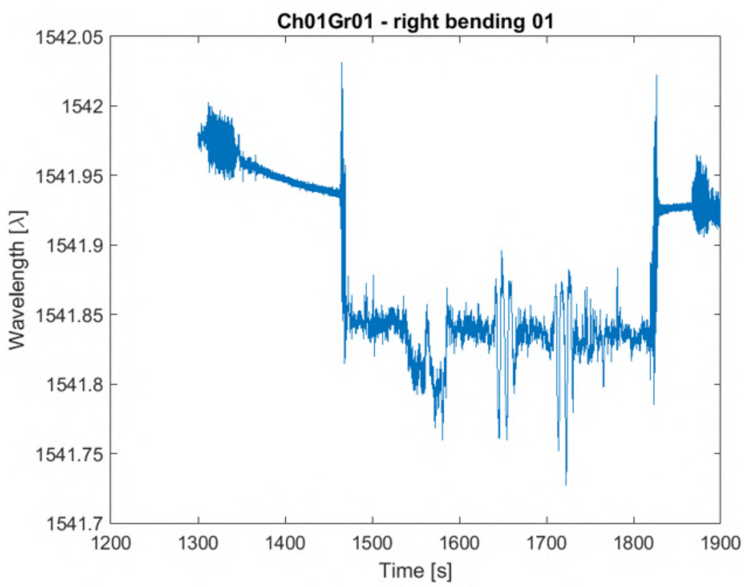


Fig. 13.14 Example of raw signal measured by a dorsal sensor during flight.

### 13.5.2 On Ground / Touch-and-Go

During the flight corresponding to the dataset shown in the figures, a touch-and-go maneuver was performed at $t = 1782$ s. As confirmed by the video recorded from the runway, the brief ground contact cannot always be identified through a sharp instantaneous strain peak, unlike what was observed for the landing gear sensor in the Anubi configuration. In particular, during smooth touch-and-go maneuvers, the structural response associated with ground contact may be comparable in magnitude to deformation peaks generated by flight maneuvers. However, by focusing on a time window centered around the touch-and-go event, the ground contact becomes clearly identifiable. The interaction between the landing gear and the ground generates transient oscillations that propagate throughout the wing structure and are consistently detected by the FBG sensors (Figures 13.15 and 13.16). A more detailed inspection of the exact instant of wheel contact reveals a clear discontinuity in the measured signal, corresponding to the onset of mechanical vibrations induced by the impact with the ground. This behavior demonstrates that, even in the absence of a distinct peak in the raw signal, the structural response still contains sufficient information to detect touchdown events through appropriate signal processing.

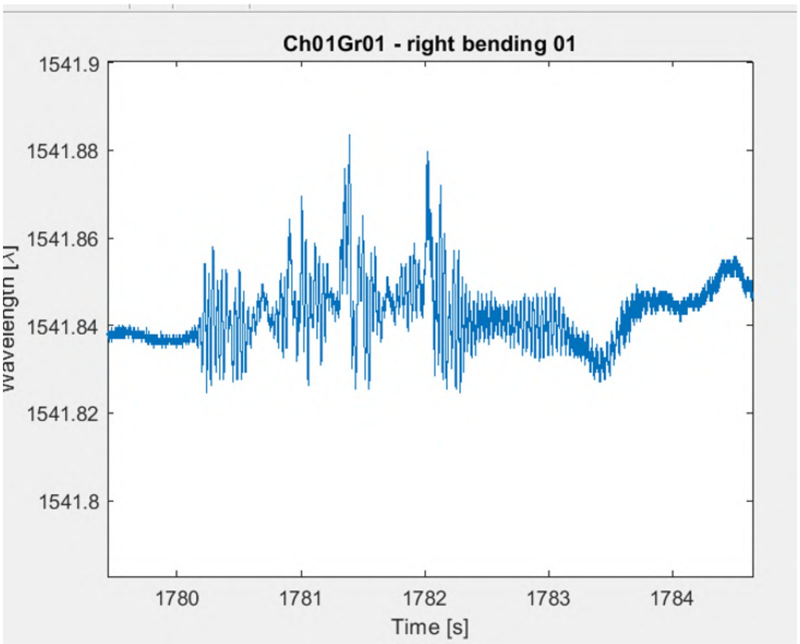


Fig. 13.15 Detailed view of the structural response during the touch-and-go maneuver.

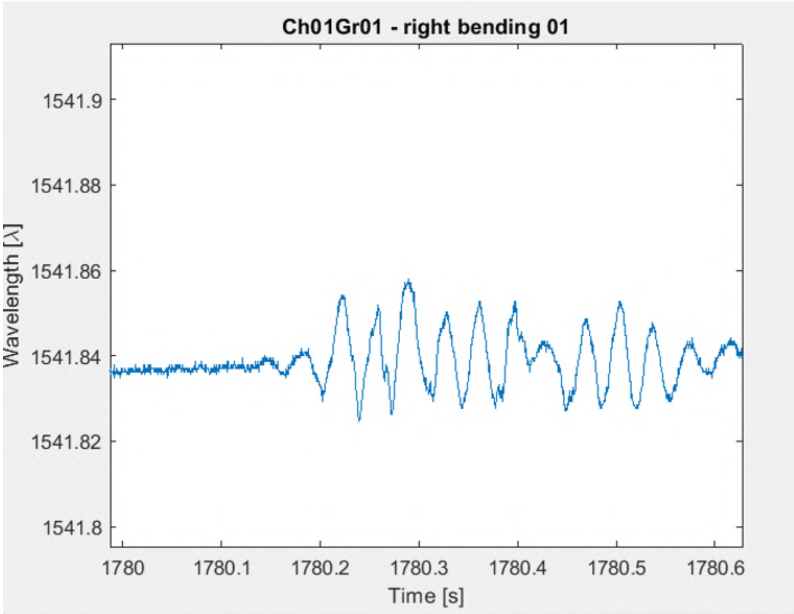


Fig. 13.16 Zoom on the signal discontinuity associated with ground contact.

### 13.5.3 Aileron Deflection and Servo Housing Sensor

Figure 13.17 shows the filtered signal measured by the sensor installed on the aileron. The following features can be clearly identified:

- a well-defined baseline corresponding to the equilibrium position;
- a non-symmetric response with respect to the baseline, consistent with aerodynamic loading conditions;
- distinct signal variations associated with control surface deflections during flight maneuvers;
- no evidence of hysteresis or delay introduced by the sensor packaging, indicating a prompt and reliable mechanical coupling.

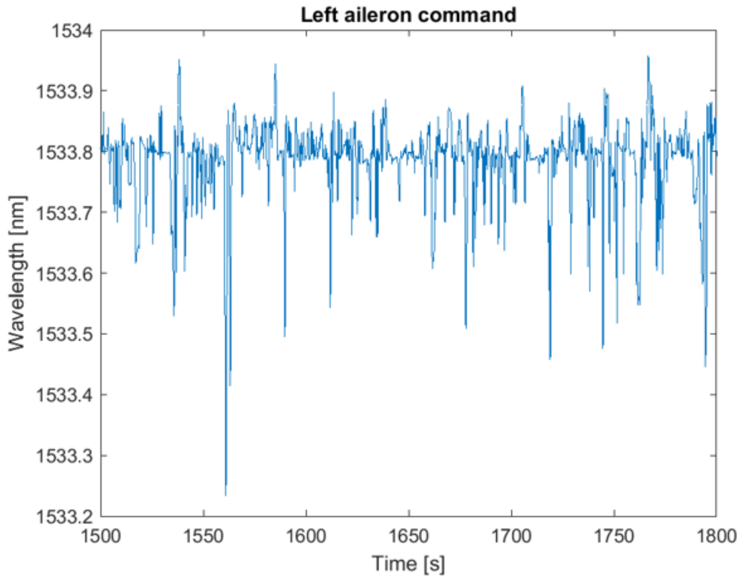


Fig. 13.17 Filtered signal measured by the aileron sensor during flight.

The original design concept involved the instrumentation of both ailerons in order to exploit their antisymmetric motion for quantitative estimation of control surface deflections. However, during the autoclave integration process, the fiber associated with the left wing tip was irreversibly damaged. Despite this limitation, the results obtained from the remaining sensor clearly demonstrate the feasibility of the proposed approach and confirm the capability of FBG sensors to capture control surface dynamics in flight. These findings suggest that, with a fully operational sensor network, it would be possible to reconstruct control inputs directly from structural measurements. With regard to the second sensor installed on the servo housing, the objective was to verify the correspondence between the measured strain and the motion of the mechanical linkage driving the control surface, following the concept previously introduced in Chapter 9. The data collected during the five flight tests revealed a critical issue related to the bonding procedure. Due to assembly constraints, it was not possible to use the same resin adopted for the wing root sensors, leading to reduced stability of the bonding interface. In one of the flight tests, the measured signal exhibited a significant drift, likely caused by a combination of environmental conditions and adhesive behavior. Nevertheless, even in the presence of drift, the qualitative correlation between signal peaks and control surface actuation was consistently observed, especially after appropriate filtering. This confirms the sensitivity of the sensor to the mechanical motion of the linkage system. Further work is required to improve the bonding strategy and to establish a quantitative relationship between the measured signal amplitude and the actual mechanical deflection. Achieving this objective would enable the detection of anomalies or degradation in the control actuation system, which represents a safety-critical subsystem of the aircraft.

### 13.5.4 Linear Combination of FBG Sensors and Extraction of IMU Data

Once the raw signals have been filtered, the next step consists in performing linear combinations of the measurements provided by the sensors in order to extract the physical quantities identified in the theoretical model and to determine the corresponding correlation coefficients experimentally. A direct combination of the measured Bragg wavelengths is not sufficient for accurate estimation. Even when symmetric nominal wavelengths are selected for sensor pairs, the actual Bragg wavelength $\lambda_B$ is affected by non-negligible uncertainties and offsets. For this reason, the signal associated with each sensor is expressed in differential form as:

$$\Delta\lambda_i = \lambda_i - \lambda_{ref} \tag{13.80}$$

where $\lambda_i$ is the instantaneous measured wavelength and $\lambda_{ref}$ is a reference value computed under quasi-steady flight conditions characterized by $p \approx 0$, $q \approx 0$, and $n \approx 1$.

The symmetric contribution associated with vertical acceleration is obtained through the sum of sensor pair (1):

$$\Delta\lambda_n = \Delta\lambda_{1,l} + \Delta\lambda_{1,r} \tag{13.81}$$

Due to the positioning of these sensors on the upper wing surface, an increase in bending moment produces compressive strain, leading to a decrease in wavelength. Therefore:

$$n \propto -\Delta\lambda_n \tag{13.82}$$

In order to improve robustness and detect potential sensor malfunctions, an additional pair of sensors (3) was introduced further along the span, acting as a redundant measurement channel. Figure 13.18 shows the sum of data coming from sensors placed on dorsal (upper) side, while Fig. 13.19 the comparison between $\Delta\lambda_n$ and the load factor $n$ measured by the IMU. Despite the difference in scale, a strong correlation between the two signals is clearly observed.

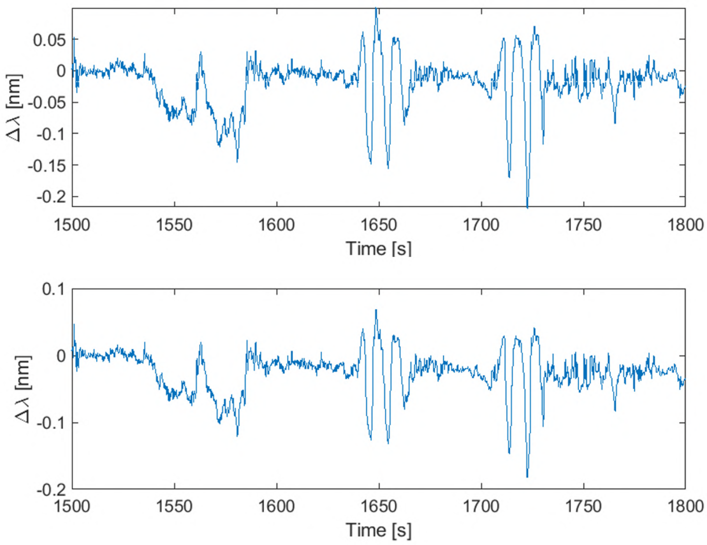


Fig. 13.18 Sum of data coming from sensors placed on dorsal (upper) side.

The antisymmetric contribution associated with roll motion is obtained through the difference of sensor pair (1):

$$\Delta\lambda_p = \Delta\lambda_{1,l} - \Delta\lambda_{1,r} \tag{13.83}$$

which leads to:

$$p \propto \Delta\lambda_p \tag{13.84}$$

Figure 13.20 shows the resulting signal Ccoming from FBG, while Figure 13.22 shows the comparison between the FBG-derived quantity and the roll rate measured by the IMU.

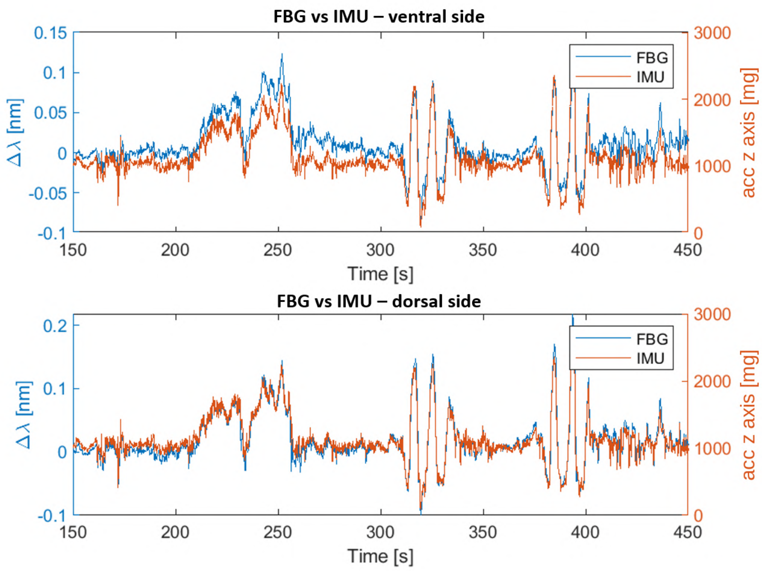


Fig. 13.19 Comparison between FBG-derived signal and IMU acc z rate.

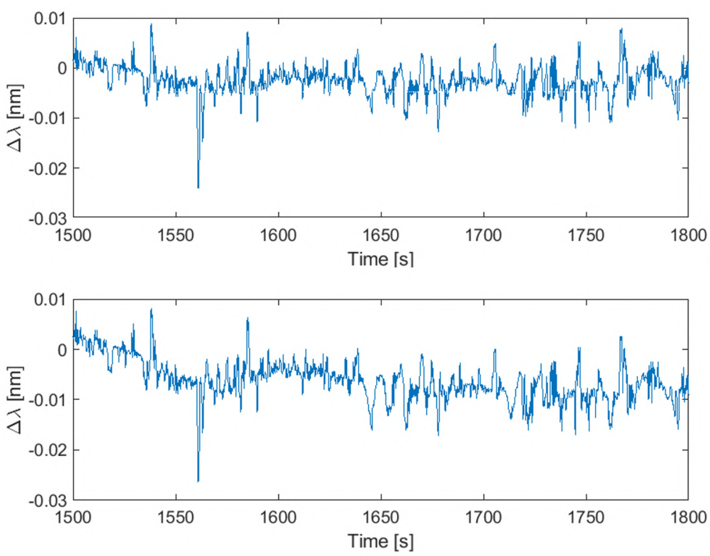


Fig. 13.20 Differential data coming from sensors placed on dorsal (upper) side..

The symmetric contribution associated with torsion is obtained through the sum of sensor pair (2):

$$\Delta\lambda_q = \Delta\lambda_{2,l} + \Delta\lambda_{2,r} \tag{13.85}$$

which leads to:

$$q \propto \Delta\lambda_q \tag{13.86}$$

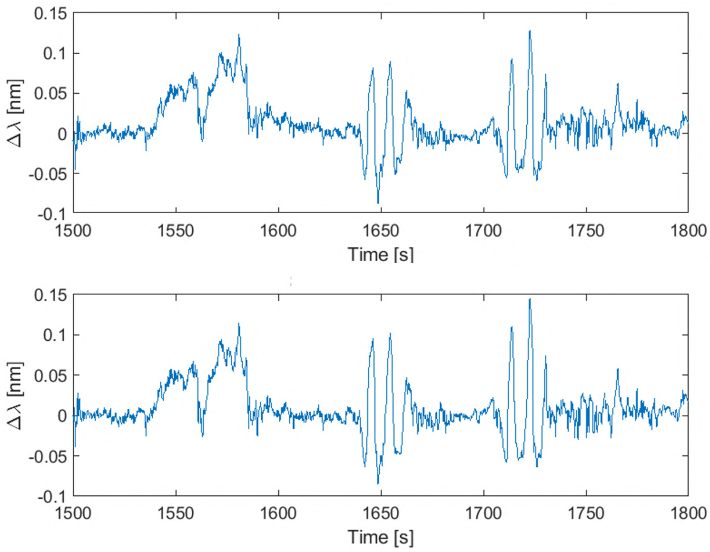


Fig. 13.21 Summed FBG signal from torsion-sensitive sensors.

Figure 13.21 shows the data coming from FBG, while Figutr 13.22 shows the comparison between the FBG-derived quantity and the pitch rate measured by the IMU, highlighting once again a clear correlation between the two signals.

Overall, the results demonstrate that the linear combinations of the FBG sensor outputs allow the extraction of meaningful physical quantities directly related to the aircraft dynamics, confirming the validity of the theoretical model derived in the previous section.

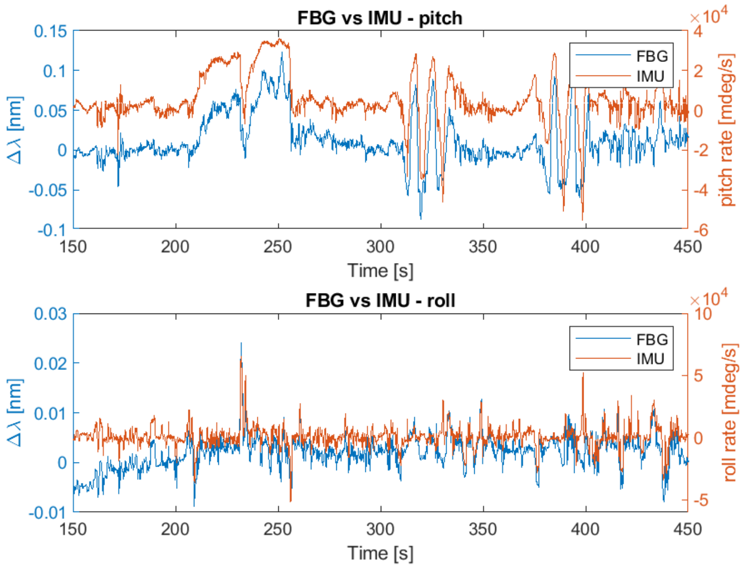


Fig. 13.22 Comparison between FBG-derived signal and IMU pitch and roll rate.

### 13.5.5 Estimation of Correlation Factors and Quantitative Comparison

The correlation factors were estimated by evaluating the ratios between corresponding peaks generated by clearly identifiable flight maneuvers in both measurement systems. By analyzing the mapping between the optical quantities $\Delta\lambda_n, \Delta\lambda_p, \Delta\lambda_q$ and the corresponding inertial variables $n, p, q$, it is possible to assess the quantitative validity of the proposed approach. The load factor estimation shows a very high level of accuracy. This result confirms that the sensors are effectively positioned close to the torsional axis of the wing section and that the bonding and installation procedures preserved the structural symmetry required by the theoretical model.

The roll rate estimation also demonstrates strong agreement with the IMU measurements. The most significant dynamic peaks are accurately captured by the optical sensing system, both in terms of response time and amplitude. This confirms the capability of the differential measurement approach to isolate antisymmetric bending contributions associated with roll motion. The estimation of the pitch rate is generally accurate, although some localized discrepancies can be observed. The comparison shown in Figure 13.24 is based on the simplified formulation introduced in Eq. 13.64. Two specific regions exhibit more pronounced deviations. The first, at $t \approx 250$ s, corresponds to a climbing turn. In this condition, the roll rate returns close to zero

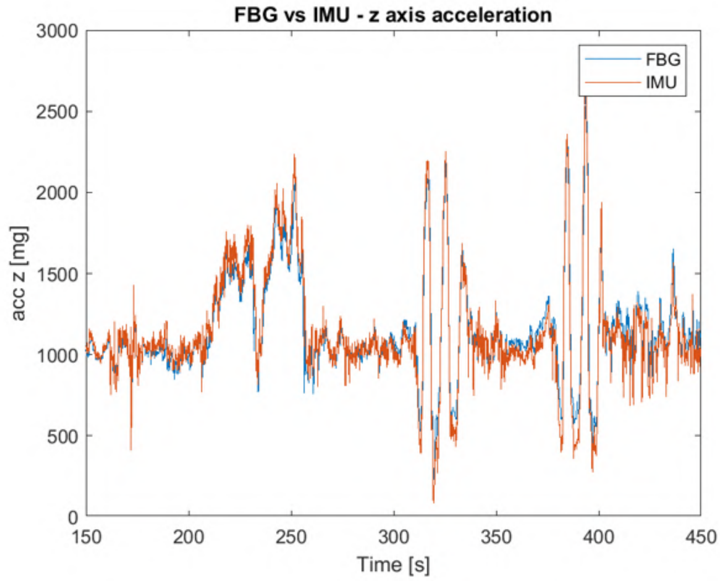


Fig. 13.23 Comparison between FBG-derived and IMU load factor.

after the initial maneuver, while the pitch rate remains positive and the load factor varies. Since the simplified formulation does not fully compensate for the bending contribution induced by vertical acceleration, this component introduces a bias in the estimation of $q$ from the FBG signals. The second region, between $t \approx 300$ s and $t \approx 400$ s, corresponds to a sequence of dives and pull-ups. In this case, a slight underestimation of the FBG-derived signal with respect to the IMU measurement can be observed. However, a closer inspection reveals that the IMU dataset contains isolated out-of-scale measurements (tending toward $-\infty$), which, when filtered, generate artificial peaks not representative of the actual physical behavior. This effect highlights an important aspect: while inertial measurements may be affected by numerical artifacts or sensor saturation, the optical sensing system directly measures structural deformation and therefore provides a physically consistent response.

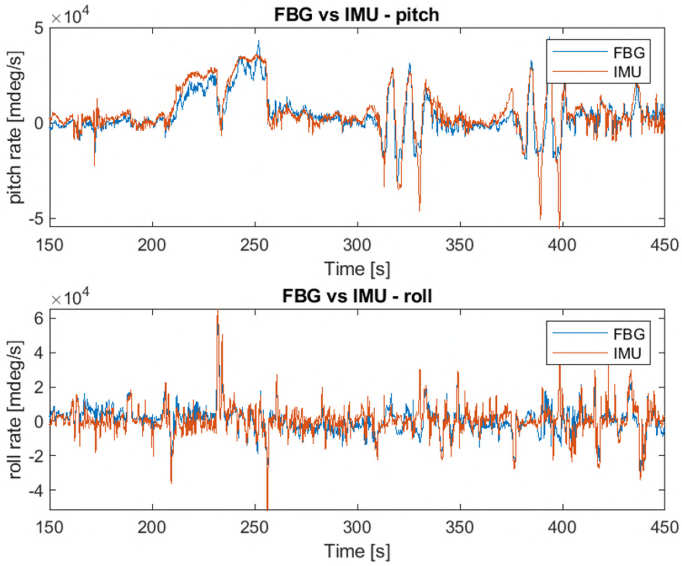


Fig. 13.24 Comparison between FBG-derived and IMU roll and pitch rates.

### 13.5.6 Validation on Different Flight Campaigns

The same correlation coefficients identified in the previous section were applied to a second flight test characterized by different maneuver profiles, including combined and more aggressive flight conditions.

The results confirm both the validity of the proposed methodology and the repeatability of the measurements obtained through the optical sensing system. For all three estimated quantities $(n, p, q)$, the same level of agreement observed in the previous case is maintained, demonstrating the robustness of the approach across different flight conditions.

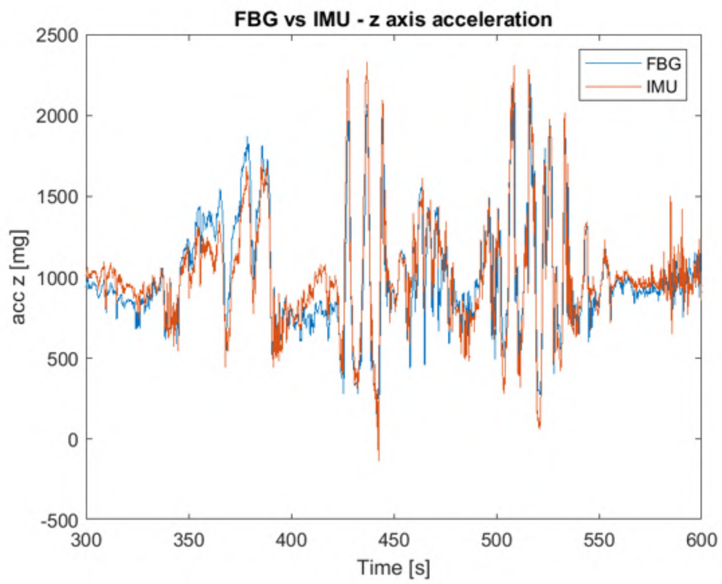


Fig. 13.25 Load factor estimation on a second flight campaign.

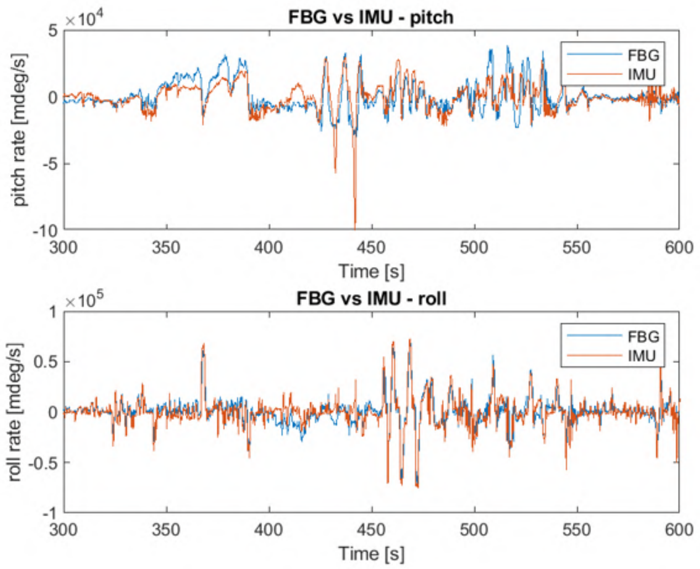


Fig. 13.26 Roll and pitch rate estimation on a second flight campaign.

## 13.6 Results and Further Developments

The results described in this chapter represent the highest level of technological maturity achieved through the research activities conducted in this work. The Sirius platform, in fact, made it possible to simultaneously satisfy several functional requirements that had previously only been formulated conceptually or tested in laboratory conditions, validating them in a highly relevant operational environment, namely in flight.
First, the Sirius platform represents a first demonstrator of a distributed, integrated, and fully connected FBG optical sensor network embedded within the reference structure. The integration of the optical fibers was performed directly during the lamination and assembly phases of the aircraft. At the end of the manufacturing process, the sensing network becomes an integral part of the structure itself, requiring only the connection of a simple optical patch cord before the start of data acquisition. This level of sensor integration is closely related to the capability of estimating flight kinematic parameters directly through the optical sensors and comparing them with the measurements recorded by the onboard inertial platform. The excellent experimental agreement observed allows the Sirius platform to be considered a prototype of an intelligent structure validated under operational conditions. At the same time, the platform demonstrated the high modularity of the measurement system. In addition to the sensors laminated within the structure, it was possible to connect dedicated measurement points designed for monitoring specific local components, such as the servo support and the aileron deflection.
Due to constraints in terms of time, cost, and available onboard space, the thermal characterization of the propulsion system previously carried out with Anubi was not replicated in the Sirius configuration, nor were the near real-time telemetry and augmented reality visualization systems implemented. Nevertheless, the results presented in this chapter allow envisioning, in the near future, the integration of both sensing architectures within the same platform. This would enable the simultaneous execution of all the measurements previously performed separately on the two aircraft. Overall, the proposed approach demonstrates that optical fiber sensing is not limited to structural monitoring but can be extended to real-time estimation of flight dynamics, paving the way for a new class of sensing-enabled aerospace systems.

# Chapter 14

# Conclusions and Future Perspectives

This thesis presented the development, implementation, and validation of an integrated optical sensing framework based on Fiber Bragg Grating (FBG) technology for structural monitoring and flight dynamics estimation in unmanned aerial vehicles (UAVs). The work addressed the problem from a system-level perspective, spanning from sensor design and integration to data acquisition, transmission, processing, and visualization in both laboratory and real flight conditions.

The research activities were structured in progressive phases, starting from the characterization of FBG sensors and their bonding methodologies, followed by the development of data acquisition architectures, and culminating in full-scale experimental validation on flight platforms.

## 14.1 Main Contributions

The main contributions of this work can be summarized as follows:

- Development of a complete sensing chain based on FBG technology, including sensor design, bonding procedures, and integration within composite structures;
- Design and implementation of two different data acquisition architectures (Raspberry Pi–based and mini-PC–based), highlighting trade-offs between simplicity, flexibility, and achievable sampling performance;

- Development of a cloud-based data management system enabling near real-time acquisition, storage, and visualization of sensor data;
- Implementation of advanced visualization tools, including a 3D desktop viewer and an augmented reality interface, improving human–machine interaction and situational awareness;
- Experimental validation of distributed optical sensing for structural monitoring in both laboratory and flight conditions;
- Demonstration of the capability to estimate key flight parameters (load factor, roll rate, and pitch rate) directly from strain measurements obtained through embedded FBG sensors;
- Formulation of a mathematical model linking structural strain measurements to aircraft kinematics, enabling the use of optical sensors as virtual inertial sensors;
- Validation of the proposed approach through flight testing campaigns, showing strong agreement with traditional IMU measurements.

## 14.2 Scientific and Technological Impact

The results obtained in this thesis demonstrate that FBG-based sensing systems can go beyond traditional structural health monitoring applications. In particular, the capability to estimate flight dynamics parameters directly from structural deformation introduces a paradigm shift in the role of embedded sensors within aerospace systems.

The concept of *smart structures* is here concretely demonstrated: the structure is no longer a passive element to be monitored, but an active sensing component capable of providing information on its own operational state.

From a technological standpoint, the work shows that:

- optical sensing systems can be effectively integrated into composite UAV structures without compromising structural integrity;
- distributed sensing networks can provide high-resolution, physically meaningful data under real operational conditions;

- optical sensors can complement, and in some cases support, validate or substitute, traditional inertial measurement systems;
- advanced data visualization techniques, including augmented reality, can significantly enhance the usability and interpretability of complex datasets.

## 14.3 Limitations of the Current Work

Despite the encouraging results, several limitations emerged during the experimental campaigns:

- the sensor layout, particularly in early configurations, was not fully optimized for complete observability of all flight dynamics parameters;
- the integration process of optical fibers within complex structures remains sensitive to manufacturing constraints and potential damage during assembly;
- the estimation models rely on linear assumptions and require calibration procedures that may limit direct scalability;
- environmental effects (temperature variations, humidity, and vibrations) introduce disturbances that require advanced filtering and compensation strategies;
- some functionalities (e.g., full integration of telemetry, thermal monitoring, and AR visualization) were validated separately but not yet unified in a single platform.

## 14.4 Future Perspectives

The results obtained open several directions for future research and development.

From a methodological perspective, future work will focus on:

- the development of advanced sensor fusion algorithms combining FBG data with inertial and navigation measurements;

- the implementation of adaptive and nonlinear models to improve the accuracy of flight parameter estimation;
- the extension of the sensing network to include additional structural components (e.g., tail surfaces) to enable full state reconstruction.

From a technological perspective, key developments include:

- the integration of all sensing architectures (structural, thermal, telemetry, and AR visualization) into a single unified system;
- the optimization of fiber routing and connector design to improve robustness and ease of installation;
- the development of miniaturized and embedded interrogators for fully onboard autonomous operation.

Finally, from an application perspective, the proposed approach can be extended beyond UAVs to a wide range of aerospace and mechanical systems, including:

- full-scale aircraft structural monitoring;
- space structures and deployable systems;
- advanced composite components with embedded sensing capabilities;
- smart infrastructures and distributed monitoring systems.

## 14.5 Final Remarks

This work demonstrates that optical fiber sensing, when combined with appropriate system-level design and data processing strategies, can enable a new generation of sensing-enabled aerospace systems. The ability to extract both structural and dynamic information from the same sensing network represents a key step toward the realization of fully integrated, multifunctional, and intelligent structures.

The transition from *sensing structures* to *structures that sense and interpret their own behavior* represents not only a technological advancement, but also a conceptual evolution in the design of future aerospace systems.

# References


[1] Safa O Kasap et al. *Optoelectronics and photonics*. Vol. 218. Pearson Education UK, 2013.

[2] Satish Addanki, I Sadegh Amiri, and P Yupapin. “Review of optical fibers-introduction and applications in fiber lasers”. In: *Results in Physics* 10 (2018), pp. 743–750.

[3] KTV Grattan and YN Ning. “Classification of optical fiber sensors”. In: *Optical Fiber Sensor Technology: Devices and Technology*. Springer, 1998, pp. 1–35.

[4] Jinjie Chen, Bo Liu, and Hao Zhang. “Review of fiber Bragg grating sensor technology”. In: *Frontiers of Optoelectronics in China* 4.2 (2011), pp. 204–212.

[5] R. Measures. *Structural Monitoring with Fiber Optic Technology*. Academic Press, 2001.

[6] Farhad Ansari. *Fibre optic methods for structural health monitoring*. 2009.

[7] Kenneth TV Grattan and Tong Sun. “Fiber optic sensor technology: an overview”. In: *Sensors and Actuators A: Physical* 82.1-3 (2000), pp. 40–61.

[8] Eric Udd. “Fiber optic smart structures”. In: *Fiber Optic Sensors: An Introduction for Engineers and Scientists* (2011), pp. 373–398.

[9] Byoungho Lee. “Review of the present status of optical fiber sensors”. In: *Optical fiber technology* 9.2 (2003), pp. 57–79.

[10] A. Hartog. *Distributed Optical Fibre Sensors*. CRC Press, 2017.

[11] X. Bao and L. Chen. “Recent progress in distributed fiber optic sensors”. In: *Sensors* (2012).

[12] B. Culshaw. “Optical fiber sensor technologies”. In: *Journal of Lightwave Technology* (2004).

[13] E. Udd. *Fiber Optic Smart Structures*. Wiley, 1995.

[14] T. Erdogan. “Fiber grating spectra”. In: *Journal of Lightwave Technology* (1997).

[15] K. et al. Cook. “Regenerated fiber Bragg gratings for high-temperature sensing”. In: *Optics Letters* (2004).

[16] L. Zhang and K. Grattan. “Optical fiber sensors for high temperature environments”. In: *Measurement Science and Technology* (2008).

[17] X. et al. Wu. “Sapphire fiber Bragg grating sensors for extreme temperature sensing”. In: *Optics Express* (2025).

[18] S. et al. Girard. “Radiation effects on silica optical fibers”. In: *IEEE Transactions on Nuclear Science* (2013).

[19] S. Mihailov. “Fiber Bragg grating sensors for harsh environments”. In: *Sensors* (2012).

[20] Alberto Rovera et al. “Fiber Optic Sensors for Harsh and High Radiation Environments in Aerospace Applications”. In: *Sensors* 23.5 (2023).

[21] T. et al. Yokogawa. “Fiber optic sensing in chemically aggressive environments”. In: *Sensors and Actuators B* (2004).

[22] A. et al. Cusano. “Fiber optic chemical sensors”. In: *Sensors* (2009).

[23] A. et al. Leal-Junior. “Optical fiber sensors in aerospace applications”. In: *IEEE Sensors Journal* (2018).

[24] A. D. et al. Kersey. “Fiber grating sensors”. In: *Journal of Lightwave Technology* (1997).

[25] E. et al. Lally. “Fiber Bragg grating sensors for strain and vibration measurements”. In: *IEEE Sensors* (1998).

[26] T. et al. Guo. “Embedding fiber sensors in metallic structures”. In: *Optics and Lasers in Engineering* (2012).

[27] H. et al. Li. “Strain transfer analysis of bonded FBG sensors”. In: *Smart Materials and Structures* (2004).

[28] B. Glisic and D. Inaudi. *Fibre optic methods for structural health monitoring*. Wiley, 2007.

[29] J. Leng and A. Asundi. “Structural health monitoring of composite materials using fiber optic sensors”. In: *Sensors and Actuators A* (2002).

[30] S. et al. Takeda. “Impact damage detection in composite structures using FBG sensors”. In: *Composites Science and Technology* (2007).

[31] D. et al. Kinet. “Fiber Bragg grating sensors toward structural health monitoring”. In: *Sensors* (2014).

[32] B. et al. Childers. “Use of thousands of Bragg grating strain sensors distributed on an aircraft structure”. In: *Smart Materials and Structures* (2001).

[33] M. et al. Nicolas. “Large scale applications using FBG sensors”. In: *Aerospace* (2016).

[34] R. Di Sante. “Fibre optic sensors for structural health monitoring of aircraft composite structures”. In: *Sensors* (2015).

[35] Helena Rocha, Christopher Semprimoschnig, and João P Nunes. “Sensors for process and structural health monitoring of aerospace composites: A review”. In: *Engineering Structures* 237 (2021), p. 112231.

[36] Iker García et al. “Optical fiber sensors for aircraft structural health monitoring”. In: *Sensors* 15.7 (2015), pp. 15494–15519.

[37] D. et al. Wada. “Flight demonstration of aircraft wing monitoring using optical fiber sensing”. In: *Smart Materials and Structures* (2019).

[38] A. et al. Iele. “Load monitoring of aircraft landing gears using fiber optic sensors”. In: *Sensors and Actuators A* (2018).

[39] A. Gustafsson. “FBG-based acquisition systems for overheat detection”. In: *Avionics Systems* (2019).

[40] A. et al. Behbahani. “Optical communications and sensing for avionics”. In: *Springer* (2020).

[41] Massimiliano Gabardi et al. “Embedding fiber Bragg grating sensors in carbon composite structures for accurate strain measurement”. In: *IEEE Sensors Journal* 23.15 (2023), pp. 16882–16892.

[42] Z. et al. Ma. “Aircraft wing shape measurement using FBG sensors”. In: *Sensors* (2018).

[43] J. et al. Nicolas. “Large scale applications using FBG sensors”. In: *Aerospace* (2016).

[44] H. et al. Choi. “In-flight structural monitoring using FBG sensors”. In: *Measurement* (2018).

[45] Y.J. Rao. “In-fibre Bragg grating sensors”. In: *Measurement Science and Technology* (1997).

[46] M. et al. Pakmehr. “Optical fiber sensors for gas turbine engines”. In: *Aerospace Conference Proceedings* (2013).

[47] J. et al. Kim. “Embedded fiber Bragg grating sensors in turbine blades”. In: *Additive Manufacturing* (2022).

[48] T. et al. Berexa. “Fiber optic temperature sensors embedded in turbine blades”. In: *ASME Turbo Expo* (2023).

[49] M. Froggatt and J. Moore. “Distributed strain measurement in optical fiber”. In: *Applied Optics* (1998).

[50] E. et al. Friebele. “Optical fiber sensors for spacecraft applications”. In: *Smart Materials and Structures* (1999).

[51] S. et al. Kabashima. “Structural health monitoring using FBG sensors in space”. In: *Aerospace* (2001).

[52] D. et al. Shi. “Distributed FBG sensors for spacecraft health monitoring”. In: *Sensors* (2017).

[53] T. et al. Juwet. “Monitoring of composite structures for reusable space applications”. In: *Sensors* (2024).

[54] Hong-Il Kim et al. “Measurement of the thermal expansion of space structures using fiber Bragg grating sensors and displacement measuring interferometers”. In: *Measurement Science and Technology* 21.8 (2010), p. 085704.

[55] S. et al. Abad. “Fiber optic sensing subsystem for temperature monitoring in space”. In: *IEEE* (2017).

[56] C. et al. Wang. “FBG temperature measurement methods for space applications”. In: *Review of Scientific Instruments* (2020).

[57] Stephen J Mihailov. “Femtosecond laser-induced Bragg gratings in silica-based fibers for harsh environment sensing”. In: *Apl Photonics* 8.7 (2023).

[58] D. et al. Kinet. “Fiber Bragg grating sensors toward structural health monitoring”. In: *Sensors* (2014).

[59] P. et al. Wei. “Shape monitoring of satellite structures using FBG sensors”. In: *IEEE* (2017).

[60] Y. et al. Jiang. “3D reconstruction of spacecraft using FBG arrays”. In: *Optoelectronics Letters* (2022).

[61] J. et al. Jin. “Micrometeoroid and orbital debris impact detection using FBG”. In: *IEEE Transactions* (2021).

[62] M. et al. Perikala. “FBG flow sensor for space applications”. In: *IEEE Sensors Journal* (2021).

[63] S. et al. Park. “Usage of fiber Bragg grating sensors in low Earth orbit”. In: *Sensors* (2008).

[64] L. et al. Zhu. “On-orbit measurement method using optical sensing”. In: *IEEE Transactions* (2025).

[65] R. et al. Kruzelecky. “Fiber Optic Sensor Demonstrator for spacecraft monitoring”. In: *ESA / Demonstrator* (2017).

[66] Iain Mckenzie and Nikos Karafolas. “Fiber optic sensing in space structures: the experience of the European Space Agency”. In: *17th International Conference on Optical Fibre Sensors*. Vol. 5855. SPIE. 2005, pp. 262–269.

[67] Iain McKenzie et al. “Fiber optic sensing in spacecraft engineering: An historical perspective from the European space agency”. In: *Frontiers in physics* 9 (2021), p. 719441.

[68] Carlo Giovanni Ferro et al. “Experimental development and evaluation of a fiber bragg grating-based outside air temperature sensor for aircraft applications”. In: *Transportation Engineering* 14 (2023), p. 100214.

[69] Hon Man Chan. “Novel Fiber Optic Sensing Arrays with Enhanced Sensitivity in Cryogenic Temperatures”. In: (2021).

[70] Alessandro Aimasso, Matteo Davide Lorenzo Dalla Vedova, and Paolo Maggiore. “Sensitivity analysis of FBG sensors for detection of fast temperature changes”. In: *Journal of Physics: Conference Series*. Vol. 2590. 1. IOP Publishing. 2023, p. 012006.

[71] Belema P Alalibo et al. “Investigation of the effect of bonding points on metal surface-mounted FBG sensors for electric machines”. In: *Progress in Electromagnetics Research C* 97 (2019), pp. 255–265.

[72] Gaetano Quattrocchi et al. “Preliminary Analysis on Environmental and Intrinsic Factors on FBG-Based Vibration Sensors”. In: *Journal of Physics: Conference Series*. Vol. 1977. 1. IOP Publishing. 2021, p. 012011.

[73] Oliver Humbach et al. “Analysis of OH absorption bands in synthetic silica”. In: *Journal of non-crystalline solids* 203 (1996), pp. 19–26.

[74] Govind P Agrawal. “Nonlinear fiber optics”. In: *Nonlinear Science at the Dawn of the 21st Century*. Springer, 2000, pp. 195–211.

[75] Masataka Nakazawa. “Rayleigh backscattering theory for single-mode optical fibers”. In: *Journal of the Optical Society of America* 73.9 (1983), pp. 1175–1180.

[76] DF Welch et al. “High-power diode laser arrays with silicon Impurity-Induced disordered nonabsorbing mirrors”. In: *Optical Fiber Communication Conference*. Optica Publishing Group. 1987, ME3.

[77] Dietrich Marcuse. “Curvature loss formula for optical fibers”. In: *Journal of the Optical Society of America* 66.3 (1976), pp. 216–220.

[78] Ross T Schermer and James H Cole. “Improved bend loss formula verified for optical fiber by simulation and experiment”. In: *IEEE journal of quantum electronics* 43.10 (2007), pp. 899–909.

[79] European Cooperation for Space Standardization. *ECSS-E-HB-32-21A – Adhesive bonding handbook*. ECSS Executive Secretariat. ECSS Secretariat. ESA-ESTEC, Noordwijk, The Netherlands, Mar. 2011. URL: https://ecss.nl/hbstms/ecss-e-hb-32-21a-adhesive-bonding-handbook/ (visited on 03/30/2026).

[80] Marshall Smith et al. “The artemis program: An overview of nasa’s activities to return humans to the moon”. In: *2020 IEEE aerospace conference*. IEEE. 2020, pp. 1–10.

[81] Roberto Torre, Aidan Cowley, and Carlo Giovanni Ferro. “Low binder content bricks: a regolith-based solution for sustainable surface construction on the Moon”. In: *Discover applied sciences* 6.3 (2024), p. 88.

[82] Edoardo Piovano. “Development of an experimental testbench for systems performance monitoring through optical fiber-based sensors”. Politecnico di Torino, 2024.

[83] Leonardo Baldo et al. “Implementing phm for legacy flight control actuators through operational aircraft data: Approach and lessons learned”. In: *Results in Engineering* (2025), p. 107214.

[84] Leonardo Baldo et al. “Mission Profile Clustering for Usage-Based Health Modeling of Flight Control Actuators Applied to a Fleet of Advanced Jet Trainers”. In: *Annual Conference of the PHM Society*. Vol. 17. 1. 2025.

[85] Leonardo Baldo et al. “A systematic literature review on phm strategies for (hydraulic) primary flight control actuation systems”. In: *Actuators*. Vol. 14. 8. MDPI. 2025, p. 382.

[86] A. C. Marceddu and B. Montrucchio. “Storage and Visualization On-The-Ground and in Near Real-Time of the Data Measured by the Optical Sensors Connected to a Flying Test Bench”. In: *Materials Research Proceedings*. Vol. 33. 2023, pp. 277–280.

[87] Politecnico di Torino. *PhotoNext Middleware*. https://github.com/CARDIGANSPoliTo/PhotoNext_Middleware. [Online]. Accessed on Jan. 12, 2023.

[88] Mauro Guerrera. “Algorithms and methods for Fiber Bragg Gratings sensor networks”. MA thesis. Politecnico di Torino, 2018.

[89] Politecnico di Torino. *PhotoNext 3D Viewer*. https://github.com/CARDIGANSPoliTo/PhotoNext_3D_Viewer. [Online]. Accessed on Jan. 12, 2023.

[90] The Qt Company. *Qt*. https://www.qt.io/. [Online]. Accessed on Oct. 30, 2023.

[91] Politecnico di Torino. *PhotoNext FBG Data Analyzer*. https://github.com/CARDIGANSPoliTo/PhotoNext_FBG_Data_Analyzer. [Online]. Accessed on Oct. 30, 2023.

[92] Amazon.it. *Box Android TV 4GB RAM 32GB ROM, Quad Core Processor 4K HD*. Consultato il 30 marzo 2026. 2026. URL: https://www.amazon.it/dp/B0CGRJ7D38 (visited on 03/30/2026).

[93] Jaziar Radianti et al. “A systematic review of immersive virtual reality applications for higher education: Design elements, lessons learned, and research agenda”. In: *Computers & Education* 147 (2020), p. 103778.

[94] Simone Restivo et al. “Interacting with Ancient Egypt Remains in High-Fidelity Virtual Reality Experiences”. In: *Eurographics Workshop on Graphics and Cultural Heritage*. Ed. by Alberto Bucciero et al. The Eurographics Association, 2023.

[95] Antonio Bernardo. “Virtual Reality and Simulation in Neurosurgical Training”. In: *World Neurosurgery* 106 (2017), pp. 1015–1029.

[96] Yousuf M. Khalifa et al. “Virtual Reality in Ophthalmology Training”. In: *Survey of Ophthalmology* 51.3 (2006), pp. 259–273.

[97] Shih-Ching Yeh et al. “A multiplayer online car racing virtual-reality game based on internet of brains”. In: *Journal of Systems Architecture* 89 (2018), pp. 30–40.

[98] Emrah Akman and Recep Çakır. “The effect of educational virtual reality game on primary school students’ achievement and engagement in mathematics”. In: *Interactive Learning Environments* 31.3 (2023), pp. 1467–1484.

[99] Giancarlo Avalle et al. “An Augmented Reality System to Support Fault Visualization in Industrial Robotic Tasks”. In: *IEEE Access* 7 (2019), pp. 132343–132359.

[100] Claudio Kirner and Tereza G. Kirner. “A Data Visualization Virtual Environment Supported by Augmented Reality”. In: *2006 IEEE International Conference on Systems, Man and Cybernetics*. Vol. 1. 2006, pp. 97–102.

[101] Federico Manuri et al. “A Workflow Analysis for Implementing AR-Based Maintenance Procedures”. In: *Augmented and Virtual Reality*. Ed. by Lucio Tommaso De Paolis and Antonio Mongelli. Cham: Springer International Publishing, 2014, pp. 185–200.

[102] Fabrizio Lamberti et al. “Challenges, Opportunities, and Future Trends of Emerging Techniques for Augmented Reality-Based Maintenance”. In: *IEEE Transactions on Emerging Topics in Computing* 2.4 (2014), pp. 411–421.

[103] Francesco De Pace et al. “A systematic review of Augmented Reality interfaces for collaborative industrial robots”. In: *Computers & Industrial Engineering* 149 (2020), p. 106806.

[104] Petr Hořejší. “Augmented Reality System for Virtual Training of Parts Assembly”. In: *Procedia Engineering* 100 (2015). 25th DAAAM International Symposium on Intelligent Manufacturing and Automation, 2014, pp. 699–706.

[105] Harald Schaffernak et al. “Novel Mixed Reality Use Cases for Pilot Training”. In: *Education Sciences* 12.5, 345 (2022).

[106] Tuomas Kantonen, Charles Woodward, and Neil Katz. “Mixed reality in virtual world teleconferencing”. In: *2010 IEEE Virtual Reality Conference (VR)*. 2010, pp. 179–182.

[107] Tom Williams et al. “Virtual, Augmented, and Mixed Reality for Human-Robot Interaction”. In: *Companion of the 2018 ACM/IEEE International Conference on Human-Robot Interaction*. HRI ’18. New York, NY, USA: Association for Computing Machinery, 2018, pp. 403–404. ISBN: 9781450356152.

[108] Antonio Costantino Marceddu et al. “Creation of a Support Software for the Development of a System for Sending and Visualizing FBG Sensor Data for Aerospace Application”. In: *2023 IEEE 10th International Workshop on Metrology for AeroSpace (MetroAeroSpace)*. 2023, pp. 487–491.

[109] Leonardo Baldo et al. “Hybrid Offline-Online Machine Learning Framework for Real-Time UAV Battery Voltage Prediction”. In: *Aerospace Science and Technology* (2026), p. 112217.

[110] Jorge E García Bustos et al. “In Situ Estimation of Li-Ion Battery State of Health Using On-Board Electrical Measurements for Electromobility Applications”. In: *Batteries* 11.12 (2025), p. 451.

# Appendix A

# Design of Experiments (DOE)

Design of Experiments (DOE) is a systematic methodology used to plan, conduct, and analyze experiments in order to efficiently investigate the relationship between input variables (factors) and output responses. The primary objective of DOE is to maximize the amount of information obtained from a limited number of experiments, while ensuring statistical significance and reproducibility of the results.

## A.1 Basic Concepts

In the DOE framework, an experimental process is described in terms of:

- **Factors**: independent variables that can be controlled or observed (e.g., load, temperature, input signals);
- **Levels**: the specific values or conditions assigned to each factor;
- **Responses**: measured outputs of the system (e.g., strain, temperature, displacement);
- **Noise variables**: uncontrolled factors that may affect the response (e.g., environmental conditions).

The goal is to determine how variations in the factors influence the responses, and to identify possible interactions among them.

## A.2 Experimental Design Strategies

Several DOE strategies can be adopted depending on the complexity of the system:

- **One-factor-at-a-time (OFAT)** approaches, where only one variable is changed while others are kept constant;
- **Full factorial designs**, where all combinations of factor levels are tested;
- **Fractional factorial designs**, which reduce the number of experiments while preserving the ability to estimate main effects and selected interactions;
- **Response surface methods (RSM)**, used to model nonlinear relationships between factors and responses.

In practice, the choice of the experimental design depends on the available resources, the number of factors, and the desired level of accuracy.

## A.3 Advantages of DOE

Compared to unstructured experimental approaches, DOE provides several advantages:

- efficient use of experimental resources;
- ability to identify interactions between multiple factors;
- improved repeatability and robustness of results;
- support for model development and system identification.

## A.4 Limitations

Despite its advantages, DOE may be difficult to apply in systems characterized by:

- strong environmental variability;

- limited controllability of input factors;
- high operational costs (e.g., flight testing scenarios);
- safety constraints limiting the range of test conditions.

In such cases, DOE principles are often adapted rather than strictly applied.

## A.5 Remarks

In this work, DOE principles are used as a methodological reference to guide the planning and interpretation of experimental activities, particularly in the definition of test conditions and in the analysis of sensor responses under varying inputs.